Etude de solutions OFDM en technologie "Photonique Silicium" pour les futures générations de réseaux optiques passifs

Giovanni Beninca de Farias Beninca de Farias

UNIVERSITÉ DE GRENOBLE

THÈSE

Pour obtenir le grade de

DOCTEUR DE L'UNIVERSITÉ DE GRENOBLE

Spécialité : **Signal, Image, Parole et Télécom**

Arrêté ministériel :

Présentée par

Giovanni BENINCA DE FARIAS

Thèse dirigée par **Alexei TCHELNOKOV**

préparée au sein du **CEA-Leti**
et de **EEATS**

Future Passive Optical Networks : Silicon Photonics based Optical OFDM Solutions

Thèse soutenue publiquement le **05/12/2013**,
devant le jury composé de :

M. , Jean-Emmanuel BROQUIN
Grenoble INP, Président
M. , Peter O'SSIEUR
Tyndall UCC, Rapporteur
Mme. , Christelle AUPETIT-BERTHELEMOT
XLIM, Rapporteur
M., Didier ERASME
Télécom ParisTech, Examinateur
M., Benoit CHARBONNIER
Orange Labs, Examinateur
M., Alexei TCHELNOKOV
CEA-Leti, Directeur de thèse
Mme. , Sylvie MENEZO
CEA-Leti, Encadrante de thèse

Dedicated to my wife Nadia...

Acknowledgements

The work for this PhD thesis was carried out at the CEA-Leti, Grenoble, France. The success of this thesis would not be possible without the support of so many people.

I would like to start by acknowledging my thesis co-supervisor and head of the Silicon Photonics Laboratory in the CEA-Leti, Sylvie Menezo. She was always there for me during the three years of my PhD with her precious comments and suggestions. I believe I would not be here today without her advices and above all her encouragements to be always the best I can be. Many thanks also to Alexei Tchelnokov, former head of the Silicon Photonics Laboratory and my thesis supervisor, for the encouragements and precious remarks. He always was there for me when I needed. I consider myself lucky for having worked under the supervision of Sylvie and Alexei.

A special thanks to Denis Mestdagh, the person who started this project and gave me the opportunity to pursue my PhD. I am also very grateful to Jean-Marc Brossier, Olivier Michel, Yannis LeGuennec and Ghislaine Maury for the fruitful discussions we had during the first year of my PhD that guided me to the right path in my thesis.

Thanks to the thesis reviewers, Peter Ossieur and Christelle Aupetit-Berthelemot as well as the jury members, Benoit Charbonnier, Dider Erasme and Jean-Emmanuel Broquin for having accepted to be a part of the jury and spent their precious time to review and comment on my thesis. It is a pleasure to have such a qualified jury for evaluating my work.

I am very grateful to my colleagues at the Silicon Phonics Laboratory of the CEA-Leti for all the support during the three years. I believe that the good atmosphere in the laboratory was essential for the success of this thesis. Special thanks to Badhise Ben Bakir and Antoine Descos for their work on the hybrid III/V-on-silicon laser sources that led to key achievements in this thesis. Also thanks to Philippe Grosse, Karen Ribaud, Edouard Grellier, André Myko, Benjamin Blampey, Olivier Dubray, Boris Caire-Remmonay, Stéphane Bernabe, Leopold Virot, Jean-Marc Fédéli, Maryse Fournier among many others. I also acknowledge members of the micro-electronic department in the CEA-Leti, Luc Maret, Matthiew Des Noes, Patrik Rosson, Jerome Prouvée, among others, for their contribution to the success of this thesis. A thanks to the heads of the photonics service, Patrick Chaton and later, Ludovic Poupinet for their support during the thesis.

Thanks to Luiz Anet Neto and the Orange Labs staff that welcomed me in their research center for a collaboration work that succesfully led to a publication in a leader international conference. I also acknowledge the IEF research staff for the design of the silicon ring-resonator modulator that led to one of the most important results of this thesis.

The unconditional support of my family, specially my father Armando, my mother Regina and my sister Maria Amélia, gave me the strength to overcome the difficulties found on the way even if they were far away from France. Many thanks for all my friends in Grenoble, specially the Brazilian community for the many days and nights spent together and the friendship achieved over the years ; they are too many to be cited here.

Last but not least, I thank my wife Nadia for her unconditional love and her belief on the

success of my work. Thank you for being there for all the ups and downs of my work during this three years and for putting up with me during the very stressful period of writing the thesis. I dedicate this PhD to her.

Table des matières

General Introduction

Context and Motivations

In the last 30 years, we have experienced a digital revolution that changed the way we live. The earliest form of bidirectional communication, the electric telegraph, was invented in 1836. With the invention of the telephone in 1876, the main form of communication became voice transmission. At the end of the Second World War, television was manufactured in very large scale, and operators started to broadcast their signals. Back then, television was a unidirectional service - user could not control the content scheduling. In 1969, the Arpanet was invented. It was the first network in the world to use TCP/IP protocols, and the progenitor of Internet. Since then, Internet has experienced an exponential growth. According to Intel [1], the number of connected devices to the internet is equal today, to the world population, and it is forecasted a twofold increase by 2015. Media and voice services are now being transferred through the IP network (VoIP and IPTV). Video-on-Demand (VoD) applications enable any user to access video content at any time at their convenience.

High-speed internet access and digital media services were firstly provided by copper-based access networks with the Digital Subscriber Line (xDSL) technology. However, the scaling of this technology in terms of power consumption and bandwidth has become an issue since the beginning of the 2000's. Back then, the operators started to consider deploying optical fiber for access networks. In this context, it is generally agreed that optical fiber communication is required in order to respond to the growing bandwidth demand. The network architecture that brings the optical fiber to the user's home is called Fiber-to-the-Home/Building (FTTH/B), enabled by the large deployment of optical access networks. Indeed, in the year of 2011, the number of FTTH/B users grew by 54% to reach almost 67 million worldwide [2]. A recent report [3] indicates that Japan is the leader in fiber broadband access, with 60% of FTTH/B subscribers and 90% of the population being covered by the optical fiber.

The bandwidth requirements for next-generation optical access networks are driven by media services over IP such as UltraHD ($> 180 Mbps$), 3D HDTV (100Mbps) and 3D UltraHDTV (300Mbps), among others. Additionally, more and more computing applications are moving into the cloud. Public cloud service providers like Amazon AWS, Microsoft and Google offer access through the internet. Cloud services may include data storage and Software as a Service (SaaS) - where applications are not run locally by the user, but in data-centers, and the inputs/outputs are transferred over the networks. This requires a very high data-rate for file-transfer between the user and data-centers. According to a Cisco forecast for traffic growth from 2012 to 2017 [4], the global IP traffic will increase from 56 Exabytes to 121 Exabytes per month. From this traffic, Cisco forecasts that by 2017 more than 73% of the total traffic will be governed by video services (Internet and IP-based), and the rest divided between file sharing and web/data (cf. figure 1).

Current optical access networks architectures make use of traditional On-Off Keying (OOK) modulation because of the low-complexity of the transceivers. This modulation format sends one bit of information every symbol. For simplicity, throughout this thesis, the OOK notation assumes Non-Return to Zero (NRZ)-OOK modulation, which is detailed in subsection 3.2.1.

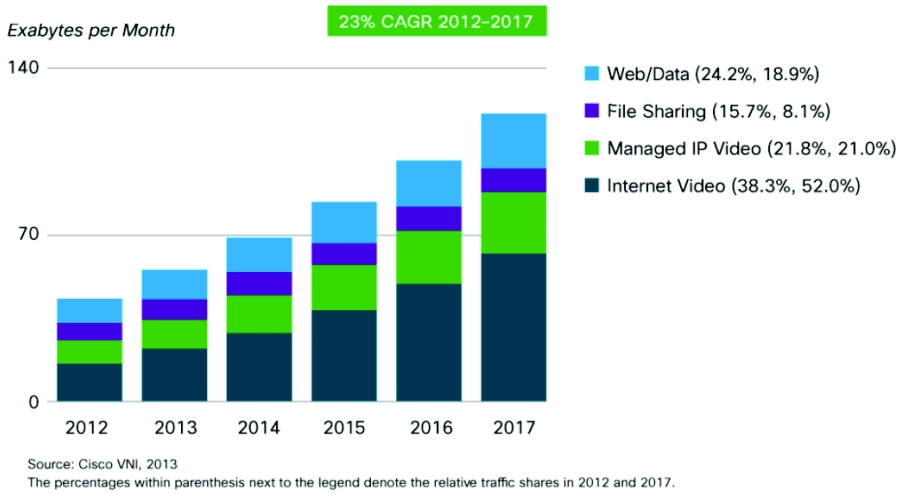

FIGURE 1: Cisco forecast for global IP traffic growth from 2012 to 2017 (Source [4]).

However, the [bit-rate × reach] product is limited because of the fiber chromatic dispersion and the transmitter characteristics, which represents a bottleneck for future generations of optical access networks. In summary, new technologies should allow 1) to increase [bit-rate × reach] product of the network and 2) to be as low-cost as possible in terms of operating and implementation expenses (network and transceivers).

a. Improving Performance

Performance can be improved by using advanced modulation techniques that are spectrally efficient (spectral-efficiency, equal to the ratio between the bit-rate and usable bandwidth, is expressed in bps/Hz) and immune against Inter-symbol Inteference (ISI) caused by chromatic dispersion of the Single-mode Fiber (SMF). Orthogonal Frequency Division Multiplexing (OFDM) modulation has both these features. Direct-detection optical OFDM is preferred for Passive Optical Networks (PON) applications as the associated receiver architectures are much simpler than coherent-detection ones.

OFDM modulation is a widely used technique for Radio-Frequency (RF) communications. A high serial data stream with high bit rate B is divided into N multiple parallel streams with bit-rate B/N. Each stream is transmitted over a different subcarrier, and the N subcarriers are multiplexed in the frequency domain. A key feature of OFDM that attracted much attention from the RF community is the immunity against ISI caused by dispersive characteristic of the RF channel. This is because the symbol-rate of each subcarrier is much lower than the equivalent symbol-rate of a single-carrier. For the same reason, optical OFDM is an interesting solution for optical transmission systems. The particularity of OFDM over classical Frequency Division Multiplexing (FDM) schemes is that the OFDM subcarriers partially overlap while still maintaining orthogonality between each other. In this way, the spectral efficiency is maximized. The OFDM modem can be implemented through a Digital Signal Processor (DSP) using dedicated Application-Specific Integrated Circuits (ASIC) technology, which can be produced with the mass-production Complementary Metal-Oxide-Semiconductor (CMOS) technology. Finally, in order to maximize the data-rate, the modulation order (number of bits per symbol) per subcarrier can be easily adapted to the link conditions. This technique is known as "bit and power loading".

The OFDM technique requires a high data-rate digital processing electronics at both ends of the transmission (namely DSPs, Digital-to-Analog Converters (DACs) and Analog-to-Digital

Converters (ADCs)) which can be very complex as compared to classical single-carrier techniques. This is why it was not considered as a solution for improving performance in optical transmission systems up to a few years ago. However, significant breakthroughs in the processing-electronics have been reported in the last few years, as it will be detailed in this thesis. And optical OFDM solutions for PON applications can benefit from those CMOS electronics.

b. Providing Low-Cost Transceivers - Silicon Photonics

At the same time, FTTH/B transceivers that are fabricated today are based on the assembly of discrete components. A single FTTH/B transceiver have about 100 components and takes about 20-30 manual assembly steps to be built [5]. Among the components, the laser and the detectors are based on the III/V technology with 2 or 3 inch-wafer-scale fabrication processes. The epitaxial layers are expensive, and the yield is poor.

As optics is displacing electrical links on transmission distances that decrease continually, silicon photonics is expected to accelerate this shift in the next five years. This is because the main functions were demonstrated (transmitters and receivers) but mostly because this technology has unprecedented manufacturing capabilities. Silicon photonics technology is indeed developed to be fully compatible with the existing CMOS infrastructure. Technological advances in CMOS design and manufacturing enable electronic devices with high integration complexity to be fabricated in very large scale and very low-cost.

The combination of CMOS electronics and silicon photonics is further expected to leverage the Electro/Optic (E/O) devices performance due to the opportunity to tightly integrate the active photonic building blocks with their electronic driving and reading circuitries (analog electronics), as well as with CMOS digital signal processing circuits.

Scope and Contributions of this Thesis

Optical OFDM has already shown its potential using commercially available optical components, but its use with silicon photonics Directly Modulated Laser (DML) and modulators is more challenging. The objective of this work is to study the performance of OFDM-based solutions for future PON, using silicon photonics transmitters. For that purpose, a dedicated simulation platform is developed. The OFDM modem is implemented numerically, as well as models of silicon photonic devices built during this thesis, which are validated by characterizing physical components available for test. In parallel, an experimental test-bed is developed. The silicon photonics transmitters are benchmarked with commercial-available transmitters for OFDM-based optical systems.

The use of optical OFDM with adaptive bit and power loading is proposed to maximize spectral efficiency. Considering Intensity-Modulated/Directly-Detected (IM/DD) links, two types of silicon photonics transmitters are considered : directly-modulated III/V-on-silicon lasers (experiment) and external optical modulators such as Mach-Zehnder Modulator (MZM) (simulation) and ring-resonator (simulation and experiment). Experimental results show that hybrid III/V-on-silicon directly-modulated lasers (DMLs) can provide more than 10Gbps aggregated data-rate over at least 50km. For the silicon ring modulator, because of the high coupling loss in and out of the photonic chip, reach was limited to 20km, but simulations show that reach can be indeed improved up to 100km if the optical signal is amplified or the coupling loss reduced. These are the first experimental demonstrations of OFDM modulation with hybrid III/V-on-silicon lasers and silicon ring-resonator modulator. In addition, the silicon photonics transmitters are benchmarked in both simulation and experiments with state-of-the-art components such as directly-modulated Distributed Feedback Laser (DFB) laser and $LiNbO_3$ modulators.

A modulation technique called Single-Side Band (SSB)-OFDM is known to improve the [bandwidth $\times$ reach] product of the link, as compared to IM/DD (Dual-side Band (DSB)-based) systems. However, it requires expensive transmitters with several discrete optical components.

As silicon photonics technology allows a very high level of integration between different optical components and between electrical and optical devices, a silicon optical IQ modulator enabling SSB-OFDM technique is investigated.

The solutions presented in this thesis are demonstrated to be compliant with future PON in terms of data-rate, with relatively low bandwidth ($< 6.25GHz$) electronics, which is a great asset for the considered application. The driving voltages required for typical IM/DD systems showed to be closer to what CMOS driving circuitry can provide ($2V_{pp}$). On the other hand, more complex solutions with optical IQ modulators, external drivers are necessary due to the high modulation depth required ($> 6V_{pp}$).

Organization of the Thesis

In a first part, an introduction to optical access networks is presented. It starts with a description of the existing architectures for FTTH/B systems. An insight into the currently deployed standards is given. In the following, the drivers and requirements for future generation of broadband access are detailed. The chapter 1 concludes with a study of the proposed solutions in the literature for future PON.

Chapter 2 reports the principle of operation of the typical components implemented in an optical communication link. It is divided in 1) propagation in the optical fiber, 2) E/O converters, and 3) O/E converters. In each part, lumped-element models based on the physical characteristics of the components are presented, which are later implemented in the simulation platform. The modeling of the E/O converters - both commercial and silicon photonics - to be evaluated in the simulation platform is detailed and its accuracy is assessed through characterization of the physical components. The models for the optical components of the link describe the transfer function and noise that each component adds to the transmission.

In the third chapter, the different transmission techniques and modulation formats for optical communication are reviewed. It starts with a brief analysis of single-carrier modulation formats - OOK (intensity) and M-Quadrature Amplitude Modulation (QAM) (amplitude and phase). The multi-carrier modulation technique OFDM is described, and a review of the features and impairments of the OFDM technique is given. The main principles and particularities of OFDM applied to optical communications are then considered. As the electronic implementation for optical OFDM can be an issue for its development when large bandwidths are required ($> 2GHz$), a study of existing DACs/ADCs and real-time implementation using Field-Programmable Gate Array (FPGA) and ASIC is presented.

The fourth chapter describes the experimental validation of the simulation platform developed during this thesis, based on commercial-available devices. It is divided in single-carrier OOK, IM/DD optical OFDM with bit and power loading and optical SSB-OFDM with direct-detection.

Chapter 5 is dedicated to the simulations and experiments of optical OFDM using silicon photonics transmitters. In the first part, intensity-modulators are considered. For the directly modulated III/V-on-silicon lasers, an experimental test-bed is developed to demonstrate efficient OFDM modulation in three different types : Fabry-Perot, tunable single-mode lasers with double-ring filtering and DBRs. In the following, silicon modulators (MZM and ring-resonator) enabling OFDM modulation are also assessed. In the second part, a silicon photonics implementation of an optical IQ modulator suitable for SSB-OFDM modulation is analyzed, and the performance of such a transmitter is assessed by using the simulation platform. Performance evaluation is made in terms of the achievable data-rate, sensitivity, reach and optical budget.

This thesis ends with the concluding remarks and future research directions.

Chapitre 1

Introduction to Optical Access Networks

Optical transmission systems were first considered for ultra-long-haul submarine communications. With the development of innovative technologies that lowered the costs of deployment and operation of optical systems, combined with the explosion of internet and media services, the optical fiber eventually reach metro networks, and finally the access networks, namely Fiber-to-the-x (FTTx) architectures. The different FTTx networks are divided in Fiber-to-the-Node (FTTN) (optical link reaches up to 300m from the subscriber), Fiber-to-the-Curb (FTTC) (optical link reaches less than 300m from the subscriber) and FTTH/B, where the optical fiber reaches the end user. This chapter is dedicated specifically to FTTH/B architectures.

This chapter intends to give an overview of the current deployed technologies for FTTH/B and the proposed solutions for future generations of access optical networks. In the first section, the different types of architectures for FTTH/B networks are detailed - Point-to-Point (PtP), Active Optical Networks (AON) and PON. Different multiplexing schemes for PON are discussed. The following section reports the standards, and requirements of next-generations of PON, as well as the recent standardization of Next Generation Passive Optical Networks : Stage 2 (NG-PON2). In the final section, a description of the different technologies for future PON being developed is given : Wavelength-Division Multiplexing (WDM)-based PON, pure Time-division Multiplexing (TDM)-PON, Time and Wavelength Division Multiplexing (TWDM)-PON, FDM-PON and finally OFDM-PON.

1.1 FTTH/B Architectures

A general form of access networks has a central distribution unit routing the data from the core network (internet) to a group of N users. This is the Central Office (CO) or Optical Line Terminal (OLT). Each user/subscriber in the network is called Optical Network Unit (ONU) or Optical Network Terminal (ONT). In the case a single fiber is used to distribute the data to the N users (AON or PON), an Optical Distribution Network (ODN) distributes the optical signal from the single fiber to the N users. The physical location of the ODN is rather closer to the subscribers than the CO to decrease the capital expenditure of the network. The equipment used on the ODN depends if the network is active or passive, and it may depend on the multiplexing scheme used. Downlink direction (or downstream) is defined as the transmission from the CO to the ONU and uplink (upstream) vice-versa. There are three basic architectures of FTTH/B networks. They are displayed in figure 1.1 - PtP, AON and PON.

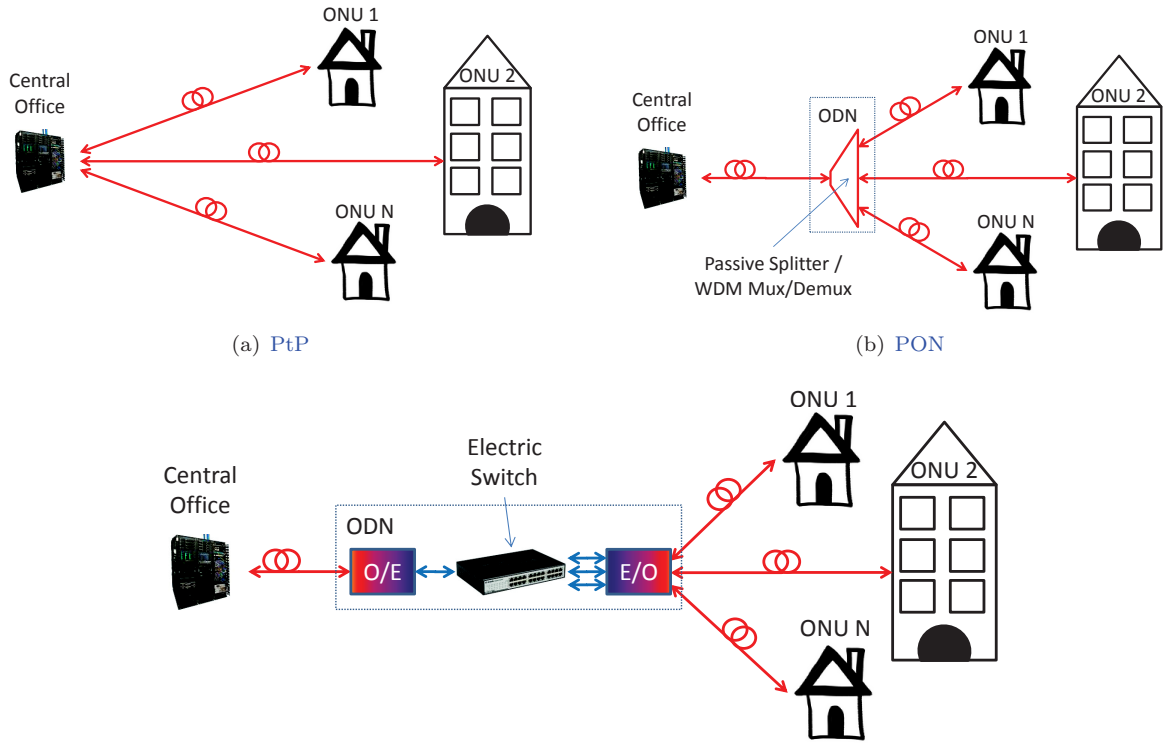

(a) PtP (b) PON

(c) AON

FIGURE 1.1: FTTH/B Architectures.

1.1.1 Point-to-Point (PtP)

The first type of FTTH/B architecture proposed was PtP, with the first field trial successfully demonstrated in 1977 [6]. In this type of network, each user has a dedicated fiber from the CO to the ONU. The advantage of this type of network is the flexibility - the data-rate for each user can be adapted very easily - and no multiplexing scheme is required. On the other hand, the high cost of the networks due to the use of one fiber per user makes it very unattractive as the number of ONUs per CO is increased. By availing the low loss and high bandwidth of the optical fiber, the cost can be reduced by using a single fiber to feed several users, as it is proposed in AON and PON architectures.

1.1.2 Active Optical Networks (AON)

In AON, there is only one fiber from the CO to the ODN as shown in figure 1.1(c). The different optical signals of the different subscribers are multiplexed in the time domain. At the ODN, an electrical switch is used to route the signals at each time slot to the correct user. The optical signal is converted to the electrical domain, routed to the right path, and sent to the ONU after being converted back to the optical domain. This solution is much more efficient than PtP but the fact that active components are required at the ODN (in general a couple of E/O and O/E converters and an electrical switch for N users) greatly increases the operating expenses of the network.

1.1.3 Passive Optical Networks (PON)

PON architectures have only passive optical components at the ODN. Several multiplexing schemes are possible - TDM, FDM, WDM as illustrated in figure 1.2. In most cases, a simple

passive splitter is used at the ODN. As an alternative, in the case of WDM, a WDM mux/demux can be employed at the ODN as illustrated in figure 1.2(c).

The terminology used in this work is the following : 1) Multiplexing schemes refers to downlink direction, it allows to group data streams addressed to different users and to send over the same medium ; and 2) Multiple access techniques refers to uplink direction, it allows different subscribers to share the same transmission medium.

1.1.3.1 Time-Division Multiplexing (TDM)

In TDM/Time Division Multiple Access (TDMA)-PON, the ODN is a simple passive splitter. The time domain is divided in several time-slots, each one or several dedicated to a single user. Bandwidth allocation can be done simply by attributing more or less time slots to one ONU. For example, in figure 1.2(a), user 2 takes 2 out of 4 time slots available - its data-rate is twice the data-rate of the other users. Generally, OOK modulation is used, but OFDM modulation combined with TDM (TDM/TDMA-OFDM) can be employed to improve the [bit-rate $\times$ reach] product. However, current transceivers at the CO and ONU do not have the ability to generate and process OFDM signal. As a consequence, an upgrade of the transceivers would be required.

In downlink direction (TDM), one subscriber in the network receives the entire signal from the CO. It selects only its dedicated time slot. In uplink direction (TDMA), the ONU is synchronized with the CO to know when to send a packet. This way, different packets sent by different users do not collide as illustrated in figure 1.2(a). The main drawback of this scheme is that the ONU transceivers have to operate at the system data-rate, while the effective data-rate per subscriber is often much less than that. As a consequence, the transceivers are more expensive and very difficult to scale. In spite of these drawbacks, TDM-based PON is the primary solution for current standards by IEEE (e.g. 10-Gigabit Ethernet Passive Optical Network (10G-EPON)) and Full Service Access Network (FSAN) (e.g. 10-Gigabit Passive Optical Network (XG-PON)) and widely deployed for FTTH/B networks.

1.1.3.2 Frequency-Division Multiplexing (FDM)

The available frequency band for the transmission is divided into several frequency-band slots. In uplink direction, the data from different users are multiplexed in the frequency domain. One or more RF carriers are associated with a single ONU. In uplink direction, each subscriber sends data over a pre-defined RF-carrier. Bandwidth allocation may be done simply by increasing data-rate in one RF-carrier (as illustrated in figure 1.2(b) at ONU 2) or by assigning multiple carriers to a single user. The advantage over TDM/TDMA-PON is that the ONU transceiver can operate at the actual bit-rate per user. In addition to that, it is much more robust against fiber chromatic dispersions because individual channels have much less bandwidth than the aggregated signal. However, it requires a tunable RF local oscillator in both CO and ONU transceiver, or high-speeds DAC/ADC to generate and demodulate the RF signals.

1.1.3.3 Wavelength-Division Multiplexing (WDM)

This multiplexing scheme is a virtual PtP topology, where a single wavelength is addressed to a single user (or even two wavelengths if downlink/uplink transmission are done using different wavelengths). The WDM-PON groups the advantages of both PtP and PON architectures at the cost of complexity of the transceivers to manage the different wavelengths.

The ODN can be made using a single passive splitter as for the TDM and FDM-PON. In this case, all the downlink wavelengths are routed to every user. This simplifies ODN implementation, but wavelength filtering should performed at the ONU, increasing the complexity of the receiver.

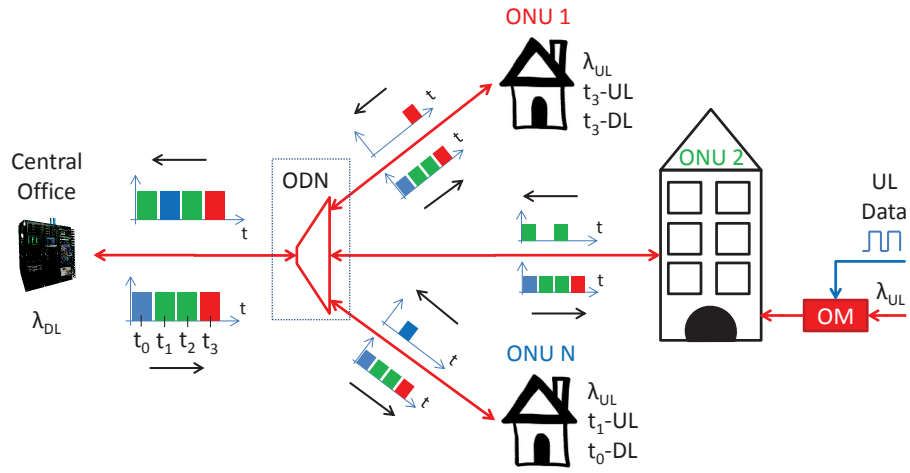

(a) TDM/TDMA

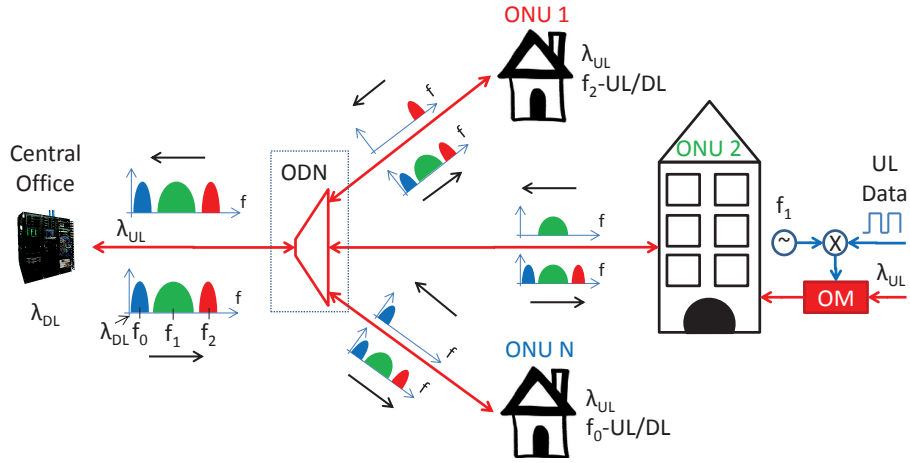

(b) FDM/FDMA

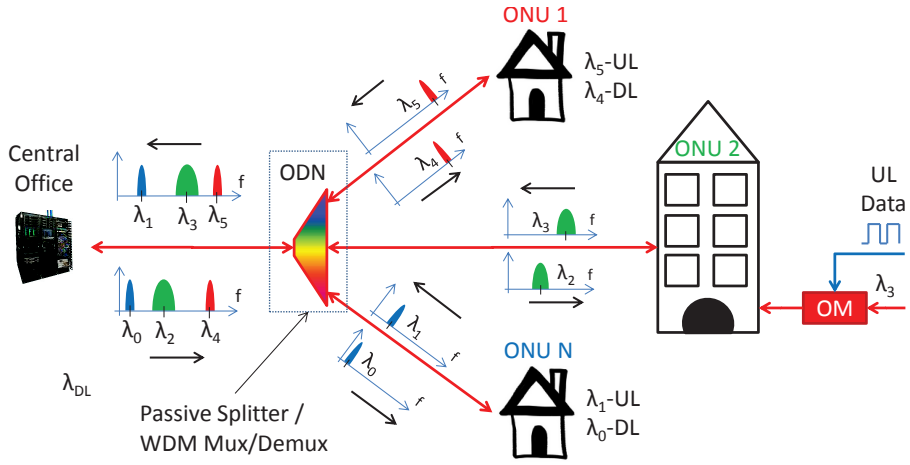

(c) WDM/WDMA

FIGURE 1.2: Multiplexing choices in PON architecture. Acronyms : Downlink (DL), Uplink (UL) and Optical Modulator (OM).

As an alternative to avoid high insertion losses of the passive splitter as the number of users per ODN increases (for N users, the optical loss in dB is $-10log_2(N)$), a WDM mux/demux can be used at the ODN. In this way, as illustrated in figure 1.2(c), the wavelength filtering is performed at the ODN, and each user receives only its own wavelength. Typical loss of an array waveguide grating for WDM mux/demux is about 3-4dB, independent of the number of users.

A major advantage of WDM-PON is that ONU transceivers work at the effective data-rate per subscriber. However, the ONU transceiver is quite complex to implement for two main reasons : 1) "Colorless" transmitters and receivers are necessary in order to have flexible networks - where any wavelength of the grid can be attributed to any user ; 2) Scaling is also an issue because of the large number of required wavelengths. In addition, the PtP topology requires a transceiver per user at the CO. In spite of these drawbacks, extensive research on WDM techniques is being done to demonstrate low-cost transceivers.

1.1.3.4 Summary of Multiplexing Techniques

Using a single multiplexing technique (between TDM/FDM/WDM) can be very costly and difficult to scale. Different multiplexing techniques can be combined in order to group the advantages of each one. It is generally agreed that WDM will be present in future generations of optical access networks, combined with some other multiplexing technique. Proposed hybrid solutions for upgrading optical access networks are investigated in subsection 1.3.

These multiplexing techniques can be implemented with different modulation formats, e.g. single-carrier OOK, M-QAM, or even multi-carrier OFDM. Depending on the multiplexing technique, one or other modulation format is more advantageous. This is detailed in subsection 1.3.

1.1.4 Alternative Architectures - Ring-based PON

In 2007, Yeh *et al.* have proposed a new type of FTTH/B architecture in a ring form [7]. The schematic view is shown in figure 1.3. Basically, in a system with N users the CO is directly connected with the first and the N^{th} ONU. Two adjacent ONUs are connected one with another. At the ONU, the unit is able to either send the uplink signal or receive the downlink signal in any of the two direction "a" or "b" as illustrated in the right side of figure 1.3. As a consequence, the unit is actually composed of two transceivers (or Line Terminal (LT) in figure 1.3), but that do not work necessarily at the same time. The advantage of this type of architecture is that it is robust against fiber-fault. If a fiber-fault occurs between any two adjacent users, all ONUs are still connected to the CO, in either clockwise or counterclockwise direction. Then, any of the multiplexing schemes detailed above can be used [7, 8].

1.2 Standards, Deployed Networks and Requirements for Future Optical Access Networks

As internet started to expand rapidly, broadband xDSL technologies over copper were developed in order to satisfy to the growing bandwidth demand. In spite of the fact that the latest xDSL networks (Very-high-bit-rate DSL 2 (VDSL2) [9]) can offer bit-rates up to 200Mbps per users, the data-rate is degraded after 300m because of the link attenuation. Also because of the very high link attenuation, PtP or AON topology is mandatory - increasing the cost of deployment as the number of users increases. The short-reach of such copper-based networks implies that fiber-based transmission (FTTx) is required to cover most of the distance between subscriber and CO. It should be noted that the success of Very-high-bit-rate DSL (VDSL)

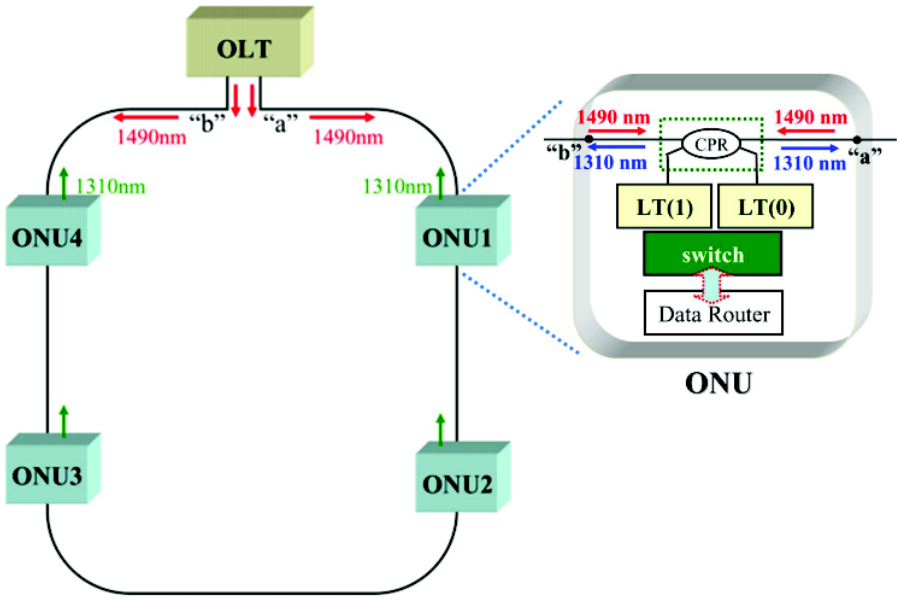

FIGURE 1.3: Schematic view of the Ring-based PON architecture (Source [7]). Acronyms : 2x2 Optical Couplers (CPR), Line Terminal (LT).

enabled broadband media applications and cloud computing, driving the demand for even higher data-rates.

Because it was not economically advantageous at that time, alternative architectures rather than FTTH/B were more successful in the 90's - like Fiber-to-the-Node and Fiber-to-the-Curb. This means that the optical fiber did not reach the end-user, but it would get as close as possible and copper was used to reach the final destination. The massive deployment of FTTH/B network started in the mid-2000's [10]. Back then, the fiber broadband access already accounted by 2% of the total broadband access in North America, while in Japan a tenfold higher percentage of homes were already connected to the fiber and in-service. The inherent low-loss of the fiber allows to increase the reach and the number of users served by CO. In addition, electric-based links have considerably high power consumption for high data-rates as compared to optical-based links. As indicated in [11], power savings of Gigabit Passive Optical Network (G-PON) (standard to be detailed in subsection 1.2.1) compared to VDSL2 can reach 29MWh (which represents a $2.9M power cost saving) per one million broadband subscribers. This can potentially decrease both capital and operational expenditures for high-speed telecom operators. In [11], the author forecasts a fourfold increase in the number of FTTH/B subscribers from 2008 (30 million) to 2014 (115 million) worldwide. The penetration of FTTH/B networks into the market varies strongly by country [3]. Asian countries are the leaders in FTTH/B market penetration, with Japan in the top with more than 60% of broadband subscribers being connected to FTTH/B services in 2011 [3].

The first deployments FTTH/B networks were based on PtP architectures. As described in the previous section, PtP architecture has many disadvantages in terms of cost and scalability. It became clear that in order to enable the feasibility of FTTH/B technologies, PON-based architectures were and still are the ultimate choice. Despite the many technological advances in PON in the 90's, it became evident that only trough standardization the operators would consider deploying such a network. Standardization enables the inter-operability, large-volume manufacturing and minimizes investments risks. In this context, two standardization groups have proposed high data-rate standards for PON networks : FSAN and IEEE. The G-PON standard from FSAN is mostly deployed in North-America and Europe, while Gigabit Ethernet

Passive Optical Network (G-EPON) from IEEE is dominant in Asia [12] nowadays. Both families of standards are detailed in the following.

1.2.1 Evolution of G-PON - FSAN Standards

In 1995 most leading telecom operators grouped up to form the FSAN - a study group to propose and define innovative technologies aiming to standardize PON networks by the International Telecommunication Union (ITU). Because WDM techniques were not mature enough to allow low-cost deployment of PONs at that time, TDM/TDMA-PON was chosen as the preferred architecture. The first standard defined was Asynchronous Transfer Mode PON (APON) in 1998 [13], with an aggregated bit-rate of 622Mbps in downlink and 155Mbps in uplink. An upgraded version of APON, called Broadband PON (BPON) was standardized in 2002. By 2005, ITU standardized G-PON [14], with a downlink data-rate of 2.5Gbps and uplink data-rate of 1.25Gbps. The sustained bit-rate per users ranges from 20-30Mbps to 100Mbps in downlink (mostly Europe and a few multiple service operators in the USA) [15]. A summary of characteristics of G-PON is detailed in table 1.1.

Back in 2006, the FSAN group started to think about the system that would follow G-PON. This was rather a difficult task because of the many technological options that appeared as candidates - TDM, WDM, Code-Division Multiple Access (CDMA). As a consequence, FSAN divided all possible solutions into two groups as shown in figure 1.4. The Next Generation Passive Optical Networks : Stage 1 (NG-PON1) is the group of solutions that should co-exist with G-PON. In this way, the cost of upgrading existing G-PON systems is minimized. The second group, called NG-PON2, consists in the solutions that do not require necessarily compatibility with the G-PON networks, or technologies that were not mature enough at the time being.

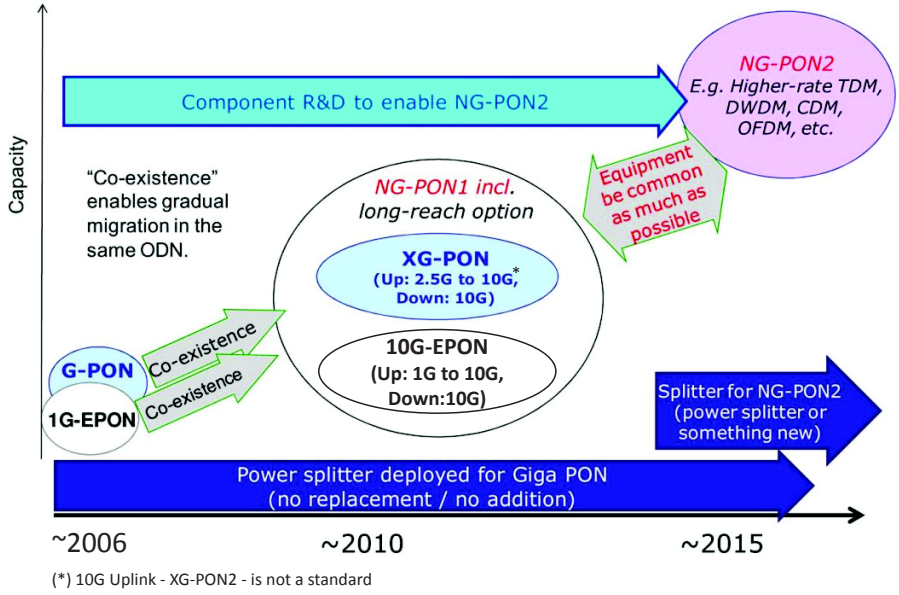

FIGURE 1.4: Evolution of PON standards by FSAN and IEEE. (Source [16]).

FSAN chose TDM-PON as the primary solution for NG-PON1. By 2009, the 10-Gigabit Passive Optical Network 1 (XG-PON1) standard was defined [17], with 10Gbps/2.5Gbps data-rate in downlink/uplink, respectively. A symmetrical version of the standard (10-Gigabit Passive Optical Network 2 (XG-PON2)) was considered (10Gbps in uplink) but never became a standard. In order to make it compatible with G-PON standard, the wavelength plan was carefully defined (cf. figure 1.5). The first field trial for XG-PON1 was reported in [18] and XG-PON2 in [19]. General characteristics of the XG-PON1 standard are detailed in table 1.1. XG-PON

transceivers are already commercially available and deployment of these networks is in an initial state. More details on XG-PON can be found in [16].

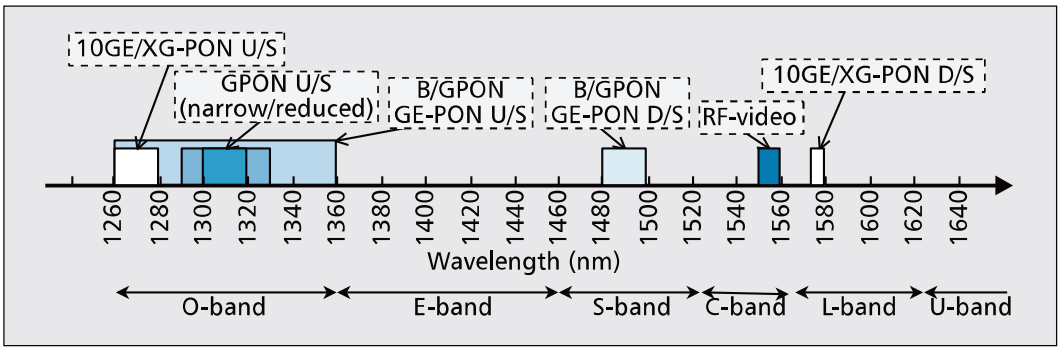

FIGURE 1.5: Wavelength plan for current PON standards. (Source [20]).

The requirements for NG-PON2 are discussed in subsection 1.2.4, while the proposed technical solutions for NG-PON2 are detailed in section 1.3.

1.2.2 Evolution of G-EPON - IEEE Standards

A second group of standardization - the IEEE - also defined standards for PON architectures, based on the popular Ethernet protocol. The G-EPON was proposed in 2004 [21] ; a data-rate of 1Gbps was defined for both uplink and downlink. Later, in 2009, the 10G-EPON was defined with 10Gbps in downlink direction and 1Gbps (asymmetric) and 10Gbps (symmetric) [22]. The characteristics of both standards are detailed in table 1.1. A disadvantage of the 10G-EPON standard is that a part of the uplink wavelength plan overlaps with the one of G-EPON [23] as indicated in figure 1.5. As a consequence, the two standards cannot co-exist in the same network without some other kind of multiplexing. Migration from 1G to 10G IEEE networks requires considerable more efforts than upgrading FSAN networks from 2.5G to 10G standard [15]. A comprehensive summary of the 10G-EPON is reported in [23].

1.2.3 Summary of Current Standards

A summary of the current standards proposed by FSAN/ITU and IEEE is shown in table 1.1. In terms of power budget (difference between launched and received optical power to achieve a target Bit Error Rate (BER)) and number of users (split-ratio), G-PON and XG-PON1 network provide higher capacity than G/10G-EPON. The maximum reach is 20km, except for an extended reach version of the XG-PON which is defined in the International Telecommunication Union-Telecommunication Standardization Sector (ITU-T) recommendations G.987.4 [24].

1.2.4 Requirements for NG-PON2

The drivers for the NG-PON2 are divided in service, end-user requirements and network drivers. The growing bandwidth demand with the rise of rich-content media services such as UltraHDTV and 3D HDTV and cloud-computing services which demand high data-rate for file transfer in both downlink/uplink directions may be cited as service drivers for NG-PON2. Some reports suggest that by 2015, the residential data-rate requirements could exceed 250Mbps [25]. In addition, the end-user requires security and integrity of its data, simple and low-cost equipment and network availability. Finally, NG-PON2 technologies must enable a smooth migration from currently deployed network. The deployed optical fiber must be re-used as much as possible to decrease migration costs. The system should be as flexible as possible - different

	G-PON	XG-PON1	G-EPON	10G-EPON
Aggregated data-rate	2.5G (DL) / 1.25G-2.5G (UL)	10G (DL) / 2.5G (UL)	1G (UL) / 1G (DL)	10G (DL) / 1G-10G (UL)
Power Budget	28dB	29-35dB	20dB-24dB	20dB-29dB
Number of users	64-128	32-64	Up to 32	Up to 32
Reach	Up to 20km	20km-60km	Up to 20km	Up to 20km
Wavelength	1.48μm-1.5μm (DL) 1.29μm-1.33μm (UL)	1.57μm-1.58μm (DL) 1.26μm-1.28μm (UL)	1.57μm-1.58μm (DL) 1.26μm-1.36μm (UL)	1.48μm-1.5μm (DL) 1.26μm-1.28μm (UL)

TABLE 1.1: Summary of the most popular standards for PON, by FSAN and IEEE.

services and data-rates should be supported and easily manageable. It is evident that developing a technology that group all these features is not an easy task.

NG-PON2 requires an aggregated data-rate of 40Gbps in downlink and 10Gbps/40Gbps in uplink direction [20]. The network should provide a sustainable data-rate of 1Gbps per user in downlink direction. For uplink transmission, it could be less than that for residential users. However, a generic transceiver that can support symmetric data-rates is desirable. In a first scenario, NG-PON2 would require 40km of passive reach and up to 60km in the extended reach version, and support at least 64 users to be compatible with the existing standards G-PON and XG-PON. A second class of NG-PON2 solutions is called Long-reach Passive Optical Networks (LR-PON) [12]. The reach could be extended up to 100km, serving more than 1000 users per CO. By increasing the number of ONUs per CO, the capital and operational expenses of the network can be minimized. In addition, LR-PONs are suited to lighten high-costs associated with sparsely distributed subscribers in rural and remote areas. A careful study on technologies enabling LR-PON is reported in [26]. Spectrum flexibility is also a requirement for NG-PON2. It means that any candidate technology should enable the transceivers to access any wavelength or group of wavelengths in the spectrum. To facilitate this task, ONU transceivers should be "colorless", e.g. not specific to one wavelength.

1.2.4.1 Recent Standardization of TWDM-PON

During the course of this thesis, in April 2012, FSAN chose TWDM as the primary solution for NG-PON2 [27, 28]. The basic idea is simply to stack 4 wavelength of XG-PON. In this way, aggregated data-rate is improved by four-fold.

A schematic view of the proposed TWDM solution is shown in figure 1.6. To cope with the increased optical budget required by the insertion of the WDM Mux/Demux at the CO, a bi-directional optical amplifier (OA) is placed at the CO output. In order to maintain compatibility with existing ODN, a passive splitter is used. At the ONU, tunable transmitters and receivers are required, which can tune to any of the 4 downlink and uplink wavelengths, respectively. The main technological challenge of this solution is to provide a low-cost and "colorless" ONU. Proposed solutions for this challenge are detailed in subsection 1.3.1.1.

The wavelength plan is still open to discussion. According to [29], three options are available. They are illustrated in figure 1.7. The first option (figure 1.7(a)) is simply to re-use XG-PON wavelength plan. The four wavelengths are defined by slicing a finer grid inside the range of wavelengths available. As a reminder, XG-PON uses the range 1.575μm-1.58μm for downlink

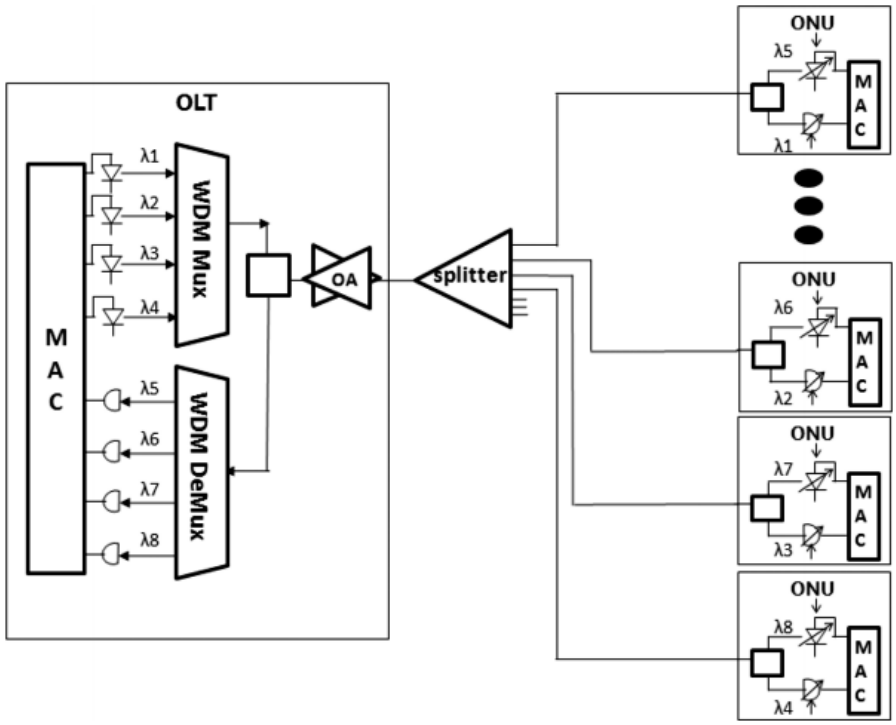

FIGURE 1.6: Proposed TWDM-PON architecture for NG-PON2 (Source [29]).

and 1.26μm-1.28μm for uplink. This solution is not compatible with XG-PON meaning that it cannot co-exist in the same network without a secondary multiplexing scheme. The second option (figure 1.7(b)) is to place both downlink and uplink wavelengths in the C-band, which is attractive for the use of Erbium-dopped Fiber Amplifiers (EDFAs). This option is not compatible with RF-video overlay. In the third option (figure 1.7(c)), the downlink is the same as the first option, while the uplink is placed in the L-minus band (1.535μm-1.54μm).

1.3 Proposed Solutions for Future PON

1.3.1 WDM-based PON

Some authors advocate the use of a pure WDM for addressing next generation optical access networks [30, 31], represented in figure 1.2(a). It consists in several wavelengths ($>$ 40) carrying a low data-rate each ($<$ 1$Gbps$), where each wavelength addresses an ONU. As stated earlier, WDM-PON has many advantages over TDM-PON, but cost is a big issue for these solutions, in particular for "colorless" ONUs. In this context, a solution is to increase the data-rate per wavelength, and one single wavelength addresses several users using a second multiplexing scheme - these are called hybrid WDM schemes. As a particular case of WDM, TWDM-PON architectures is discussed in subsection 1.3.3.

The first country to deploy WDM-based optical access networks was Korea [32, 33]. However, the high-cost of optical components for such network made implementation less attractive. The only commercially available components for WDM-PON are patented by LG-Ericsson [31, 33] and cost roughly twice than G-EPON or G-PON equipment.

It is important to remind that "colorless" ONUs is a requirement for NG-PON2 regardless of the multiplexing choice. The transceiver should be able to detect and to generate modulated optical signals at any wavelength within the wavelength plan considered. There are two technological mechanisms that are considered for developing low-cost and colorless ONU transceivers

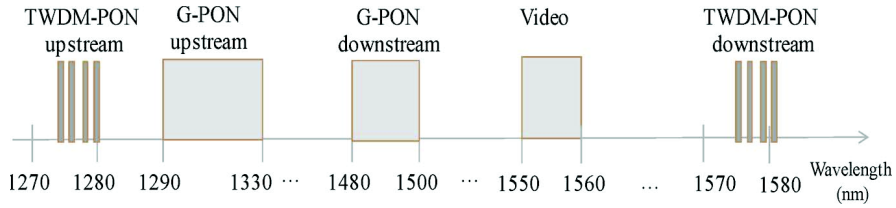

(a) First option : XG-PON wavelength reuse

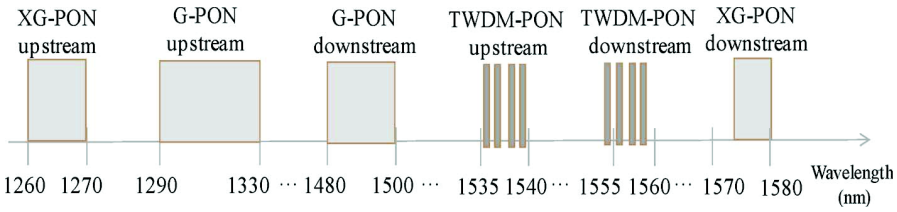

(b) Second option : C-band

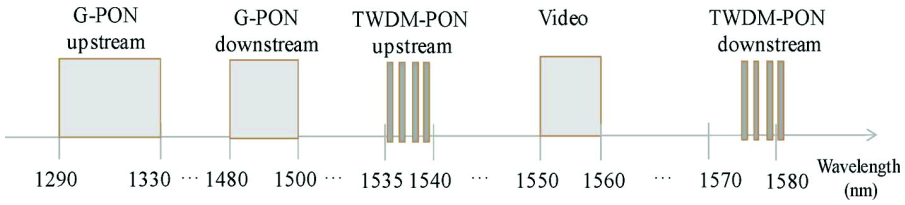

(c) Third option : XG-PON wavelength reuse for downlink and L-minus band for uplink

FIGURE 1.7: Wavelength plan proposals for NG-PON2 (Source [29]).

as illustrated in figure 1.8 : a) tunable laser source at the ONU and b) lightwave-centralized solution.

1.3.1.1 Tunable Laser Source at the ONU

The straightforward solution is to implement a tunable laser source at the ONU. This has many advantages such as higher optical output power (without the use of optical amplifiers), reach and easy scalability for higher data-rates. The drawback is obvious - today, tunable laser sources are complex and high-cost. There is an implicit trade-off between complexity of the transceiver and admissible traffic in the network. In order to increase capacity of the network, one can add more wavelengths to the system. This means that the ONU laser source should be able to tune over a broader range of wavelength, increasing the complexity. This tradeoff is studied in [34]. Extensive research in showing the feasibility of tunable laser sources for NG-PON2 is being done. A very wide state-of-the-art in developments of low-cost III/V tunable lasers implementations can be found in [29, 31, 35].

A FP7-financed project called GigaWaM, which is developed by major actors in Norway, Denmark, Sweden, Germany, U.K. and Canada, proposes a pure WDM-solution using 64 wavelengths with a data-rate of 1Gbps per wavelength, providing a symmetrical aggregated bit-rate of 64Gbps [31]. The purpose of the project is to develop innovative technologies to enable a pure-WDM solution : DBR-based low-cost tunable laser sources, athermal array waveguide gratings for wavelength mux/demux and a high level of integration.

Silicon Photonics Lasers

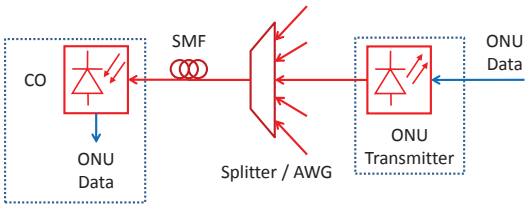

(a) Tunable laser source at the ONU

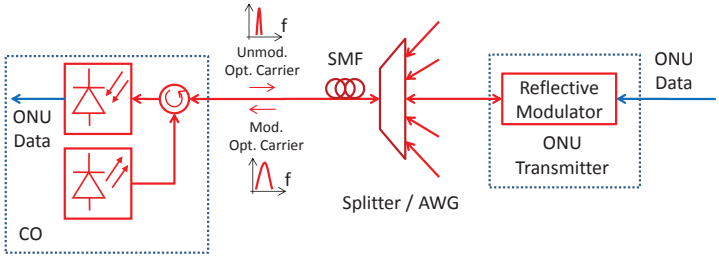

(b) Lightwave-centralized solution

FIGURE 1.8: Technologies for colorless ONU transceivers.

Moreover, tunable hybrid III/V-on-silicon laser sources have been demonstrated recently, either based on ring-resonators [36–40] or DBR mirrors [41, 42] as filters to achieve single-wavelength operation. Integrated heaters can be placed on top of Silicon-on-Insulator (SOI) to make them tunable. The the local temperature variation mechanism varies the effective index of the silicon waveguide, which changes the resonance wavelength of the filters. In addition, silicon photonics lasers enable large volume fabrication, which is very suitable to this application.

Tunable single-wavelength lasers using ring-resonators to filter the adjacent modes have been proposed in the literature. A couple of rings with slight different Free Spectral Ranges (FSRs) benefiting from the Vernier effect can be used to increasing tuning range of the laser [43]. This structure was first demonstrated using InP [43]. Then, based on a flip-chip bonding of the III/V to the SOI substrate, a similar structure was reported in [36, 37]. The coupling between the active region and the silicon waveguide was optimized using a SiON tapered waveguide. Finally, using the wafer-bonding technique and adiabatic coupling, C-band hybrid III/V-on-silicon lasers with 8nm (single ring resonator), 45nm and 40nm (double ring) tunability-range are demonstrated in [38–40], respectively. The basic structure of the double-ring tunable laser presented in [39] is shown in figure 1.9. This laser enabled direct modulation of 10Gbps OOK signals up to 25km SMF [44]. We demonstrate 10Gbps direct-OFDM modulation of this laser, which is detailed in subsection 5.1.3 of this work.

More details about the principle of operation and different types of hybrid III/V-on-silicon lasers using wafer/die bonding technique in subsection 2.2.1.4.

Very recently, widely tunable CMOS lasers using flip-chip bonding were reported at Optical Fiber Communication Conference (OFC) 2013 by Skorpios [41] and Aurrion [42] based in a grating Y-branch geometry, which is illustrated in figure 1.10. In one side of the cavity, two DBR mirrors with slightly different FSRs (Vernier effect) are connected with the active region using a Multimode Interferometer (MMI) coupler. In this structure, the MMI coupler acts as an "And" port - the wavelength is coupled only if it is reflected by both left and right mirrors at the same time. The tunability is achieved by integrating resistive metal heaters in top of the mirrors.

Big network operators such as Google are working towards pure-WDM-PON solution [30], proposing a tunable laser source at the ONU. They claim that hybrid laser sources using silicon

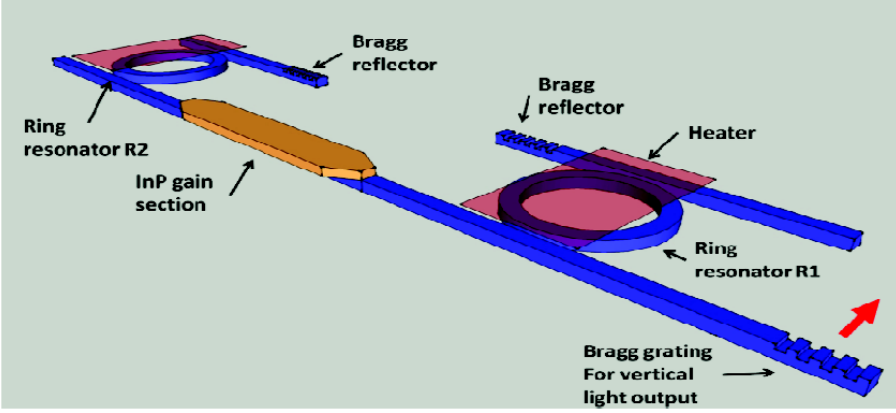

FIGURE 1.9: Single-mode hybrid III/V-on-Silicon laser using a double-ring structure (Source [39]).

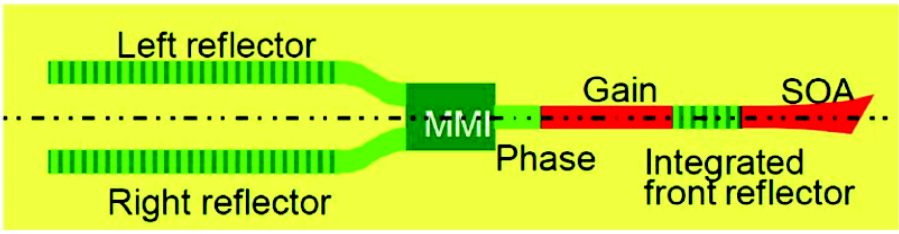

FIGURE 1.10: Modulated grating Y-branch geometry laser (Source [31]).

photonics is the key technology to enable low-cost and colorless ONUs.

1.3.1.2 Centralized-Lightwave Solutions

The second proposed solution for minimiwing the transceiver cost at the ONU is to send an unmodulated carrier from the CO to the ONU (cf. figure 1.8(b)). The optical carrier is modulated using a reflective modulator and sent back to the CO. In general, this approach is much cheaper than having a tunable laser source at the ONU. However, a few drawbacks can be identified. First, the optical budget required for uplink transmission is doubled because the optical signal travels round-trip the optical link. In addition, Rayleigh backscattering and other parasite reflections can degrade receiver sensitivity. A comprehensive overview of reflection-based solutions for NG-PON2 are reported in [45].

Increasing Optical Budget and Mitigating RBS

In order to cope with the increased optical loss, using an optical modulator that amplifies the signal at the same time is very useful. In this context, Reflective Semiconductor Optical Amplifier (RSOA)-based [46] or injection-locked Fabry-Perot (FP) lasers [47] are investigated as possible solutions for the ONU transceiver. In this way, more than 20dB optical gain can be achieved. In fact, injection locked FPs are already commercialized as transmitters for PON networks, and used in Korea's WDM-PON deployment [33]. However, these modulators have typically low bandwidth and high chirp. As a consequence, OOK modulation is limited to 2.5Gbps. It is still compatible with pure WDM solutions or TWDM for NG-PON2, but difficult to scale to higher data-rates. A record data-rate of 5Gbps is demonstrated in [48] without any equalization technique, using an optimized RSOA structure. However, sensitivity is strongly degraded at this bit-rate. A Decision Feedback Equalizer (DFE) technique is proposed in order to increase data-rate to 10Gbps in [49], and electronic equalization to increase data-rate to

Reference	Optical Modulator	Data-rate (Band-width)	Max reach	Sensitivity optical B2B (BER target)	Penalty at max reach	Observation
[55]	RSOA	10Gbps	20km	-21.5dBm (10^{-4})	2.5dB	
[56]	RSOA	7.5Gbps (2GHz)	25km	-10.5dBm (10^{-3})	0dB	Real-time OFDM
[57]	RSOA	$4 \times 10Gbps$ (1.67GHz)	75km	-12.8dBm (3.8×10^{-3})	5.3dB	4 wavelengths
[58]	RSOA	10Gbps (2.5GHz)	20km	-14.5dBm (10^{-3})	2dB	Downlink signal re-modulation*
[8]	RSOA	10Gbps	20km	-12.5dBm	0.1dB	Ring-based architecture
[59]	Injection-locked FP	20Gbps (5GHz)	52km	-	0.3dB	
[60]	Injection-locked FP	20.25Gbps (5GHz)	25km	-10dBm (3.8×10^{-3})	2dB	
[61]	Injection-locked FP	10Gbps (2.5GHz)	60km	-16.6dBm (10^{-3})	2dB	
[62]	REAM	19.25Gbps (2x2GHz)	25km	-3dBm (2.3×10^{-3})	0dB	Real-time OFDM

*To be detailed further on this section.

TABLE 1.2: State-of-the-art of OFDM-based WDM-PON with lightwave-centralized solutions employing reflective modulators.

25Gbps in [50], but at the expense of higher complexity and power consumption electronics. An interesting scheme is proposed in [51] to improve data-rate to 10Gbps in a 1GHz-bandwidth RSOA, using an offset optical filter as an optical equalizer. The use of a Reflective Electro-absorption Modulator (REAM) was also proposed to improve data-rate - 10Gbps is reported in [52], and 40Gbps using digital equalization is demonstrated in [53]. However, the REAM does not amplify the optical signal ; hence an additional component to provide optical amplification is required.

As an alternative, many authors propose to efficient modulation formats such as adaptive OFDM to achieve data-rates beyond 2.5Gbps using cost-effective RSOAs, injection-locked FPs, or even REAMs. In this way, one can increase aggregated data-rate and reach at the same time. Table 1.2 summarizes state-of-the-art of OFDM-based for uplink WDM-PON, showing that OFDM modulation can very effectively surpass bandwidth limitations of reflective modulators and increase reach at the same time. In [8], the author proposed a ring-based architecture, which can mitigate Rayleigh Backscattering (RBS) noise and protect the network against fiber-fault simultaneously. Using a rigorous theoretical model for the RSOA, the author shows in [54] that more than 30Gbps capacity can be achieved, and that the negative chirp of RSOAs can improve the performance over the fiber of IM/DD adaptive optical OFDM signals.

In order to mitigate RBS reflection noise, the use of phase modulation and a Delay Interferometer (DI) in reception is proposed [63, 64]. As an alternative, chirped Return to Zero (RZ)

modulation is also proposed to minimize penalty due to RBS [65]. When using OFDM modulation, the transmission is naturally robust against RBS noise because it is located mostly at frequencies below 100kHz [66].

Silicon Photonics for Low-Cost ONU Transceiver

Since 2007, the use of silicon photonics technologies to provide large volume fabrication of CO/ONU transceivers is proposed [67], using planar-gratings and a 3-stage Mach-Zehnder Interferometer (MZI) to separate the 1310nm, 1490nm and 1550nm wavelengths (for uplink, RF-video and downlink signals). Later, in 2009, [68], a concept of an integrated FTTH/B transceiver compatible with CMOS fabrication is presented. It is based in add-drop ring resonators as WDM filters, monolithically grown SiGe photodiodes and an off-chip laser. Back in 2010, a monolithic 10Gbps WDM transceiver for the ONU was demonstrated [69]. The block diagram of the transceiver module is shown in figure 1.11, and the footprint of the module was $2 \times 4mm^2$. It consisted in a WDM filter based on MZI, a SiGe photo-detector and carrier-depletion silicon MZM. Crosstalk of the WDM filter was higher than 20dB. Extinction ratio of the MZM was 4dB at 10Gbps. Receiver sensitivity for BER=10^{-3} was -13dBm in the input of the WDM filter.

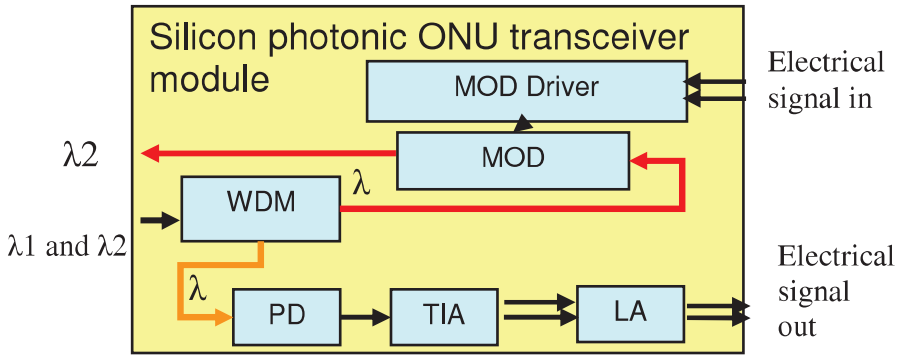

FIGURE 1.11: Silicon photonics based FTTH/B transceiver for the ONU (Source [69]). Acronyms : Photodiode (PD) ; Transimpedance Amplifier (TIA) ; Limiting Amplifier (LA).

In [70], the author proposes an all-silicon WDM transmitter for downlink using cascaded micro-rings. Basically, a comb of wavelengths is generated and passed through a MZM biased in the null intensity point, modulated by a RF signal of frequency f_{RF}. In this way, for each wavelength, the optical carrier is suppressed and first-order sidebands appear, spaced apart from $2f_{RF}$. One of the sidebands is modulated by the ring modulator tuned on its wavelength, and the other sideband is unmodulated. At the receiver, the sidebands are separated by an optical filter, and the unmodulated optical carrier is used to transmit the uplink signal using phase modulation. The receiver at the CO is equipped with a DI in order to suppress RBS. In a second work [71], the author demonstrates an all-silicon ONU transceiver with a similar topology of the one in figure 1.11. The differences from [69] are : 1) an add-drop ring is used to extract the unmodulated carrier and 2) A carrier-injection ring modulator is used to modulate the uplink data using OOK, which is sent back to the CO by a second fiber. A pre-emphasis circuit is used to achieve data-rates of 5Gbps. Reach was 25km in both downlink and uplink. For uplink transmission, the 5Gbps signal had an Extinction Ratio (ER) of 5dB (with a driving voltage of $1V_{pp}$ before the pre-emphasis circuit). In downlink direction, the SiGe photo-diode demonstrated a sensitivity of about -2dBm (for 10Gbps and for BER of 10^{-5}), mainly limited by waveguide and coupling losses. Negligible sensitivity penalty to the optical fiber is observed in both downlink and uplink (BER$< 10^{-5}$).

Reference	Modulator type	Max data-rate	Max reach	Sensitivity penalty (BER target)
[74]	Ring	12.5Gbps	80km	2.5dB (10^{-9})
[72]	Ring	10Gbps	70km	6.5dB (-)
[73]	MZM	11Gbps	80km	6dB (10^{-5})
[75]	MZM	10Gbps	80km	1.2dB (10^{-10})

TABLE 1.3: State-of-the-art of silicon optical modulators enabling LR-PON with OOK modulation.

Also, many authors demonstrated the feasibility of silicon optical modulators for LR-PON using cost-effective OOK modulation. Table 1.3 summarizes the state-of-the-art in silicon photonics modulators for LR-PON. It is observed that high data-rates ($> 10Gbps$) long-reach transmission can be achieved with silicon modulators with low optical power penalty. For example, in [72], a relatively high power penalty of 6.5dB is reported, but the author shows that such high sensitivity penalty is mainly caused by bandwidth-limitation of the modulator. It shows that due to the intrinsic negative chirp of the modulator, a sensitivity penalty for 70km transmission at 10Gbps of less than 2dB is expected. In [73], a zero-chirp OOK modulation is demonstrated using a dual-driven push-pull MZM. Lower power penalty can be expected if modulation with negative chirp is intentionally introduced as explained in subsection 2.1.2.3.

Re-Modulation of Downlink Signal

In a particular implementation of lightwave centralized scheme, the same wavelength can be used for both downlink and uplink. In this way, the downlink signal is re-modulated at the ONU. To allow re-modulation of the downlink signal, a multiplexing scheme or orthogonal modulation formats should be employed to avoid interference between downlink and uplink signal. This was first proposed in [76], using Binary Phase-Shift Keying (BPSK) modulation for downlink and OOK for uplink. In [77], the author proposes an efficient Inverse Return-to-Zero (IRZ)/RZ modulation for multiplexing downlink and uplink signals. This technique is attractive because mitigates RBS reflection noise [65] at the same time. Frequency multiplexing is proposed in [58, 78, 79] - the downlink is converted to an Intermediate Frequency (IF) and the uplink is in baseband.

Coherent WDM-PON

A subgroup of pure WDM-based solutions advocate the use of a centralized-lightwave solution combined with a coherent receiver at the CO [80]. As illustrated in figure 1.12, the coherent WDM-PON takes advantage of the fact that the optical carrier for the ONU is generated at the CO : the same optical laser source used to generate the optical carrier for a given ONU is used as the Local Oscillator (LO) in reception.

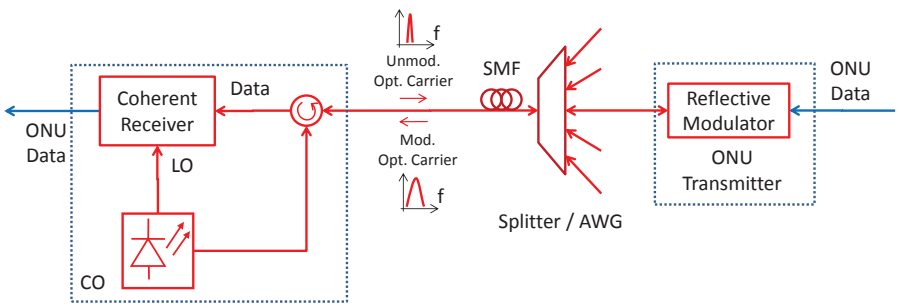

FIGURE 1.12: Coherent WDM-PON.

In a first implementation of coherent WDM-PON, the author uses a polarization diversity receiver to deal with the random polarization state of the uplink signal [80]. The proposed coherent receiver employed a 3×3 coupler instead of the regular 2×2 coupler of the conventional receiver. In this way, together with differential and Manchester coding of the modulating signal, the author shows to mitigate reflection noise. In addition, the coherent receiver improves sensibility by 4dB as compared to conventional direct-detection. Later, in 2011, the author shows a self-polarization-stabilization technique by using a Faraday rotator in the ONU - the uplink output signal is rotated by 90° as compared to the input signal [81]. In this way, the State of Polarization (SOP) of the uplink received signal at the CO is orthogonal to the one of the seed light, regardless of the fiber birefringence. This is true as long as the polarization rotation caused by fiber birefringence do not vary significantly in time as compared to the round-trip time of the optical signal. The author reports sufficient polarization stability over 68km of SMF, with 8km being deployed buried fiber, thus submitted to the usual mechanical and thermal stresses that exist in installed fiber. This type of analysis was also carried out in [82], where the author reports polarization stability over 51km of installed fiber. Therefore, the complexity of the coherent receiver is decreased twice because no polarization diversity is required. In addition, the author shows that, because of the high chirp of the Semiconductor Optical Amplifier (SOA), one can achieve BPSK modulation even if NRZ electrical modulation is applied [83]. In this way, 10Gbps Quadrature Phase-Shift Keying (QPSK) modulation of the RSOA is demonstrated in [84] and even 40Gbps with Polarization-Multiplexing (PM)-QPSK and an optical offset filter to overcome the RSOA bandwidth limitation [85].

With proper optimization of the transmission parameters, a record 42dB optical budget is demonstrated in [66] with a sensitivity of -51dBm and a reach of 100km. In this work, the author eliminates RBS noise by using a 8B/10B coding (to minimize signal power in the low-frequencies), together with a high-pass filter. This is mainly because RBS noise Power Spectral Density (PSD) is rather concentrated in low frequencies (up to 100kHz) as mentioned before. Finally, coherent-PON has shown to be compatible with burst-mode TDM-PON with negligible impact on the performance [86].

1.3.2 Pure TDM-PON

The straightforward idea to increase the data-rate per user is to upgrade current TDM-based PON architectures from 10/2.5Gbps to 40/10Gbps in downlink/uplink direction. In this way, the delivered data-rate per user can be improved fourfold. The group of TDM-based solutions for next generation optical access networks beyond 10Gbps is called XLG-PON. A schematic view of TDM-PON architecture is shown in figure 1.2(a). The major advantage is the full compatibility with the deployed network. Hence, only the transceivers at CO and ONU needs to be upgraded.

Bell Labs proposes this solution for next-generation optical access networks [87]. In a detailed study on bandwidth demand per user, driven by media services over IP, and the growth of the bandwidth supply in the last few years, the author claims that TDM-PON will deliver future high-speed services more efficiently than WDM-PON [88].

There are however many technological barriers for this ugrade. Firstly, the serial line-rate of 40Gbps in downlink direction at the C-band (around $1.55\mu m$) would limit the transmission reach to a few km of SMF, assuming that OOK modulation with direct detection is used and no dispersion compensation is made. The author in [87] proposes to use the O-band (around $1.3\mu m$) rather than the C-band to avoid chromatic dispersion impairment at the expense of higher optical loss. Another issue is the bandwidth required for the electrical and optical components of the transceivers. In downlink, the author proposes to use duo-binary modulation. This effectively reduces by a factor of 2 the bandwidth required for the transceiver components and mitigates residual dispersion by a factor of 3 [87]. For instance, a 26Gbps duo-binary optical transmission

at 40km of SMF at a wavelength of 1.3μm was demonstrated in [89]. It used a cost-effective 7GHz-Avalanche Photodiode (APD) at the receiver, achieving a sensibility of -22dBm (at a BER of 10^{-3}). For 40Gbps transmission, the required APD bandwidth would be 11GHz.

In [90], the author demonstrates a 40Gbps OOK transmission over 12km of SMF, using a dual-electroabsorption modulator. The principle of operation is to control the chirp by adjusting the relative modulation depth between direct laser modulation and the Electro-absorption Modulator (EAM).

As an alternative, high-order modulation formats can be employed in order to increase data-rate without necessarily increasing symbol-rate. In [91, 92], the authors propose the use of single-carrier PM-QPSK with coherent detection for 40Gbps and 112Gbps downlink LR-PON, respectively. The coherent receiver can definitely increase receiver sensitivity ; however, it is unattractive for the ONU because of the high cost. A very interesting approach is proposed in [93]. It advocates the use of single-carrier multi-level modulation formats detected by a non-coherent receiver. For that purpose, differential modulation formats such as Differential 8-Phase Shift Keying (D8PSK) or specially designed modulation formats such as star-16-QAM or coded 16-QAM are studied. An example of the non-coherent receiver proposed is shown in figure 1.13 suitable for star-16-QAM. The great asset of this scheme is that it removes the need for a local oscillator at the receiver as well as the phase and carrier recovery, thus greatly decreasing the cost and complexity. Up to 40Gbps is demonstrated in [93].

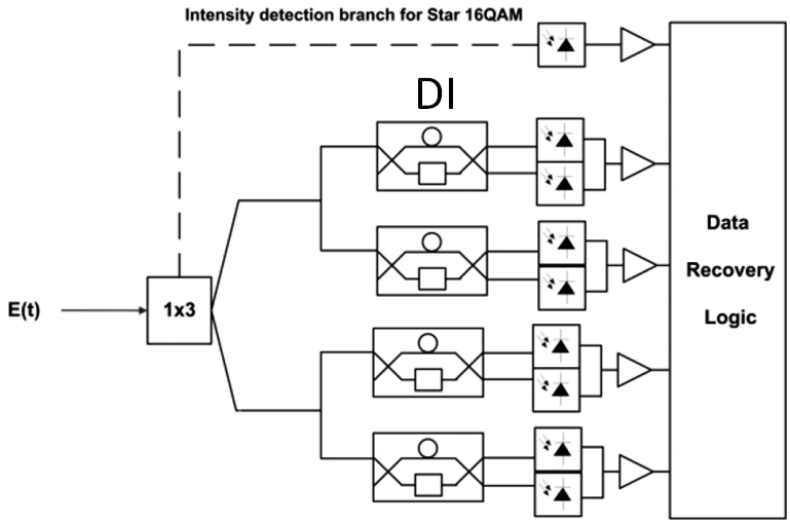

FIGURE 1.13: Non-coherent optical receiver for detecting multi-level differential modulation formats (Source [93]). DI : Delay Interferometer.

To finish, burst-mode TDMA combined with adaptive OFDM modulation is reported in [94], using low-cost Vertical Cavity Surface Emiting Lasers (VCSELs) with 2GHz bandwidth, achieving up to 9Gbps per user. This works shows the feasibility of OFDM in burst-mode using components originally designed for continuous operation. Furthermore, in [95] the author shows a smooth evolution scheme from OOK-based TDM-PON to OFDM-based TDM-PON. It shows that the two modulation formats can co-exist in the same TDM network.

1.3.3 TWDM-PON

As compared to a pure WDM solution, the Time and Wavelength Division Multiplexing (TWDM)-PON requires a lower tunability range for the transceivers because a single wavelength carries a higher data-rate and addresses several users. As already mentioned in subsection 1.2.4.1, TWDM has been chosen as a primary solution for NG-PON2 in April 2012.

Before 2012, a few works already demonstrated the potential of TWDM-PON for improving performance in FTTH/B networks. In 2009, a 10Gbps uplink transmission was demonstrated with 4 multiplexed 2.5Gbps wavelengths, using injection-locked FPs at the ONU, with negligible power penalty after 25km of SMF [96]. Later, 4 multiplexed 10Gbps OOK channels were demonstrated with a potential reach of 100km employing MZM [97].

The Tyndall group in Ireland proposes to used TDM-PON with Dense Wavelength Division Multiplexing (DWDM) for increased capacity [35]. The author proposes an original External Cavity Laser (ECL) design for low-cost and colorless ONUs. Very impressive results are achieved. A total of 32 wavelengths with 10Gbps each are demonstrated, for both downlink and uplink, spaced from 50GHz. A reach of 100km and a split-ratio of 512 are reported. However, this solution is quite complex to implement. In order to extend the reach to 100km, a Dispersion-compensation Fiber (DCF) is used. As a consequence, the system is not flexible in terms of reach. In addition, the ODN is not completely passive - optical amplifiers are used with the purpose of extending the reach.

1.3.4 FDM-PON

As an alternative to TDM-PON, FDM/Frequency Division Multiple Access (FDMA) can bring several advantages as the multiplexing scheme for future generations of optical access networks, as mentionned previously. A general scheme of FDM-based PON is illustrated in figure 1.2(b).

The group of B. Charbonnier at Orange Labs has proposed this solution back in 2010 [98]. Since then, two projects in collaborations with major actors in France (including the CEA-Leti) and across Europe started with the objective of demonstrating the feasibility of this architecture for optical access networks - FAON [99] (ANR French financed) and FABULOUS [100] (FP7 European financed). Besides evaluating the performance of this scheme, another objective of these projects is to develop a low-cost ONU transceiver based in low-speed ADC/DAC, DSP and silicon photonics components in order to provide a sustained bit-rate of 1Gbps per user [101].

The author shows in [101] that 250MHz of baseband bandwidth (total 500MHz of complex bandwidth), which is feasible with two 500Msps DAC/ADC, is enough to provide each user a sustainable and symmetric bit-rate of 1Gbps. This is the strength of this scheme : each user is provided with a data-rate of 1Gbps using very low-bandwidth electronics. As an example, figure 1.14 illustrates the RF transceiver required at the ONU.

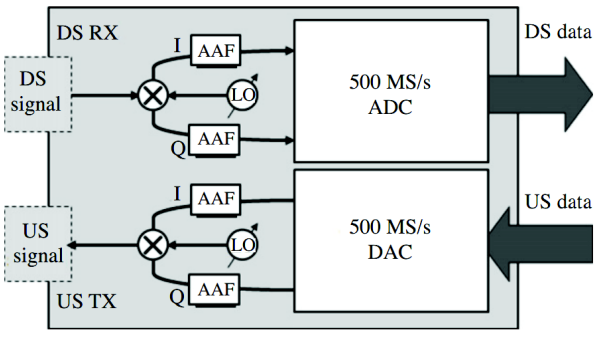

FIGURE 1.14: Cost-effective RF transceiver front-end for FDM/FDMA-PON (Source [101]).

In addition, the proposed architecture can be easily scalable by stacking wavelengths to the network. This can be done effectively by using an wavelength mux/demux in the CO and placing a WDM filter in the user's side as proposed in [101].

1.3.4.1 Downlink Transmission Performance of FDM-PON

In the proposed solution, the downlink transmission is quite straightforward. A single wavelength addresses a group of N users. The signal of each user is located at a pre-defined RF frequency. In order to avoid enhanced DSB cancellation frequency-fading due to frequency chirp (to be detailed in subsection 3.3.3.1), a MZM is used at the transmitter and an EDFA is placed after the optical modulator to boost the optical signal before being launched into the network. As mentioned in [101], the downlink RF signal could be generated with a single high-speed DAC, or several lower-speed dual-output DACs with IQ mixers and RF local oscillators to up-convert the signals to an intermediate frequency.

An allocation algorithm defines for each user an adequate modulation order and RF power of the frequency band allocated to that user according to the data-rate requested. The bandwidth is attributed as a function of the modulation order (bits per symbol) and the data-rate requested by the user. The input to the algorithm is the bit-rate request and optical budget from each user. By using theoretical models which fit well with experimental results [102], the algorithm can calculate the Signal-to-Noise ratio (SNR) as a function of the RF power driving the MZM and the RF carrier frequencies available in the spectrum. In this way, the algorithm attributes a RF driving power, a RF-frequency and a modulation format from M-QAM (hence bandwidth) to each user in order to maximize the capacity.

In order to calculate the system's capacity, the optical budget is considered to be a Gaussian variable with 21dB mean and 2dB standard deviation (minimum of 13dB and maximum of 29dB), based on the statistic of deployed networks. In this way, the calculated capacity ranges from 35Gbps to 39Gbps within a 12GHz bandwidth [103].

1.3.4.2 Uplink Transmission Performance of FDM-PON

The uplink transmission for FDM/FDMA-PON is trickier than the downlink transmission. If a single wavelength should address several users, two conditions on the uplink optical signal must be respected in order to avoid optical beat interference between adjacent ONUs : 1) Optical carrier should be suppressed ; and 2) A coherent receiver is required at the CO. In addition, the optical carrier should be sent by the CO (centralized lightwave) because the optical wavelength should be strictly equal among all users to avoid inter-ONU interference.

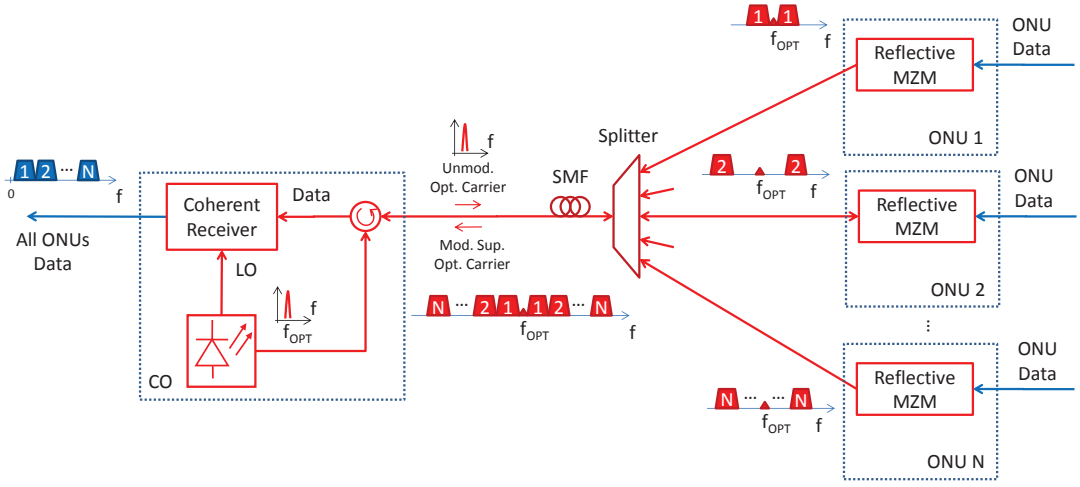

FIGURE 1.15: Schematic of the FDM/FDMA-PON proposed by B. Charbonnier *et al.* in [101]

As a consequence, the uplink transmission for the scheme proposed by B. Charbonnier *et al.* is based in coherent-PON architecture, as illustrated in figure 1.15. The originality of this

solution is the reflective optical modulator at the ONU. In order to provide a carrier-suppressed and polarization-insensitive optical signal, a dual-arm reflective MZM structure is proposed [98]. It is illustrated in figure 1.16. Basically, the optical signal arrives from the CO and it is split by a Polarization Beam Splitter (PBS). The signals from both polarizations are sent to the MZM, in clockwise and counterclockwise direction. The RF signal modulates the MZM in a forward and backward direction. In this way, each one of the polarization branches is modulated in a co-propagation of the optical and RF wave in one of the electrodes, and in a counter-propagation in the other electrode. A SOA is included to compensate the high insertion loss of the MZM. It can be shown that this structure provides the Faraday rotator mirror effect [104] - hence no polarization-diversity receiver is required at the CO, simplifying the optical receiver. The polarization stability over a 51km installed fiber plant in Turin, Italy, is analyzed in [82], showing negligible received optical power variation over 24 hours.

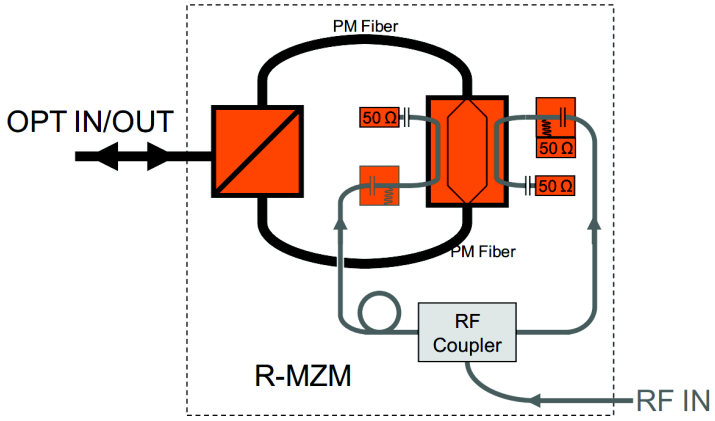

FIGURE 1.16: Reflective MZM for uplink FDMA-PON (Source [98]).

The latest results in the performance of uplink transmission are reported in [101]. Basically, the BER is counted considering several modulation formats (from QPSK to 32-QAM) with fixed data-rates of 0.5Gbps and 1Gbps as a function of the optical budget (from 13dB to 28dB) and the frequency of the RF carrier (up to 7GHz). Hence, for each modulation format, the bandwidth is adjusted accordingly to keep the same data-rate. A PON serving 64 users is mimic by 1) Introducing a 18dB degradation ($10\log_{10}(63)$) in the Optical Signal-to-Noise ratio (OSNR); 2) Using a second electrical waveform generator to reproduce RF noise from the other ONUs. In order to calculate the system's capacity, the optical budget is considered to be a Gaussian variable with 21dB mean and 2dB standard deviation, based on realistic deployed networks. The capacity of the network is then calculated to be from 16.5Gbps to 20Gbps, over a 7GHz bandwidth. A reach of 20km SMF is included in the system's capacity calculations.

1.3.4.3 All silicon ONU transmitters for FDMA-PON

In order to enable large-volume fabrication of the proposed ONU transmitter, silicon photonics implementation has been discussed in [101]. A schematic of the silicon ONU transmitter is represented in figure 1.17. It is composed by :

– 2D surface grating coupler : it allows to couple the optical signal from the optical fiber to the chip and to split orthogonal polarizations (X and Y) into two branches (as a PBS) at the same time [105]. Both X and Y polarization states of the fiber are transformed into Transverse Electric (TE) mode in the silicon waveguide.

- Tunable WDM filter : In a WDM configuration, this filter is necessary to select the predefined ONU wavelength. The filter can be built with add-drop ring resonators [68] and integrated heaters on top to dynamically adjust the resonance wavelength.
- SOA : it is used to overcome the high insertion losses of the coupler and the MZM. The SOA can be fabricated using a III/V material in top of a silicon waveguide to provide the optical gain. In [106], a 13dB gain SOA is demonstrated using a wafer-bonding technique and adiabatic mode transformers to couple the light from the silicon waveguide to the III/V waveguide (cf. subsection 2.2.1.4).
- Travelling-wave MZM : An extensive state-of-the-art of silicon MZM is detailed in section 2.2.3.1.
- Monitoring photodiode : A low-speed monitoring photodiode serves to control the bias point of the MZM (null intensity point). It can be fabricated using monolithically growth Ge-on-Si [107] or defect-enhanced silicon waveguides [108] for absorption around $1.55\mu m$.

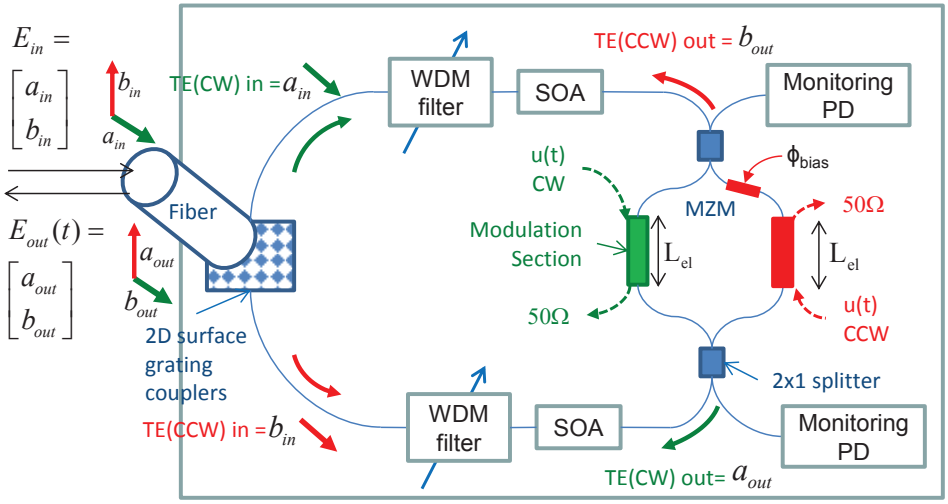

FIGURE 1.17: Representative diagram of the silicon photonics ONU transmitter (Source [101]). Acronyms : Clockwise (CW), Conterclockwise (CCW).

1.3.5 OFDM-PON

OFDM-based PON can be seen as a particular case of FDM-PON, illustrated in figure 1.2(b). The principle of operation of the OFDM transmission technique is detailed in section 3.3. As compared to the previous FDM/FDMA architecture, OFDM-PON is more spectral efficient since the subcarriers partially overlap. Dynamic bandwidth allocation can be easily performed simply by assigning more or less subcarriers to each user. However, OFDM-PON requires OFDM transceivers at the CO and the ONU, which can be quite costly and power-consuming as compared to the other solutions. An analysis of existing components for OFDM modem implementation is presented in subsection 3.3.3.3.

1.3.5.1 Downlink for OFDM-PON

In order to have low-cost receivers at the ONU, the downlink signal should enable direct detection at the user's side. Still, a few authors consider using coherent OFDM for downlink [109].

Technical solutions for direct-detection OFDM-PON in downlink direction can be divided in two classes : IM/DD-based and SSB-based. Technical details about these types of optical

OFDM is given in subsection 3.3.3. It will be shown that SSB-based enables a long transmission reach with negligible sensitivity power penalty, at the expense of transceiver complexity.

IM/DD-based OFDM-PON

The general scheme for IM/DD-based OFDM-PON transmission in downlink direction is shown in figure 1.18. Basically, the general form is the same as the classical FDM-PON of figure 1.2(b) with an OFDM modulator in the CO and an OFDM demodulator at the ONU. At the CO, an OFDM signal with baseband OFDM signal of bandwidth B is generated and modulated with an optical intensity-modulator. The intensity modulation generates an optical DSB signal, which is defined in subsection 3.3.3.1. In order to overcome the reduced sensibility of optical OFDM signals, some authors use optical amplifiers in the link [110–112]. Concerning the position of the optical amplifier in the link, three configurations can be defined - booster (the optical amplifier is placed at the transmitter, before the fiber span), pre-amplifier (the optical amplifier is placed at the receiver, after the fiber span and splitter) and in-line amplifier (the optical amplifier is placed between fiber spans). Because of the relative cost and power consumption of the optical amplifiers, it is desirable booster configuration over the others. In this way the optical amplifier is placed at the CO.

In the following we detail two techniques proposed with the objective of reducing the complexity of the OFDM transceivers. The first one is called multi-band OFDM and concerns the transmitter. The entire OFDM signal band is divided in sub-bands that are generated with independent modems. The second one it is called scalable OFDM and it is intended for the receiver.

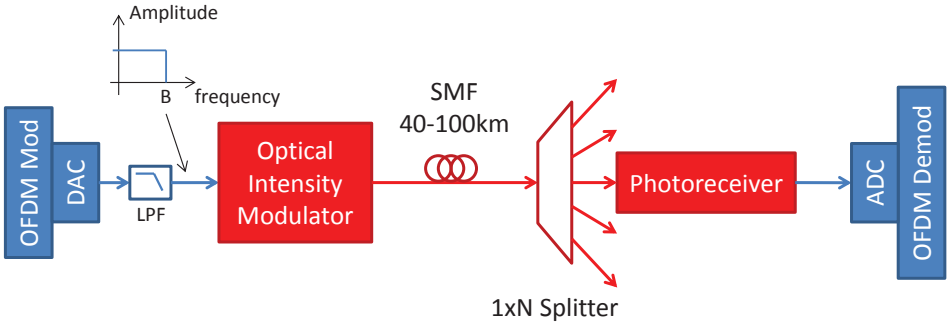

FIGURE 1.18: General scheme for OFDM-PON with intensity-modulation in downlink direction. Acronyms : Lowpass Filter (LPF).

Multi-band Optical OFDM Transmitter A major disadvantage of OFDM technique is the complexity of the DSP and DAC/ADC of the OFDM modem. It is generally assumed that a baseband bandwidth of at least 10GHz is necessary in order to generate the 40Gbps optical OFDM signal. Using a single DAC/ADC and assuming that the OFDM signal occupies the frequency band from 0 to 10GHz, it would require a sampling-rate of $f_s = 20Gsps$ and a DSP powerful enough to process the entire 40Gbps OFDM signal. Some authors proposed to split the OFDM bandwidth into several N_{sb} sub-bands generated separately [109, 111, 112] - solution called multi-band OFDM. In this way, the DACs/ADCs sampling-rate and processing requirement for the DSP are reduced by a factor equal to the number of sub-bands. After the baseband generation of each one of the sub-bands, they are up-converted to different intermediate frequencies and added together.

The principle of operation of the multi-band OFDM is shown in figure 1.19. Generally, the lowest frequency sub-band is generated using only one DAC, requiring a sampling-rate of B/N_{sb}. The other sub-bands are generated using two DACs, a LO, 2 mixers and 2 low-pass filters each in

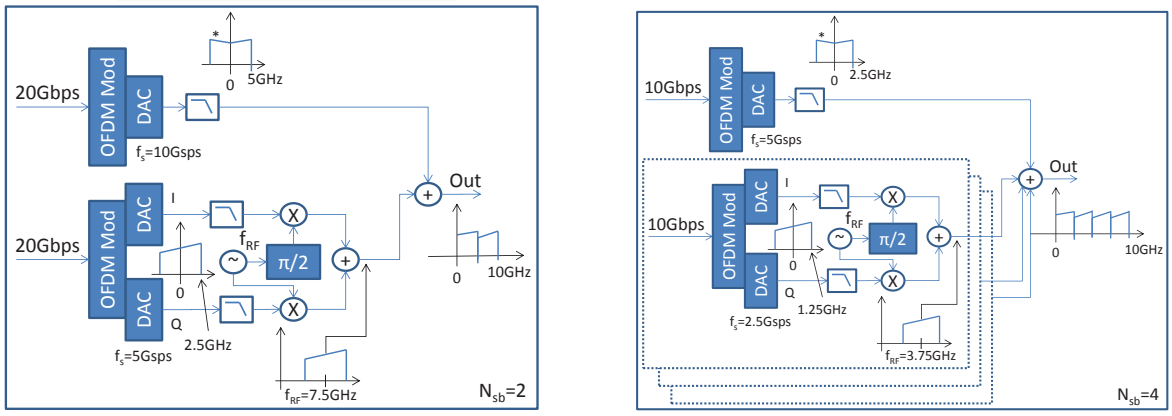

(a) (b) PON

FIGURE 1.19: Scheme of a 10GHz multi-band OFDM signal generation, (a) $N_{sb} = 2$ and (b) $N_{sb} = 4$).

order to up-convert the baseband OFDM signal to an intermediate frequency. The sampling-rate of each DAC/ADC in this case is $B/(2N_{sb})$. As a result, the number of DACs scales as $2N_{sb} - 1$. An example of the additional components, number and sampling-rate of DACs necessary for 1, 2 and 4 sub-bands is shown in table 1.4 (for a 10-GHz baseband bandwidth OFDM signal).

Number of sub-bands (N_{sb})	Number of DACs	DACs sampling-rate	Additional Components
1	1	20Gsps	-
2	3	10Gsps (1) and 5Gsps (2)	1 LO, 2 Mixers, 2 LPF
4	7	5Gsps (1) and 2.5Gsps (4)	3 LO, 6 Mixers, 6 LPF

TABLE 1.4: Example of number of DACs, sampling-rate and additional components for 10GHz multi-band OFDM signal generation.

Scalable OFDM With the purpose of reducing the front-end speed in the receiver at the ONU, the authors in [113, 114] propose to use a technique that they called scalable OFDM. For each user, an analog front-end (a local oscillator, two RF-mixers and two low-pass filters) is used to convert to baseband select only the subcarriers allocated to that user. The LO frequency is set to central frequency of the subcarriers allocated to a single user. Then, the sampling-rate required by the ADC depends only on the bandwidth reserved to the user. Figure 1.20 illustrates the principle. In this example, three users A, B and C (green, red and blue respectively) have different allocated subcarriers and bandwidths (N=128 from 5 to 6.25GHz for A, N=256 from 6.25 to 8.75GHz for B and N=128 from 8.75 to 10GHz). The LO frequency for each user is set to 5.625, 7.5 and 9.375GHz respectively, and the sampling-rate (Fast-Fourier Transform (FFT) size) required for each user is decreased from 20Gsps (1024) to 2.5Gsps (128), 5Gsps (256) and 2.5Gsps (128) respectively.

State-of-the-art The optical IM/DD-OFDM may suffer from severe frequency fading as a result of the DSB cancellation caused by chromatic dispersion. This is detailed in section 3.3.3.1 of this work. As a consequence, most authors propose to use bit and power loading algorithms

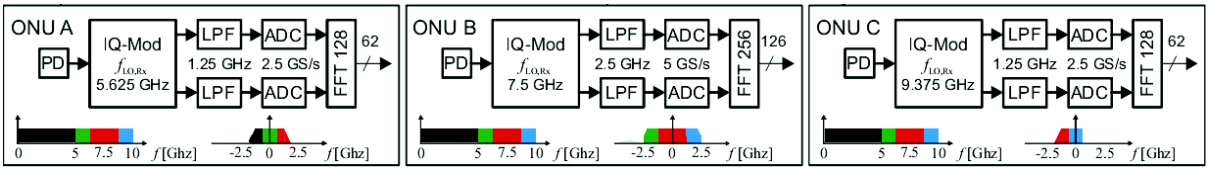

FIGURE 1.20: Scalable OFDM technique to reduce ONU front-end speed (Source [113]).

(cf. appendix C) in order to maximize transmission capacity [110, 111, 115, 116], solution called Adaptive OFDM.

A summary of the state-of-the-art publications for experimental demonstrations of IM/DD OFDM-PON in the downlink direction are shown in table 1.5. Concerning DML-based transmitters, the first work showing the feasibility of 40Gbps OFDM PON is [115], without any optical amplifier in the link. Very recently, by using a high-speed 65Gsps DAC and ADC from Fujitsu, the authors demonstrated a record data-rate : more than 100Gbps data-rate up to 10km, and more than 60Gbps over 40km using a baseband bandwidth of 24GHz also without any optical amplifier [116]. In order to improve performance, the authors use a digital non-linear equalizer at the reception. Furthermore, in [110], the author compares the performances of booster and pre-amplifier configurations of the optical amplifier. The author concludes that the pre-amplifier configuration can achieve better [bit-rate $\times$ distance] product than the booster configuration.

A 4-band optical OFDM signal transmission using a MZM is demonstrated in [112]. According to the transmission distance, one or more OFDM sub-bands are turned-off if the minimum BER required is not achieved. The modulation-order in each sub-band is optimized according to the quality of the link. In this way, the bit-rate is changed adaptively from 9.37 to 40Gbps (from 0 to 100km of SMF). A 2-band optical OFDM transmission using an EAM is shown in [116], achieving more than 40Gbps in a 100km SMF-link, with an in-line optical amplifier at 50km. Multi-band OFDM is also proposed by N. Cvijetic *et al.* in [109], but with a coherent-receiver at the ONU.

We have developed our own test-bed to evaluate the performance of the downlink IM/DD optical OFDM-PON with bit and power loading using commercial-available components. It is described in subsection 4.2.1. A summary of these results DML and MZM are shown in the last two lines of table 1.5.

A few authors propose a lower data-rate of 10Gbps per wavelength in downlink transmission in order to reduce the cost of the OFDM modem [117–119]. In this way, a 40Gbps aggregated data-rate can be achieved by stacking 4 wavelengths.

SSB-based OFDM-PON

Due to its resilience against fiber chromatic dispersion, SSB-OFDM transmission has been first proposed to long-haul transmission [120] in 2007. Later, it was proposed as a solution for future generations of PON in 2009 [121]. Following this first work, a number of authors worked towards this solution [58, 122–125].

The state-of-the-art in SSB-based solutions for OFDM-PON is detailed in table 1.6. The challenge of such a solution is to provide an efficient transceiver for generating the SSB-OFDM signal. Most of the proposed solutions in table 1.6 propose the use of intensity modulation and then optical filtering of one of the sidebands. This solution is quite complex because an optical filter with steep edges is necessary in order to filter only one of the sidebands, and it is not "colorless" because the optical filter must be tuned to the working wavelength. In [122], the author proposes to use an optical IQ modulator biased in the null transmission point and using a second laser to re-insert the optical carrier.

In this thesis, the SSB-OFDM transmitter proposed in [126] for long-haul is analyzed as

Reference	Bit-rate (optical B2B)	Bit-rate at max reach	OFDM signal bandwidth	Max reach	Optical Trans-mitter	Optical Amplifier
[115]	40Gbps	25Gbps	10GHz	60km	DML	No
[110]	40Gbps	8Gbps	12GHz	100km	DML	Booster / Pre-amplifier
[112]	40.3Gbps	9.4Gbps	10.3GHz	100km	MZM	Pre-amplifier
[111]	48.5Gbps	40.2Gbps	10GHz	100km	EAM	In-line at 50km
[103]*	-	39Gbps	12GHz	20km	MZM	Booster
[116]	107Gbps	60Gbps	24GHz	40km	DML	No
This work**	40.4Gbps	25.3Gbps	10GHz	50km	DML	No
This work**	42.6Gbps	41.4Gbps	10GHz	50km	MZM	No

* This reference corresponds to the FDM-PON described in subsection 1.3.4.1.
** The experimental test-bed of this thesis is described in sub-section 4.2.1.

TABLE 1.5: State-of-the-art of IM/DD optical OFDM with adaptive bit-rate for downlink PON.

a possible solution for future PON. It proposes to add an electrical RF carrier located at the side of the OFDM spectrum, before the optical modulation of the complex OFDM signal. This solution is interesting because it is "colorless" and a single laser source is required. A silicon photonics implementation of this solution is discussed in subsection 5.2. The performance in terms of sensitivity degradation as compared to "ideal" $LiNbO_3$ modulators is assessed.

Reference	Exp/Sim	Data-rate / λ	Reach	Split-ratio (Optical Budget)	Method of generation
[121]	Exp	10Gbps	10km	-	Optical filtering
[122]	Exp	43.6Gbps	20km	1 :32 (15dB)	2-laser Optical Carrier Insertion
[123]	Sim	40Gbps	20km	1 :32 (15dB)	Optical filtering
[124]	Exp	40Gbps	90km	1 :32 (15dB)	Optical filtering
[125]	Sim/Exp	20Gbps	100km / 26.7km	1 :32 (15dB) - Sim	Optical filtering
[58]	Exp	40Gbps	20km	-	Optical Filtering

TABLE 1.6: Summary of the state-of-the-art works of optical SSB-OFDM-based PON for next-generation optical access networks.

1.3.5.2 Uplink for OFDM-PON

There are two technical solutions for uplink OFDM-PON, which can be divided in direct-detection or coherent-detection at the CO. Basically, if a single photo-diode is used at the receiver (CO), it is mandatory that a different wavelength should be used for each ONU in order to avoid optical beat interference between adjacent ONUs. On the other hand, assuming a centralized wavelength scheme with coherent detection, a single-wavelength can be used to address several users. This is similar to the scheme proposed by B. Charbonnier *et al.* detailed in subsection 1.3.4.2, except that applied to OFDM.

Direct-Detection at the CO

In order to effectively use a single photodiode at the CO to perform the O/E conversion of a group of N users multiplexed in frequency, each user should have different wavelengths. This is why this scheme is sometimes called WDM-Orthogonal Frequency Division Multiple Access (OFDMA)-PON. The principle of operation of OFDMA-PON with direct-detection at the CO in shown in figure 1.21. The electric signal at the ONUs can be generated either by using a high-speed DAC, or two low speed DACs (to generate the baseband OFDM signal) and an analog up-conversion stage (an electric LO, 2 lowpass filters and 2 RF mixers) as illustrated in figure 1.21. A wavelength λ_n and a RF frequency f_{RF_n} are attributed to the n^{th} user. At the receiver, the signals from different ONUs do not interfere because each one is located at a different frequency band.

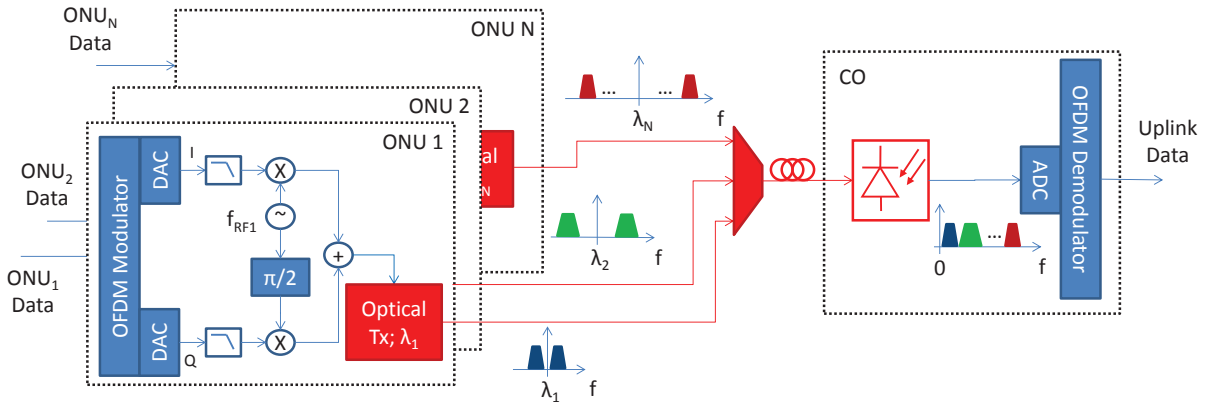

FIGURE 1.21: General scheme of OFDMA-PON with single photodiode at CO.

The idea was first proposed by Qian *et al.* in 2007 [127]. It demonstrated the feasibility of this solution with 2 ONUs, reporting an aggregated data-rate of 10Gbps within a total bandwidth of 2.5GHz. A reach and split-ratio of 20km and 1 :32 were demonstrated. Later, the same scheme with a third ONU carrying a WiMAX signal was demonstrated [128]. It showed that there was no throughput degradation when the WiMAX signal was passed through the OFDMA-PON network together with the two other ONUs. A performance study with 8 ONUs is reported in [129], but the uplink aggregated data-rate was decreased to 5Gbps (within 2.9GHz bandwidth). Finally, a hybrid 2.5Gbps/10Gbps OFDMA-PON was demonstrated in [130], where an ONU carried a 2.5Gbps OFDM signal and the other carried 10Gbps. With proper optimization of the relative power between the ONUs, an optical budget of 31dB is achieved, using an EDFA as a pre-amplifier (hence at the CO). Finally, an OFDMA-PON experimental demonstration with real-time OFDM transceivers is reported in [131], with an aggregated data-rate of 11.25Gbps.

In [132], in a collaboration between CEA-Leti with Orange Labs, the authors studied the influence of the laser chirp for OFDMA-PON using DMLs in the ONUs. This experience is performed with 2 ONUs using DFBs as transmitters. The main conclusions of this work are that,

because of spectral broadening caused by frequency chirp, the minimum wavelength spacing for a 4.4GHz total OFDM bandwidth (considering all ONUs) is measured to be 16GHz instead of the theoretical 8.8GHz, considering a maximum modulation depth of the laser. Also, it is shown that the laser chirp influences the frequency response of the link. As a consequence, the performance of each OFDMA sub-band depends on the fiber span length and the laser frequency chirp.

Following this work, a similar analysis was made in [133], where the author considers an ONU with a DFB laser and another with a RSOA. With a total bandwidth of 2GHz, the author shows that the minimum wavelength spacing to avoid optical beat interference is 0.15nm (16.67GHz). This is about the same value found in [132] but with lower OFDM bandwidth (2GHz instead of 4.4GHz). This may be a consequence of the higher constellation order used in [133] and the fact that a RSOA is used as the optical transmitter, which may exhibit higher chirp than a DFB [134]. In a further work [135], using a comprehensive theoretical model for the laser and RSOA behavior and validated with experimental results, the author shows that the number of ONUs does not have an impact in the minimum wavelength spacing. The author also demonstrates that, by doubling the number of ONUs, there is a sensibility power penalty of 1.9dB per ONU (thus reducing uplink power budget by 1.9dB). This is a consequence of the decrease of the signal-to-carrier ratio with the increase of users in the network - hence a smaller signal-to-carrier ratio represents lower received electrical power for the same received optical power.

Coherent-detection at the CO

A group of authors defend the use of a coherent receiver at the CO, mainly driven by N. Cvijetic *et al.* in NEC laboratories [109, 118, 136, 137]. A summary of the state-of-the-art is shown in table 1.7.

An interesting approach is proposed in [136] in order to increase spectral efficiency. The optical OFDM signal at the ONU is generated in a classic manner using an intensity modulator - hence an optical DSB signals. The ONUs are divided into two groups : "odd" and "even". To each ONU within a group, a different RF carrier frequency is attributed. The ONUs within a group are added together using an optical coupler. An optical interleaver is used to combine both groups. In this way, the left sideband is filtered from the odd group, and the right sideband from the even group, hence they do not interfere between each other. Spectral efficiency is increased twofold using this technique.

Reference	Agregated Data-rate / λ	Max reach	Split-ratio
[118]	10Gbps	20km	1 :32
[136]	44Gbps	20km	1 :32
[137]	48Gbps	90km	1 :32
[138]	48Gbps	100km	1 :64

Table 1.7: Summary of the state-of-the-art of OFDM-PON with coherent detection at the CO.

1.4 Summary of the Chapter

As a conclusion, there are several promising technologies to upgrade current TDM-PON systems deployed in optical access networks, each one with its own advantages/disadvantages. In spite of the recent choice of FSAN of TWDM as a primary solution for NG-PON2, there are

many strong candidates for improving performances beyond NG-PON2 in terms of data-rate, reach and split-ratio that will become feasible in the next few years.

It was shown that many authors consider silicon photonics as the key-enabling technology for NG-PON2 and beyond, due to its mass-production and E/O integration abilities. As this technology becomes more and more mature, it is evident that the large-volume capability can decrease the unit-cost of the ONU transceiver, together with improved performances as compared to commercial components.

Chapitre 2

Building Blocks of Optical Transmission Systems and their Modeling

In this chapter, we review the basic concepts of the building blocks of an optical communication system. It is divided in three main parts : 1) Propagation in the optical fiber, 2) E/O converters and 3) O/E converters. In each part, the objective is to discuss the physical effects considered in this work and to detail the transfer function and eventually noise added by the element in the optical link, as a realistic description of the behavior of that component. This study includes silicon photonics transmitters such as hybrid DML and external modulators. This is implemented in a simulation platform used to analyze the performance of the optical link, which is detailed in chapter 5.

An overview of a generic optical transmission system is shown in figure 2.1, from the transmitter to the receiver through the optical channel. At the transmitter side, the digital data (e.g. binary data) drives an electronic front-end, converting the digital data to an analog electric signal. This modulated signal drives itself an optical transmitter that converts it into an optical modulated signal (E/O converter). The electronic front-end architecture depends on the modulation format that is used. When a binary digital data is used (OOK), it is made up with an analog amplifier followed by filter. When complex high-order modulation formats are used, born by a single carrier or multiple-carriers (cf. section 3.3), the electronic circuit is made up with DSP cells and a DAC.

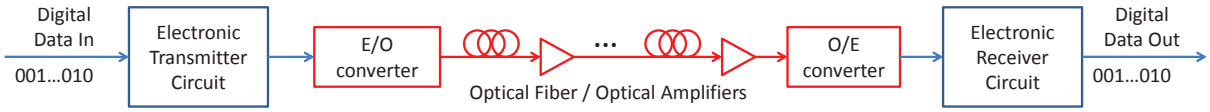

FIGURE 2.1: Overview of an optical transmission system.

The optical signal is transmitted over an optical link which may have several optical amplifiers and filters. Each set of optical fiber in between optical amplifiers is called a fiber span. The fiber length in each fiber span may vary depending on the system's requirements, but for long-haul optical transmissions at $1.55\mu m$ wavelength, the most common value used is 80km of SMF. An optical receiver performs the opto-electric conversion (O/E converter) and delivers the analog electrical signal to the electronic receiver circuit. The latest demodulates the analog signal into digital data.

2.1 Propagation in the Optical Fiber

The propagation of an optical carrier in a waveguide is based on the total internal reflection principle. An optical fiber is formed by a core, with a refractive index n_1, surrounded by a cladding, with a refractive index n_2 as illustrated in figure 2.2(a). If an optical wave strikes the boundary between the two materials with an angle (measured perpendicularly to the propagation direction) higher than the critical angle $\Phi_c = \sin^{-1}(n_2/n_1)$, the total reflection occurs. So as to have real values for the critical angle, this imposes that $n_1 > n_2$. The wave is reflected back into the core with the same angle of incidence Φ_i but opposite sign. Due to the symmetrical nature of the optical fiber, the total reflection repeats until the optical wave gets absorbed or it reaches its destination, characterizing the total internal reflection. The total internal reflection mechanism is illustrated in figure 2.2(a).

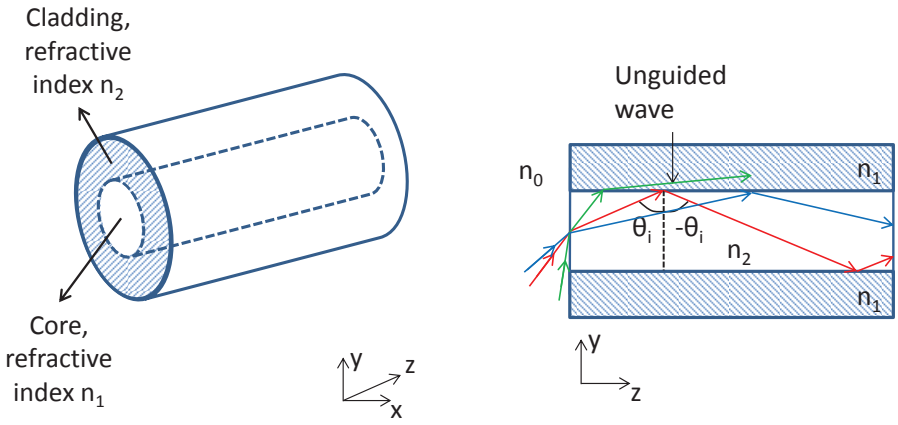

FIGURE 2.2: Optical fiber geometry in (a) 3D view and (b) cross-section in x-cut (illustration of the total internal reflection mechanism).

An optical mode is characterized by the angle of incidence θ_i of the optical wave at the interface core-cladding. For instance, the red and blue curve in figure 2.2(b) represent two different guided modes. The optical mode describes the distribution of light across the fiber. In this way, two types of fiber can be identified : Multi-Mode Fiber (MMF) and Single-mode Fiber (SMF). The number of modes than can propagate in the fiber is characterized by the diameter of the fiber core. Typical values for MMFs are $50\mu m$ and $62.5\mu m$, which can carry from 300 to 500 modes, while for SMFs $9\mu m$ is generally used.

The dominant mechanism of time-dispersion in MMF is the inter-modal dispersion. It is caused by the fact that two modes propagating in the fiber have different speeds and travel different paths until they reach their destination. This can be intuitively understood by analyzing the two guided waves of figure 2.2(b) (red and blue). The red wave has an angle of incidence lower than the blue wave. Hence, the red wave will travel a longer path-length than the blue wave to the end of the fiber.

On the other hand, SMF do not suffer from inter-modal dispersion because the energy of the injected optical signal is carried by a single mode of propagation. However, time dispersion does not disappear entirely, which is dominated by chromatic dispersion. It comes from the dependency of the group index (to be defined in the following) with the frequency, which causes different spectral components of the optical signal to travel at different speeds. The physical origin of the chromatic dispersion phenomenon is divided in material and waveguide dispersion as explained in [139].

Considering an optical pulse in the fiber input, the consequence of dispersion is a broadening of the pulse as illustrated in figure 2.3. This imposes a limitation on the [bit-rate × reach] product if single-carrier modulation is used. It is discussed in subsection 2.1.2.

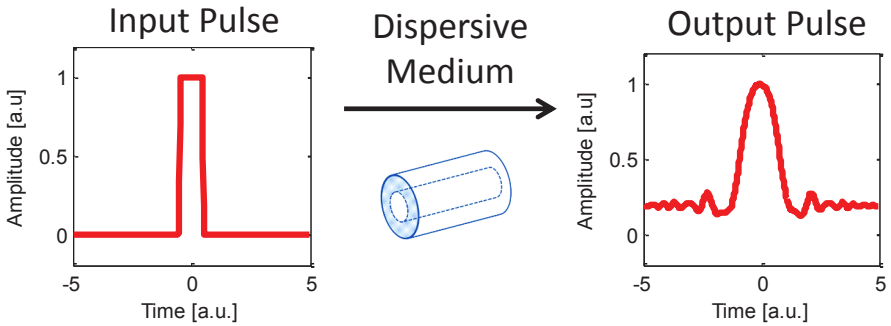

FIGURE 2.3: Dispersive effect on squared pulse.

The SMF allows the propagation of one single mode of propagation only, but this mode can propagate according to two orthogonal polarizations (generally called X and Y), which are perpendicular to the propagation direction. Due to the fiber birefringence, the two polarizations travel with slightly different speeds, causing another type of dispersion, called Polarization Mode Dispersion (PMD). It is not considered in this work because for medium-reach optical systems ($< 100km$), the Polarization Mode Dispersion (PMD) is negligible compared to chromatic dispersion.

Basic Concepts

An optical signal propagating in a SMF of length L arrives at the end of the fiber after a time delay $T = L/v_g$ where v_g is the group velocity. It is defined by [139]

$$v_g = \frac{1}{d\beta/d\omega}. \tag{2.1}$$

where $\beta = 2\pi n_{eff}/\lambda_{opt} = \omega_{opt} n_{eff}/c$ is the phase propagation constant of the optical mode, which is a measure of the change undergone by the phase of the wave as it propagates in a given direction. The effective refractive index $n_{eff} = c/v_{phase}$ of a waveguide is defined as the ratio between the speed of light in vacuum and the phase speed of the light in the waveguide. It depends on the waveguide geometry, n_1 and n_2. Replacing $\beta = \omega_{opt} n_{eff}/c$ in (2.1), the group velocity v_g is written as

$$v_g = \frac{c}{n_g} \tag{2.2}$$

where n_g is the group index given by

$$n_g = n_{eff} + \omega_{opt}\frac{dn_{eff}}{d\omega} = n_{eff} - \lambda_{opt}\frac{dn_{eff}}{d\lambda}. \tag{2.3}$$

Note that n_g is related to the propagation of the wave's amplitude in a given direction, while n_{eff} is defined with respect to the phase velocity, as already mentioned.

Basic Propagation Equation

The optical field $E(x, y, z, t)$ of an optical signal propagating in the z-direction through an optical fiber is defined as

$$E(x,y,z,t) = \begin{bmatrix} E_x \\ E_y \end{bmatrix} \cdot F(x,y) \cdot A(z,t) \cdot \exp \hat{a}A\c{a}(j(\beta z - \omega_{opt} t)) \cdot \exp\left(-\frac{\alpha_{abs}}{2} z\right) \tag{2.4}$$

where $F(x,y)$ is the spatial distribution of the optical mode propagating in the fiber, $A(z,t)$ is the complex slow-varying envelope in time-domain (as compared to the frequency of the optical carrier ω_{opt}), of the optical field, α_{abs} is the intensity attenuation coefficient of the optical carrier in the fiber in m^{-1} and $\begin{bmatrix} E_x \\ E_y \end{bmatrix}$ is the Jones vector describing the state of polarization of the optical field. The spatial distribution $F(x,y)$ of the fundamental mode for weakly guiding waveguides (typically for optical fibers) can be approximated by a Gaussian distribution. In the following analysis, a single state of polarization is assumed ($E_x = 1, E_y = 0$), for simplicity.

The propagation of an optical field in a SMF can be derived from the Maxwell's equations and it is described by the following equation [140]

$$\frac{\partial \tilde{A}(z,\Delta\omega)}{\partial z} - \left(\frac{\alpha_{abs}}{2} + j\beta\right) \cdot z\tilde{A}(z,\Delta\omega) = 0 \tag{2.5}$$

where $\tilde{A}(z,\Delta\omega)$ is the frequency-domain representation of the complex slow-varying envelope $A(z,t)$ of the optical-field. The attenuation coefficient depends on the optical carrier frequency ω_{opt} but it can be considered constant in the interval $\Delta\omega$ (if $\Delta\omega << \omega_{opt}$).

As a remark, the attenuation coefficient is sometimes included in the propagation constant β. In this case, the effective index is a complex number $\overline{n_{eff}} = n_{eff} + j\kappa_{abs}$, where the real part is the phase index and the imaginary part represents the absorption in the optical medium. The attenuation coefficient α_{abs} is defined as $\alpha_{abs} = 4\pi\kappa_{abs}/\lambda_{opt}$.

The chromatic dispersion in the optical fiber comes from the fact that the propagation constant $\beta = f(\omega)$ varies with the frequency. In other words, different spectral components of an optical wave propagating through an optical medium travel with different speeds. Considering an optical carrier of frequency ω_{opt} carrying a signal with bandwidth $\Delta\omega << \omega_{opt}$, the propagation constant can be expanded according to Taylor series up to the third order

$$\beta(\omega) \approx \beta_0 + \beta_1\Delta\omega + \frac{\beta_2}{2}(\Delta\omega)^2 + \frac{\beta_3}{6}(\Delta\omega)^3 \tag{2.6}$$

where $\beta_m = (d^m\beta/d\omega^m)_{\omega=\omega_{opt}}$. From (2.1), the β_1 variable is related to the group index by $\beta_1 = 1/v_g$, β_2 is known as the Group Velocity Dispersion (GVD) and β_3 is the third-order dispersion parameter. Then, it is useful to define the chromatic dispersion parameter D related to the GVD parameter by

$$D = -\frac{2\pi}{\lambda_{opt}^2}\beta_2. \tag{2.7}$$

Typical values of D are $15 - 18ps/(nm \cdot km)$ at $\lambda_{opt} = 1.55\mu m$, while it is much lower at $\lambda_{opt} = 1.3\mu m$, in the order of $1ps/(nm \cdot km)$. Then, higher order dispersive effects are characterized by the dispersion slope $S = dD/d\lambda$. Using (2.7), it is given by

$$S = \left(\frac{2\pi c}{\lambda_{opt}^2}\right)^2 \beta_3 + \frac{4\pi c}{\lambda_{opt}^3}\beta_2. \tag{2.8}$$

Typical values of S are in the order of $0.05 - 0.09ps/(nm \cdot km^2)$. Replacing (2.6) in (2.5), and converting it from the frequency-domain to the time-domain (by taking the inverse Fourier transform), (2.5) can be written as

$$\frac{\partial A(z,t)}{\partial z} + \left(\frac{\alpha_{abs}}{2} + j\beta_0\right) \cdot zA(z,t) + \beta_1 \frac{\partial A(z,t)}{\partial t} + j\frac{\beta_2}{2}\frac{\partial^2 A(z,t)}{\partial t^2} - \frac{\beta_3}{6}\frac{\partial^3 A(z,t)}{\partial t^3} = 0. \quad (2.9)$$

By doing a simple variable change $t' = t - \beta_1 z$, the β_1 term can be eliminated, and (2.9) becomes

$$\frac{\partial A(z,t)}{\partial z} + \underbrace{\frac{\alpha_{abs}}{2} \cdot zA(z,t')}_{\text{attenuation}} + \underbrace{j\frac{\beta_2}{2}\frac{\partial^2 A(z,t')}{\partial t'^2} - \frac{\beta_3}{6}\frac{\partial^3 A(z,t')}{\partial t'^3}}_{\text{chromatic dispersion}} = 0. \quad (2.10)$$

The optical field of the carrier can be found in any point of the optical fiber (for any value of z) by solving (2.10) considering an initial field $A(0,t)$. The second term accounts for the attenuation of the fiber while the third and fourth terms account for the fiber chromatic dispersion (first and second order, respectively).

Equation (2.10) describes two linear effects of the optical field propagation through the fiber : attenuation and dispersion, which are described in the following subsections.

2.1.1 Optical Fiber Attenuation

Considering $\beta_2 = 0$ and $\beta_3 = 0$ in (2.10), and omitting the carrier phase shift equal to $\beta_0 z$, the complex envelope of the optical field can be written as

$$A(z,t) = A(0,t) \cdot \exp\left(-\frac{\alpha_{abs}}{2} z\right). \quad (2.11)$$

The last equation states that, in the absence of dispersion, the amplitude of the complex envelope of the optical intensity at a point z of the optical fiber is attenuated by a factor $\exp(-\alpha_{abs} z)$. Sometimes, the attenuation coefficient α_{abs} is represented in dB/m, and it is related to the linear coefficient (in m^{-1}) by

$$\alpha_{abs}[dB/m] = \frac{10}{\ln 10} \cdot \alpha_{abs}[m^{-1}]. \quad (2.12)$$

Figure 2.4 shows the dependence of the single mode fiber attenuation (in dB/km) with the wavelength of the optical carrier In the $0.8\mu m$-$0.9\mu m$ window, historically dedicated to short reach applications, the attenuation ranges from 2 to $3dB/km$. The attenuation has two minimum values, about $0.4dB/km$ and $0.2dB/km$ at the wavelengths $1.3\mu m$ and $1.55\mu m$, respectively. (telecom applications, medium and long-haul reach applications).

2.1.2 Chromatic Dispersion

In order to analyze the effect of the chromatic dispersion on an optical pulse after its propagation over a certain length ($z = L$) of single mode fiber, one can solve (2.10), describing the complex envelope of the optical carrier $A(0,t)$, as a pulse. The pulse has a time duration T_0 at the input of the fiber, and it is broaden to $T_0 + \Delta T$ at the output $z = L$ of the fiber.

For wavelengths around $1.55\mu m$, the effect of the third-order dispersion parameter can be neglected compared to the GVD parameter. In this way, the relationship between the time spread ΔT of a pulse with spectral width $\Delta\omega$ after propagation in an optical fiber of length L is given by

$$\Delta T = \frac{dT}{d\omega}\Delta\omega = \frac{d(L/v_g)}{d\omega}\Delta\omega = L\Delta\omega\left(\frac{d^2\beta}{d\omega^2}\right)_{\omega=\omega_0} = L\Delta\omega\beta_2. \quad (2.13)$$

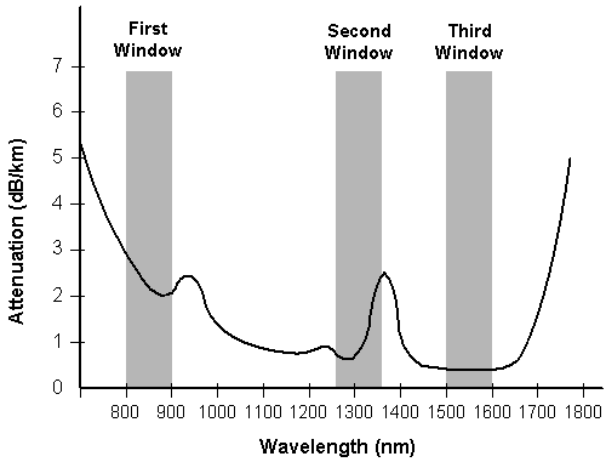

FIGURE 2.4: The attenuation-wavelength curve and the transmission windows of an optical fiber.

In most lightwave systems, it is more common to represent the Root Mean Square (RMS) spectral width of a signal in wavelength units ($\Delta\lambda$) rather than pulsation ($\Delta\omega$). Assuming that $\Delta\lambda << \lambda_{opt}$ they are related by

$$\Delta\omega = \frac{2\pi c}{\lambda_{opt} + \Delta\lambda} - \frac{2\pi c}{\lambda_{opt}} = \frac{-2\pi c\Delta\lambda}{\lambda_{opt} \cdot (\lambda_{opt} + \Delta\lambda)} \approx -\frac{2\pi c\Delta\lambda}{\lambda_{opt}^2}. \tag{2.14}$$

Replacing (2.14) in (2.13), the time spread of the pulse can be expressed as

$$\Delta T = -L\frac{2\pi c\beta_2}{\lambda_0^2}\Delta\lambda = LD\Delta\lambda. \tag{2.15}$$

Once the broadening ΔT of a pulse due to chromatic dispersion is defined, one can calculate the theoretical [bit-rate $\times$ reach] product for single-carrier OOK modulation as a function of the dispersion parameter and the RMS spectral width of the optical carrier. For the following analysis, a Gaussian pulse is considered rather than a squared pulse because of the bandwidth-limited nature of the Gaussian pulse.

The following analysis is divided in three parts. A case 1) where the RMS spectral width of the optical carrier is large as compared with the bit-rate ; a case 2) where the RMS spectral width of the carrier is small as compared with the bit-rate, and the optical signal has no frequency chirp ; a case 3) where the optical pulse is chirped (for small RMS spectral width of the optical source). Frequency chirp causes the instantaneous frequency of the optical signal to vary with the amplitude. This is typical of DML or in a few cases of external modulators as explained in section 2.2.2.2. The RMS spectral width of the optical carrier is denoted as $\sigma_{\lambda_{opt}}$ and the one of the optical pulse as $\sigma_{\omega_{pulse}}$.

A parameter of discussion is the relation between the spectral width of the optical pulse and the period (or bandwidth) of the pulse. Some authors assume simply that the spectral width is twice the bandwidth of the pulse [139]. However, we consider a -10dB bandwidth (point where the PSD of the pulse is decreased by 10dB from the maximum value), which results $\sigma_\omega \approx 1.5B$, where $B = 1/T$ is the bit-rate of the optical signal (for single-carrier OOK modulation). It shows to be a good approximation because the theoretical results agree well with the experimental results reported in subsection 4.1. If the maximum bit-rate is assumed to be 10Gbps (which results in $\sigma_{\omega_{pulse}} \approx 15GHz$ or equivalently $0.12nm$ around $\lambda_{opt} = 1.55\mu m$), the three cases are defined as :

1. $\sigma_{\lambda_{opt}} >> 0.12nm$;

2. $\sigma_{\lambda_{opt}} << 0.12nm$ and no frequency chirp ;
3. $\sigma_{\lambda_{opt}} << 0.12nm$ with frequency chirp.

2.1.2.1 1^{st} Case : $\sigma_{\lambda_{opt}} >> \sigma_{\omega_{pulse}}$

In this case, the [bit-rate × reach] product is independent of the bit-rate. This is often the case for transverse-multimode VCSELs and Fabry-Perrot lasers, with typical values of σ_λ of about $0.25nm$-$10nm$. In order to achieve the transmission of a given data-rate B over a SMF distance L with single-carrier OOK modulation, the time-spread ΔT caused by the fiber chromatic dispersion has to be lower than the time duration of one bit (equal to $1/B$). A commonly used rule of thumb is $\Delta T < 1/(4B)$ [139]. Then, for a Gaussian pulse, 95% of the pulse energy remains within the bit slot. Using (2.15) with $\Delta\lambda = \sigma_\lambda$ and the previously mentioned condition, the [bit-rate × reach] product in this case is upper-bounded by

$$B \cdot L \leq \left| \frac{1}{4D\sigma_\lambda} \right|. \tag{2.16}$$

Figure 2.5(a) shows the bit-rate as a function of the fiber length L (limited by chromatic dispersion only) with σ_λ of $0.25nm$ and 1nm and $D = 16ps/(km \cdot nm)$. The [bit-rate × reach product is about $62.5Gbps \cdot km$ for $\sigma_\lambda = 0.25nm$, which limits the reach for $10Gbps$ transmission at about $6.25km$ of standard SMF.

2.1.2.2 2^{nd} Case : $\sigma_{\lambda_{opt}} << \sigma_{\omega_{pulse}}$ and no frequency chirp

Single-longitudinal mode lasers such as DFB or DBR lasers have Full Width at Half Maximum (FWHM) spectral width of about 1-10MHz [139]. The spectral width of the carrier is therefore much smaller than that related to modulation. The [bit-rate × reach] product in this case is upper-bounded by

$$B \cdot \sqrt{L} \leq \frac{1}{\lambda_{opt}} \sqrt{\frac{\pi}{3|D|}}. \tag{2.17}$$

Compared to the previous case, for fixed value of D, the achievable bit-rate is inversely proportional to the square-root of L rather than inversely proportional to L. Figure 2.5(b) shows the bit-rate as a function of the reach L $D = 16ps/(nm \cdot km)$ and $\lambda_{opt} = 1.55\mu m$. The [bit-rate $\times\sqrt{reach}$] product in this case is around $90Gbps \cdot \sqrt{km}$. This results in a transmission distance limitation of about 80km at a data-rate of 10Gbps.

2.1.2.3 3^{rd} Case : $\sigma_{\lambda_{opt}} << \sigma_{\omega_{pulse}}$ and with frequency chirp

If the pulse is now considered to be chirped, by solving (2.10) it can be shown that the interaction between chromatic dispersion and frequency chirp will have an impact on the pulse broadening ΔT, hence the achievable bit-rate for a given propagation distance. The effect of the frequency chirp was studied in [141] considering an optical source with small RMS spectral width. The author considers a super-Gaussian chirped model given by

$$A(0,t) = A_0 \cdot \exp\left[-\frac{1+j\alpha}{2} \cdot \left(\frac{t}{T_0} \right)^{2m} \right] \tag{2.18}$$

where A_0 is the peak amplitude, α the chirp parameter (to be detailed in section 2.2), T_0 is the half-width at the $1/e$ intensity point and m is related to the shape of the pulse. For $m = 1$, the pulse is Gaussian and it becomes rectangular as m increases. This means that higher values of m, the transitions between the "on" and "off" states is more abrupt. The [bit-rate × distance]

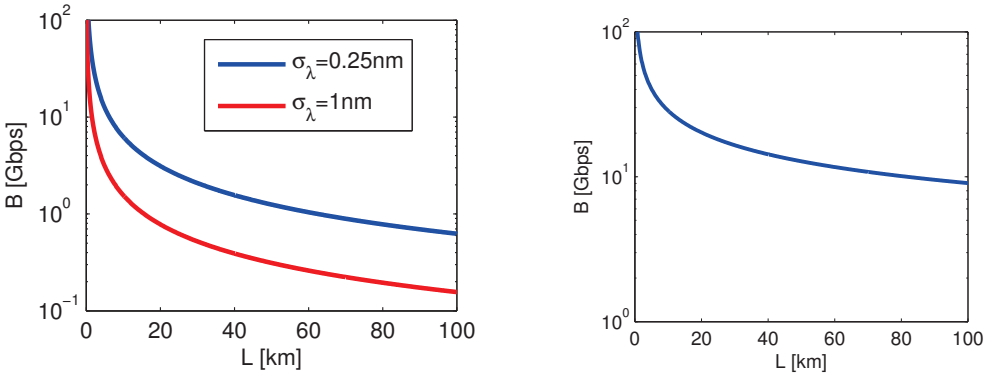

(a) $\sigma_{\lambda_{opt}} >> \sigma_{\omega_{pulse}}$ (b) $\sigma_{\lambda_{opt}} << \sigma_{\omega_{pulse}}$

FIGURE 2.5: Bit-rate as a function of the reach L for OOK modulation with (a) large and (b) narrow spectral width optical source.

product can be calculated numerically by solving (2.10), considering the initial pulse given by (2.18). We obtain then the pulse broadening ΔT, as function of the optical fiber length L. In [141], the [bit-rate × reach] product is calculated using $\Delta T \geq 1/(5B)$. Using standard values for the fiber dispersion at $1.55\mu m$, the results obtained in [141] are displayed in figure 2.6, considering a Gaussian pulse ($m = 1$) and super-Gaussian pulse ($m = 3$).

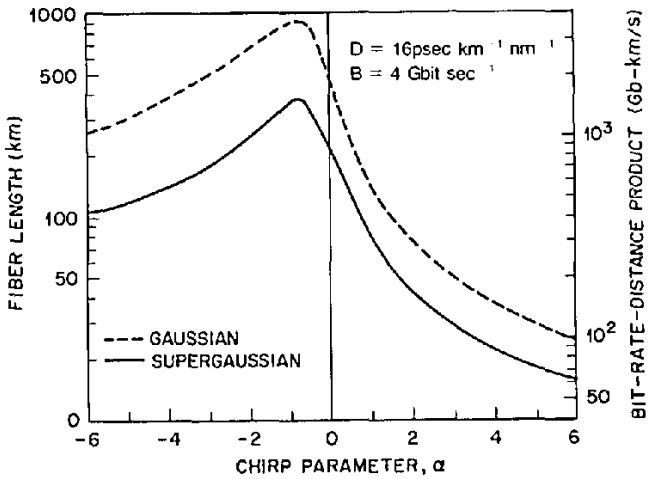

FIGURE 2.6: Achievable [bit-rate × reach] product for chirped optical pulse (Source [141]).

The [bit-rate × reach] product decreases for super-Gaussian pulses because of the increased bandwidth due to sharper transition between "on" and "off" states. The performance of the OOK transmission decreases rapidly for positive values of α, and it peaks around $\alpha = -1$. Unfortunately, for DMLs, the chirp parameter is always positive and generally above 2.8 for most semiconductor lasers as discussed in section 2.2.1. The [bit-rate × reach] product in this case is around $100 - 200 Gbps \cdot km$ for $\alpha = 3$. On the other hand, the frequency chirp can be controlled by using a MZM as shown in subsection 2.2.2.2. It can be used to cause a negative chirp and optimize the transmission performance [142].

2.1.2.4 Zero-Dispersion Wavelength

For standard single-mode fibers, there is a given wavelength, called zero-dispersion wavelength (λ_{ZD}) where the value of D is zero. The value of λ_{ZD} is in the range of $1.28\mu m$ to

$1.31\mu m$. The [bit-rate $\times$ distance] product is increased when working around this wavelength (at the price of $2\times$ higher optical loss as compared to $\lambda_{opt} = 1.55\mu m$). It should be noted that some dispersion will nevertheless occur because of the wavelength dependence of D. Since the optical pulse has a certain spectral width $\Delta\lambda$, the value of D is not zero at all the wavelengths within the pulse spectrum centered at λ_{ZD}. This is characterized by the slope dispersion parameter of (2.8). For $\lambda_{opt} \approx \lambda_{ZD}$, $\beta_2 \approx 0$ and the S parameter is proportional to β_3. In order to calculate the time spread due to the S-dispersion parameter, the D parameter in (2.15) should be replaced by $D_{ZD} = S\Delta\lambda$.

For multimode lasers with $\sigma_{\lambda_{opt}} = 1nm$ and a dispersion slope $0.05ps/(nm \cdot km^2)$ at $\lambda_{opt} = 1.55\mu m$, the [bit-rate $\times$ reach] product approaches $20Tbps \times km$. At 10Gbps, the achievable reach is about 2000km. This can be improved using single-mode lasers with narrower emission spectrum bandwidth.

This is a very important characteristic in order to design a lightwave communication system. While in the wavelength region of $1.3\mu m$ the chromatic dispersion is minimized, the optical loss is about $2\times$ higher for standard SMF. Hence, in loss-limited lightwave systems, it is better to work around $\lambda_{opt} = 1.55\mu m$ and cope with the higher dispersion, while for dispersion-limited lightwave systems, it is better to work around $\lambda_{opt} = 1.3\mu m$ and cope with higher optical loss.

2.2 Electro-optic Converters

This subsection is intended to give an overview of electro-optic converters used at the transmitter side for transmissions in single mode fiber. Discrete components with state-of-the-art performance will be reviewed : this includes III-V DFB lasers and $LiNbO_3$ MZM. Silicon photonics lasers and modulators performance will be given as a comparison.

The electro-optical conversion operation consists in translating a variation of an electrical voltage or current into a variation of one or more characteristics of the optical carrier. A general case is that the both the amplitude and phase of the optical carrier are modulated (field modulation of its complex envelope). The optical field $E_{opt}(t)$ of the modulated optical carrier with single polarization can be represented by

$$E_{opt}(t) = \Re\left\{A(t) \cdot \exp\left(j\omega_{opt}t\right)\right\} \tag{2.19}$$

where ω_{opt} is defined as $\omega_{opt} = 2\pi f_{opt}$, and f_{opt} is the frequency of the optical carrier. Two different time-scales are identified : 1) $1/f_{opt}$ (about $f_{opt} = 193THz$ for $\lambda_{opt} = 1.55\mu m$) and 2) $1/\Delta f$ - a complex slow-varying envelope $A(t)$ with bandwidth of typically $\Delta f \approx 20GHz$ for the applications considered in our work. A representation of the spectrum of $E_{opt}(t)$ is given in figure 2.7(a), whereas the spectrum of $A(t)$ is depicted in figure 2.7(b).

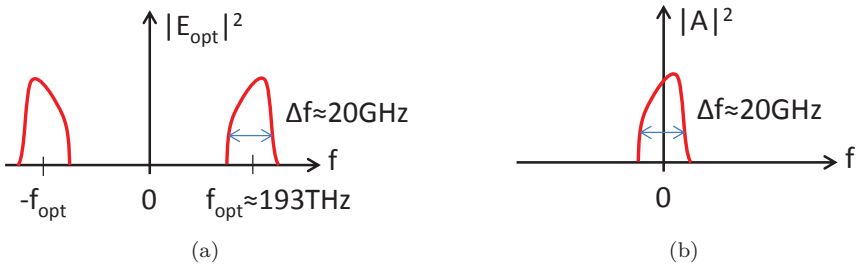

FIGURE 2.7: Representation of the spectrum of the (a) optical intensity and (a) complex slow-varying envelope.

Denoting $u(t) = u_I(t) + ju_Q(t)$ the complex electrical signal modulating the field of the optical carrier, then $A(t) \propto u(t)$. The optical field of the modulated carrier is written as

$$E_{opt_{FM}}(t) \propto u_I(t) \cdot \cos(j\omega_{opt}t) - u_Q(t) \cdot \sin(j\omega_{opt}t). \tag{2.20}$$

This is the case of MZM biased at the null transmission point, as it will be detailed in this section. In DMLs and MZMs biased in the quadrature point, the electrical signal modulates the intensity of the optical carrier, thus $u(t)$ necessarily real and $A(t) \propto \sqrt{u(t)}$. In this case, the field of the optical carrier is proportional to

$$E_{opt_{IM}}(t) \propto \sqrt{u(t)} \cdot \cos(j\omega_{opt}t). \tag{2.21}$$

The performance of an optical transmitter is related not only to the E/O conversion efficiency but also to the amount of distortion and noise it adds to the signal. It is related to the sensitivity penalty introduced when using this component as compared to an ideal optical transmitter. The sensitivity is the amount of received optical power required to achieve a target BER, at a given data-rate. It can be affected by a finite (poor) ER in the case of OOK modulation with an intensity modulator (cf. subsection 2.2), a non-linear electro-optic conversion operation, and intensity/phase noise for example. The frequency chirp of the optical transmitter adds also a major impact on the transmission performance as shown in subsection 2.1.2.3. Intensity modulators without specific chirp-compensation means do have intrinsic positive chirp while field-modulators may have either positive, zero or negative chirp.

2.2.1 Directly-Modulated Lasers

The major success of optical communications in general is due to the development of semiconductor laser sources. The first semiconductor laser operation using GaAs was demonstrated in 1962 by two North-American groups at the General Electric research center. In practice, semiconductor lasers became available in 1970 when room temperature operation was demonstrated by North-American and Russian teams. Since then, extensive research and development was done because of their importance to optical communication systems.

2.2.1.1 Principle of Operation

The basic physical mechanism behind light emission in semiconductor lasers is the stimulated emission process, illustrated in the inset of figure 2.8. A recombination of a pair of electron+hole is stimulated by an incoming photon. The emitted photon possesses the same energy, direction and polarization as the incoming one. More details can be found in [139].

The optical gain of semiconductor laser is provided by an active region. Common III/V materials used in the active region for telecom wavelength range $1.3\mu m - 1.6\mu m$ are InP-related (ex. InGaAsP, InGaAlAs, ...) [139] due to their high quantum efficiency (fraction of the electron-hole recombination that generates a photon). Modifications in the composition of the quaternary alloys allow to adjust the emission wavelength [139]. In order to pump the active region with electrical current, the active region is sandwiched between a P and an N semiconducting contact layers and form a P-I-N junction, as illustrated in figure 2.8. By directly polarizing the junction, a condition called population inversion is achieved. This means that there are more electrons in the conduction band than in the valence band. In order to return to the equilibrium state, electron and holes recombine and emit photons. The active region exhibits optical gain which increases with the electrical current density applied to the junction. The laser starts to emit coherent light when the optical gain of the active region overcomes the optical loss, which includes absorption and mirror out-coupling losses, condition known as threshold.

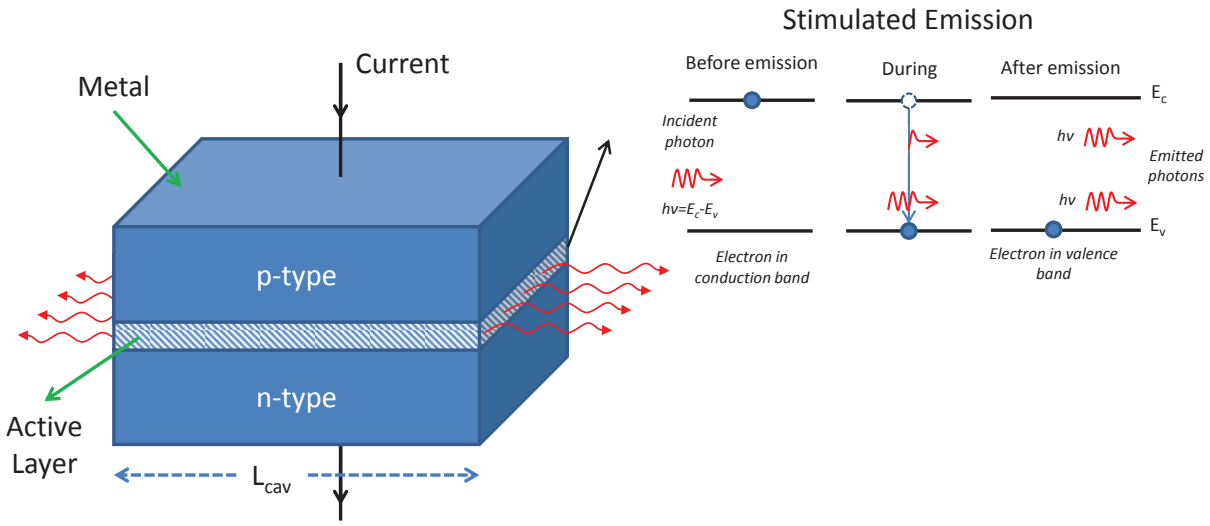

FIGURE 2.8: Basic structure for a semiconductor laser. Inset : Stimulated emission mechanism.

The active region itself is not enough to create a laser. In order to convert the amplifier (active region) to an oscillator, an optical feedback is required. This can be done simply by cleaving the facets of the semiconductor structure orthogonally to the propagation direction, to form a Fabry-Perot cavity. The cleaved facets act as two mirrors due to the differences of the air and semiconductor refractive indices. The reflectivity R_m can then be calculated using the Fresnel equations. It is given by

$$R_m = \left(\frac{n_{sc} - 1}{n_{sc} + 1}\right)^2 \tag{2.22}$$

where n_{sc} and 1 are the refractive indices values of semiconductor and air respectively. The reflectivity is about 30% for III-V semiconductor lasers. Even with low reflectivity, the active layer gain is high enough to overcome the power loss at the mirror level. Such a structure is called a Fabry-Perot laser. Because the mirror reflect the entire spectrum of the optical signal generated in the active region, the Fabry-Perot emission spectrum is composed of several longitudinal modes (resonances) which are centered on the gain spectrum of the active region as illustrated in figure 2.9. The relative intensity of the longitudinal modes fluctuate because of the competition between them in the cavity. The resonance frequency ν_m of m^{th} order is the given by

$$\nu_m = \frac{m \cdot c}{2n_{eff} \cdot L_{cav}} \tag{2.23}$$

where c is the speed of the light, L_{cav} is the cavity length and n_{eff} is the effective index of the waveguided optical mode in the cavity.

Single-mode operation (only one longitudinal mode is emitted) can be achieved by filtering out all the longitudinal modes that are reflected back to the cavity, except for one. For that purpose, two particular structures for III/V lasers were invented : Distributed Bragg Reflector (DBR) and Distributed Feedback Laser (DFB) lasers, illustrated in figure 2.10. In both cases, the optical signal is filtered using Bragg gratings. In a DBR, the gratings are placed outside the active region, in both ends. By correctly designing the gratings, they act as mirrors that only reflect a single longitudinal mode. In DFB lasers, the gratings are placed all along the active region, and a distributed feedback occurs throughout the cavity length. A parameter that characterizes the single-mode operation is the Side-mode Suppression Ratio (SMSR) - the

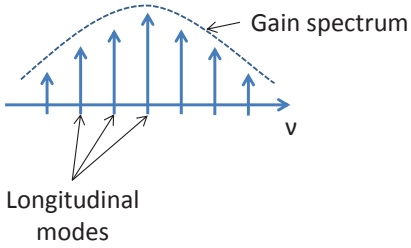

FIGURE 2.9: Emission spectrum of a Fabry-Perot laser.

ratio between the main longitudinal mode and the secondary one with higher relative power. More details can be found in [139].

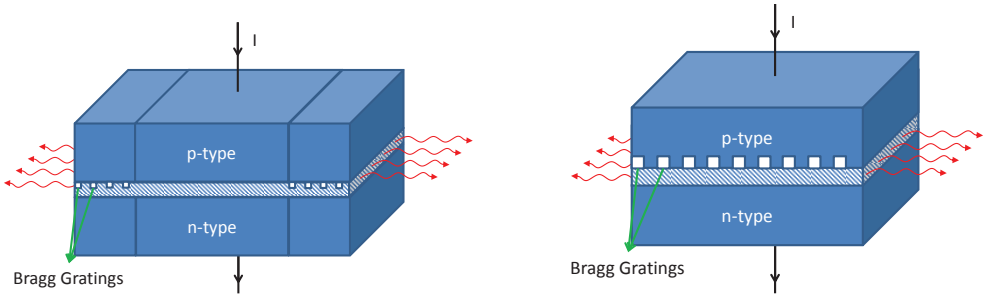

(a) Distributed Bragg Reflector (b) Distributed Feedback Laser

FIGURE 2.10: Schematic view of single-mode lasers.

Laser Rate-Equations

The set of equations describing the behavior of a single-mode semiconductor laser are called the rate-equations. They establish how the averaged carrier density N, the averaged photon density P_h and the phase ϕ of the output signal vary in time within the cavity. They are given by [143]

$$\frac{dP_h}{dt} = \frac{\Gamma v_g \sigma_g \cdot (N - N_T) \cdot P_h}{1 + \epsilon_{NL} P_h} + \Gamma \beta_{sp} B \cdot N^2 - \frac{P_h}{\tau_p} \tag{2.24}$$

$$\frac{dN}{dt} = \frac{I}{e \cdot V} - \frac{\Gamma v_g \sigma_g \cdot (N - N_T) \cdot P_h}{1 + \epsilon_{NL} P_h} - \frac{N}{\tau_c} \tag{2.25}$$

$$\frac{d\phi}{dt} = \frac{\alpha}{2} \cdot \left(\Gamma v_g \sigma_g \cdot (N - N_T) - \frac{1}{\tau_p} \right) \tag{2.26}$$

where Γ is the confinement factor of the optical mode in the cavity, $v_g = c/n_g$ is the group velocity (c - speed of light and n_g - group index of the active layer), σ_g is the optical differential gain in the active region ($\sigma_g = dg_p/dN$, where g_p is the optical gain in the cavity), N_T is carrier concentration in transparency, β_{sp} is the fraction of the spontaneous emission that is emitted into the lasing mode, B is the spontaneous radiative recombination coefficient, ϵ_{NL} is a non-linear gain parameter, I is the injected current, e is the elementary electron charge, V is the active region volume, α is the linewidth enhancement factor (commonly called the chirp parameter), τ_p and τ_c are the photon lifetime in the cavity and the carrier lifetime.

The photon lifetime τ_p is related to the cavity loss α_{cav} as $\tau_p = 1/(v_g \alpha_{cav})$. The cavity loss $\alpha_{cav} = \alpha_{int} + \alpha_{mir}$ includes absorption α_{int} and mirror α_{mir} losses. The carrier lifetime τ_c depends on the radiative τ_r electron-hole recombination time (that generates a photon) and

non-radiative τ_{nr} recombination time (that does not generate a photon). The carrier lifetime can be expressed by $1/\tau_c = 1/\tau_r + 1/\tau_{nr} = A_{nr} + B \cdot N + C \cdot N^2$, where A_{nr} is the non-radiative coefficient and C is the Auger coefficient [139]. The most common non-radiative recombination mechanism is the Auger [144]. The energy associated to this process is transferred to another electron as kinetic energy. One can define a variable called internal quantum efficiency as

$$\eta_{int} = \frac{\tau_{nr}}{\tau_r + \tau_{nr}}. \tag{2.27}$$

Typically, because of its indirect bandgap [143], group IV material have very low quantum efficiency ($\eta_{int} \approx 10^{-5}$). On the other hand, group III and V materials have direct band-gap, and perform much better. The efficiency approaches 100% when stimulated emission dominates.

Equation (2.24) gives the time evolution of the photon density P_h within the cavity in time. It is the difference between the net rate of stimulated emission (which takes into account the rate of the spontaneous emission into the lasing mode) and the loss of photons due to absorption and mirror losses. The factor $1/(1 + \epsilon_{NL} P)$ accounts for the gain saturation at high photon densities due to spatial and spectral hole burning. Equation (2.25) gives the time variation of the number of carrier in the active region. It is the difference between the injected carriers ($I/(e \cdot V)$) and the electrical carriers lost due to electron-hole recombination, both spontaneous and stimulated.

Because the refractive index of the active region also changes with the carrier concentration in the active region, intensity modulation of the laser is also accompanied by phase modulation, which is described by (2.26). This is the physical origin of the frequency chirp introduced by direct modulation of the laser.

2.2.1.2 Behavior of the Semiconductor Lasers

In DC (or steady-state) operation, the laser behavior is characterized by the optical power P versus current I curve. The relationship between the physical characteristics of the laser and the optical output power P as a function of the injected current I above threshold can be found by setting $dP_h/dt = 0$ and $dN/dt = 0$ in (2.24) and (2.25) as explained in [139]. The result is that the optical output power increases linearly with I, until it achieves saturation. The slope efficiency of a laser is given by

$$SE = \frac{dP}{dI} = \frac{P}{I - I_{th}}; I > I_{th} \tag{2.28}$$

where I_{th} is the threshold current. Typical values for the threshold current and optical output power at room temperature for semiconductor lasers such as FP, DFB or DBR for telecom applications are $\approx 20mA$ and $5mW - 20mW$, respectively. Typical P-I curves for a commercial DFB in three different temperatures are shown in figure 2.11.

In AC operation, an analytical form of the laser modulation frequency response $H_{AM}(f)$ can be obtained by assuming small signal modulation and linearizing (2.24) and (2.25). It is given by [139]

$$H_{AM}(f) = \frac{\Omega_R^2 + \Gamma_R^2}{(\Omega_R + 2\pi f - i\Gamma_R) \cdot (\Omega_R - 2\pi f + i\Gamma_R)} \tag{2.29}$$

where Ω_R and Γ_R are the value and damping rate of relaxation oscillation frequency, and they are related to the physical parameters of the laser and the bias current as indicated in [139]. The frequency response is almost flat for $f << \Omega_R$, it achieves a maximum at $f \approx \Omega_R$ and decreases rapidly for $f >> \Omega_R$ as illustrated in figure 2.12. The modulation bandwidth f_{3dB} is found to increase with the bias current $f_{3dB} \propto \sqrt{I_b}$ [139], until it achieves saturation. In figure 2.12, the measured frequency response of the DFB is fitted with (2.29) using the method described in [134].

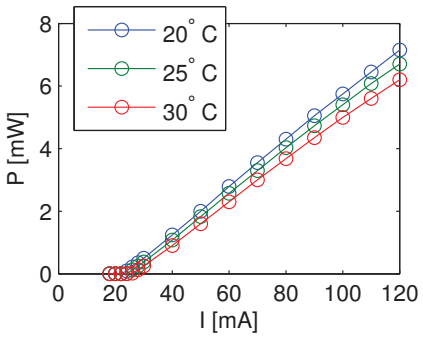

FIGURE 2.11: Typical optical power P versus electrical current I for a DFB laser.

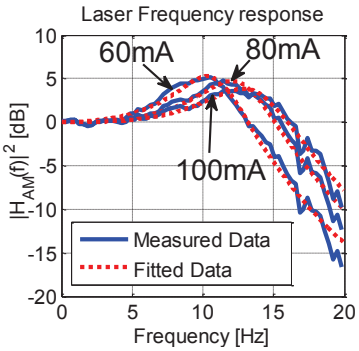

FIGURE 2.12: Typical frequency response to small signal modulation of a DFB laser.

The frequency chirp $\Delta\nu(t)$ in semiconductor lasers can be found by developing (2.26) as a function of the instantaneous optical output power of the laser $P(t)$. According to [143] it is given by

$$\Delta\nu(t) = \frac{\alpha}{4\pi} \cdot \left(\frac{d}{dt} \left[\ln(P(t)) \right] + \kappa P(t) \right) \tag{2.30}$$

where the $\kappa = 2\Gamma\epsilon_{NL} / (V\eta_{tot}h\nu)$ parameter is called the adiabatic chirp coefficient and η_{tot} is the total quantum efficiency including the coupling efficiency into the fiber. The first term is proportional to the derivative of the logarithm of $P(t)$; it is called transient chirp. The second term is directly proportional to $P(t)$; it is called adiabatic chirp.

The output optical signal of semiconductor lasers exhibit intensity fluctuations even if it is biased at constant electrical current with negligible variations. This is mainly a consequence of the spontaneous emission process, even if the spontaneous emission rate is much lower than the stimulated emission rate. This is characterized by the Relative Intensity Noise (RIN) parameter. A detailed explanation of the RIN in given in [139], where it shows that the PSD peaks at resonance, with typical values from $-120dB/Hz$ to $-160dB/Hz$, and decreases for frequencies above resonance. It also shows that RIN is inversely proportional to the optical output power of the laser.

Besides the intensity fluctuations of the optical output signal of the laser, the instantaneous phase also fluctuates for the same reason. This leads to a finite spectral linewidth of the laser. This characteristic is analyzed with details in [139]. The linewidth typical for DFB and DBR lasers is between $1 - 10MHz$. In general, for direct-detection systems below 100km SMF, the laser phase noise has negligible impact on the transmission performance [145].

2.2.1.3 Modeling DML

Because the differential laser rate equations (2.24),(2.25) and (2.26) are coupled one with the others, an analytical resolution to find a general equation to represent the optical output power as a function of the electrical current is not possible.

In the simulation platform, the laser behavior is modeled by the numerical resolution of the rate-equations. The main issue is to find the physical parameters that are related to a given semiconductor laser to be modeled. By using a commercial tool from Rsoft, the "Best-fit Laser Toolkit", the physical parameters can be found by fitting with the behavioral parameters of the laser, such as the threshold current, optical output power, relaxation oscillation frequency and overshoot, linewidth and RIN for instance. In addition, if some physical parameters are

known, they can be forced to their known value. This procedure is detailed in appendix A for a commercial DFB laser prototype, model 1915LMA from 3S photonics. The fitted physical parameters are presented in table A.4.

Figure 2.13 and figure 2.14 show the DC (optical output power versus current) and small-signal AC (frequency response) behavior of the laser, obtained from characterization of the DML and simulated from the model by solving the laser rate equations, showing a good agreement. The simulated and experimental results of the laser for OOK and OFDM modulation are reported in subsection 4.1 and 4.2.1.1, respectively, which shows that the model can accurately predict the chirp and intensity noise of the DML. This work is very important because it shows that, by knowing the behavior parameters of any single-mode semiconductor laser, the simulation platform can accurately predict its performance in an optical communication system with an arbitrary transmission technique.

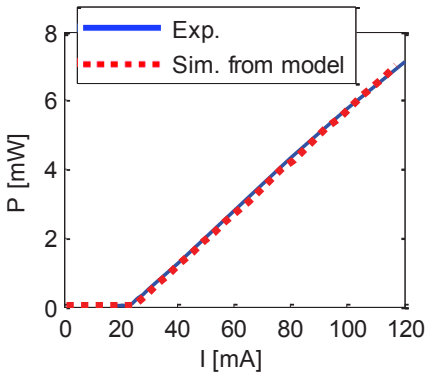

FIGURE 2.13: 3S Laser optical power (P) vs. current (I), experimental measures and simulation from model.

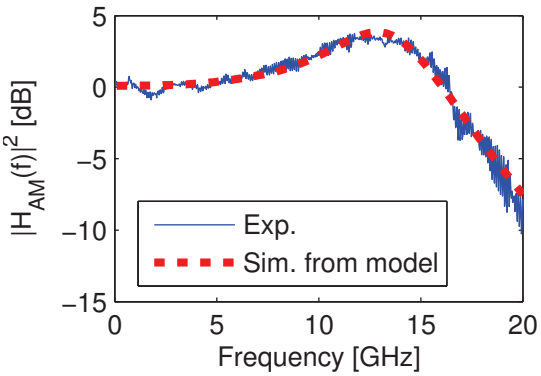

FIGURE 2.14: 3S Laser frequency response, experimental measures and simulation from model ($I_b = 100mA$).

2.2.1.4 Hybrid III/V-on-Silicon Laser Sources

The interest of fabricating light sources compatible with the CMOS-fabrication technology is to benefit from its mass-production and E/O integration capabilities. In addition, the wavelength tunability functionality in single-mode lasers can be achieved by heating the silicon structure by means of integrated resistive heaters, as a part of the CMOS fabrication process. However, as stated in subsection 2.2.1.1, silicon is a poor light emitter. Due to its indirect bandgap nature, the internal quantum efficiency is lower than 10^{-5} and fabricating laser source using silicon in the active layer is unpractical. Electrically-pumped Germanium lasers with epitaxial growth on silicon shows promising results [146], but further development is still required.

An alternative to provide CMOS-compatible laser sources is basically to use hybrid integration of III/V-materials on top of a SOI. In this way, the III/V material provides the optical gain required by the laser source.

The first technique that was employed to integrate III/V waveguides on top of silicon is the flip-chip technique [147]. The III/V waveguide is pre-fabricated directly in the III/V wafer and bonded into the silicon waveguide. In spite of the fact that the cost of silicon photonic chip is small, the flip-chip process is very expensive and time-consuming because a very precise alignment is required. As an alternative, direct bonding of III/V dies or wafer on top of the pre-fabricated silicon waveguide was proposed [148] (cf. figure 2.15). In this way, no precise alignment between the III/V wafer/die is required. Then, the III/V material is etched to define the active region of the hybrid laser.

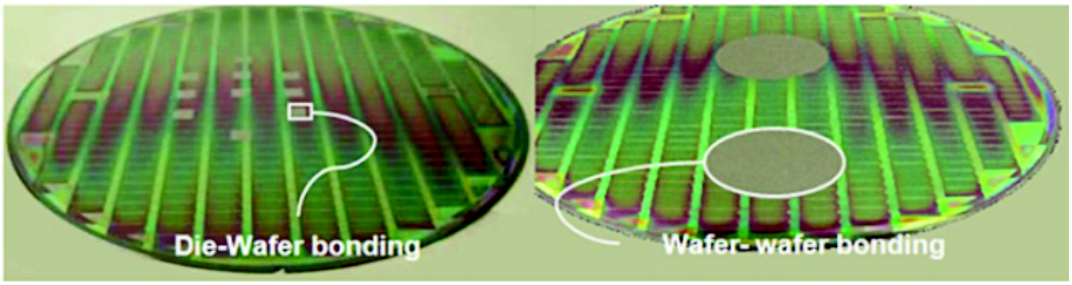

FIGURE 2.15: SOI wafers bonded with III/V dies or wafers.

Silicon Evanescent Lasers

The first architecture using direct bonding of wafer/die of the III/V on top of the SOI is called silicon evanescent lasers and it was first proposed by Fang *et al.* from UCSB and Intel [149]. In this type of hybrid laser, the III/V material is bonded to the silicon waveguide using a very thick bonding layer ($< 5nm$). In this way, the evanescent part of optical guided mode is coupled to the III/V waveguide and experiences optical gain. Then, the energy of the evanescent wave is transferred to the fundamental mode inside the silicon waveguide through evanescent coupling and the optical mode experiences gain. The basic principle is illustrated in figure 2.16. For instance, in the design done in [149], the optical mode is confined in the silicon waveguide by 75% and overlaps with the III/V waveguide by 3%.

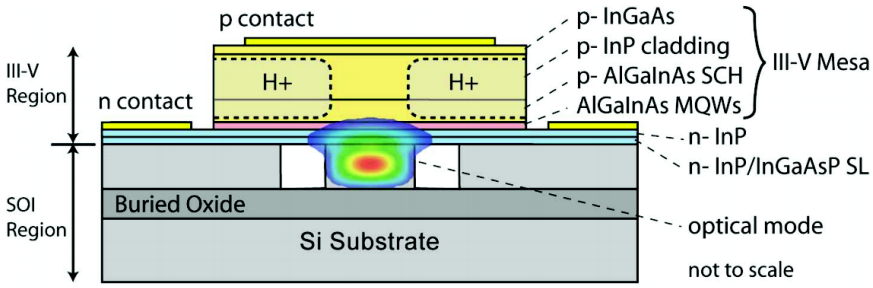

FIGURE 2.16: Cross section of the silicon evanescent laser (Source [149]).

A summary of the different laser structures than have been fabricated using this architecture is presented in table 2.1. The results displayed are at room temperature ($20 - 25°C$) and the values for the optical output power described do not include coupling into the fiber (optical power in the silicon waveguide). Fabry-perot configuration using silicon-to-air facet reflection as mirrors were firstly demonstrated [149]. Later, racetrack [150] configurations with integrated photodetectors were demonstrated, achieving a record of $29mW$ of optical power in the silicon waveguide. In racetrack configuration, the cavity is formed by connecting together both ends of the active region, creating a loop (cf. figure 2.18(b)). The light is coupled out of the racetrack cavity using a directional evanescent coupler. Finally, single-mode DFB and DBR lasers are reported in [151]. These are made by partial etching of silicon waveguide in a periodical structure either below the active region (DFB) or in the passive waveguide at both ends of the active region. Modulation capabilities are shown in the DBR laser [151], reporting 4Gbps OOK modulation with a -3dB bandwidth of 2.5GHz.

Hybrid III/V-on-silicon Lasers Based on Adiabatic Mode Transformers

The disadvantage of silicon evanescent lasers is that there is a trade-off between high modal gain and coupling efficiency between silicon waveguide and the active region. Additionally, the

Structure (Reference)	Maximum optical power (Bias current)	Minimum threshold current	SMSR
Fabry-perot [149]	1.5mW (200mA)	65mA	-
Racetrack [150]	22.5mW (500mA)	175mA	-
DFB [151]	3.5mW (100mA)	25mA	50dB
DBR [151]	8.5mW (200mA)	65mA	50dB
Sampled-gratings DBR [151]	0.6mW (160mA)	50mA	35dB

TABLE 2.1: Different structures for silicon evanescent lasers.

fabrication process is quite complex because, in order to maximize the modal gain in the III/V waveguide, the bonding layer should be as thick as possible.

A different approach was proposed by A. Yariv [152] and later realized by B. Ben Bakir *et al.* at the CEA-Leti [153]. In order to overcome the modal gain and coupling efficiency trade-off inherent to silicon evanescent lasers, it proposes an architecture were the optical mode is completely transferred from the silicon waveguide to the III/V waveguide. The architecture can be divided in two parts : the gain region and coupling region. In the gain region, the optical mode is entirely confined in the III/V waveguide. In the coupling region, the optical mode is transferred to the silicon waveguide by varying the waveguide width, providing an adiabatic transition. The coupling mechanism is shown in figure 2.17(b). As illustrated in figure 2.17(c), the mode transformers are placed over the edges of the active region. By carefully designing the mode transformers, one can maximize the coupling efficiency between III/V and silicon waveguide ($> 90\%$ is reported in [154, 155]), thus improving modal gain. Compared to silicon evanescent lasers, the fabrication process is eased because the width of the bonding layer can be increased (typically 100nm of SiO_2) without reducing the modal gain.

The structure proposed in [153] uses a low-index bonding layer (SiO_2). As an alternative, the author in [156] proposes to use Benzocyclobutene (DVS-BCB) bonding instead of molecular bonding. In addition, the proposed architecture is based in a double adiabatic taper coupler. In this architecture, the width of the III/V waveguide is decreased from the end of the gain region to the end of the coupling region. The final width of the III/V waveguide (the tip of the waveguide) should be as narrow as possible to maximize coupling efficiency [157].

Then, the cavity can be formed by cleaving the facets, using DBR mirrors or in racetrack configuration as detailed in the next paragraphs.

Cavity Structures In order to define the cavity of the laser, two mechanisms can be defined : DBR mirrors and racetracks. By using broadband high-reflectivity DBR mirror in one side and 50% reflectivity DBR mirror on the other side (cf. figure 2.18(a)), every longitudinal mode in the cavity is reflected back - Fabry-Perot lasers are defined. In the 50% mirror reflectivity side, a grating coupler is used to collect the generated light with an optical fiber. In order to have broadband DBR mirrors, the gratings are defined by complete etching of the silicon waveguide. The difference between Fabry-Perot configuration and DBR configuration is that DBR lasers have mirrors with much narrower reflectance bandwidth. In this way, all longitudinal-modes are filtered out except one single lasing mode, which is reflected back to the cavity. For example, in [155], the etching depth of the DBR mirrors is about 10nm and the reflectance bandwidth is reported to be 2.58nm and 3.98nm for the 100% and the 50% DBR mirrors, respectively, with a longitudinal mode spacing of approximately 0.45nm. Using DVS-BCB bonding, Fabry-Perot lasers were demonstrated in [157] using the silicon-to-air facet reflection as mirrors. In this case, the optical light can be collected using a lensed fiber in one of the facets.

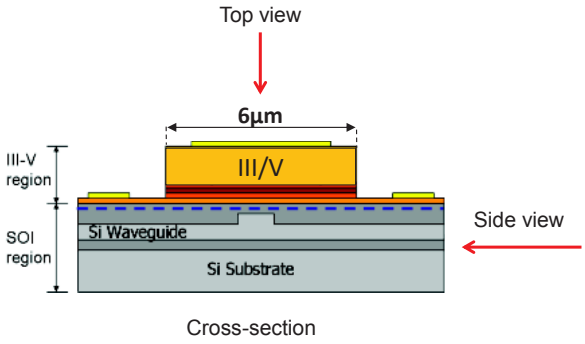
Top view
6µm
III/V
III-V region
SOI region
Si Waveguide
Si Substrate
Side view
Cross-section

(a)

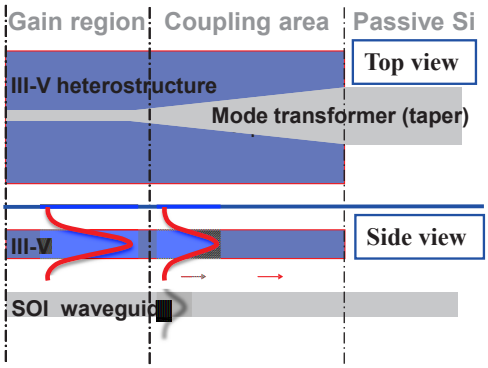
Gain region
Coupling area
Passive Si
Top view
III-V heterostructure
Mode transformer (taper)
III-V
Side view
SOI waveguide

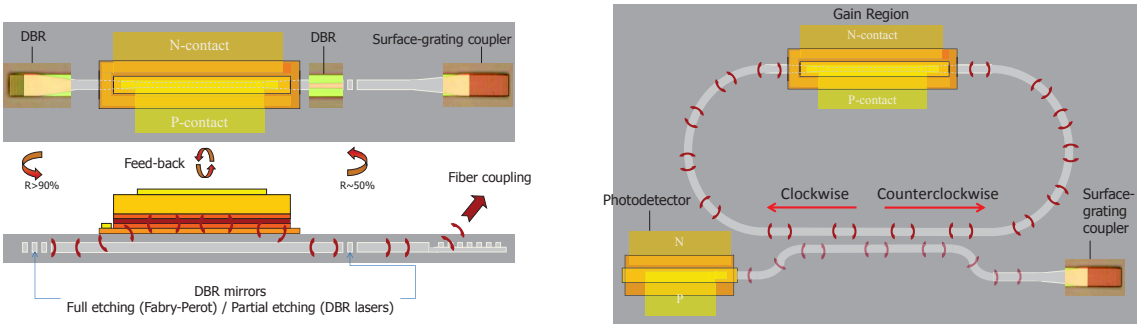

(a) (b)

FIGURE 2.18: Examples of cavities for hybrid III/V-on-silicon lasers with adiabatic couplers, (a) DBR cavity and (b) Racetrack configuration.

and the SMSR and tunability range if it is applied. All the lasers mentioned can work at room temperature except for [40] which worked only at $10°C$. OOK modulation of a hybrid DBR laser up to 12.5Gbps is reported in [155] with a -3dB modulation bandwidth of 7.2GHz.

Structures (Reference)	Bonding technique	Adiabatic taper coupler type	P_{OPT} in the fiber (waveguide)	Minimum I_{th}	SMSR	Tunability range
Fabry-Perot [154]	Molecular	Single	(15mW) at 325mA	50mA	-	-
Fabry-Perot [157]	DVS-BCB	Double	(4.5mW) at 175mA	30mA	-	-
Racetrack [154]	Molecular	Single	2.8mW	30mA	-	-
Double-ring [39]	Molecular	Double	1.25mW (10mW)	21mA	50dB	45nm
Double-ring [40]	-	-	(3.3mW)	160mA	35dB	40nm
Single-ring [38]	Molecular	Double	(10mW) at 100mA	45mA	50dB	8nm
DBR [155]	Molecular	Single	15mW (5mW) at 160mA	17mA	$> 50dB$	-

TABLE 2.2: Summary of the state-of-the-art of hybrid III/V-on-silicon lasers based on adiabatic coupling.

2.2.2 External Modulators

2.2.2.1 Electroabsorption Modulator (EAM)

Electro-absorption Modulator (EAM) are based on the Franz-Keldysh effect - when an electrical field is applied to the material (commonly the same III/V materials used for the semiconductor lasers, or Germanium), the material band-gap decreases, and, consequently, the absorption coefficient of the material is increased. The advantage of this type of modulator is that, since the same material can be used for both the laser and the modulator, they can be

monolithically integrated. The frequency chirp can be made very close to zero [134] but it is inherently positive due to the physical characteristics of the semiconductor materials, leading to smaller [bit-rate × distance] capabilities as compared with phase modulators that can be designed to have negative frequency chirp. Additionally, since the electrical modulating signal is related to the intensity of the optical signal rather than the field, it is not straightforward to achieve M-QAM (phase and amplitude) with this kind of modulators [158].

2.2.2.2 Mach-Zehnder Modulator (MZM)

As the frequency chirp induced by the directly-modulated laser limits the [bit-rate × distance] product (cf. subsection 2.1.2.3), it can be improved by using MZM with negative or zero chirp [159]. This has been experimentally demonstrated in [142].

In a particular configuration, called push-pull, the resulting frequency-chirp is nulled. It will be shown that the modulating voltage-signal is converted linearly into an optical field. This is a very interesting characteristic because it allows high-order modulation formats that use amplitude and phase modulation of the optical carrier (M-QAM).

The most common material for MZM is Lithium Niobate ($LiNbO_3$). It is a trigonal crystal. Its birefringence varies when an external electrical field is applied. The change in the refractive index of the waveguide modifies the phase of the optical carrier. The effect is linear with the applied electrical field.

The basic structure of a pure phase modulator is shown in figure 2.19. The phase shift $\Delta\phi(t)$ as a function of the effective index change Δn_{eff}, which is varied with the applied voltage $u(t)$ is given by [160]

$$\Delta\phi(t) = \frac{2\pi}{\lambda_{opt}} \cdot \Delta n_{eff}(t) \cdot l_{el} \approx \frac{u(t)}{V_\pi}\pi \tag{2.31}$$

where l_{el} is the length of the electrodes and V_π is the voltage required to cause a π-phase shift of the optical field. Typical values of V_π for $LiNbO_3$ are in the order of $5V$ to $10V$. The field-transfer function of the phase modulator is then given by

$$\frac{E_{out}(t)}{E_{in}(t)} = \exp\left(j\frac{u(t)}{V_\pi}\pi\right) \tag{2.32}$$

where E_{in} and E_{out} are the optical field at the input and output of the phase modulator, respectively.

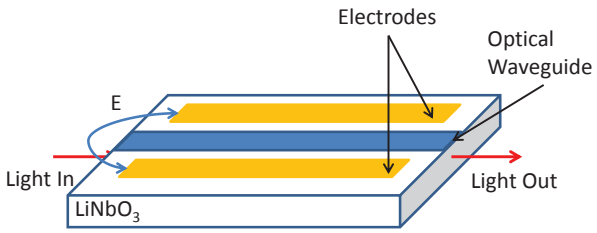

FIGURE 2.19: Basic structure of a $LiNbO_3$ phase modulator (E=electrical field).

Intensity modulation can be achieved by arranging two phase modulation sections in a MZI. The basic structure of a MZM in Travelling-wave Electrode (TWE) configuration is shown in figure 2.20. In this configuration, the electrodes are seen by the RF signal as transmission lines. The RF signal propagates in the same direction as the optical signal. In order to maximize the transmission bandwidth and avoid any reflections, the transmission line impedance as well as the charge impedance Z_c at the end of the electrode should be adapted to the output impedance of the RF source. The optical field transfer-function of the MZM is given by

$$\frac{E_{out}(t)}{E_{in}(t)} = \frac{1}{2} \cdot \left(\exp\left(j \frac{u_1(t)}{V_\pi} \pi \right) + \exp\left(j \frac{u_2(t)}{V_\pi} \pi \right) \right) \tag{2.33}$$

$$= \cos\left((u_1(t) - u_2(t)) \cdot \frac{\pi}{2V_\pi} \right) \cdot \exp\left(j(u_1(t) + u_2(t)) \cdot \frac{\pi}{2V_\pi} \right) \tag{2.34}$$

where $u_1(t)$ and $u_2(t)$ are the voltage-signals applied on the upper and bottom phase modulation sections. We assume that $u_1(t) = V_1 \cdot u(t)/2 + V_{bias}/2$ and $u_2(t) = V_2 \cdot u(t)/2 - V_{bias}/2$. Then, (2.34) can be written as

$$\frac{E_{out}(t)}{E_{in}(t)} = \cos \text{âĄą}\left((V_1 - V_2) \cdot u(t) \frac{\pi}{4V_\pi} + \phi_{bias} \right) \cdot \exp\left(j(V_1 + V_2) \cdot u(t) \frac{\pi}{4V_\pi} \right) \tag{2.35}$$

where ϕ_{bias} is defined as

$$\phi_{bias} = V_{bias} \cdot \frac{\pi}{2V_\pi}. \tag{2.36}$$

In (2.35), the first term (cosinus) corresponds to the amplitude modulation while the second one (exponential) represents the phase modulation of the MZM. Two configurations can be distinguished. When $V_1 = V_2$, the amplitude modulation term is null, and a pure phase modulation of the optical field is achieved. This configuration is called "push-push". When $V_1 = V_2$, the phase modulation term is made null and a pure amplitude modulation is applied on the optical field, configuring a "push-pull" operation. Any other configuration leads to both amplitude and phase modulation.

Figure 2.21 shows the amplitude (E_{out}/E_{in}) and intensity ($|E_{out}/E_{in}|^2$) transfer function as a function of V_{bias}. It indicates two particular biasing points : Quadrature ($V_{bias} = V_\pi/2$) and Minimum ($V_{bias} = V_\pi$) points. These biasing points represent the most linear regions of the intensity and amplitude transfer function, respectively.

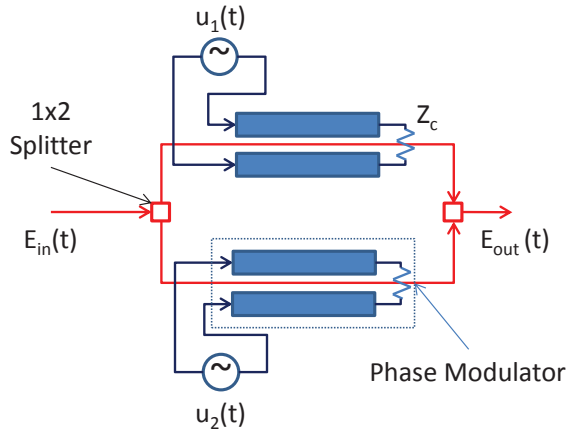

FIGURE 2.20: Schematic view of the MZM.

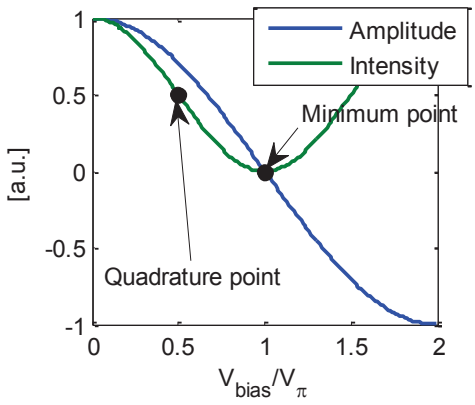

FIGURE 2.21: Intensity and amplitude transfer function of the MZM.

Intensity Modulation of the MZM

When biased at the quadrature point, the intensity transfer function of (2.35) is developed to

$$\frac{I_{out}(t)}{I_{in}(t)} = \left| \frac{E_{out}(t)}{E_{in}(t)} \right|^2 = \frac{1}{2} \cdot \left(1 + \sin\left((V_1 - V_2) \cdot u(t) \frac{\pi}{2V_\pi} \right) \right). \tag{2.37}$$

As shown in subsection 2.1.2.3, the modulator chirp plays an important role for optimizing the transmission performance for intensity modulated signals. The chirp parameter α_{MZM} in a MZM is given by [159]

$$\alpha_{MZM} = \frac{d\phi/dt}{dI/dt} \cdot 2I \tag{2.38}$$

where $\phi(t) = Arg\{E_{out}(t)/E_{in}(t)\}$ is the phase and $I = |E_{out}(t)/E_{in}(t)|^2$ is the intensity transfer function, through the MZM, of the optical field. Equation (2.38) can be found by developing (2.30) with $\kappa = 0$. Assuming that the modulator is biased at the quadrature point of operation ($V_{bias} = V_\pi/2$) and developing (2.37) in (2.38) the chirp in the dual-drive MZM modulator is given by [142]

$$\alpha_{MZM} = \frac{1 + r_{MZM}}{1 - r_{MZM}} \tag{2.39}$$

where $r_{MZM} = V_1/V_2$. Equation (2.39) shows that the frequency-chirp parameter can be chosen by adjusting r_{MZM}. Figure 2.22 shows a plot of the frequency chirp α_{MZM} as a function of r_{MZM}, with $V_1 + V_2 = 1$. As expected, the chirp is zero for $r_{MZM} = -1$ (push-pull configuration - pure amplitude modulation) and increases for $r_{MZM} = 1$ (push-push configuration - pure phase modulation). As r_{MZM} goes to infinity (modulation in a single-arm), the value of α_{MZM} converges to -1.

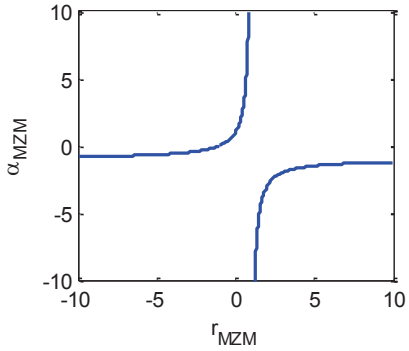

FIGURE 2.22: Chirp parameter for dual-driven MZM as a function of r_{MZM}.

The MZM chirp analysis presented here is the most classical one. However, alternative definitions for the effective chirp parameter α of external modulators can be found in the literature. In [161], for example, the author compares 4 different effective α-parameters for external modulators.

Field Modulation of the MZM - Optical I/Q Modulator

As discussed in the previous subsection, in a push-pull configuration ($V_1 = -V_2$), the second term of (2.35) is null and a pure amplitude modulation is achieved. Assuming the minimum biasing point ($V_{bias} = V_\pi$) (2.35) can be rewritten as

$$\frac{E_{out}(t)}{E_{in}(t)} = \sin \hat{a}A\c{a} \left(u(t) \cdot \frac{\pi}{2V_\pi} \right). \tag{2.40}$$

An optical I/Q modulator is a device that can modulate both the amplitude and the phase of an optical carrier. It can be built using two MZMs. A phase modulator sets the relative phase between both arms to $\pi/2$ so that the arms do not interfere within each other. A basic structure for the optical IQ modulator is shown in figure 2.23. The input light is split in two paths. Both

of the paths contain a MZM in a push-pull configuration biased at the minimum point, and the second path contains an additional phase-shifter, biased at $V_\pi/2$. In this way, the transfer function of the optical IQ modulator is

$$\frac{E_{out}(t)}{E_{in}(t)} = \sin \hat{a}\text{Ą}\text{ą}\left(u_I(t)\cdot\frac{\pi}{2V_\pi}\right) + j\sin \hat{a}\text{Ą}\text{ą}\left(u_Q(t)\cdot\frac{\pi}{2V_\pi}\right) \tag{2.41}$$

where $u_I(t)$ and $u_Q(t)$ are the modulating electrical in-phase and quadrature signals. If assuming small-signal modulation ($u_I(t) << 2V_\pi/\pi$ and $u_Q(t) << 2V_\pi/\pi$), (2.41) can be approximated by

$$\frac{E_{out}(t)}{E_{in}(t)} \approx \frac{\pi}{2V_\pi}\cdot(u_I(t) + ju_Q(t)) = \frac{\pi}{2V_\pi}\cdot u(t) \tag{2.42}$$

where $u(t) = u_I(t) + u_Q(t)$ is the complex representation of the electrical signal $u(t)$. Observing (2.42), an interesting remark can be made. In small-signal regime, the modulated output optical field is proportional to the electrical field of $u(t)$. This indicates that the output optical field is a replica of the modulating electrical field.

A common use for the optical IQ modulator is to generate an arbitrary M-QAM signal. By modulating independently the in-phase and quadrature arms of the optical IQ modulator, all the constellation points of the IQ-complex plane can be achieved as illustrated in figure 2.24.

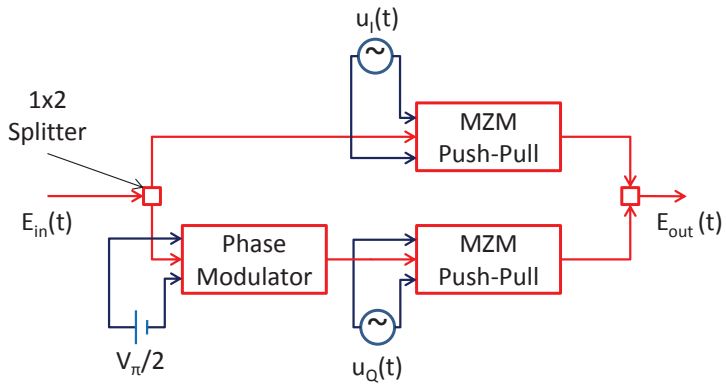

FIGURE 2.23: Schematic view of the Optical IQ Modulator.

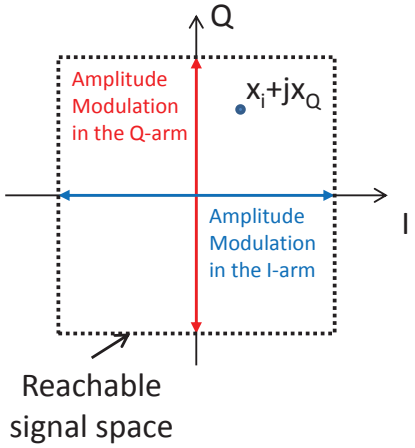

FIGURE 2.24: Reachable IQ-complex plane with optical IQ modulator.

2.2.3 Silicon-based Optical Modulators

Lithium Niobate ($LiNbO_3$) modulators are very efficient but too expensive to be used in applications that require low-cost per unit, such as optical access networks. Before 2004, a few silicon modulators were demonstrated but with very low modulation speed $< 20MHz$ [162]. A significant breakthrough was achieved in 2004 with the first silicon modulator capable of modulating at 1Gbps [163]. Since then, the research and development in silicon modulators enabled more efficient structures, with modulation speeds beyond 40Gbps.

Refractive Index and Absorption Variation in Silicon

Contrary to $LiNbO_3$, the Pockels effect does not occur in silicon. In order to vary either the phase or amplitude of an optical wave confined in a silicon waveguide, Soref *et al.* demonstrated in 1987 [164] that both the refractive index and absorption coefficient of the silicon waveguide

can be varied by changing the concentration of free-carriers (electrons or holes) in the material. At a wavelength of $1.55\mu m$, the refractive index Δn and absorption variation $\Delta\alpha_{abs}$ as function of the electron ΔN and hole ΔP density is given by

$$\Delta n = -8.8 \times 10^{-22}\Delta N - 8.5 \times 10^{-18}\Delta P^{0.8} \tag{2.43}$$

$$\Delta\alpha_{abs} = 8.5 \times 10^{-18}\Delta N + 6 \times 10^{-18}\Delta P \tag{2.44}$$

It can be seen from (2.43) that the contribution of the holes and electrons for the effective index and absorption coefficient variation is not the same. Holes contribute more for the effective index change than electrons (for concentrations below $8.4 \times 10^{-19} cm^{-3}$). In this way, for the same concentration of holes and electrons, the effective index variation is higher when induced by hole variations than when induced by electron variations.

In theory, direct intensity modulation using silicon could be achieved because of the change of the absorption coefficient with the free-carrier variation (as indicated in (2.44)). However, it can be shown that the refractive index variation is much more efficient than the absorption coefficient variation in silicon (cf. subsection 2.2.3.2). The refractive index variation modulates the phase of the optical carrier, which can be converted into amplitude modulation using interferometric structures.

In order to vary the free carrier concentration in the silicon waveguide, the most classical way is to embed a PN junction within the waveguide. By applying a voltage between the P and N regions, the free carriers can be injected (if junction is polarized directly) or removed (if junction is polarized inversely). As an alternative, a Metal-oxide-semiconductor (MOS) capacitor structure can be used to accumulate the free-carriers in the silicon waveguide.

Figures of Merit

In order to compare the many different solutions proposed for silicon optical modulators, the most common figures of merit used for silicon modulators are defined below.

As explained in subsection 2.2.2.2, in a MZM, the V_π is the voltage required to cause a π-shift in one of the arms of the modulator. Because the optical propagation in silicon modulators can be quite lossy, the length of the device is also an issue. The modulation efficiency is then referred as $V_\pi L_\pi$ - the product of V_π and the required length to achieve it. From (2.31), the $V_\pi L_\pi$ is written as

$$V_\pi L_\pi = V \cdot \frac{\lambda_{opt}}{2\Delta n_{eff}} \tag{2.45}$$

where V is the voltage required to cause an effective index variation of Δn_{eff}. Modulation efficiency can be also quantified as the peak-to-peak modulating voltage to achieve a target ER, for a given data-rate.

A key figure of merit specific to OOK modulation is the Extinction Ratio (ER) (cf. subsection 3.2.1.2). Denoting the optical power at the "1" bit P_1 and at the "0" bit as P_0, the ER is defined as

$$ER[dB] = 10\log_{10}\left(\frac{P_1}{P_0}\right) \tag{2.46}$$

It is important to maximize the extinction ratio in order to minimize the receiver sensitivity penalty. In subsection 3.2.1.2 the sensitivity penalty due to finite ER is quantified.

The insertion loss of a device is defined as the ratio P_{max}/P_{in} where P_{max} is the maximum optical output power of the modulator. It is generally normalized by the length of the active

region in dB/cm. However, additional loss can be experienced in the case of a MZM, for example, for non-ideal splitters.

Finally, the bandwidth of the device is also a figure of merit which it will impact on the bit-rate that the device can achieve (without electrical pre-emphasis). We note that there are several trade-offs between efficiency, loss and modulation speed. However, as it will be shown in the state-of-the-art, a robust design may enable high-speed, low-loss and efficient modulators.

2.2.3.1 State-of-the-Art

Carrier Accumulation

One of the first silicon optical modulators that enabled Gbps modulation was based on carrier accumulation by means of a MOS capacitor. It was proposed first by Intel in 2004 [163]. The structure is depicted in figure 2.25. The optical wave is guided in the $2.5\mu m$-wide P-doped poly-Si waveguide. By applying a positive voltage V_D to the p-type poly-Si, and the n-type connected to the ground, the free carriers accumulate on both sides of the gate oxide as illustrated in the picture (holes in the p-region and electrons in the n-region). Then, it was embedded in a MZM structure.

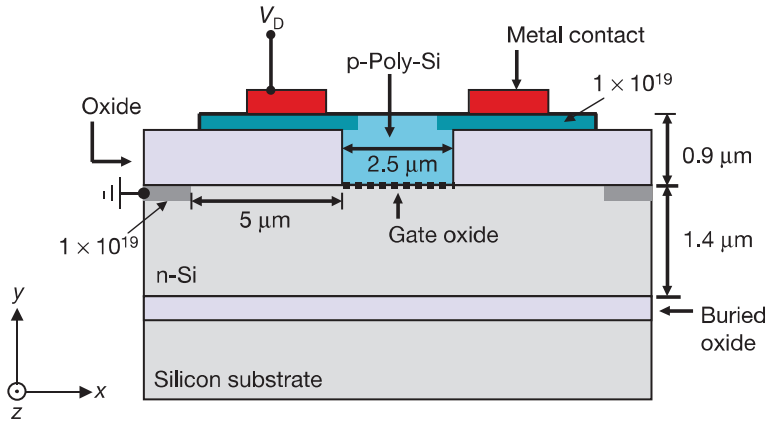

FIGURE 2.25: Cross-section of the carrier accumulation-based silicon optical modulator (Source [163]).

The first structure proposed in 2004 [163] could modulate up to 1.5Gbps (OOK modulation) with low modulation efficiency of about 8V.cm. By optimizing the design of the modulator, the modulation efficiency and modulation speed were improved to 3.3V.cm and 10Gbps, respectively [165]. A very efficient Differential Quadrature Phase-Shift Keying (DQPSK) modulator based on carrier accumulation was demonstrated recently, achieving an efficiency lower than 0.2V.cm [166]. It is detailed in the following section dedicated to silicon modulators for advanced modulation formats.

The drawback of this solution is the necessarily high capacitance value of the junction, which may limit modulation bandwidth and increase power consumption. Since then, other solutions based in the carrier injection and depletion are extensively studied.

Carrier Injection

This mechanism is known to offer the best modulation efficiency over the other three mechanisms of varying the free electrons concentration in the waveguide [167], as indicated in table 2.3. Typically, silicon modulators employing carrier injection are based in a PIN junction. It is simply a PN junction with an intrinsic region between the P and N regions. Figure 2.26 illustrates a

typical example of a PIN junction embedded in a ring resonator (to be detailed in section 2.2.3.2). The intrinsic region is generally made larger than the silicon waveguide so as to reduce optical loss when no voltage is applied. The carrier injection is achieved simply by polarizing directly the PN junction. In this way, electrical current flows through the waveguide and the free carriers are brought by the current source polarizing the diode.

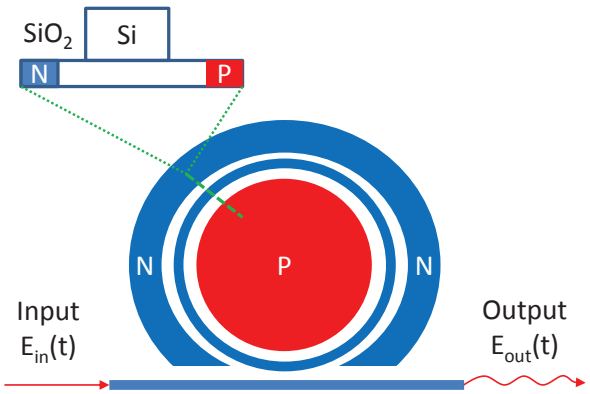

FIGURE 2.26: PIN junction embedded in a silicon ring modulator for carrier-injection based modulation.

The drawback of this solution is the very low speed of modulation. The diffusion of the free electrons (holes) in the P (N) zone is rather a slow process. It may take several nanoseconds to diffuse over a distance of about $1\mu m$ [139]. In this way, the intrinsic bandwidth is limited to less than 1GHz. An electrical pre-emphasis technique can be employed to achieve higher modulation speed at the expense of higher power consumption. It can be implemented with an electronic circuit to amplify the higher frequencies of the signal to compensate the low modulator bandwidth. Modulation speeds as high as 12.5Gbps (9dB ER, $16V_{pp}$ driving voltage) [168] and 50Gbps (4.3dB ER, $4.35V_{pp}$ driving voltage) can be achieved in this way [169]. In [170], the author demonstrates a carrier-injection ring modulator achieving 50Gbps and 5.2dB ER with a pre-emphasis technique, using only $2V_{pp}$ modulation voltage (modulation efficiency of 0.011V.cm at 10MHz and 0.3V.cm at 25GHz).

Carrier Depletion

The carrier-depletion type offers typically the best modulation bandwidth. The idea of using carrier depletion for high-speed silicon modulators was first proposed in [171]. Optical modulators based on carrier depletion have intrinsically high free-carrier concentration in the waveguide when no voltage is applied by means of a PN junction. When an inverse tension is applied in the junction, an electric field repels the free carriers from the waveguide, creating a space charge region. The width of the space charge region increases with the square-root of the applied voltage (cf. subsection 2.2.3.2). The variation in the carrier concentration changes both the refractive index and absorption of the waveguide as indicated by Soref's equations ((2.43) and (2.44)).

Classically, the lateral PN junction is simply formed by a N-doped material to the side of a P-doped material with no intrinsic zone between P and N regions as illustrated in Figure 2.27(a). In this way, the modulation efficiency is maximized. The drawbacks of this type of junction are twofold : 1) Increased junction capacity compared to the PIN junction because it is inversely proportional to the space charge region width, which is minimum for low bias voltages. 2) Increased optical loss because the entire waveguide is doped.

One approach to decrease the junction capacity and optical loss in PN junctions is to insert an undoped intrinsic zone between P and N regions - establishing a PIN junction (cf. 2.27(b)) [172]. However, a trade-off between modulation efficiency and junction capacity is identified

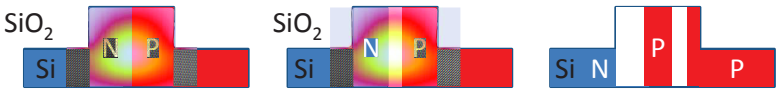
SiO2
Si
N
P
SiO2
Si
N
P
Si
N
P
P

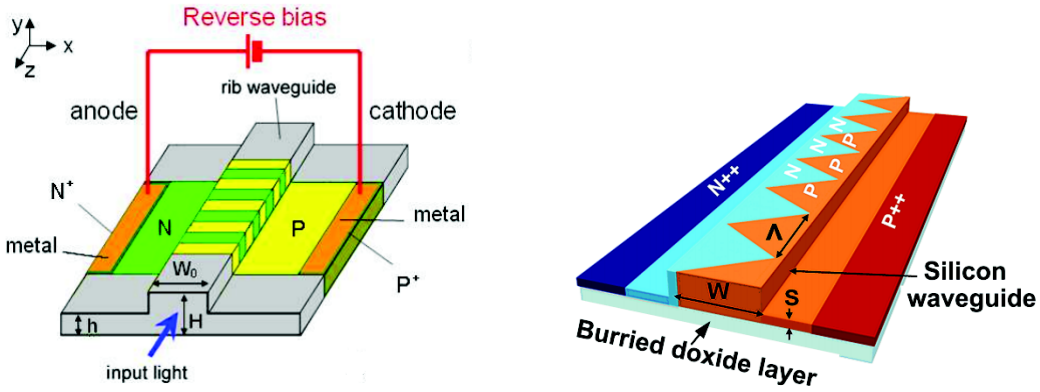

(a) (b)

FIGURE 2.28: Interleaved PN junction for carrier-depletion optical modulators. (a) Typical form, first proposed in [178]. (b) Zigzag form, first proposed in [176].

In [179], the author achieves a record data-rate of 224Gbps with PM-16-QAM modulation format and 112Gbps with PM-QPSK (28Gbaud) with an integrated MZM-based optical IQ modulator. The structure is based on a lateral PN junction, with a modulation efficiency of 2.4V.cm and 4.2dB insertion losses in a 2.4mm-long active region.

An optical QPSK modulator was also demonstrated using ring modulators [180], with a data-rate of 56Gbps. This is achieved thanks to the 2π phase shift observed in overcoupled rings across the resonance wavelengths (cf. subsection 2.2.3.2, equation (2.58)). However, this scheme results in higher insertion losses, for example 10.5dB is reported in [181].

Very recently, OFDM modulation of a lateral-PN silicon MZM was reported in [182]. Optical insertion loss of the 1.5mm modulator is 7dB. QPSK, 8-QAM and 16-QAM are demonstrated, but the data-rate is limited to 4.38Gbps.

Summary

Table 2.3 details the state-of-the-art in silicon modulators. The modulation efficiency is given in DC operation. Note that insertion losses do not include coupling losses into the chip (except when indicated), as explained in the beginning of the chapter (figures of merit). The modulation format is mostly OOK, except in the carrier-accumulation type, which is DQPSK.

2.2.3.2 Modeling Silicon Optical Modulators

In this part, a model for silicon modulators arranged either in a MZI or a ring resonator structure is developed. The objective of this section is to define a realistic model for the behavior of such modulators and not to optimize the design process. The reader should refer to [172] for further details on the design of silicon modulators. In this part, a lateral PN junction based on carrier depletion is considered.

A top-view schematic of the modeling process used in this work is shown in figure 2.29. It consists in 2 main steps : 1) Simulation of the active region and 2) Complete model of the modulator (MZM or ring-based). For the silicon MZM, only a static model is considered, while for the silicon ring modulator, a dynamic model is also presented, which takes into account the photon lifetime in the ring.

Simulation of the Active Region

The objective of the conception of the active region is to define a model for the variation of the effective index and absorption coefficient as a function of the applied voltage for a given

Reference	Interfero-meter	Junction type	$V_\pi L_\pi$ [V.cm]	Insertion Loss [dB] (Length)	Max bit-rate [Gbps]	ER [dB] (Voltage swing)
Carrier Accumulation						
[166]	MZM	MOS Capacitor	0.2	-	112 (28 Gbaud)	- ($1V_{pp}$)
Carrier Injection						
[170]	Ring	PIN	0.011	7 (includes coupling)	50	4.6 ($2V_{pp}$ with pre-emphasis)
Carrier Depletion						
[183]	MZM	Lateral PN	1.4	2.5 (L=1mm)	12.5	7.2 ($6V_{pp}$)
[184]	MZM	Lateral PN	2.8	4.2 (L=1mm)	50	3.1 ($6.5V_{pp}$)
[177]	MZM	Lateral PN	1.65	2 (L=0.75mm)	60	4.4 ($6V_{pp}$)
[185]	Ring	Lateral PN	-	5	40	7 ($1V_{pp}$)
[186]	MZM	Lateral PIPIN	6	6 (L=1.8mm)	10	8.1 ($7V_{pp}$)
[187]	MZM	Lateral PIPIN	3.5	6 (L=3.5mm)	40	6.6 ($7V_{pp}$)
[188]	Ring	Vertical PN	-	1.59	25	6.9 ($0.6V_{pp}$)
[189]	Ring	Interleaved PN	0.76	2	40	4 ($1.6V_{pp}$)
[176]	Ring	Interleaved PN (Zigzag)	1.7	-	44	3 ($3V_{pp}$)
[177]	Ring	Interleaved PN (Zigzag)	-	-	60	4.2 ($6V_{pp}$)

TABLE 2.3: Summary of the state-of-the-art of all-silicon optical modulators.

structure. The parameters of the structure (waveguide and PN junction) necessary for the modeling are shown in figure 2.30. The wavelength considered is $1.55\mu m$. For this analysis, we consider two existing structures which were available in the laboratory for testing. The samples were tested, and the experimental results were compared with the results obtained from simulations.

The block schematic for the simulation of the active region used in this work is summarized in figure 2.31. Each step is detailed in the following.

Calculating Local Electron/Hole Concentration as a Function of the Voltage The physical equations that relate the spatial distribution of the free carrier/hole concentration of a PN junction with the applied electric field are the Poisson and continuity equations.

The Poison equation relates the local free-charge density $\rho(x, y, z)$ with the applied electrostatic potential $\phi(x, y, z)$. It is given by

$$\nabla^2 \phi = -\frac{\rho(x, y, z)}{\epsilon} \tag{2.47}$$

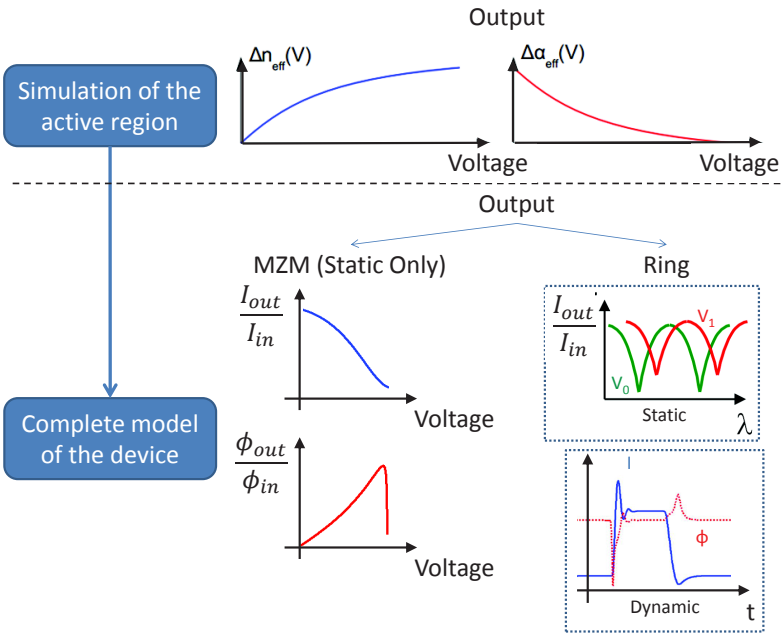

FIGURE 2.29: Top-view schematic of the modeling process of the silicon modulators. I=intensity, V=voltage, λ=wavelength, ϕ=phase.

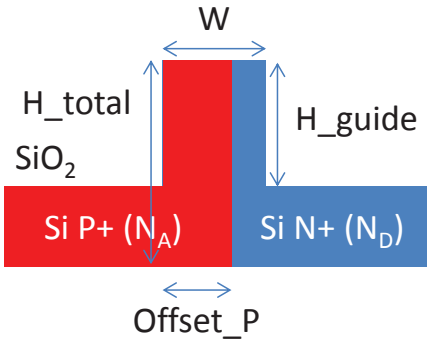

FIGURE 2.30: Necessary parameters for the modeling of the silicon modulator. N_A - Doping concentration of the P doped region, N_D - Doping concentration of the N doped region.

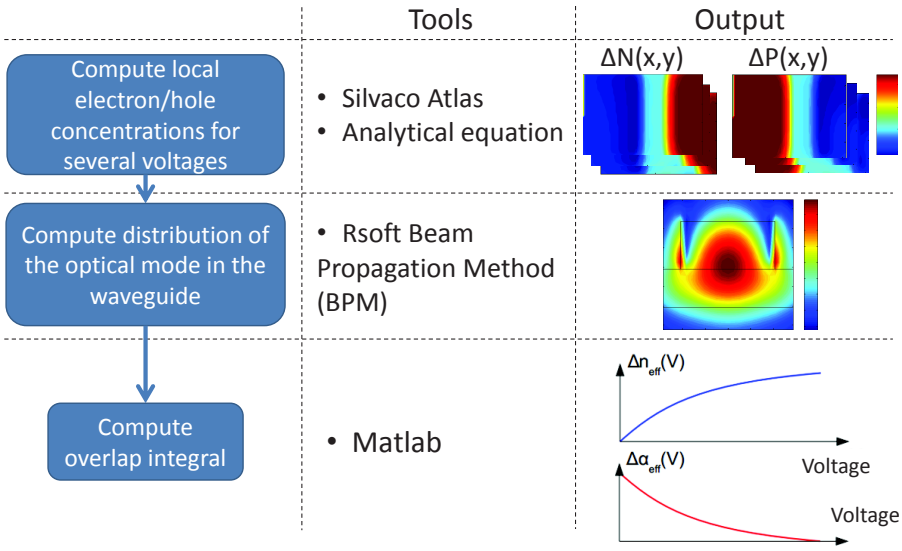

FIGURE 2.31: Schematic of the active region simulation.

where ϵ is the silicon permitivity, defined by $\epsilon = \epsilon_r \times \epsilon_0$ with $\epsilon_r = 11.68$ the relative permitivity of silicon and ϵ_0 the vacuum permitivity. Then, the local free-charge density in a doped material is given by

$$\rho(x, y, z) = q\left(\Delta P(x, y, z) - \Delta N(x, y, z) + N_D - N_A\right) \tag{2.48}$$

where ΔP and ΔN represent the local electron and hole concentrations, respectively, and N_D and N_A the donor and acceptor impurity concentration (namely the electron/hole density at equilibrium), respectively and q is the elementary electron charge. The resolution assuming only one dimension, complete depletion (meaning that there are no free carriers at the space charge region of the junction) and uniform electron and hole concentration, (2.47) leads to the following expression for the space charge region width W_{SCR} as a function of the applied voltage V

$$W_{SCR}(V) = \sqrt{\frac{2\epsilon}{q} \cdot \left(\frac{1}{N_A} + \frac{1}{N_D}\right) \cdot (\Delta V - V)} \tag{2.49}$$

where ΔV is the built-in voltage. It is defined by

$$\Delta V = \frac{kT}{q} \ln\left(\frac{N_A N_D}{n_i^2}\right) \tag{2.50}$$

where k is the Boltzmann constant, T is the temperature and n_i is the intrinsic carrier concentration of silicon, equals to $10^{10} cm^{-3}$ at T=300K. The built-in voltage is the intrinsic differential electric potential in equilibrium. It can be observed that even at equilibrium the space charge region is non-zero and it is about 80nm for $N_A \approx N_D \approx 3 \times 10^{17} cm^{-3}$. This is an important observation for optimizing the modulation efficiency of the silicon modulator. As most of the optical mode power is placed in the middle of the waveguide, it is useful to intentionally shift the center of the junction from the center of the waveguide because in this region no free carrier variation occurs with the applied voltage.

The continuity equation describes the temporal behavior of the junction. In this work, we consider only the static behavior for the PN junction. For more details, on the dynamic modeling of the junction, refer to [172].

An important remark is that when the doping concentration between the P and N regions is uneven, the depletion will not occur symmetrically around the junction center. It is intuitive that the depletion is higher in the less doped region because there are less free carriers to deplete. To characterize this effect, a parameter $r = N_A/N_D$ is defined. Considering W_{SCR} the total depletion width, the partial p w_p and n w_n regions depletion widths, such that $W_{SCR} = w_p + w_n$, are approximated by [190]

$$w_p = \frac{W_{SCR}}{r+1} \tag{2.51}$$

$$w_n = \frac{W_{SCR}}{1/r+1} \tag{2.52}$$

An important aspect of the modeling of the PN junction is the doping profile of the junction. In a first assumption, we can approximate it by a uniform distribution. For a more accurate model, one should consider simulating the implantation conditions (material, energy, tilt, annealing, among others) using for instance the software Silvaco Athena and then use the resulting doping profile to simulate the junction. In this case, the one-dimensional assumption made before for (2.47) is not valid and a numerical resolution of Poison equation is required.

In this work, the uniform doping profile is considered for simplicity. For the electric simulation (calculation of the free carrier/hole concentration as a function of the applied voltage),

we use two methods : 1) (2.49) is used for calculating the width of the space charge region ; and 2) the simulation tool Silvaco Atlas is used to numerically solve (2.47) for several values of the applied voltage.

Calculating the Distribution of the Optical Mode in the Waveguide In this work, we use the software RSoft to compute the spatial distribution of the optical mode inside the waveguide through the method Beam Propagation Method (BPM) [191].

As mentioned in subsection 2.1, the fundamental mode in an optical fiber can be approximated by a 2D Gaussian profile, but it does not work well in silicon waveguides because of the much larger refractive index difference between core and cladding. In [190], the authors approximate the spatial profile of the optical mode in the silicon waveguide by a Pearson VII distribution, for instance. For a more accurate approach, the numerical method BPM is used in this work.

Calculating the Overlap Integral The final step of the modeling of the active section of the silicon modulator based on carrier depletion is to calculate the overlap integral between the spatial profile of the effective index/absorption coefficient variation and the distribution of the optical mode with the purpose of finding the total effective index and absorption variation. In a discrete form, it is defined mathematically by [190]

$$\Delta n_{eff} = \frac{1}{N_P} \sum \sum |\psi(x,y)|^2 \cdot \Delta n(x,y) \tag{2.53}$$

$$\Delta \alpha_{abs} = \frac{1}{N_P} \sum \sum |\psi(x,y)|^2 \cdot \Delta \alpha_{abs}(x,y) \tag{2.54}$$

where $\psi(x,y)$ is the normalized spatial distribution of the optical mode inside the waveguide and N_P is the total number of the points of the discrete grid. Note that $\Delta n(x,y)$ and $\Delta \alpha_{abs}(x,y)$ are obtained from Soref's equations (2.43) and (2.44) using the spatial distribution of the holes $\Delta P(x,y)$ and $\Delta N(x,y)$ calculated previously.

Comparison with the Experimental Measurements The first sample tested is a 3.5mm-long silicon MZM from Surrey University. The structure is described in [192]. The second sample is a 4.7mm silicon MZM from the FAON project. The active region for the FAON modulator is illustrated in figure 2.32.

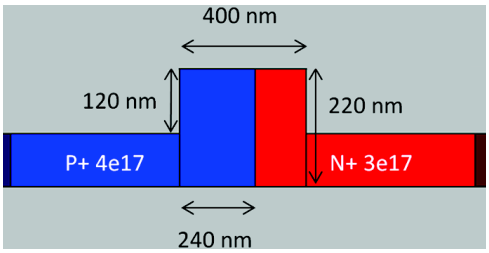

FIGURE 2.32: Cross-section of the active region of one of the arms of the FAON modulator.

In the silicon MZMs, the effective index variation is found by calculating the phase shift as a function of the applied voltage [183] and then using (2.31).

The results obtained from the simulation (with analytical and numerical approach for calculating the free electron/hole concentration) are displayed in figure 2.33 and figure 2.34 for the active region of Surrey and FAON modulators, respectively. Note that both the effective index and absorption coefficient variation are normalized to the 0V value. The absolute value of the

absorption loss due to doping can be effectively predicted, but the actual loss of the modulator can be higher due to propagation loss and splitter loss, which are not taken into account in the calculations.

For the Surrey's results, one can observe that the predicted performance for the Δn_{eff} are below the measured ones. This suggests that the intrinsic P-region doping may be actually higher than the target doping used in the simulations. This is confirmed by figure 2.33(b) which shows that the measured variation of the absorption coefficient is higher than the predicted through simulation.

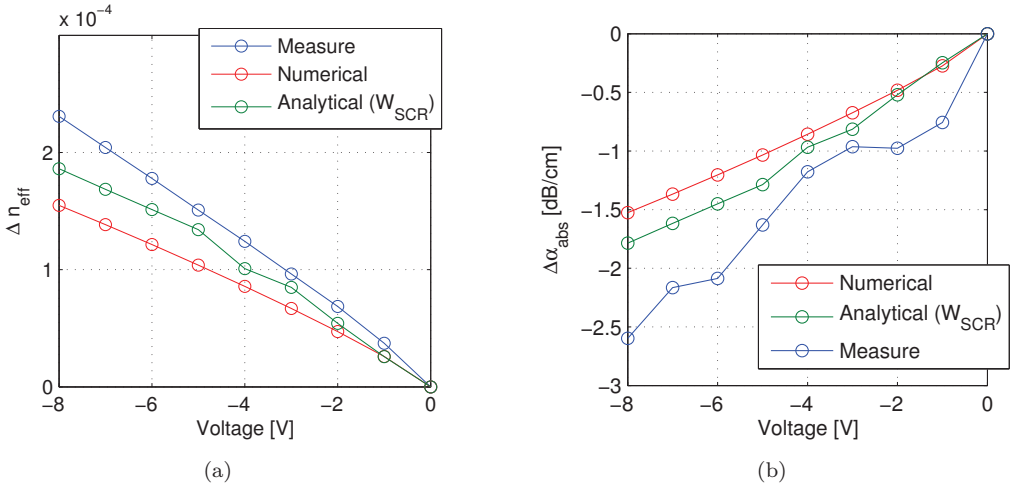

(a) (b)

FIGURE 2.33: Comparison between measured and simulated results for the active region of Surrey's modulator. (a) Effective index Δn_{eff} variation and (b) absorption coefficient α_{abs} variation as a function of the applied voltage.

As the FAON modulators are concerned, the results from the effective index (figure 2.34(a)) may also suggest an over-doping of the P-region of the junction. However, this is not confirmed by the absorption coefficient variation in figure 2.34(b) because the $\Delta\alpha_{abs}$ variation predicted by the model is actually higher than the measured value. This may indicate that the position of the junction differs from the targeted value, or that the approximation of the uniform doping distribution is not very accurate in this case.

To conclude, we observe that the numerical and analytical results are very close (17% in the Surrey 2% in the FAON modulator for the effective index variation). Therefore, in the simulation platform, it can be of interest to consider the analytical model with the purpose of reducing the complexity of the calculation. The higher difference in the Surrey modulator between numerical and analytical results may be attributed to the high difference between the doping levels of the P and N regions, which makes (2.51) and (2.52) less accurate. In order to have a more rigorous model of the active region of the modulator, one should consider the implantation conditions of the doped regions of the junction. For the purpose considered in this work, which is to provide a model accurate enough to represent the non-linear form of the Δn_{eff} and $\Delta\alpha_{abs}$ as a function of the applied voltage, the method presented is good enough.

As the predicted performance is closer to the measured results for the FAON structure, we will use this numerical model for the rest of this work. The effective index and absorption coefficient change as a function of the voltage can be very accurately approximated by a four-degree polynomial

$$\Delta n_{eff}(v) = a_0 + a_1 V + a_2 V^2 + a_3 V^3 + a_4 V^4 \tag{2.55}$$

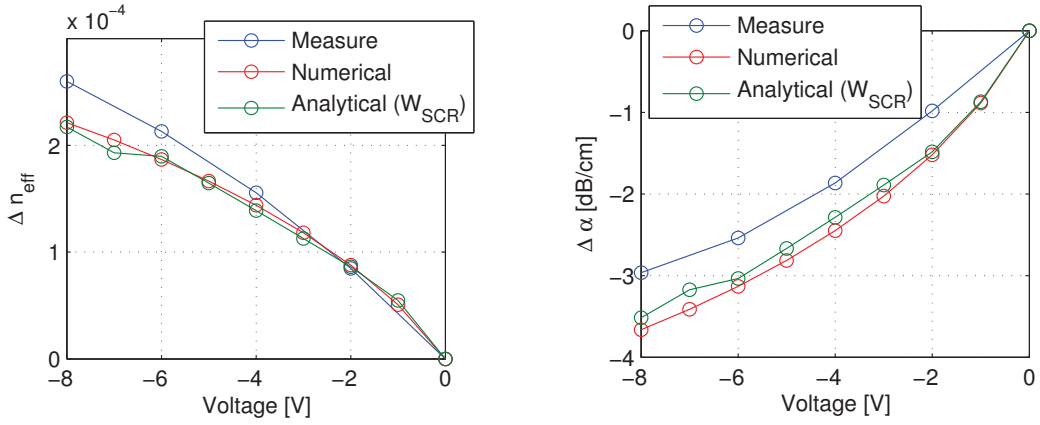

(a) (b)

FIGURE 2.34: Comparison between measured and simulated results for the active region of FAON's modulator. (a) Effective index Δn_{eff} variation and (b) absorption coefficient α_{abs} variation as a function of the applied voltage.

$$\Delta\alpha_{abs}(v) = b_0 + b_1 V + b_2 V^2 + b_3 V^3 + b_4 V^4 \tag{2.56}$$

where $a_0 - a_4$ and $b_0 - b_4$ are the polynomial coefficients for the effective index and absorption change, respectively.

Complete Model of the Modulator - MZM

The basic structure of the MZM was presented in subsection 2.2.2.2. The general form of a silicon MZM is the same as the one given in figure 2.20. The upper arm is denoted with index 1 and the bottom arm with index 2. Assuming a perfect 1×2 splitter, the transfer function of the silicon MZM with length l_{MZM} is given by

$$\frac{E_{out}(t)}{E_{in}(t)} = \frac{1}{2} \cdot \left(\exp\left(-\frac{\alpha_{abs,1}}{2} \cdot l_{MZM} - j\frac{2\pi}{\lambda_{opt}} n_{eff,1} \cdot l_{MZM} \right) + \exp\left(-\frac{\alpha_{abs,2}}{2} \cdot l_{MZM} - j\left(\frac{2\pi}{\lambda_{opt}} n_{eff,1} \cdot l_{MZM} + \phi_0 \right) \right) \right) \tag{2.57}$$

where ϕ_0 indicates the biasing point when the junction is not polarized (V=0). This biasing can be achieved by thermal variation using integrated heaters [193]; or designing an asymmetrical MZM (with a length difference ΔL between the two arms) and properly choosing wavelength to achieve the desired bias. If the $\Delta L << l_{MZM}$, this does not affect the MZM operation. This is very practical for characterization purposes, but for real applications it is unpractical because it limits the optical bandwidth of the device.

Two cases are distinguished. In the first one, the silicon MZM is assumed to be modulated in only one arm. In the second, a push-pull configuration is analyzed.

Silicon MZM Modulated in only one Arm For the single-drive MZM, we assume $\alpha_{abs,2} = \alpha_{abs,1} + \Delta\alpha_{abs}(V)$ and $n_{eff,2} = n_{eff,1} + \Delta n_{eff}(V)$. In figure 2.35, the intensity and phase response of the silicon MZM is traced as a function of the applied voltage, for $l_{MZM} = 4mm$ and $\phi_0 = 0$. In subsection 5.1.6.1, the chirp of the silicon MZM based on the developed model is analyzed numerically.

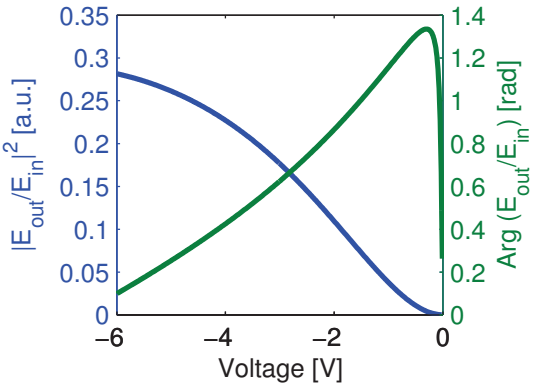

FIGURE 2.35: Intensity and phase transfer function of the silicon MZM with the previous simulated model of the active region, for 4mm length, and modulation in a single-arm.

Dual-drive push-pull Silicon MZM With the purpose of minimizing the frequency chirp induced by the optical modulator, a push-pull configuration is suitable as discussed in subsection 2.2.2.2. The issue compared to classical $LiNbO_3$ modulators is that, contrary to Lithium Niobate, the electro-optic effect in silicon is not completely linear as explained in the previous subsections. In addition, the absorption coefficient of the waveguide also varies with the applied voltage. In other words, ideal push-pull operation in silicon MZM is not possible, and this causes a residual phase modulation that needs to be quantified.

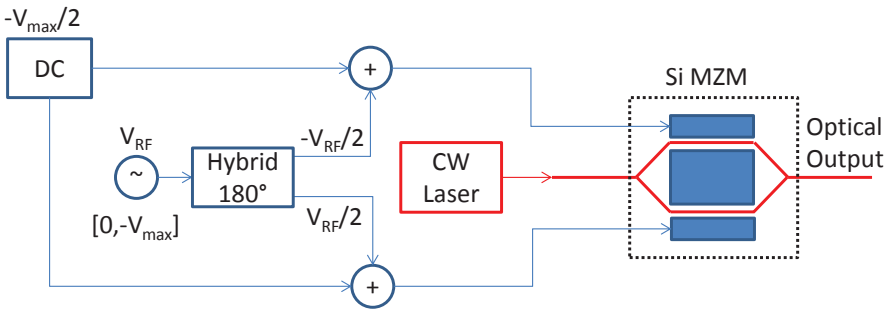

FIGURE 2.36: Driving scheme for push-pull silicon MZM.

An example of a push pull driving scheme is shown in figure 2.36. The driving signal (ranging from 0 to $-V_{max}$) is split in two branches dephased by 180°. In each branch, a bias signal of $-V_{max}/2$ is added to the signals before driving each arm of the silicon MZM. Considering a $V_{max} = 6V$, figure 2.37 shows the phase shift and absorption coefficient variation in each arm of the MZM. Residual phase modulation appears because of the difference in the modulation efficiency and absorption between the two arms. Considering the general equation for the transfer function of a dual drive silicon MZM given in (2.57), figure 2.38 illustrates the overall intensity and phase transfer function of the push-pull MZM, in which the residual phase modulation can be clearly observed, with an excursion of about 0.0875rad/mm from 0V to -6V. The effect of the residual phase modulation in this structure is studied in subsection 5.2.1, where the residual chirp in terms of the chirp parameter α_{MZM} is evaluated numerically using the model presented. The impact of this residual chirp in an optical SSB-OFDM transmission is analyzed in subsection 5.2.3.

Non-Linearity of the Silicon MZM E/O Response In general, the silicon MZM is less linear than classical $LiNbO_3$ MZM because of the non-linear relation between the effective index

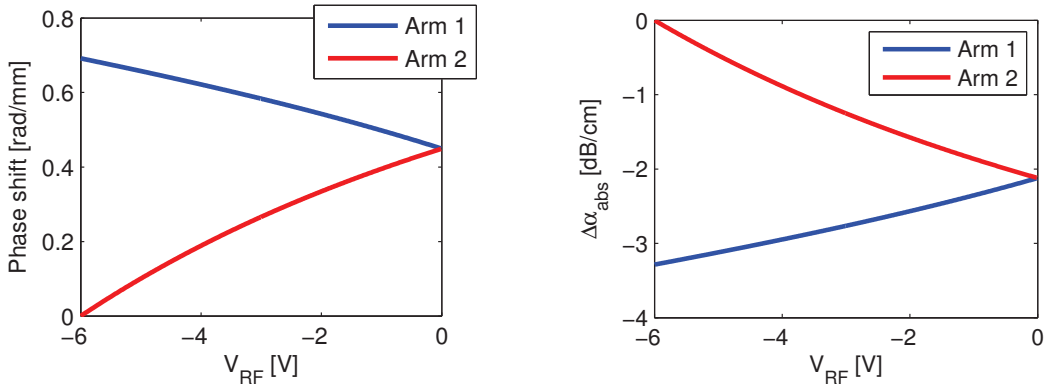

FIGURE 2.37: (a) Phase shift and (b) absorption coefficient variation in each arm of the Silcon MZM in push-pull configuration, $V_{max} = 6V$.

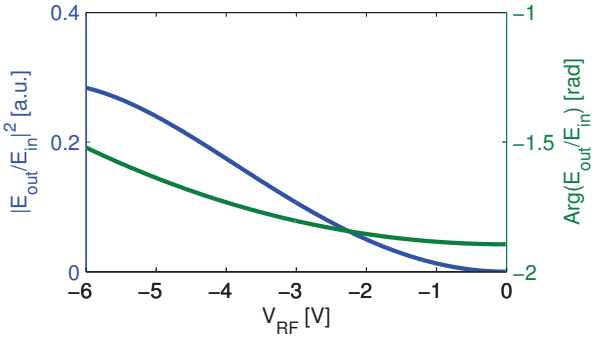

FIGURE 2.38: Amplitude and intensity transfer function of the silicon MZM in push-pull configuration.

variation with the applied voltage. A few authors have addressed this issue [167, 194–196]. As an order of magnitude, the linearity requirement in terms of Spurious-free Dynamic Range (SFDR) for Wireless Local Area Network (WLAN) applications in on the order of $95dB.Hz^{2/3}$ [197]. Considering a single-tone at f_{RF}, the SFDR is a measure of the relative amplitude ratio between the signal at frequency f_{RF} and the highest harmonic in the spectrum (generally second or third order) measured at a level just above the noise floor of the system [198]. A SFDR of $95dB.Hz^{2/3}$ and $97dB.Hz^{2/3}$ for silicon MZM is reported in [196] and [167], respectively, which shows the feasibility for this type of application [194]. In addition, the authors show in [167] that modulators based on carrier-depletion have $20dB.Hz^{2/3}$ better SFDR than carrier-injection based modulators. This compares with $120dB.Hz^{2/3}$ for $LiNbO_3$ MZM [199]. It will be shown in subsection 5.1.6.2 that the non-linearity of the silicon MZM causes a sensitivity penalty in for the optical OFDM transmission. As a remark, the relationship between SFDR and Third-Order Interception Point (IP3) is given in [198].

Complete Model of the Modulator - Ring Resonator

Another very popular interferometer structure commonly employed in silicon optical modulators is the ring resonator. The basic structure is depicted in figure 2.39. A part of the input optical signal is coupled to a ring-shaped waveguide. The light with wavelength λ_{opt} that propagates inside the ring with radius R undergoes a phase shift of $2\pi n_{eff}(2\pi R)/\lambda_{opt}$ in one tour. A resonance occurs when this interference is destructive.

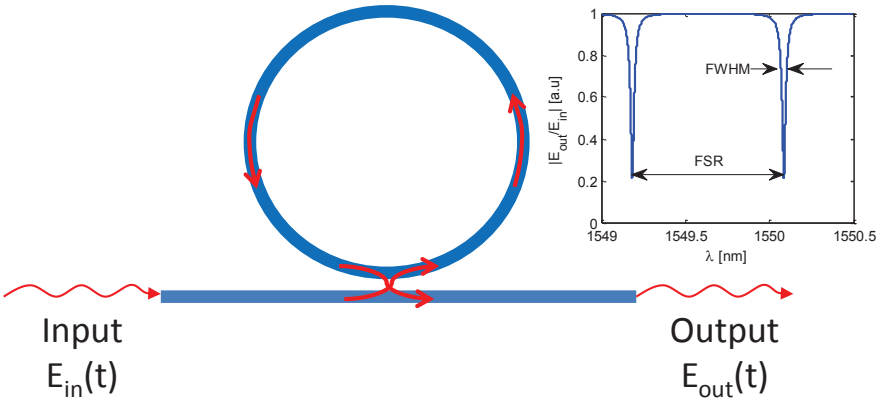

FIGURE 2.39: Principle of operation of a ring resonator. Inset : Typical spectral response of a ring resonator. Acronyms : Free Spectral Range (FSR), Full Width at Half Maximum (FWHM).

Static Model The transfer function of a ring resonator can be obtained using a matrix approach [200]. The amplitude coupling ratio between the waveguide and the ring is denoted κ_1. This parameter can be obtained as a function of the ring radius, the waveguide geometry and the gap between the waveguide and the ring through Finite Difference Time Domain (FDTD) simulations [200]. In this way, the amplitude of the transmitted signal (off-resonance) is given by $t_1 = \sqrt{1-\kappa_1^2}$. Assuming a_{ring} is the intensity loss in a half tour of the ring (defined by $a_{ring} = \exp(-\alpha_{abs} \cdot \pi R)$), the field transfer function is given by

$$\frac{E_{out}(t)}{E_{in}(t)} = \frac{\frac{t_1}{\sqrt{a_{ring}}} \cdot \exp(-j\beta\pi R) - \sqrt{a_{ring}} \cdot \exp(j\beta\pi R)}{\frac{1}{\sqrt{a_{ring}}} \cdot \exp(-j\beta\pi R) - t_1 \cdot \sqrt{a_{ring}} \cdot \exp(j\beta\pi R)} \tag{2.58}$$

where β is the propagation constant given by $\beta = 2\pi n_{eff}/\lambda$. The intensity transfer function is defined by

$$\left|\frac{E_{out}(t)}{E_{in}(t)}\right|^2 = \frac{\frac{t_1^2}{a_{ring}} + a_{ring} - 2t_1\cos(2\beta\pi R)}{\frac{1}{a_{ring}} + t_1^2 a_{ring} - 2t_1\cos(2\beta\pi R)} \tag{2.59}$$

The inset of figure 2.39 shows the typical spectral response of a ring resonator with $\kappa_1 = 0.25$, $\alpha_{abs} = 10dB/cm$, $n_{eff} = 2.75$ and $R = 100\mu m$. The FWHM is the wavelength width of the resonance at $(P_{max} + P_{min})/2$, where P_{max} and P_{min} are the maximum and minimum values of the intensity transfer function, respectively.

An important design rule for the ring resonator with a direct impact on the modulator performance is the coupling coefficient κ_1. Observing the spectral response example given by the inset of figure 2.39, one can note that the amplitude at the resonance wavelengths is not completely zero. From (2.59), one can show that if $\kappa_1^2 = (1 - a_{ring}^2)$ is satisfied, E_{out} reaches zero at the resonance. This is called the critical coupling condition. Figure 2.40 shows the output amplitude as a function of κ_1 for three values of the optical loss in the ring. When the value of the coupling-ratio is below the critical coupling, the ring is said to be undercoupled ; on the other hand, if κ_1 is higher than the critical coupling, the ring is operating in the overcoupling regime. As an example, the undercoupling and overcoupling regimes are indicated for $\alpha_{abs} = 40dB/cm$. In order to maximize the extinction ratio, the coupling ratio should be as close as possible to the critical coupling. A few authors proposed to associate a ring modulator with a MZI so as to relax this constraint [201]. This is possible thanks to the fact that when the ring is over-coupled, the phase response of the ring varies 2π from one side of the resonance to the other, independent of the value of κ_1 (in over-coupling condition).

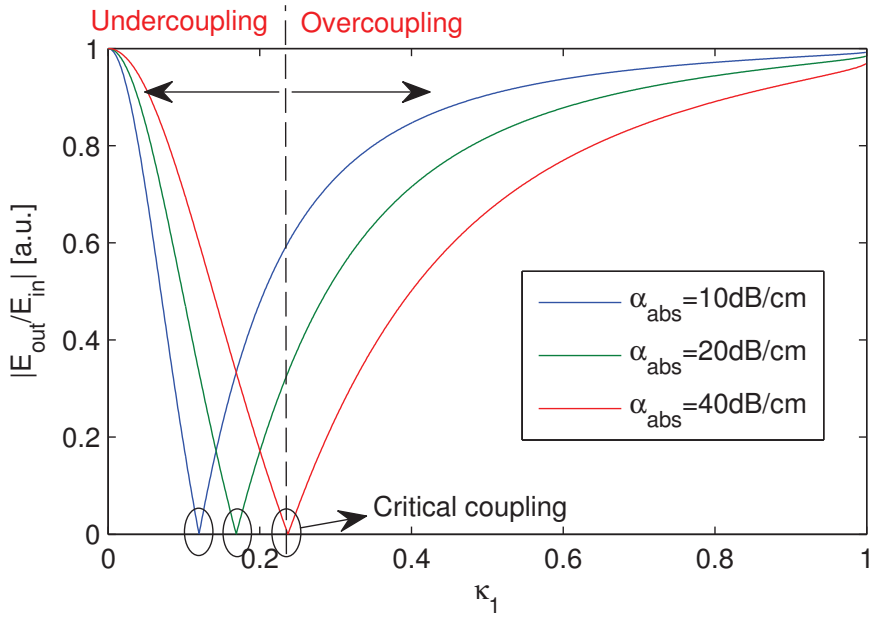

FIGURE 2.40: Amplitude transfer function of the ring resonator at the resonance for several κ_1 values.

Then, by considering the critical coupling condition, one can find the m^{th} order resonance wavelength λ_m by setting (2.58) to zero, resulting in

$$\lambda_m = \frac{n_{eff} \cdot 2\pi R}{m} \tag{2.60}$$

Using (2.3), the FSR of the spectral response around the m^{th} order of resonance $(\lambda_m - \lambda_{m-1})$ is defined by

$$FSR_m = \frac{n_g \cdot 2\pi R}{(m - (dn_{eff}/d\lambda)2\pi R) \cdot (m - 1 - (dn_{eff}/d\lambda)2\pi R)} \approx \frac{\lambda_m^2}{n_g \cdot 2\pi R} \tag{2.61}$$

The approximation holds for typical values of R $(10 - 100\mu m)$, an order of resonance around $1.55\mu m$ for $n_g = 3.75$ and typical values for $dn_{eff}/d\lambda$ found in [200].

The modulation using a ring resonator is typically done by varying the effective index of the ring. In this way, the resonance wavelength is blue or red shifted (depending if carriers are injected or depleted) as indicated by (2.60).

An important parameter with a direct impact on the performance of the ring modulator is the Q factor. In a general way, the Q factor is given by $Q = FWHM/\lambda_m$, where λ_m is the wavelength at resonance of m^{th} order. It can be described in ring resonators by the relation [202]

$$Q = \frac{2\pi \cdot (\pi R) \cdot n_g}{\lambda_m \cdot \kappa_1^2 \sqrt{1 - a_{ring}^2}}. \tag{2.62}$$

Basically, the Q factor is inversely proportional to the product between the propagation loss in the ring and the coupling coefficient κ_1. The straightforward impact in the modulator performance is that a higher Q value leads to sharper transitions from the maximum transmission value to the minimum transmission value at the resonance. Hence, to maximize modulation efficiency, one should increase the Q factor as high as possible (decrease the optical loss in the ring).

On the other side, the Q factor has an indirect impact on the modulation bandwidth of the ring. It is useful to define the photon lifetime τ_p in the ring - the mean time a photon takes to being absorbed inside the cavity. Then $\tau_p \propto 1/a_{ring}$. When the modulator goes from the "off-resonance" state to the "on-resonance" state, the optical energy stored in the ring takes a certain time interval to be charged - if the photon lifetime is high, this time interval is also high. As a consequence, a high Q-factor leads to lower modulation speed achievable by the modulator. This is a trade-off between modulation speed and modulation efficiency in ring modulators [203]. The Q factor is related to the photon lifetime by

$$\tau_p = \frac{\lambda_m \cdot Q}{2\pi c} \tag{2.63}$$

Then, the -3dB modulation bandwidth limited by the photon lifetime in the cavity is given by $f_c = 1/(2\pi\tau_p)$.

Figure 2.41 illustrates the spectral response of a ring-resonator with a quality factor of 12000 and critical coupling condition (at 0V bias), for several reverse bias voltages applied (carrier-depletion). Figure 2.42 shows the transfer function of the ring modulator as a function of the applied voltage, for several Q values. The wavelength chosen is the one at resonance when no voltage is applied.

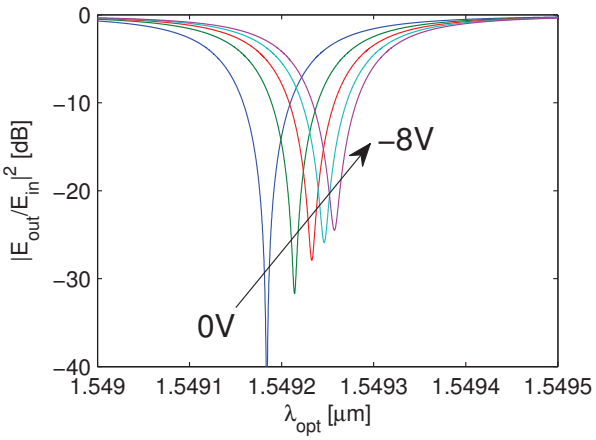

FIGURE 2.41: Spectral response of the ring modulator with Q=12000 for several applied voltages.

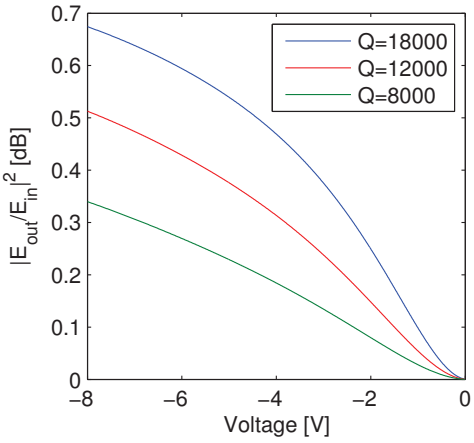

FIGURE 2.42: Intensity transfer function of the ring as a function of the applied voltage.

Dynamic Model The silicon ring modulator also presents chirp which is obvious from the ring transfer function given in (2.58). According to [204], the interference between the optical light coupled out of the ring and the Continuous Wave (CW) light induces also phase oscillations in the transitions between on and off states. This is why a static model would not predict correctly the chirp.

In the following, the bandwidth limitation imposed by the photon lifetime in the cavity is described. Note that the bandwidth limitation imposed by the junction capacity and electric geometry of the modulator driving circuit is further neglected. The dynamic model used here for the ring modulator is presented in [205]. Basically, it describes the evolution in time of the optical power stored in the ring. For example, if at equilibrium the ring is at resonance (at 0V), when an external voltage is applied to the active region, the photons stored in the resonator take some time to leave the ring. Inversely, the photons take some time to charge the resonator

if the ring is goes from off-resonance to on-resonance state. The amplitude $A_{ring}(t)$ of the energy stored in the ring is given by

$$\frac{dA_{ring}(t)}{dt} = \left(2\pi cj\left(\frac{1}{\lambda_{opt}} - \frac{1}{\lambda_m(t)}\right) - \frac{1}{\tau_c} - \frac{1}{\tau_l(t)}\right) \cdot A_{ring}(t) + j\mu E_{in}(t) \tag{2.64}$$

where c is the speed of light, λ_m is the resonance wavelength of order m, τ_c and τ_l are the amplitude decays due to the waveguide coupling into the ring and the propagation losses inside the ring, respectively, with $\mu = \sqrt{2/\tau_c}$. The resonance wavelength is modified from (2.60) to take into account the variation of the effective index with the applied voltage (which varies in time)

$$\lambda_m = \frac{(n_{eff} + \Delta n_{eff}(V(t))) \cdot 2\pi R}{m}. \tag{2.65}$$

The variables τ_c and τ_l are defined by defined by

$$\tau_c = 2 \cdot \frac{2\pi R}{\kappa_1^2 v_g} \tag{2.66}$$

$$\tau_l(t) = 2 \cdot \frac{2\pi R}{(1 - a_{ring}^2(t)) \cdot v_g} \tag{2.67}$$

where $a_{ring}(t) = \exp\left(-\left(\alpha_{abs} + \Delta\alpha_{abs}(V(t))\right)\pi R\right)$. Finally, the field of the output optical signal is defined by

$$E_{out}(t) = E_{in}(t) + j\mu A_{ring}(t) \tag{2.68}$$

Note that the resolution of (2.64) and (2.68) in a steady-state condition ($dA_{ring}(t)/dt = 0$) lead to (2.58). Equation (2.64) can be solved numerically using Euler's method. As an example, we show in figure 2.43 the simulated eye diagrams for Q factors of 38000 (5GHz photon-lifetime bandwidth limited) and 19000 (10GHz photon-lifetime bandwidth limited). The eye diagram is a visual criteria for the quality of an OOK signal, as detailed in subsection 3.2.1.2. The bias voltage is $-2V$ and the ring is modulated with a 10Gbps OOK signal with $2V_{pp}$. Prior to modulation, the electric signal is filtered by a single-pole lowpass filter with 7GHz pole frequency. The ring is assumed to be in critical coupling. Time step is 1/16 of the bit period. The eye-diagram closure due to the photon-lifetime limited bandwidth at Q=38000 can be clearly observed.

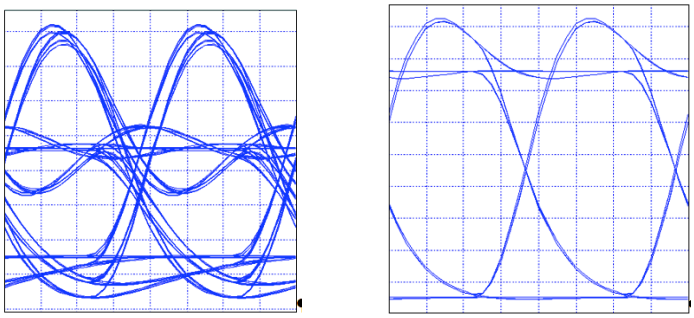

(a) Q=38000 (b) Q=19000

FIGURE 2.43: Simulated eye diagrams with the dynamic model of the ring resonator, for a 10Gbps OOK signal.

This model is used in subsection 5.1.5.2 to evaluate the performance of optical OFDM modulation in a SMF link.

Non-linearity of the Silicon Ring-resonator Modulator E/O Response As a resonator, the silicon ring modulator has inherently non-linear characteristics because of its sharp resonance. A few authors already addressed the non-linearity of silicon ring modulators [206–208], showing that reasonable linearity can be achieved for a given modulation depth in spite of the resonant nature of the ring modulator. In [206], the author assess the linearity of the ring modulator numerically using the dynamic model presented previously, showing a theoretical SFDR of $96dB.Hz^{2/3}$. Gutierrez *et al* [207] propose to a ring modulator coupled to one of the arms of a MZI (structure called ring-assisted MZM). The modulation mechanism is based on the fact that the phase of the optical signal at the output of the modulator is shifted by 2π from one side to the other of the resonance. In this way, the phase modulation is transformed in intensity modulation by the interferometer, which shows to be more linear than the intensity transfer function of the ring modulator itself. An input IP3 of 67dBm is measured in [207, 208], resulting in a SFDR of about $71dB.Hz^{2/3}$. A very interesting result is reported in [209]. The author shows that the main source of non-linearity in a silicon ring modulator is not the modulator itself but the non-linearity of the PN junction. Thus, by optimizing the design of the junction, the linearity of the device can be improved.

2.3 Opto-electrical Converters

The two basic components for O/E converters are PIN and APD photodiodes. They are based on the absorption process. Considering an incident photon in a semiconductor material, if the photon energy $h\nu$ (h - Planck constant, ν - photon frequency) is about the same as the band-gap E_g, an electron from the valence band can absorb the photon energy. The resulting electron-hole pair is then separates and give rise to the electrical current in the photodiode.

The basic structures of the PIN and the APD are shown in figure 2.44. The objective of this part is to discuss the principle of operation and differences between both types of photodiodes. Later, in subsection 3.1.1, direct-detection receivers are detailed.

2.3.1 *p-i-n* Photodiode

As already introduced in subsection 2.2.3.1, the basic structure of a PIN photodiode is basically a PN diode with an intrinsic (undoped) region between the P and N junctions as illustrated in figure 2.44(a). The photodiode works by polarizing it inversely, creating a depletion region where no free carriers exist. In this way, a strong electric field (cf. inset figure 2.44(a)) is created between the P and N regions that opposes the flow of electrons from the n-side to the p-side (and inversely the flow of holes from the p-side to the n-side).

The reason for including an intrinsic (non-doped) zone between the PN-junction is to prioritize the creation of electron-hole pairs rather in the intrinsic region rather than the P or N regions. When an electron-hole pair is created by absorption in the P or N doped zones, the electron (hole) has to diffuse to the intrinsic zone before drifting rapidly to the N (P) zone. As mentioned previously in section 2.2.2.2 for PIN modulators, the diffusion is a quite slow process, the electron (hole) takes $\tau_{tr} = 1ns$ (τ_{tr} - transit time) or longer to diffuse over a distance of about $1\mu m$ [139], while drifting can take about $\tau_{tr} = 10 - 100ps$ over the same distance.

Responsitivity-Bandwidth Trade-off

This is a classical trade-off for photodiodes. If the length L of the photodiode is increased, the responsitivity is also increased because more light is absorbed, while the bandwidth is decreased because electrons and holes will take more time to drift from the intrinsic region to the N and P regions, respectively. This is why materials with higher absorption coefficients perform better. For fixed responsitivity, the length of the device can be decreased as compared with materials

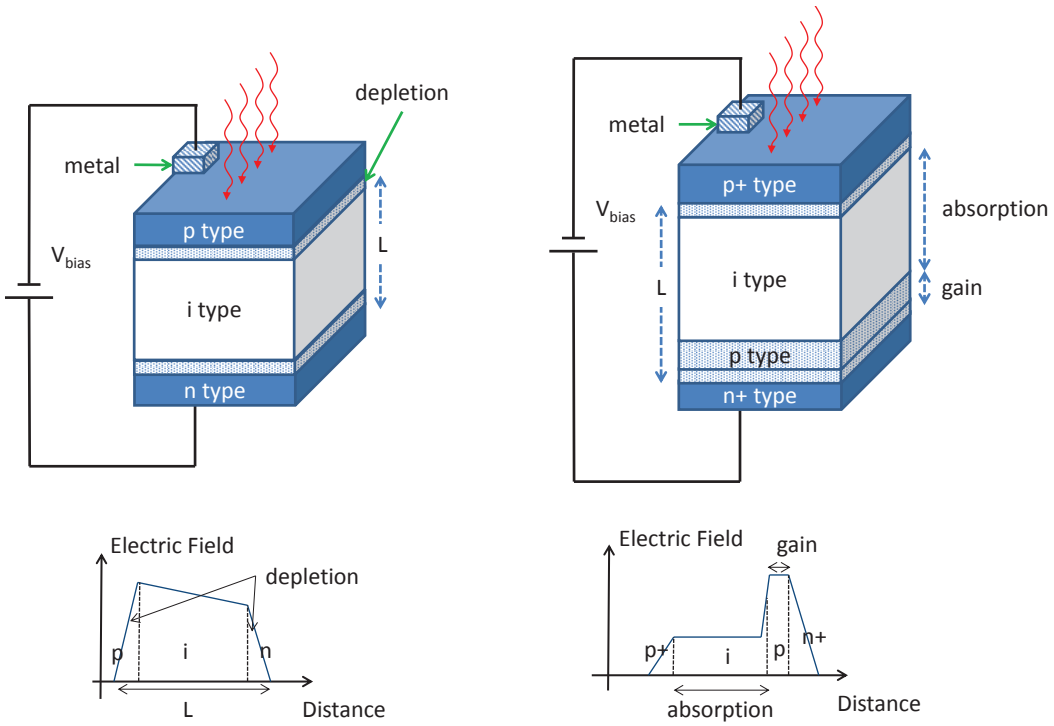

(a) PIN (b) APD

FIGURE 2.44: Basic structures of the two types of photodiodes.

with lower absorption coefficients, and bandwidth is then enhanced. Typical values for the responsitivity in InGaAs/InGaAsP photodiodes ($1.55\mu m$) are about $0.6A/W - 0.9A/W$ while achieving bandwidths of up to 40GHz. They can be operated using bias voltages of about 5-6V.

2.3.2 Avalanche Photodiodes (APD)

APDs can achieve electrical gain through the impact ionization process. The main principle of this process is that an electron with enough kinetic energy (created by a photon by the absorption process) can knock-back another electron within the valence band and promote it to the conduction band, creating an additional electron-hole pair. The process can eventually cascade. When this happens in a region with a very high electric-field, it can result in an avalanche breakdown. Basically, when the photodiode is at the avalanche, a photon creates a single primary electron-hole pair, which, in its turn, creates secondary electron-hole pairs through impact ionization.

Generally, avalanche breakdown destroys regular diodes. This is why in APDs an additional P layer (less doped than the P layer of the classical PIN photodiode) of length d is inserted between the intrinsic and the N region as illustrated in figure 2.44(b). In this way, the electric field in enhanced before the N region favoring the avalanche at lower bias voltages than PIN photodiodes (cf. inset of figure 2.44(b)). We define then the absorption region as the intrinsic zone and the gain region as the P-doped zone between intrinsic and N-doped zones.

The responsitivity in APDs is given by $R_{APD} = M \cdot R_d$, where M is the multiplication factor and R_d is the responsitivity of the absorption region. For typical III/V photodiodes for telecom applications, M can vary from 2 to 100. The intrinsic bandwidth of APDs for $M > 1$ is lower than the bandwidth of PINs simply because the impact ionization process takes an additional time. The transit time related to the impact ionization process is denoted τ_e. The bandwidth decreases with the multiplication factor. A common figure of merit for APDs is the

gain-bandwidth $\Delta f \times M_0$ product. Considering that $\tau_{RC} << \tau_e$, where τ_{RC} is the time-constant associated to the equivalent RC circuit of the photodiode, the gain-bandwidth is given by

$$\Delta f \times M_0 = \frac{1}{2\pi\tau_e} \tag{2.69}$$

where M_0 is the multiplication factor at low frequencies.

2.3.3 Noise Mechanisms

Shot-noise

The shot noise is an intrinsic noise mechanism for photodiodes. It comes from the fact that the electron-hole pairs resulting from absorption of a photon are generated at random times. This creates instantaneous fluctuation in the electrical current generated by a photodiode, even if the received optical power is constant. According to [139], for a PIN photodiode, the shot-noise can be considered as a white Gaussian noise with zero-mean and variance

$$\sigma^2_{s_{PIN}} = 2q \cdot (R_d P_{in} + I_d) \cdot \Delta f \tag{2.70}$$

where Δf is the effective noise bandwidth of the photodiode (considered as the total bandwidth of the photo-receiver), P_{in} is the average received optical power and I_d is the dark current. The dark current is the electrical current generated by a photodiode in the absence of any light. It is mostly originated by thermally generated electron-hole pairs. Hence, the dark current must be as low as possible ($I_d < 10nA$ for PIN photodiodes) in order to minimize shot-noise for a given received optical power.

Shot-noise Enhancement in APDs

As explained previously, APDs generate electrical gain through the avalanche phenomenon. The fact that the gain is generated by secondary electron-hole pairs which are generated at random times, the shot noise power in APDs is enhanced compared to PIN photodiodes. The shot noise enhancement is quantified by the excess noise factor F_A of the APD. The resulting shot noise is

$$\sigma^2_{s_{APD}} = 2qM^2F_A \cdot (R_d P_{in} + I_d) \cdot \Delta f. \tag{2.71}$$

According to [139], for $M = 1$, the noise excess factor is $F_A = 1$ and the APD shot-noise power is equivalent to the PIN shot-noise power.

Thermal Noise

Thermal noise is generated by thermal agitation of the free electrons in the semiconductor. As it is common for any particle, if it is not at the absolute zero temperature, it moves at random directions since the thermal energy is transformed in kinetic energy, which is proportional to the temperature of the particle. The movement of the free electrons due to non-zero temperature generates an electrical current even in the absence of any applied voltage. The thermal noise is also seen as white Gaussian noise with zero-mean with variance

$$\sigma^2_t = \frac{4k_B T \cdot \Delta f}{R_L} \tag{2.72}$$

where k_B is the Boltzmann constant, T is the temperature and R_L is the load resistor after the photodiode. It is important to note that $\sigma^2_{s_{PIN}}$ and $\sigma^2_{s_{APD}}$ depends on the received optical power whereas σ^2_s does not. As a consequence, the performance of the photodiodes is limited by shot noise at high received optical powers while thermal noise dominates for low received

optical powers. This is why APDs perform generally better than PINs at low received optical powers as detailed in subsection 3.1.1.

2.3.4 Silicon Photonics Photodiodes

Silicon photonics photodiodes today can achieve nearly the same performance of commercially available III/V photodiodes. Since silicon itself does not absorb light beyond $1.1\mu m$, hybridization is necessary to develop photodiodes in the telecom wavelengths ($1.3\mu m$ and $1.55\mu m$). Hybrid III/V-on-silicon photodiodes can be fabricated in a similar way that of hybrid lasers using the wafer bonding technique [210]. The hybrid photodiode reported in [210] has a 0.45A/W responsitivity and 33GHz bandwidth, reporting a dark current of 1.6nA at -4V.

Another very interesting and effective approach is the monolithically grown Germaniun on SOI [107, 211, 212]. Using this approach, PIN [107] photodiodes have been demonstrated, with more than 40GHz bandwidth and a responsitivity of 1A/W [211]. A 40Gbps zero-bias PIN Germanium photodiode was demonstrated in [107], in order to minimize dark current (but not communicated by the authors). In general, the dark currents of the Ge photodiodes are much higher than for III/V PIN photodiodes for the same responsitivity [139]. Nevertheless, the surface areas of the Ge photodiodes in guided configuration are small ($5 - 30\mu m^2$) [107, 211]. The noise figures are then often limited by the electronics of the TIAs and not by the dark currents of the photodiodes themselves, as explained in subsection 3.1.1.

Intel demonstrated high-performance Germanium APDs [212, 213]. In [213], the author demonstrates a gain-product bandwidth of 340GHz (for 10 GHz bandwidth), with an excess noise factor of about 2.5 at $M = 10$. Reported dark current was about $5\mu A$ for a device with $30\mu m$ diameter and $M = 8$, but it did not limited the performance of the device. In 2011, APDs with up to 29.5GHz bandwidth, 0.81A/W responsitivity and about $1\mu A$ of dark current (at 90% of breakdown voltage, for M between 5 and 10) were demonstrated [212]. The reported sensitivity is - 30.4dBm (10Gbps, BER of 10^{-12}), which is better than than state-of-the-art InP-based photodiodes, according to the author [212]. The operation of these components was shown at $1.3\mu m$, but they can equally perform at $1.55\mu m$ [212].

2.4 Summary of the Chapter

The basic models for the building blocks of an optical communication system were presented in this chapter. For each building block, a review of the basic concepts is given. It concludes with the transfer function and eventually noise associated with each element based on the physical effects considered. An experimental validation with silicon photonics modulators was presented, concluding that the developed model is a realistic representation of the behavior of these components.

It is important to highlight that this chapter is not only an overview of the basic components of an optical communication system, but also a reference for following of this thesis. We describe the physical effects and approximations taken into account for developing our simulation platform, which is based on lumped element models. This study is important to understand the limitations imposed by each building block of the optical system and to provide guidelines for optimizing the transmission.

Chapitre 3

Modulation Formats and Transmission Techniques

In the last chapter, the different building blocks for an optical transmission system were studied in details, as a reference for the development of the simulation platform. This chapter is intended to give an overview of the different transmission techniques and modulation formats that can be applied to optical communications.

Prior to describing the single-carrier and multi-carrier transmission techniques, direct-detection and coherent receivers are presented. The second part is dedicated to single-carrier optical modulation schemes. It is further separated in two subsections : OOK and high-order modulation formats. In each part, the modulator/demodulator is described in detail as well as parameters for analyzing the signal quality in both cases. The final part concerns OFDM modulation. After a detailed description, the main features and impairments of this type of modulation are discussed. Then, the channel model for the IM/DD and SSB-based optical OFDM are reviewed. After this, a review of the state-of-the-art components for the implementation of the OFDM modem - real-time FPGA demonstrations, ASIC implementation and DACs/ADCs - is presented.

3.1 Optical Receivers

3.1.1 Direct-Detection Receiver

A schematic of a direct detection receiver is shown in figure 3.1. It can be used when the data is coded only in the intensity of the optical carrier.

Two options for the pre-amplifier can be considered as shown in the inset of figure 3.1. One can use a high-impedance front-end - where a high load resistor R_L is inserted in parallel with the photodiode. This scheme has two main advantages 1) Increased voltage provided at the amplifier input and 2) minimization of thermal noise according to (2.72) (thermal noise is inversely proportional to R_L). However, the high impedance increases the RC time-constant of the circuit, thus limiting the bandwidth of the photo-receiver making it unpractical for high-speed optical communications ($> 1Gbps$). In order to increase the bandwidth of the photo-receiver, a TIA can be used (cf. inset figure 3.1). It converts the electrical current to voltage and amplifies the signal with gain G at the same time. The negative feedback reduces the input impedance by a factor of G.

Furthermore, an amplifier with Automatic Gain Control (AGC) is used to adjust the input voltage of the demodulator circuit to its optimum value. Eventually, a low-pass filter can be added before the demodulator circuit. After the direct detection receiver, an electric demodulator is used to convert the analog data to digital data.

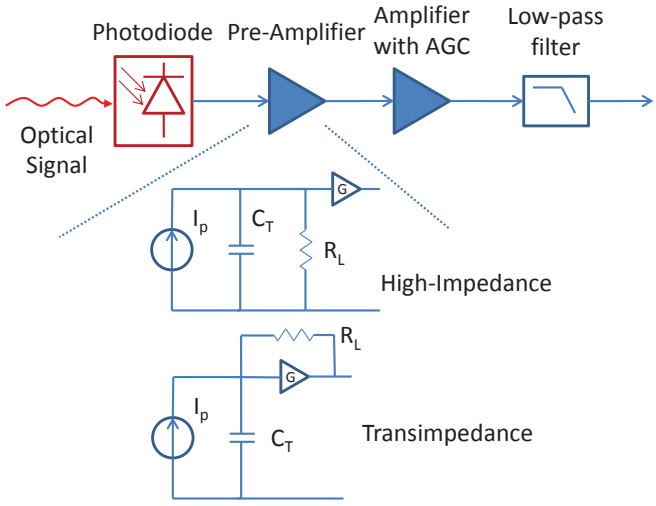

FIGURE 3.1: Typical direct-detection receiver architecture. AGC : Automatic Gain Control.

Photo-receiver Noise

The theoretical SNR of the photo-receiver as function of the received optical power is disucussed in the following. Taking into account the noise from the TIA, a noise figure N_f term is added to the thermal noise variance (2.72). It represents an enhancement of the thermal noise which results in a reduction of the SNR in the amplifier's output. The resulting thermal noise variance is written as

$$\sigma_t^2 = \frac{4k_B T N_f \cdot \Delta f}{R_L}. \tag{3.1}$$

Then, for a PIN photodiode, and considering the contribution of both thermal and shot noise, the SNR is given by

$$SNR_{PIN} = \frac{R_d^2 P_{in}^2}{\sigma_{s_{PIN}}^2 + \sigma_t^2} = \frac{R_d^2 P_{in}^2}{2q \cdot (R_d P_{in} + I_d) \cdot \Delta f + 4k_B T N_f \cdot \Delta f / R_L}. \tag{3.2}$$

For an APD, the SNR is given by

$$SNR_{APD} = \frac{M^2 R_d^2 P_{in}^2}{\sigma_{s_{APD}}^2 + \sigma_t^2} = \frac{M^2 R_d^2 P_{in}^2}{2qM^2 F_A \cdot (R_d P_{in} + I_d) \cdot \Delta f + (4k_B T N_f \cdot \Delta f)/R_L}. \tag{3.3}$$

It is useful to define a quantity called Noise Equivalent Power (NEP), which is commonly used to quantify the noise performance of a photoreceiver. It is the minimum received optical power, normalized by the bandwidth, required to achieve a $SNR = 1$. It is given by

$$NEP = \frac{P_{in}}{\sqrt{\Delta f}} = \sqrt{\frac{4k_B T N_f}{R_L R_d^2}} \tag{3.4}$$

Typical values of NEP are in the range of $1 - 40pW/\sqrt{Hz}$. The NEP is sometimes given in $pA/\sqrt{Hz}$, in this case, it is multiplied by R_d. An example of the SNR versus the received optical power is plotted in figure 3.2 with the following parameters (using the notation defined in subsection 2.3) : responsitivity $R_d = 1A/W$, temperature T=300K, dark current $I_d = 1nA$, noise figure $N_f = 4$, bandwidth $\Delta f = 10GHz$, charge resistance $R_L = 1k\Omega$ and $k_A = 0.1$. The k_A is a physical parameter of the APD, which is used to calculate the excess noise factor F_A as explained in [139]. The resulting excess noise factor is $F_A = 2.12$ for $M = 5$. The resulting NEP

is $8pW/\sqrt{Hz}$.

In figure 3.2, it is possible to observe the contributions of the shot and thermal noise in the total SNR for the cases, PIN and APD with $M = 5$. At low received optical powers, the dominating noise source is the thermal noise, whereas shot noise dominates at received optical powers above a certain level. Considering the shot noise only, one can observe the shot noise enhancement in the APD as described in section 2.3.3, decreasing the output SNR by a factor $20\log_{10} F_A$ as compared to the PIN. On the other hand, the output SNR considering thermal noise only is enhanced by a factor $20\log_{10} M$ in the APD case as compared to the PIN. The total SNR at low received optical powers is better at the APDs, since thermal noise dominates.

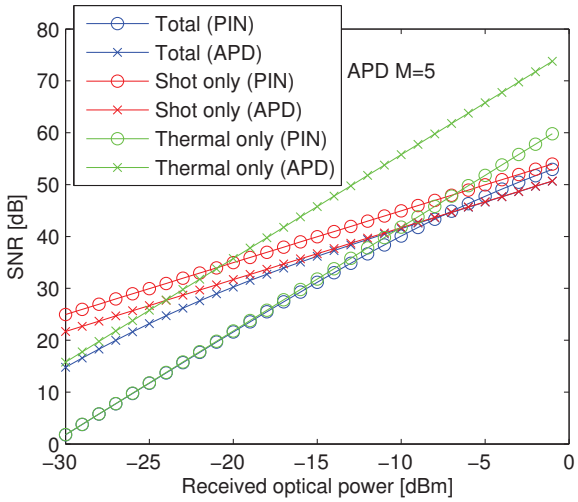

FIGURE 3.2: SNR as a function of the received optical power for PINs and APDs.

3.1.2 Coherent-Detection Receiver

Contrary to direct-detection receivers, the purpose of a coherent-detection receiver is to recover both the amplitude and phase envelope of the optical carrier. Additionally, it can recover both the states of polarization X and Y of the optical carrier. A representative diagram of a typical coherent receiver is shown in figure 3.3.

The received optical signal is divided in two branches of orthogonal states of polarization. Then, each polarization is recovered separately. The optical signal is further divided in two branches to be combined with the LO (the original LO signal in one part and 90°-phase shifted LO signal in the other part). A pair of photodiodes is used to convert each part to the electrical domain, and they are further subtracted to form the in-phase and quadrature components of the output electrical signal.

The mathematical development of a coherent receiver can be found in [160]. Denoting the received optical signal as $r(t) = E_{opt_{FM}}$ from (2.20) and the optical local oscillator as $\sqrt{P_{LO}} \cdot \exp(j\omega_{LO}t + \phi_{LO})$, the received electrical signals $x_I(t)$ and $x_Q(t)$ in a single polarization are proportional to

$$x_I(t) \propto -u_I(t) \cdot \Re\left\{\sqrt{P_{LO}/2} \cdot \exp(j((\omega_{opt} - \omega_{LO})t + \phi_{LO}))\right\} \tag{3.5}$$

$$x_Q(t) \propto -u_Q(t) \cdot \Im\left\{\sqrt{P_{LO}/2} \cdot \exp(j((\omega_{opt} - \omega_{LO})t + \phi_{LO}))\right\}. \tag{3.6}$$

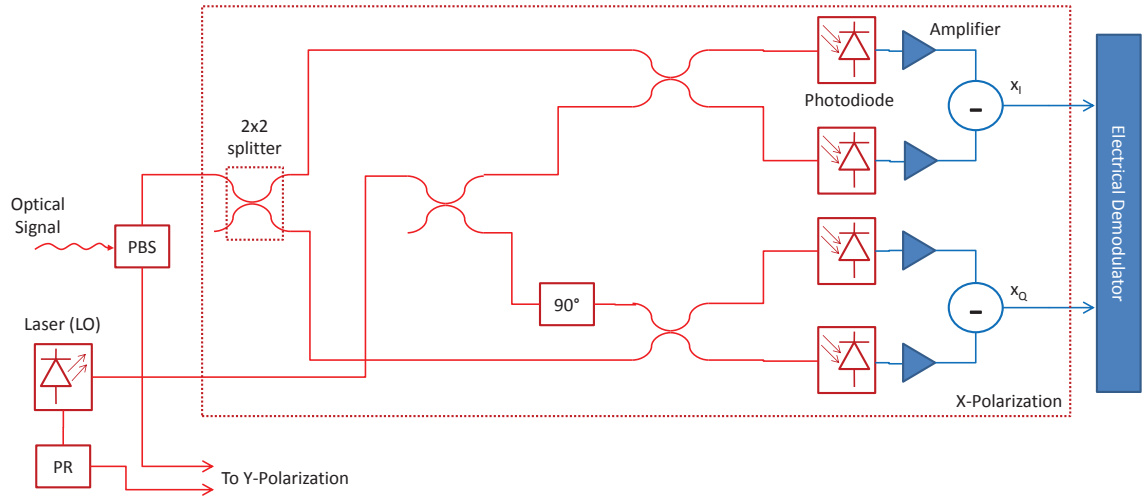

FIGURE 3.3: Schematic of a coherent optical receiver. PBS : Polarization Beam Splitter ; PR : Polarization Rotator.

In this way, if $\omega_{opt} = \omega_{LO}$, the electrical field of the received signal is proportional to the electrical field $u(t)$ of the sent signal, rotated by a factor ϕ_{LO}.

Coherent receivers have several advantages over direct-detection receivers. In general, they have better sensitivity for the same modulation format applied. In [80], the author demonstrates a 4-dB increase in the OOK receiver sensitivity (1.25Gbps, BER=10^{-3}) as compared to the direct-detection receiver. In addition, because the optical field of the optical carrier is linearly converted to electrical field, the linear transmission impairments such as chromatic dispersion and PMD can be easily corrected. In general, coherent systems employ DSPs to correct these impairments. However, it requires additional components including an optical LO at the receiver, with adjustable wavelength and narrow linewidth to minimize phase-noise at the receiver. This makes the coherent receiver very costly and, for the moment, only suitable for long-haul optical communications.

3.2 Single-carrier

3.2.1 On-Off Keying (OOK) - Intensity Modulation

The simplest modulation format for optical communications is called NRZ-OOK. In the NRZ modulation format, the signal does not return to zero between two consecutive high levels. An example of time and frequency-domain representation of an electric NRZ signal is shown in figure 3.4. The bandwidth of a NRZ-OOK signal with data-rate $B = 1/T_s$ (T_s is the duration of 1 bit) can be roughly approximated by B as shown in figure 3.4. In this modulation format, each symbol represents only one bit and the symbol-rate is equal to the bit-rate.

Then, the binary information is coded on the optical intensity of the optical carrier. The bit "1" is represented by a high level of optical power and the bit "0" is represented by a low level of optical power (ideally zero) : this is the definition of OOK modulation. The envelope of the optical signal $A(t)$ (cf. figure 3.5) is then an exact copy of the electrical modulation signal - the bit "1" is represented by a high level of voltage V_{high} and the bit "0" is represented by a low level of voltage V_{low}. In figure 3.5, the evolution in time of an optical signal with OOK modulation is represented, where the frequency of the optical carrier ($f_{opt} \approx 193THz$) being much larger as compared to the frequency of the modulating signal ($\approx 20GHz$). The analytical description of the optical field modulated in intensity by an electrical signal $u(t)$ is given in (2.21).

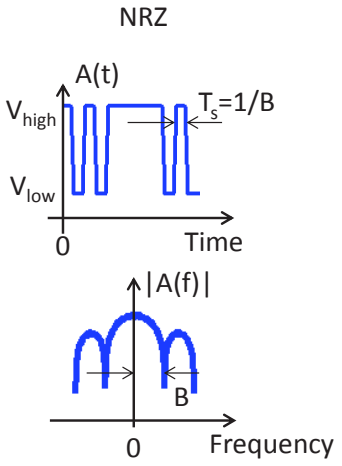

FIGURE 3.4: Time and frequency domain representations of an electrical OOK signal.

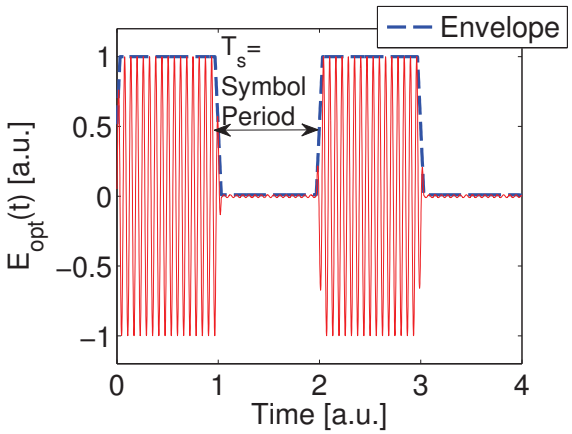

FIGURE 3.5: Time-domain representation of an OOK optical signal.

As a consequence of the intensity modulation of the optical carrier, the output optical signal is said to be DSB because it has spectral components in both sides of the optical carrier, where one of the sidebands is the complex conjugate of the other. Optical SSB modulation was first proposed to single-carrier modulation with direct-detection receivers in 1993 [214], using an optical filter to attenuate one of the sidebands. The benefits of the optical SSB modulation are twofold : 1) It reduces the chromatic dispersion effects because the total optical bandwidth is reduced twice and 2) as explained in [215], the optical SSB modulation allows to compensate chromatic dispersion in the electrical domain, similar to the coherent receiver as discussed in subsection 3.1.2.

3.2.1.1 OOK Modem

Figure 3.6 shows a schematic of an OOK electrical modem. In the transmitter part, it is as simple as a low-pass filter to attenuate high-frequency components of the signal and a driver (amplifier) to adjust the peak-to-peak modulation voltage of the optical transmitter to its optimum value. At the receiver, a direct-detection receiver (detailed in the subsection 3.1.1) performs the O/E conversion. The demodulator is constituted by a decision circuit fed by a clock recovery module. The decision circuit defines the optimum sampling instant and decides whether the received bit is a 1 or a 0 according to the optimum threshold value.

3.2.1.2 Modes of representation and Quality criteria

A commonly used method to analyze the quality of a OOK signal is the eye-diagram. It is simply a superimposition of the received symbols in time over a window of normally a few symbol periods. In this way, the eye diagram gives an overview of the signal quality. An example of eye diagram of an OOK signal is represented in figure 3.7. It is quantified by a measure of the eye opening, which increases in width and height as the signal quality improves.

A common parameter to quantify the quality of an OOK signal is the Q parameter. As illustrated in figure 3.7, the distribution of the "1" and "0" levels at the sampling instant can be approximated by a Gaussian random variable if the dominating noise mechanism is photoreceiver noise rather than Amplified Spontaneous Noise (ASE) noise (from optical amplifier). The random variables have mean I_1, I_0 and standard deviation σ_1, σ_0 for the "1" and "0" levels, respectively. Then, the Q-parameter is given by

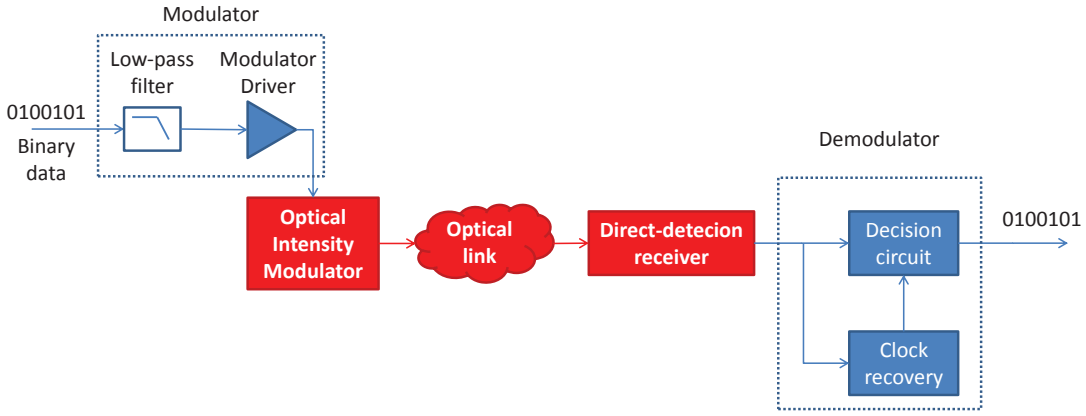

FIGURE 3.6: Typical electrical modem for OOK modulation.

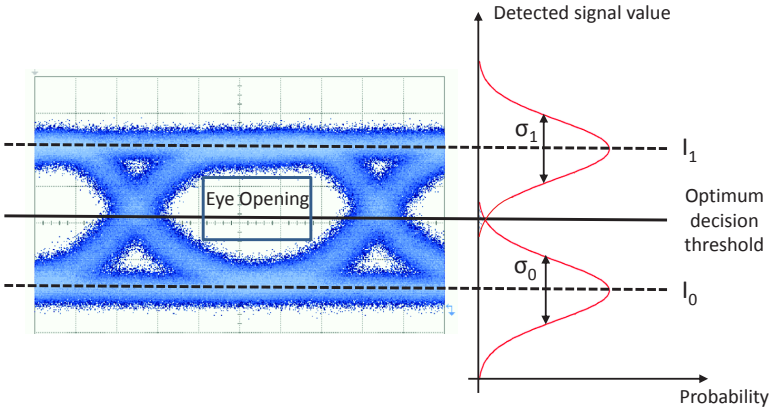

FIGURE 3.7: Left : Typical eye diagram representation of an OOK signal. Right : "1" and "0" levels distribution.

$$Q = \frac{I_1 - I_0}{\sigma_1 - \sigma_0}. \tag{3.7}$$

The BER (ratio between the number of bits detected erroneously and the total number of bits transmitted) is written as a function of the Q parameter as

$$BER = \frac{1}{2} \cdot erfc\left[\frac{Q}{\sqrt{2}}\right] \approx \frac{1}{\sqrt{2\pi}} \cdot \frac{\exp(-Q^2/2)}{Q} \tag{3.8}$$

where $erfc[x]$ represents the complementary error function.

A source of receiver sensitivity penalty is the finite extinction ratio of the optical OOK signal as mentioned in subsection 2.2.3. The extinction ratio is defined in (2.46). From the Q-parameter definition in (3.7), it can be observed that if some power is carrier by the off-state ($I_0 > 0$), the Q-parameter is degraded.

According to [139], the sensitivity power penalty δ_{ex} in dB due to finite extinction ratio is given by

$$\delta_{er}[dB] = \log_{10}\left(\frac{1+ER}{1-ER}\right). \tag{3.9}$$

Note that the ER definition of (2.46) is given in dB while in (3.9), the ER is in linear scale. On one side, it is important to fix the extinction ratio as close to zero as possible in order to minimize

receiver sensitivity penalty. However, a high extinction ratio may introduce high insertion losses depending on the efficiency of the modulator. This is a trade-off between extinction ratio and insertion losses in an optical transmitter.

Measuring BER

The BER can be estimated in two ways using Monte-Carlo approach. The straightforward method is simply to generate a stream of N_{bits} and to count the number of bit errors in the receiver. As a rule of thumb, and demonstrated in [216], the precision ϵ (the estimator standard deviation, normalized by the estimator mean) in the BER estimator is given by

$$\epsilon = \sqrt{\frac{1}{N_{bits} \cdot P_b}} \tag{3.10}$$

where P_b is the value of the BER estimated. For example, in order to have a $\epsilon = 2.5\%$ precision, it is necessary to observe at least 1600 errors. For a $BER = 2.2 \times 10^{-3}$, this results in 7.2×10^5 bits to be generated and analyzed. A $\epsilon = 2.5\%$ precision in the estimator result in a 95% confidence interval of 10% of the BER [217] (assuming that the BER estimator follows a Gaussian distribution), which is an order of magnitude lower than the estimated value, showing an accurate estimation.

Direct count of the bit errors is a practical method for estimating the BER for values higher than $BER > 10^{-3}$, or in real-time experiments. To give an order of magnitude, if a BER of 10^{-12} should be measured at 10Gbps with a precision of $\epsilon = 10\%$ ($N_{bits} = 10^{14}$), a measure period of 2.8 hours is needed, which is still feasible. However, if this number of bits is to be generated in simulation or off-line experiments, this would require a large memory of 12.5TB.

A second method consists in estimating the Q-factor and extracting the BER from the Q-factor. The variance of the estimation is evidently related to the number of bits generated and analyzed. From [217], the author shows that Q-factor uncertainty range (considering the 95% confidence interval) of the Q-factor estimator ΔQ in dB as a function of the number of bits N_{bits} simulated is

$$\Delta Q[dB] = 20 \log_{10} \left(\frac{1 + \sqrt{2/N_{bits}}}{1 - \sqrt{2/N_{bits}}} \right). \tag{3.11}$$

The 95% confidence interval means that the estimate has 95% chance of falling in this interval. Equation (3.11) is true as long as the predominant noise of the signal after the photodiode is Gaussian, which means that the SNR is limited by noise from the receiver rather than ASE noise [217]. As an example, $\Delta Q = 0.24dB$ considering $N_{bits} = 10^4$, which represents a variation of more or less a decade around a $BER = 10^{-12}$.

3.2.2 High-order modulation formats

While OOK modulation is very simple to implement, it has very low spectral efficiency. The spectral efficiency is defined as the ratio between the data-rate carried by a signal and the total bandwidth occupied by it. It is represented in bps/Hz. The spectral efficiency of an OOK signal is roughly 1bps/Hz. It may be increased by using high-order modulation formats where each symbol represents several bits. For that purpose, one can use intensity modulation, amplitude modulation, phase modulation or amplitude and phase modulation.

A modulation format is defined by an alphabet of symbols and the set of bits each symbol represents. The total number of symbols M of the alphabet defines the number of bits b carried by symbol $b = log_2(M)$. For instance, an OOK modulation format has an alphabet of $M = 2$ symbols, hence each symbol carries $b = 1$ bit. If only the intensity of the optical carrier is modulated, the alphabet symbols are necessarily real and positive (named Pulse Amplitude

Modulation (PAM)). If the amplitude and phase of the optical carrier are modulated (using a MZM, for instance), the symbols are, in general, complex. In a general form, modulation formats that use only phase modulation are called M-Phase-Shift Keying (PSK), while amplitude and phase modulation formats are called M-QAM.

3.2.2.1 Modem for high-order modulation formats

There are many different methods to generate high-order optical modulation formats, depending if the optical signal is modulated in amplitude only, phase only or both, as explained in [160]. A general method is to use an optical IQ modulator, which was introduced in subsection 2.2.2.2. The transfer function of the optical IQ modulator is given in (2.42). It allows a linear conversion of the electrical field of the modulating signal $u(t) = u_I(t) + ju_Q(t)$ to the optical field of the optical carrier. Figure 3.8 illustrates a general method to generate single-carrier optical M-QAM signals. It uses an optical I/Q modulator driven by two independent electrical signals, corresponding to the real (in-phase) and imaginary (quadrature) components.

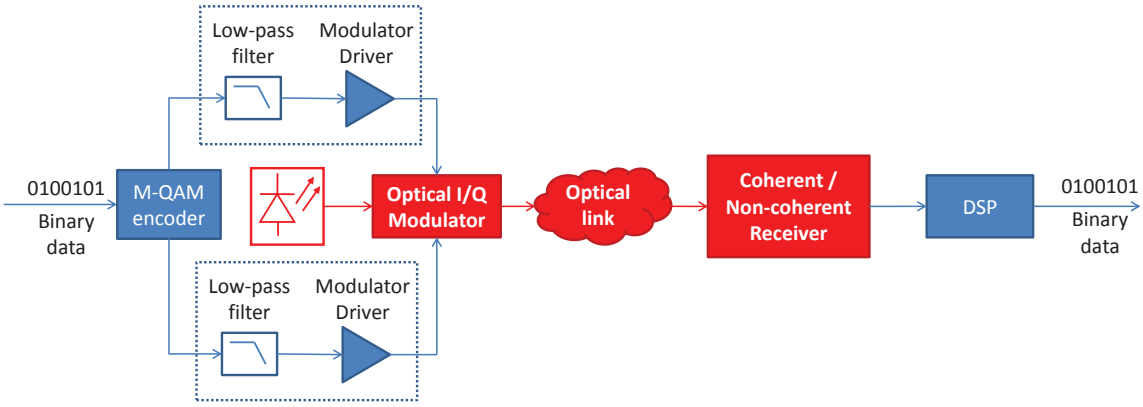

FIGURE 3.8: Typical scheme of an optical M-QAM transmission.

At the receiver, the high-order modulation optical signal can be detected either by a non-coherent receiver or a coherent receiver. In order to being detected by a non-coherent receiver, particular techniques are employed at the transmitter such as differential modulation formats as already mentioned in subsection 1.3.2.

For example, if the optical signal is phase-modulated with BPSK ($M = 2$), the symbols of the alphabet are 1 and -1, corresponding to the phase states 0 and π of the optical carrier. If differential encoding is applied, the bit-stream passes through a differential encoder prior to modulation. Denoting b_k the input bit to the differential encoder at the k^{th} time-slot, the encoder output bit is defined by $e_k = e_{k-1} \oplus b_k$, where $\oplus$ is the XOR operation. For example, a bit sequence 101000101 is encoded as 110000110 assuming $e_{-1} = 0$. The output of the modulator is then $[-1, -1, 1, 1, 1, 1, -1, -1, 1]$. A component commonly used for demodulation is the Delay Interferometer (DI), in which the demodulated optical signal $d(t)$ is a sum of the received symbol $r(t)$ at two different time instants $d(t) = r(t) + r(t + \tau)$. If the delay τ is properly adjusted as the symbol period, the resulting output symbol is 1 (constructively interference) if two consecutive symbols have same state of phase, or 0 otherwise (destructively interference). In this way, the phase modulation is converted to intensity modulation, and the original bit-stream can be recovered thanks to the differential encoding. By assembling several DIs, higher-order modulation formats can be used, such as star-16-QAM, as illustrated in figure 1.13.

A general method to detect any amplitude and phase modulation format is the coherent receiver, which is detailed in subsection 3.1.2. After the coherent receiver, a DSP is generally

employed to correct impairments (chromatic dispersion, frequency/phase offset for instance) and demodulate the M-QAM signal.

3.2.2.2 Constellation Diagram

In order to represent an arbitrary modulation format, a common form is the constellation diagram. It plots every symbol in the alphabet in a complex-plan. Examples of constellation diagrams are shown in figure 3.9. The OOK constellation is added for comparison purposes. Particular forms of M-QAM are called BPSK ($M = 2$) and QPSK ($M = 4$), since only the phase is modulated. In figure 3.9(a)-(c) examples of coding of the constellations is illustrated, in top of each symbol it is shown the set of bits it represents. The coding of M-QAM constellations used in this work is detailed in appendix C.2.

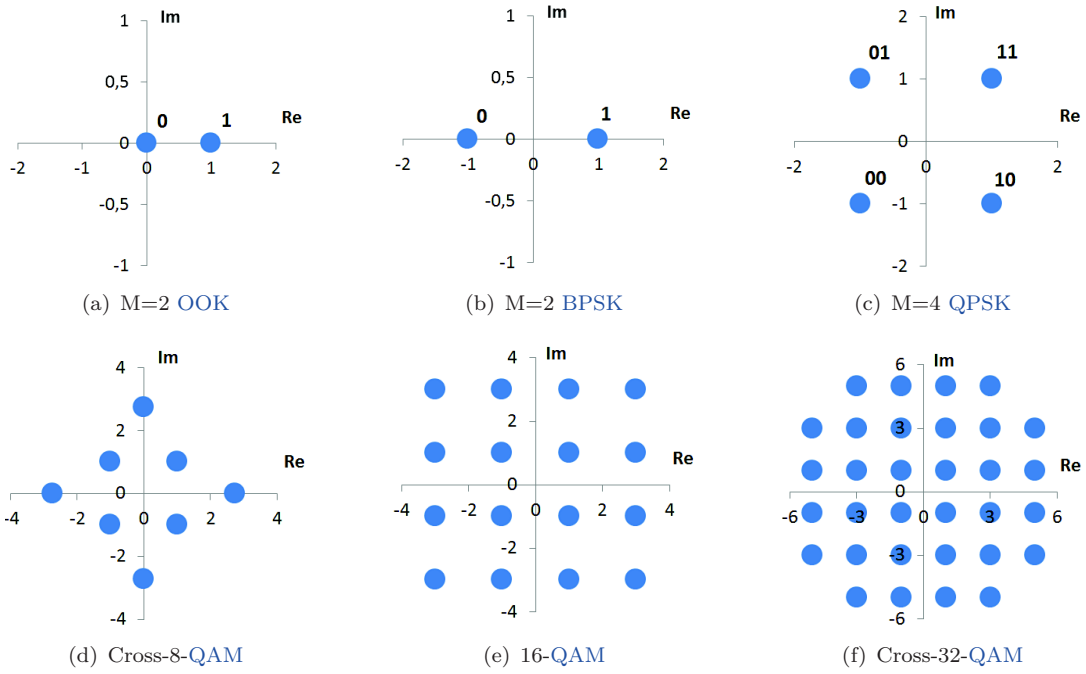

(a) M=2 OOK (b) M=2 BPSK (c) M=4 QPSK

(d) Cross-8-QAM (e) 16-QAM (f) Cross-32-QAM

FIGURE 3.9: Examples of constellation diagrams.

For constellations where each symbol represents an even number of bits, the optimum arrangement is straightforward - the same number of bits is allocated in each one of the dimensions (in-phase/quadrature). When the number of bits per symbol b is odd, the alphabet can have particular forms. First, rectangular constellations were proposed, were one of the dimensions carried an additional bit compared to the other one. However, Smith *et al.* [218] proposed a new arrangement called cross-QAM constellations concerning odd-bit QAM constellation with $M \geq 32$. An example is shown in figure 3.9(f) for the cross 32-QAM constellation. This type of constellation performs better in Additive White Gaussian Noise (AWGN) channel (less SNR is required to achieve a given BER) because the mean energy of the constellation is lower than the rectangular one [218]. For the 8-QAM, the optimum arrangement is shown in figure 3.9(d), which was first proposed in [219]. (it is also called 4-4-QAM). The "cross" notation will be dropped and for an arbitrary modulation M-QAM with $b = log_2(M)$ odd, a cross arrangement is assumed.

3.2.2.3 Error Vector Magnitude

An example of a received 16-QAM symbol stream with noise in a constellation diagram is shown in figure 3.10. A common parameter to quantify the quality of a received symbol for M-QAM is the Error Vector Magnitude (EVM). It is defined as the mean magnitude of the Cartesian distance between the ideal symbol and the received symbols as illustrated in figure 3.11. The RMS of the EVM is formally defined by

$$EVM_{RMS} = \sqrt{\frac{1/T_s \cdot \sum_{n=1}^{T_s} |S_n - S_{0,n}|^2}{1/T_s \cdot \sum_{m=1}^{T_s} |S_{0,m}|^2}} \tag{3.12}$$

where T_s is the total number of transmitted symbols, S_n is the n^{th} received symbol, $S_{0,n}$ is the n^{th} sent symbol. Then, according to [220], the SNR can be approximated with the relation

$$SNR \approx \frac{1}{EVM_{RMS}^2}. \tag{3.13}$$

Then, the theoretical BER can be extracted from the SNR. This is shown in appendix C.2 for any arbitrary constellation.

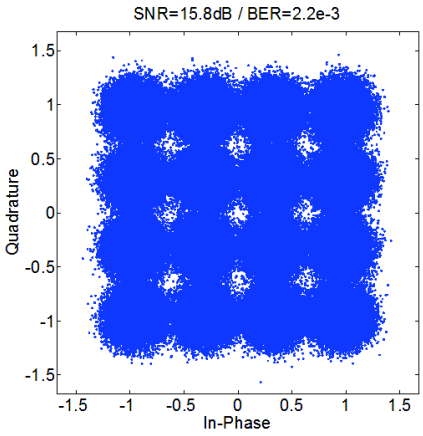

FIGURE 3.10: Example of received 16-QAM constellation with noise.

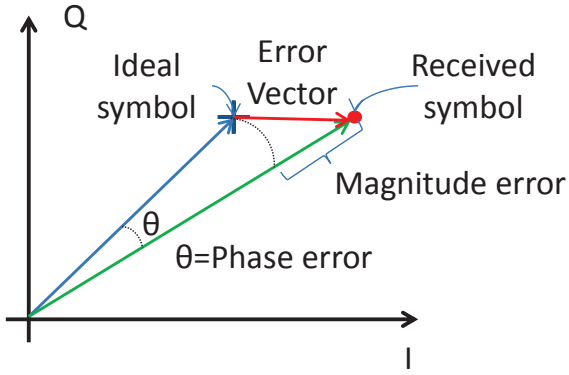

FIGURE 3.11: Representation of the Error Vector Magnitude.

Precision of the EVM (SNR) Estimator

It is important to define the number of symbols required to accurately estimate the EVM (or equivalently the SNR) of a given subcarrier. The received symbol r from an arbitrary subcarrier is denoted by $r = x + n$ where x is the sent symbol and n is a random variable with zero mean and variance σ_n^2, with Gaussian distribution. For simplicity, we assume a normalized expected value of x such that $E[|x|^2] = 1$. In this way, the variance of r is equal to σ_n^2. In this problem, the variable we want to estimate is σ_n^2, which gives directly the squared value of the EVM. Let us denote $\widehat{\sigma_n^2}$ the estimated value of σ_n^2. From the estimation theory, because the quantity we want to estimate is the variance of a random variable, the variance of the estimator $\widehat{\sigma_n^2}$ has chi-squared distribution (χ^2). Considering an average over N_{symb} symbols, with $N_{symb} > 100$, the variance of $\widehat{\sigma_n^2}$ is given by

$$Var\left[\widehat{\sigma_n^2}\right] = E\left[\left|\widehat{\sigma_n^2}\right|^2\right] = \frac{2\sigma_n^4}{N_{symb} - 1} \approx \frac{2\sigma_n^4}{N_{symb}} \tag{3.14}$$

where $Var[x]$ is the variance of the random x variable. For large N_{symb}, the chi-square distribution can be approximated by a Gaussian distribution with same mean and variance. In this way, a rule of thumb for the 95% confidence interval for the $\widehat{\sigma_n^2}$ estimator is given by [217]

$$\left[E\left[\widehat{\sigma_n^2}\right] - 2Dev\left[\widehat{\sigma_n^2}\right]; E\left[\widehat{\sigma_n^2}\right] + 2Dev\left[\widehat{\sigma_n^2}\right]\right] = \sigma_n^2 \cdot \left[1 + 2\sqrt{2/N_{symb}}; 1 - 2\sqrt{2/N_{symb}}\right] \quad (3.15)$$

where $Var[x]$ is the standard deviation of the random x variable. The SNR uncertainty range in dB is given by

$$\Delta SNR[dB] = 10\log_{10}\left(\frac{1 + 2\sqrt{2/N_{symb}}}{1 - 2\sqrt{2/N_{symb}}}\right). \quad (3.16)$$

As an order of magnitude, in this work, the minimum number of symbols used in one simulation run is 500. Considering 127 data subcarriers, a total of 63500 complex symbols are analyzed per acquisition, resulting in an uncertainty range of lower than 0.1dB in the SNR estimator. For a target BER of 2.2×10^{-3}, the BER uncertainty in this case is lower than 10^{-4}, which is more than an order of magnitude below the target BER.

In the experiment, since the number of bits per subcarrier is calculated based on the SNR of a single subcarrier, the SNR uncertainty of a single subcarrier should be evaluated. Considering 4000 OFDM symbols in the experiment, it is given by $\Delta SNR = 0.38dB$. The impact of the SNR uncertainty on the calculation of the achievable bit-rate for an OFDM signal with bit and power loading is studied a few experiments in chapters 4 and 5.

3.3 Multi-carrier OFDM

In a single-carrier transmission with a symbol-rate of B bauds, the duration of 1 symbol is $1/B$ second - it is inversely proportional to the symbol-rate. As explained in subsection 2.1.2, the transmission of a square-shaped-pulse over the optical fiber causes the pulse to broaden, which imposes a limitation in the [bandwidth × reach] product. It is becoming a bottleneck for next-generation optical access networks. An alternative to overcome the chromatic dispersion limitation is to divide the serial symbol-stream into several parallel channels multiplexed in frequency with lower symbol-rate each. This is the principle of the multi-carrier modulation, which is discussed throughout this section.

A classical electrical OFDM transceiver is shown in figure 3.12. The transmitter is made up with a DSP to generate the baseband OFDM signal (which is referred as the OFDM modulator), a DAC to convert the signal from the digital to the analog domain and a RF front-end to up-convert the OFDM signal from baseband to an intermediate frequency. Symmetrically the receiver is formed by a RF front end to convert the pass-band signal down to baseband, a DAC and a DSP to demodulate the signal.

3.3.1 OFDM Principles

3.3.1.1 From FDM to OFDM - Spectral Efficiency

In order to increase robustness against time-dispersive channels, a technique called FDM was proposed in the mid-50s. The idea was to divide the data stream carried by a single-carrier into N parallel data streams, each having a lower data-rate, and each being carried by N

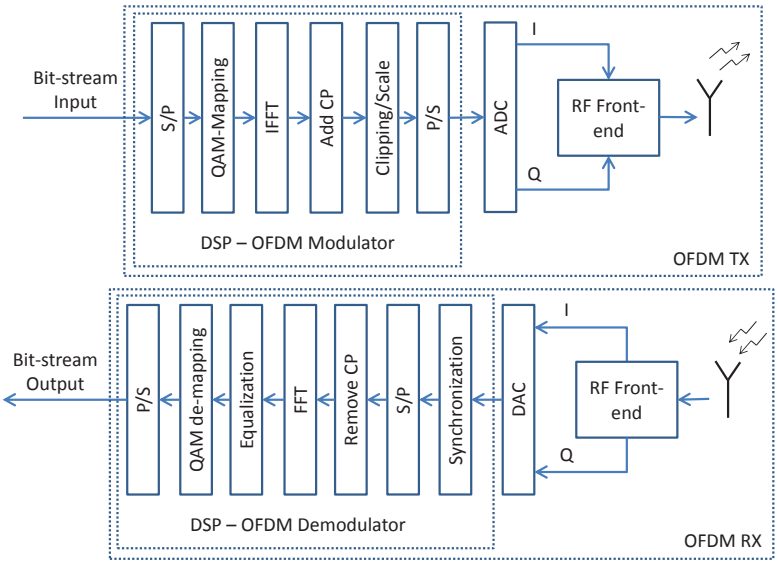

FIGURE 3.12: General overview of an OFDM transceiver. S/P : Serial-to-Parallel ; CP : Cyclic Prefix ; P/S : Parallel-to-Serial.

different subcarriers with different frequencies (cf. figure 3.13). For instance, if N subcarriers bear N signals with symbol-rate B/N bauds instead of one single carrier bearing a signal of B bauds, the signal is naturally more robust against dispersive channels because of the lower bandwidth per subcarrier. The symbol period per subcarrier is then given by $T = N/B$. The FDM signal in the time domain in its analytical form can be expressed as

$$x_{FDM}(t) = \sum_{k=1}^{N} X_k(t) \cdot \exp\left(j2\pi k\Delta f t\right) \tag{3.17}$$

where $X_k(t)$ is the signal modulating the k^{th} subcarrier and $\Delta f = f_k - f_{k-1}$ is the frequency spacing between two adjacent subcarriers. In figure 3.13, $f_k = k\Delta f$. Generally, $X_k(t)$ is a complex signal from a high-order (M-QAM) constellation.

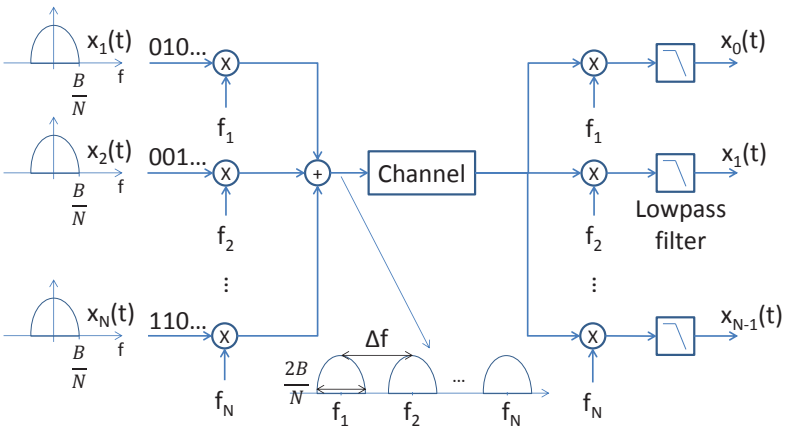

FIGURE 3.13: Classical FDM modulation and demodulation.

In classical FDM schemes, there is a frequency guard-band between each two adjacent subcarriers so that their carried signal do not overlap. In other words, assuming that each subcarrier is band-limited by B/N, the subcarrier spacing should be greater than twice the bandwidth of each subcarrier ($\Delta f \geq 2B/N$) as indicated in the inset of figure 3.13. The drawback of this

scheme is that it is less spectrally efficient than a single carrier transmission because of this frequency guard-band.

The concept of OFDM was proposed by Chang in 1966 [221]. He showed that, even if two adjacent subcarrier-signals overlap, the orthogonality condition can still be respected, meaning that the signal modulating them can be demodulated without any crosstalk. The orthogonality condition specify that two arbitrary and periodic signals $x(t)$ and $y(t)$ with period T are orthogonal if the following condition is respected

$$\langle x(t)|y(t)\rangle = \int_0^T x(t) \cdot y^*(t)dt = 0. \tag{3.18}$$

Assuming that $x(t) = \exp(j2\pi k \cdot \Delta f \cdot t)$ and $y(t) = \exp(j2\pi(k+1) \cdot \Delta f \cdot t)$ are two adjacent subcarriers, (3.18) can be written as

$$\langle x(t)|y(t)\rangle = \int_0^T \exp(-j2\pi k \cdot \Delta f \cdot t)dt = \exp(-j2\pi k \cdot \Delta f \cdot T) \cdot \frac{\sin(\pi \cdot \Delta f \cdot T)}{\pi \cdot \Delta f \cdot T}. \tag{3.19}$$

From (3.19), it can be seen that if the condition

$$\Delta f = m\frac{1}{T} = m\frac{B}{N}; m \in \mathbb{Z} \tag{3.20}$$

is respected, the two adjacent subcarriers are orthogonal. By setting $\Delta f = B/N$, the spectral efficiency is maximized while the orthogonality between subcarriers is maintained. In this way, the spectral efficiency of the OFDM signal is the same as that of a single-carrier. Figure 3.14 illustrates the frequency spectrum of FDM and OFDM carriers.

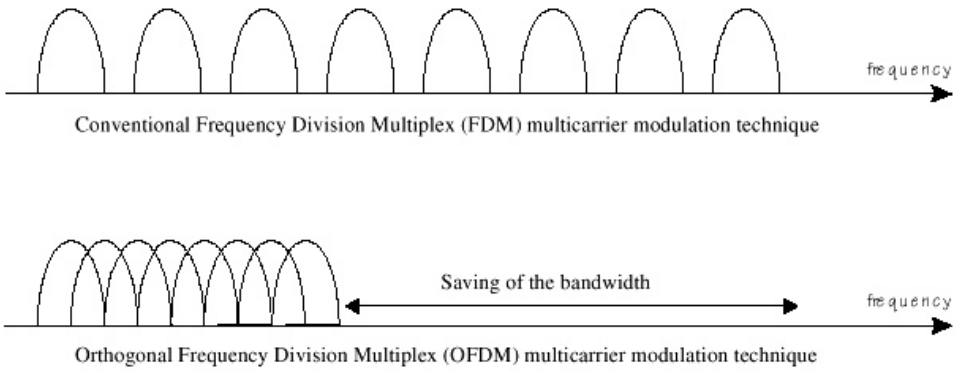

FIGURE 3.14: Advantage of OFDM over classical FDM modulation : Better spectral efficiency.

3.3.1.2 FFT/IFFT Implementation

In the following, n represents the time index, and k, the frequency index. Replacing $\Delta f = B/N$ in (3.17) and changing the interval for the k variable to $[-N/2, N/2-1]$, it becomes

$$x_{OFDM}(t) = \sum_{k=-N/2}^{N/2-1} X_k(t) \cdot \exp\left(j\frac{2\pi kt}{T}\right). \tag{3.21}$$

If the OFDM signal is sampled at a sampling-period $t_s = 1/B$, then the n^{th} sample of an OFDM symbol is defined as

$$x_{OFDM}[n] = \frac{1}{N}\sum_{k=-N/2}^{N/2-1} X_k \cdot \exp\left(j\frac{2\pi k n t_s}{T}\right); 0 < n < N-1 \tag{3.22}$$

$$= \frac{1}{N}\sum_{k=-N/2}^{N/2-1} X_k \cdot \exp\left(j\frac{2\pi k n}{N}\right); 0 < n < N-1 \tag{3.23}$$

where X_k the complex symbol from a M-QAM constellation modulating the k^{th} subcarrier with frequency $f_k = k/(Nt_s)$ and $1/N$ is a normalization factor. Note that (3.23) is the exact definition of the Inverse Discrete Fourier Transform of X_k. This is another key feature of OFDM. An efficient implementation can be made using the Inverse Fast-Fourier Transform (IFFT) algorithm for generating the digital baseband OFDM signal. At the receiver, one can easily access the complex symbols X_k modulating each subcarrier f_k, by performing the discrete FFT of the OFDM time-symbol x[n], such as

$$X_k = \sum_{n=0}^{N-1} x[n] \cdot \exp\left(-j\frac{2\pi k n}{N}\right); -N/2 < k < N/2 - 1. \tag{3.24}$$

3.3.1.3 The Cyclic Prefix

In OFDM signals, residual ISI caused by dispersive channels can be avoided by adding a time prefix with N_{CP} samples before each OFDM symbol. The last N_{CP} time samples of the symbol are simply copied at the beginning of the same OFDM symbol. This is called a cyclic prefix, and the operation is made for each transmitted symbol. The drawback is the cyclic prefix overhead, which can be expressed as the ratio between the number of extra samples added in the cyclic prefix and the number of samples effectively carrying data N_{CP}/N.

An OFDM symbol comprising the cyclic prefix can be written as

$$u[n] = \frac{1}{N}\sum_{k=-N/2}^{N/2-1} X_k \cdot \exp\left(j\frac{2\pi k((n+N-N_{CP}) \bmod N)}{N}\right); 0 < n < N_u - 1 \tag{3.25}$$

where $N_u = N + N_{CP}$ is the number of time samples per OFDM symbol including the cyclic prefix and *mod* represents the modulo operation (remainder of the division of a number by another). For demodulation, the cyclic prefix is simply removed, and the FFT is performed as described by (3.24).

Figure 3.15 illustrates how the ISI can be eliminated by using a cyclic prefix. Two subcarriers are shown as an example. We explained in subsection 2.1.2 that carriers with different frequencies travel at different speeds. In the example of figure 3.15, the blue subcarrier is the fast one, arriving earlier than the slow subcarrier (red one). In figure 3.15(a), no cyclic prefix is added. In the right, it can be seen that ISI occurs because a part of the 1^{st} symbol of the red curve interferes with the 2^{nd} symbol of the blue curve as they arrive simultaneously. In figure 3.15(b), for the purpose of illustration, a cyclic prefix of duration equal to 1/4 of the symbol duration is added. After removing the cyclic prefix at the reception, it can be seen that ISI is removed - the 1^{st} received OFDM symbol is a linear combination of the 1^{st} complex symbols sent by the two subcarriers, without any interference (equally for the second symbol). Then, the effect of the time-dispersive channel can be equalized with a linear-equalizer at the receiver.

Assuming a 10GHz-bandwidth OFDM transmission over 100km of standard SMF, with $N = 256$. Then, the duration of an OFDM symbol is $25.6ns$. For $D = 16ps/(nm \times km)$, the

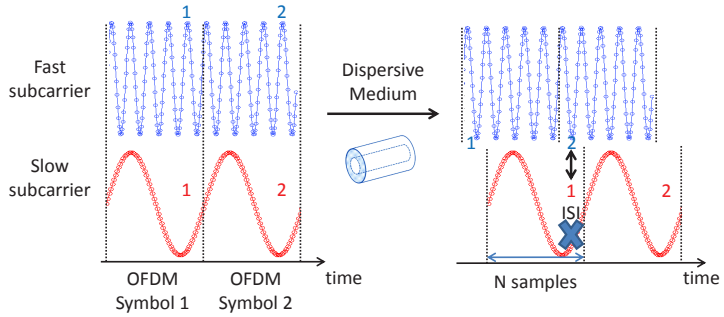

(a) Without cyclic prefix

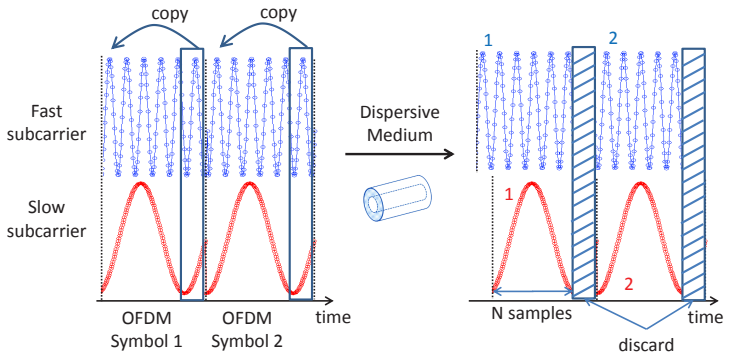

(b) With cyclic prefix

FIGURE 3.15: (a) ISI caused by chromatic dispersion and (b) principle of ISI elimination by using a cyclic prefix.

cumulated dispersion after 100km SMF is then $1600ps/nm$. If the optical source has narrow linewidth as compared to the OFDM signal, the optical bandwidth of the modulated signal is $20GHz$ $(0.16nm)$. As a result, the total time dispersion is $256ps$, which is 1% of the duration of an OFDM symbol. This shows that the overhead due to cyclic prefix is very low to the considered application.

3.3.1.4 One-tap Channel Equalization

After the OFDM signal is generated by the DSP, a DAC is used to convert the digital signal to the analog domain. Considering a DAC with sampling frequency $f_s = 1/t_s$, the n^{th} sample of the l^{th} OFDM symbol $u[n,l]$ of a frame containing several OFDM symbols is given by

$$u[n,l] = \frac{1}{N} \sum_{k=-N/2}^{N/2-1} X_{k,l} \cdot \exp\left(j \frac{2\pi k((n+N-N_{CP}) \bmod N) t_s}{N t_s}\right); 0 < n < N_u - 1 \tag{3.26}$$

where $X_{k,l}$ is the complex data symbol of the k^{th} subcarrier of the l^{th} OFDM symbol. After a conventional sample-and-hold DAC, the OFDM signal is given by

$$u(t) = \sum_{l=-\infty}^{\infty} \sum_{n=0}^{N_u-1} u[n,l] \cdot \delta(t) \otimes \Pi\left(\frac{t - t_s \cdot (n - lN_u)}{t_s}\right) \tag{3.27}$$

where Îă(t) is the pulse-shaping rectangular function defined by

$$\Pi(t) = \begin{cases} 1, & \text{if } 0 \leq t < 1 \\ 0, & \text{if } t < 0, t \geq 1 \end{cases}. \tag{3.28}$$

Considering that the received signal has passed through a channel with impulse response $h(t)$. It is then represented by $r(t) = u(t) \otimes h(t) + n(t)$, $b(t)$ being AWGN with zero mean and variance σ_b^2. At the receiver, the analog signal is sampled at the sampling rate f_s. Then, the n^{th} sample of the received signal is defined as

$$r[n] = u[n] \otimes h[n] + b[n] = \sum_{m=0}^{M-1} u[n-m] \cdot h[m] + b[n] \tag{3.29}$$

where $u[n]$ is defined in (3.25). The channel impulse response vector $h[n]$ comprises M samples, which corresponds to the duration of the impulse response $h(t)$ divided by t_s. The cyclic prefix is removed and demodulation is performed by replacing $x[n]$ in (3.24) by $r[n]$ defined in (3.29). Assuming that the clocks from the DAC and ADC are perfectly synchronized and $M < N_{CP}$, the received symbol from the k^{th} subcarrier is expressed by

$$R_k = \sum_{n=0}^{N-1} r[n] \cdot \exp\left(-j\frac{2\pi kn}{N}\right) \tag{3.30}$$

$$= \sum_{n=0}^{N-1} \left(\sum_{m=0}^{m-1} u[n-m] \cdot h[m] + b[n] \right) \cdot \exp\left(-j\frac{2\pi kn}{N}\right) \tag{3.31}$$

$$= \sum_{m=0}^{M-1} h[m] \cdot \left(\sum_{n=0}^{N-1} u[n-m] \cdot \exp\left(-j\frac{2\pi kn}{N}\right) \right) + \sum_{n=0}^{N-1} b[n] \cdot \exp\left(-j\frac{2\pi kn}{N}\right) \tag{3.32}$$

$$= \sum_{m=0}^{M-1} h[m] \cdot \exp\left(-j\frac{2\pi kn}{N}\right) \cdot \left(\sum_{n'=-m}^{N-1-m} u[n'] \cdot \exp\left(-j\frac{2\pi kn'}{N}\right) \right) + B_k \tag{3.33}$$

$$= \sum_{m=0}^{M-1} h[m] \cdot \exp\left(-j\frac{2\pi kn}{N}\right) \cdot \left(\sum_{n'=0}^{N-1} u[n'] \cdot \exp\left(-j\frac{2\pi kn'}{N}\right) \right) + B_k \tag{3.34}$$

where $n' = n - m$ and B_k is the Fourier transform of the AWGN $b(t)$ written as

$$B_k = \sum_{n=0}^{N-1} b[n] \cdot \exp\left(-j\frac{2\pi kn}{N}\right). \tag{3.35}$$

Equation (3.34) was calculated from (3.33) using the circular convolution property of the discrete Fourier transform. We can represent the channel frequency response of the k^{th} subcarrier by

$$H_k = \sum_{m=0}^{M-1} h[m] \cdot \exp\left(-j\frac{2\pi km}{N}\right). \tag{3.36}$$

Note that H_k accounts for the frequency response of the whole link, including the frequency response of the optical and electrical components of the transmitter and receiver (ADC/DAC, filters, amplifiers, optical transmitter/receiver). Replacing (3.36) in (3.34), the received data symbol of the k^{th} subcarrier is defined as

$$R_k = H_k \cdot X_k + B_k. \tag{3.37}$$

The SNR in the k^{th} carrier is then given by

$$SNR_k = \frac{|X_k \cdot H_k|^2}{\sigma_b^2}. \tag{3.38}$$

Using the maximum likelihood estimation method [222], the complex coefficient H_k can be estimated using training sequences; they are pre-defined data sequences that are known at the receiver. The SNR degradation ΔSNR from estimation error is given as a function of the number of training symbols p by [222]

$$\Delta SNR[dB] = 10 \log_{10} \left(\frac{1}{p+1} \right). \tag{3.39}$$

For 1 training symbol, 3dB SNR penalty is expected, while for 10 training symbols, the SNR penalty is less than 0.5dB. Specifically for the case of an optical fiber, the channel coefficients are considered to be static in time. This implies 2 consequences, 1) The overhead due to the channel estimation can be neglected (it is made at the beginning of the transmission, once for all) and 2) the SNR degradation due to the estimation of the noise is minimized since the estimated channel coefficients can be averaged over a large amount of time (p is high).

3.3.1.5 Bit and Power Loading

Another feature of OFDM is the ability to adapt the modulation order of each subcarrier according to the SNR and the target BER of the transmission. The drawback is that a feedback from the receiver to the transmitter is required, adding an overhead to the transmission. However, this overhead can be negligible for cabled transmissions (copper or optical fibre), where the link quality is considered static in a sufficient amount of time. Indeed, this technique is widely used in xDSL systems.

The optimum algorithm for the bit allocation problem is the water-filling, which is described in appendix C.1. The problem is that the output of the algorithm (bits per subcarrier) is a non-integer number and therefore it cannot be applied directly to the OFDM signal. For that purpose, efficient algorithms are proposed in the literature [223, 224] in which both number of bits and relative power per subcarrier are chosen to optimize data-rate for a target BER. In this work, an intuitive approach based on a very accurate $BER = f(SNR)$ approximation for the constellations is made. This approach is detailed in appendix C.2.

In this thesis, as a convention, when bit and power loading technique is used, the term adaptive OFDM is used.

3.3.1.6 Real-valued representation of an OFDM signal

Assuming that all the subcarriers of an OFDM signal carry useful data, the generated baseband OFDM signal is complex. It has two components, called the in-phase (I) and the quadrature (Q) components of the signal : $x_{OFDM}(t) = x_I(t) + jx_Q(t)$. In order to modulate the intensity of the optical carrier, the electrical signal should be real.

Heterodyning Technique

The most common method to generate a real-valued OFDM signal is the heterodyning technique. It is used in every RF communication systems. The principle is illustrated in figure 3.16. After the digital-to-analog conversion, the I and Q arms are filtered by a low-pass filter in order to eliminate high frequencies components of the signal. Then, the I signal is mixed with a LO signal at the frequency f_{RF} and the Q signal is mixed with the same LO with a 90° phase shift. Finally, they are added together. The signal is then a pass-band signal centered at the frequency f_{RF}. The equivalent pass-band signal is given by

$$x_{RF}(t) = x_I(t) \cdot \cos(2\pi f_{RF} t) + x_Q(t) \cdot \sin(2\pi f_{RF} t) \tag{3.40}$$

$$= \Re\left\{x_I(t) \cdot \cos(2\pi f_{RF} t) + x_Q(t) \cdot \sin(2\pi f_{RF} t) + j(x_I(t) \cdot \sin(2\pi f_{RF} t) + x_Q(t) \cdot \cos(2\pi f_{RF} t))\right\} \tag{3.41}$$

$$= \Re\left\{x_{OFDM}(t) \cdot \exp(-j2\pi f_{RF} t)\right\}. \tag{3.42}$$

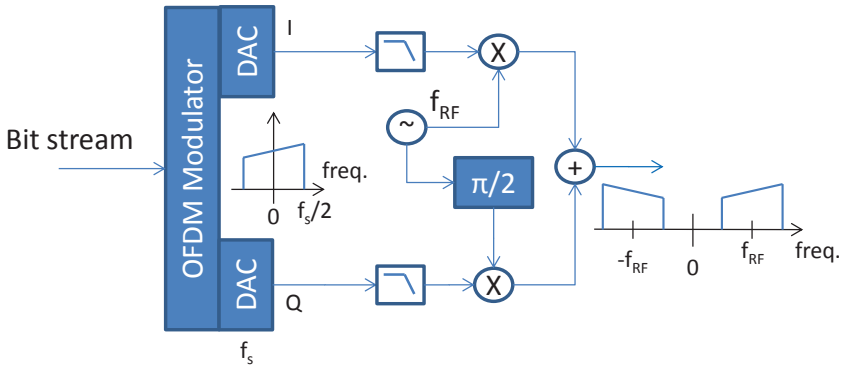

FIGURE 3.16: Heterodyning technique to generate a real-valued OFDM signal.

Baseband Real-valued OFDM Signal Generation

Another way to generate a real-valued OFDM signal is to use the Hermitian Symmetry property of the FFT. It states that if $X_k = X_k^* \forall k \in [0, N/2-1]$, where X_k is the data symbol of the k^{th} subcarrier and N is the number of subcarriers, the resulting OFDM signal is real. This property can be demonstrated from (3.21) as

$$x_{OFDM}(t) = \sum_{k=0}^{N/2-1} X_k(t) \cdot \exp\left(j\frac{2\pi kt}{T}\right) + X_k^*(t) \cdot \exp\left(-j\frac{2\pi kt}{T}\right) \tag{3.43}$$

$$= \sum_{k=0}^{N/2-1} X_k(t) \cdot \exp\left(j\frac{2\pi kt}{T}\right) + \left[X_k(t) \cdot \exp\left(j\frac{2\pi kt}{T}\right)\right]^* \tag{3.44}$$

$$= \sum_{k=0}^{N/2-1} 2\Re\left\{X_k(t) \cdot \exp\left(j\frac{2\pi kt}{T}\right)\right\}. \tag{3.45}$$

As the DSP complexity of this scheme is analyzed, a common belief is that it requires twice as much complexity than the heterodyning technique. This, however, is a misconception. Because of the symmetry properties described above, the FFT/IFFT operations can indeed be optimized and the hardware complexity is effectively halved [225, 226].
The drawback of this scheme is the DAC/ADC efficiency (the ratio between the useful OFDM bandwidth and the DAC/ADC sampling-rate required). In order to generate an OFDM signal with useful bandwidth B, the sampling-rate required is at least 2B (1/2 DAC/ADC efficiency). It is twice as much required when compared to the heterodyning technique.
This technique is called Discrete Multitone Modulation (DMT) or real baseband OFDM.

3.3.2 OFDM Impairments

3.3.2.1 High PAPR Impairment

Since an OFDM signal is a sum of independently modulated subcarriers, statistically, their amplitudes can add constructively resulting in instantaneous high voltage peaks for overall output signal. According to the central limit theorem, as the number of subcarriers increases, the probability distribution of the OFDM signal $u(t)$ can be approximated by a Gaussian distribution with zero mean (for $N > 10$). Therefore, the probability density function of an OFDM signal with $N > 10$ subcarriers and zero-mean is approximated by

$$f(u) = \frac{1}{\sqrt{E\left[|x(t)|^2\right] \cdot 2\pi}} \cdot \exp\left(\frac{u^2}{2E\left[|x(t)|^2\right]}\right) \tag{3.46}$$

where $E\left[|x(t)|^2\right]$ is the variance of the OFDM signal $u(t)$, averaged over a large number of OFDM symbols. Figure 3.17 shows in the left an example of an OFDM signal in the time domain for $E\left[|x(t)|^2\right] = 1$, and the corresponding probability density function on the right.

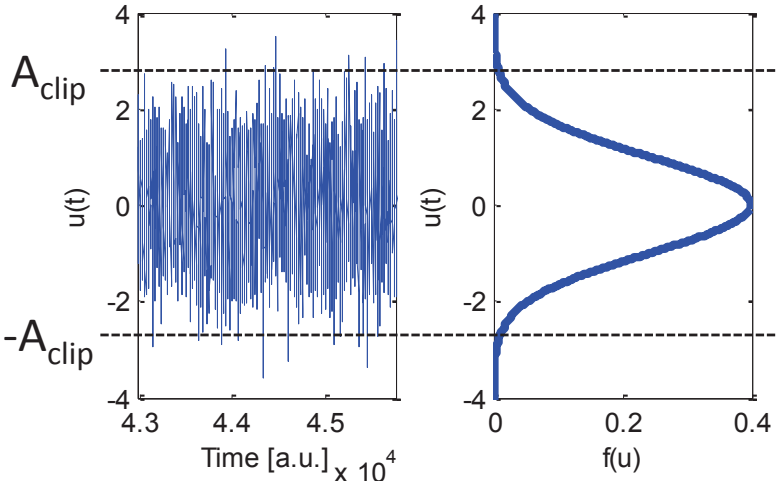

FIGURE 3.17: OFDM signal in the time domain (left) and corresponding probability density function (right).

The Peak-to-Average Power Ratio (PAPR) is a commonly used parameter to quantify the ratio between the peak value and the mean value of a random signal. The maximum value that a PAPR of an OFDM signal with N subcarriers can achieve is then N^2, in the case that all the subcarriers add constructively with maximum amplitude each. However, this is a very rare event and unlikely to happen in practice. The actual PAPR of an arbitrary OFDM signal is a random variable. The probability that the PAPR is higher than a value x is given by the Complementary Cumulative Density Function (CCDF) of a Rayleigh distribution (squared Gaussian distribution)

$$P(PAPR > x) = \exp\left(\frac{-x^2}{E\left[|x(t)|^2\right]}\right). \tag{3.47}$$

The most straightforward way to decrease the PAPR of an OFDM signal is the hard clipping technique [227]. It consists in limiting the maximum peak amplitude of the signal by clipping

it in order to reduce the PAPR to a target value A_{clip} as indicated in figure 3.17 (a formal mathematical description is presented in next subsection).

More complex techniques for reducing the PAPR have been proposed, such as coding schemes [228], partial transmit sequences [229] among many others [230]. Most of these techniques perform better than hard clipping [230]. However, the hard clipping is still considered to have the best cost-benefit. Although it intentionally introduces non-linear distortion due to clipping, it can improve the SNR if applied properly.

Clipping and Quantization Operations

The hard clipping operation can be performed digitally before digital-to-analog conversion, in order to achieve a given clipping ratio $k = A/\sqrt{E\left[|x(t)|^2\right]}$. Then, the PAPR of the clipped signal is upper-bounded by $PAPR \leq k^2$. A clipped time sample $u_{clip}[n]$ of the OFDM signal is defined mathematically as

$$u_{clip}[n] = \begin{cases} u[n] & \text{if } -A_{clip} \leq u[n] \leq A_{clip} \\ -A_{clip} & \text{if } u[n] < -A_{clip} \\ A_{clip} & \text{if } u[n] > A_{clip} \end{cases} \tag{3.48}$$

where $u[n]$ is the sampled version of $u(t)$. From the clipping ratio definition, one can see that the RMS value of the output signal can be increased with lower clipping-ratios, at the expense of higher non-linear distortion [231].

After clipping, the OFDM signal is converted in the analog domain with a DAC. Each time sample $u_{quant}[n]$ at the output of the quantifier can be written as

$$u_{quant}[n] = \text{round}\left(\left(\frac{u_{clip}[n] + A_{clip}}{2A_{clip}}\right) \cdot \left(2^b - 1\right)\right) \cdot \frac{2A_{clip}}{2^b} - A_{clip} \tag{3.49}$$

where round(x) is the rounding to the nearest integer operation, b is the DAC number of bits.

Optimum Clipping Ratio in AWGN Channel

By intentionally clipping the signal before the DAC operation, clipping noise is inevitably added to the output signal. Equally, the quantification operation described in the previous subsection adds quantization noise. Both noises can be modeled as zero-mean additive white noise with variance (power) P_{clip} and P_{quant} for clipping and quantization noise, respectively. They are computed analytically in [232], resulting in

$$P_{clip} = E\left[|x(t)|^2\right] \cdot \left((1 - (k+0.7)^2) \cdot \text{erfc}\left(\frac{k}{\sqrt{2}}\right) + (k+0.7) \cdot \sqrt{\frac{2}{\pi}} \cdot \exp\left(\frac{-k^2}{2}\right)\right) \tag{3.50}$$

$$P_{quant} = E\left[|x(t)|^2\right] \cdot \frac{k^2}{3 \cdot 2^b} \tag{3.51}$$

Assuming that the digital signal $u_{quant}[n]$ is converted to the analog domain with a DAC having an output peak-to-peak voltage V_{pp}, The signal $u_{quant}[n]$ is then multiplied by $\gamma = V_{pp}/2k$ and the signal in the DAC output is expressed by

$$u_{out}[n] = \gamma \cdot u_{quant}[n]. \tag{3.52}$$

At the receiver, we assume AWGN, with variance σ_b^2. Then, the total noise power (including clipping, quantization and AWGN) is given by $\gamma^2 \cdot (P_{clip} + P_{quant}) + \sigma_b^2$. The final SNR is then

written as

$$SNR_{CQ} = \frac{\gamma^2 \cdot \left(E\left[|x(t)|^2\right] - P_{clip}\right)}{\gamma^2 \cdot (P_{clip} + P_{quant}) + \sigma_b^2} \tag{3.53}$$

Note that if $P_{clip} = 0$ and $P_{quant} = 0$, (3.53) reduces to $SNR_0 = \gamma^2/\sigma_b^2$, which is the SNR of the OFDM signal in the absence of the clipping and quantization operation. Figure 3.18 plots the results of (3.53) for V_{pp}=1, an 8 bits DAC and three values of SNR_0. The value of σ_b^2 is calculated from the SNR_0 value with k=5 ("unclipped case"). We observe that the hard clipping effectively increases the SNR value of the OFDM signal, up to 4dB. As an example, for the case where $SNR_0 = 20dB$, it is shown that at a clipping ratio of $k = 3$, the total SNR is improved to about 24dB with the clipping operation. Additionally, it shows that the optimum value of the clipping ratio depends on the noise power of the system. We find that the optimum clipping ration for 8 bits DAC resolution is 3, 2.8 and 2.6 for SNR_0 values of 20dB, 17dB and 14dB respectively.

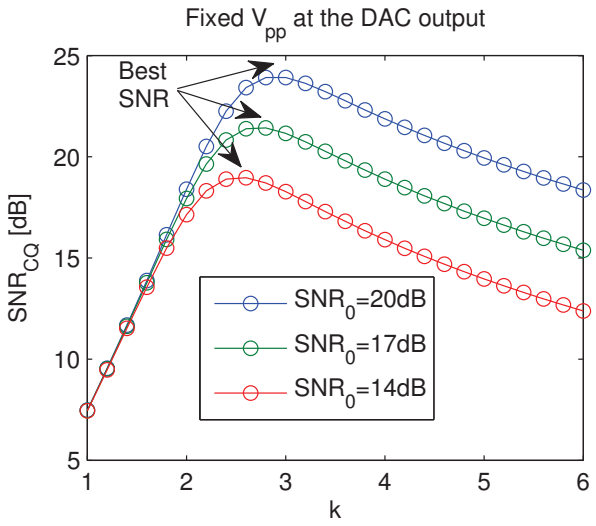

FIGURE 3.18: Analytical computation of SNR_{CQ} as function of the clipping ratio considering fixed peak-to-peak voltage DAC output.

3.3.2.2 Weakness against Non-linearity

The previous sections considered linear transmission systems, i.e. linear emitters, receivers and channel. The section below describes the impairments caused by non-linearity. A linear signal chain is crucial for OFDM signal transmission since a non-linear device distorts the OFDM signal, degrading transmission performance, and increases out-of-band spectrum power.

Non-Linear Model

A non-linear device along the transmission may be modelled as a polynomial function. Considering that an arbitrary signal $u(t)$ is passed through a non-linear device, the output $y(t)$ is related to the input by

$$y(t) = G_1 u(t) + G_2 u^2(t) + G_3 u^3(t) + G_4 u^4(t) + \ldots \tag{3.54}$$

where G_n is the coefficient of the non-linear term of order n. In real-life devices, the gains G_n are frequency-dependent. However, in this model, they are considered frequency-independent

for simplicity. This assumption has negligible impact on the results. Generally, the third-order non-linear term is predominant over all others. Therefore, in this analysis, $G_n = 0$ for $n \neq 1$ and $n \neq 3$ is considered.

The two most common parameters to quantify non-linearity are the IP3 and the 1dB Compression Point (CP1dB), which are introduced in subsection 5.1.1.3. The relationship between input RF power at the IP3 P_{IIP3} (assuming a 2-tone signal at f_1 and f_2 at the input of the Device Under Test (DUT)) and the G_3 parameter of the proposed model is calculated to be

$$G_3 = \frac{2G_1}{3P_{IIP3}}. \tag{3.55}$$

Furthermore, the input RF power at the CP1dB P_{ICP} and P_{IIP3} are related by

$$P_{IIP3}[dBm] = P_{ICP}[dBm] + 9.6. \tag{3.56}$$

Note that the result of (3.56) assumes that the non-linear device follows the model proposed in (3.54). In practice, it is not always the case. As a consequence, the relation of (3.56) can deviate from a few dB's.

SNR Penalty Due to Non-linear Devices

A simulation routine has been developped in order to evaluate the SNR penalty induced by a device non-linearity along an OFDM transmission chain. We can then measure the non-linearity of the device (using IP3 or CP1dB), calculate the non-linear coefficient G_3 of the model using (3.55) (and (3.56) in the case the CP1dB is measured) and use the simulation routine to calculate the SNR penalty due to the device non-linearity. For a given modulation format applied on each subcarrier, the SNR penalty induced by the device non-linearity is computed at a target BER. In order to achieve a BER target of $2.2 \times^1 0{-}3$, a 15.75dB SNR (respectively 21.75dB) is required to achieve a 16-QAM modulation format (respectively 64-QAM) considering a linear system. For example, if a SNR of 16.75dB is required to achieve a BER of $2.2\times^{-3}$ for 16-QAM in the non-linear system, the SNR penalty is 1dB.

The output of the simulation routine is displayed in figure 3.19. The parameters of the simulation are $N = 128$ subcarriers (with 63 data subcarriers, one nulled subcarrier and the other 64 subcarriers set as the complex conjugates of the first 63 data subcarriers in order to form a real-valued OFDM signal), $N_{CP} = 0$. A total of 4000 OFDM symbols are processed for each value of the OFDM signal input power, resulting in 10^6 bits for 16-QAM modulation. For the target BER considered (2.2×10^{-3}), we find a total of 2.2×10^3 errors per acquisition, resulting in a 2% precision (cf. (3.10)) in the BER estimator. We conclude that, the SNR penalty increases from 0 to 2dB with an input OFDM signal power increasing from 9 to 13dBm for a 64-QAM modulation, and from 14 to 17dBm for a 16-QAM modulation. These results were obtained with no clipping, resulting in a PAPR of approximately 25 at each point, hence the only source of SNR penalty is the non-linearity of the device.

It is interesting to observe how the hard clipping manages to mitigate non-linear impairments. Figure 3.20 displays the simulation results for a 64-QAM modulation considering that the signal is clipped before the non-linear device, with clipping ratios from 2.5 to 4 (resulting in an upper-bound in the PAPR from 6.25 to 16). The power loss due to clipping at the worst case ($k = 2.5$) is negligible. It is observed that, at low OFDM input powers, we have a higher penalty for high clipping ratios since clipping distortion dominates over non-linear distortion. At high OFDM input powers, higher values of clipping ratio manage to mitigate non-linear distortion and give lower SNR penalties.

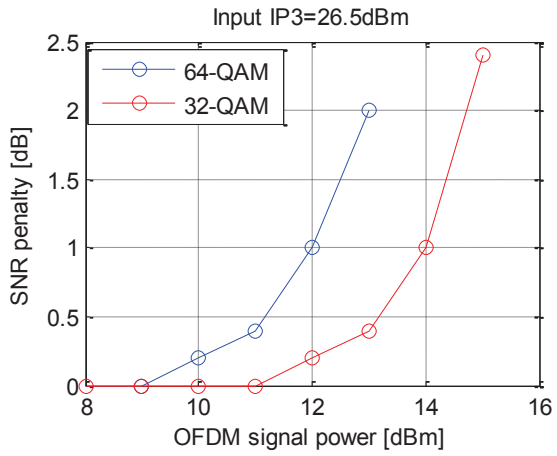

FIGURE 3.19: SNR penalty due to non-linearity for 16-QAM and 64-QAM.

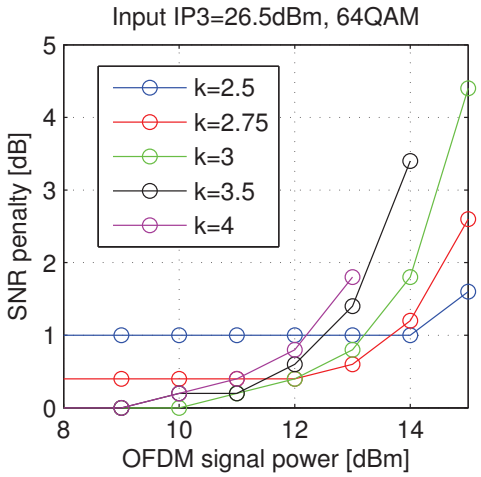

FIGURE 3.20: SNR penalty due to non-linearity (64-QAM) with clipping.

3.3.2.3 IQ imbalances, Carrier and Frequency Offset Impairments

A schematic representation of the IQ imbalance, carrier and frequency offset impairments is depicted in figure 3.21.

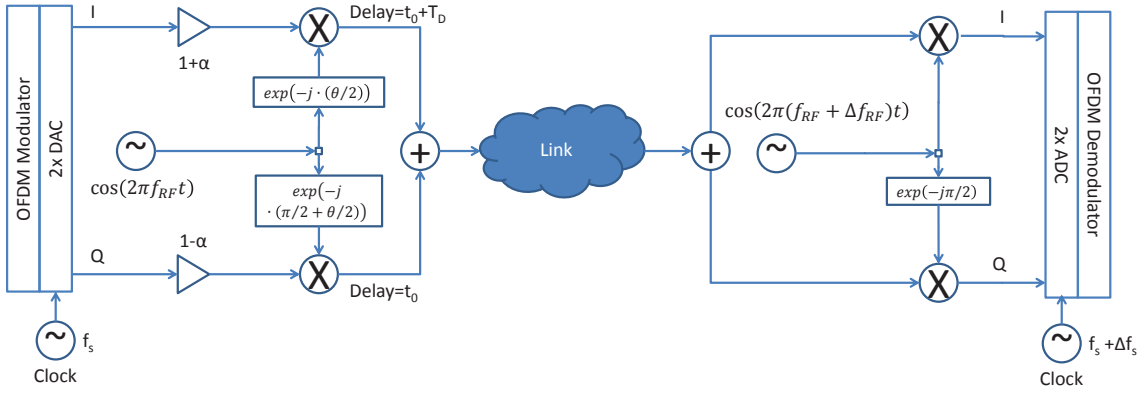

FIGURE 3.21: Representation of IQ imbalances, carrrier and sampling frequency offset impairments.

The IQ imbalances are threefold : amplitude (α), phase (θ) and time misalignment (T_D). Note that these impairments occur in both electrical and optical domain (if an optical IQ modulator is employed). The effect on the OFDM signal is that an interference between the left (negative) and right (positive) sides of the spectrum (known as Inter-carrier Interference (ICI)). The received symbol R_k in the k^{th} subcarrier is written as [233]

$$R_k = X_k \cdot H_{11} + X^*_{-k} H_{12} \tag{3.57}$$

where X_k is the sent complex symbol of the k^{th} subcarrier, H_{11} and H_{12} are complex gains related to the IQ imbalances parameters (α, θ and T_D). This impairment can be corrected by estimating both H_{11} and H_{12} parameters [233]. A method for estimating these parameters in reported in [234]. In a few words, two probe signals are generated : one where all the negative-index subcarriers are set to zero and the other one where positive-index subcarriers are nulled, allowing to estimate separately H_{11} and H_{12}.

The Carrier Frequecy Offset (CFO) and Sampling Frequecy Offset (SFO) are caused by a frequency offset in the LO (Δf_{RF}) between up/down-conversion and in the reference clock for sampling between DAC/ADC, respectively. The received complex symbol in the k^{th} subcarrier of the l^{th} OFDM symbol (l denotes a time-domain index) in the presence of CFO and SFO is defined by [235]

$$R_{k,l} = X_{k,l} \cdot H_k \cdot \exp\left(j2\pi \cdot \left(\frac{lN_u + N_{CP}}{N}\right) \cdot (\Delta f_{RF} T + \Delta f_s k / f_s)\right) \tag{3.58}$$

where $X_{k,l}$ is the sent symbol of the k^{th} subcarrier of the l^{th} OFDM symbol, N is the number of subcarriers, N_{CP} is the number of cyclic prefix samples, $N_u = N + N_{CP}$ is the number of samples of an OFDM symbol and H_k is the channel frequency response which is invariable in time.

As a result, the CFO and SFO impairments cause a phase shift which increases in time. In the case of the SFO, this phase-shift is also proportional to the subcarrier index k. In this work, the CFO and SFO parameters are estimated by calculating the phase shift $\Delta\phi = Arg\{R_{k,l+1}\} - Arg\{R_{k,l}\}$ and using (3.58). For efficient CFO and SFO estimation algorithms, refer to [236], which is widely used for RF applications.

3.3.3 OFDM for Optical communications using Direct-detection receivers

As mentioned previously, OFDM modulation is widely used in RF applications, such as Wi-Fi, WiMAX, digital radio/video systems (DAB/DVB) and more recently to Long-Term Evolution (LTE), among many others. For cooper-cabled communications, it is also used for xDSL systems, where is known as Discrete Multitone Modulation (DMT). In order to adapt this kind of modulation to the optical fiber, a few considerations must be made.

In general, optical OFDM can be divided in two major groups - direct-detection and coherent optical OFDM, which is related to the type of receiver used. Coherent OFDM is mostly considered for long-haul optical systems. An extensive review of this type of OFDM is found in [237].

We classify direct-detection optical OFDM into two types : IM/DD (DSB-based) and SSB-based which are detailed in the following sub-sections. Since one of the major bottlenecks for implementing OFDM for optical access networks is the complexity of the electrical transceiver, the last subsection details the state-of-the-art in DSP implementation using FPGA and ASIC, and high-speed DACs/ADCs.

3.3.3.1 IM/DD (DSB-based) Optical OFDM

In order to modulate the intensity of the optical carrier, the modulating signal must be real. Techniques for generating a real-valued OFDM signal are discussed in sub-section 3.3.1.6.

DSB Cancellation over the Fiber

As a consequence of the fact that the modulating signal is real, the resulting optical modulating signal is called DSB. Because of the Hermitian symmetry property, the spectrum of a real-valued signal is mirrored around the 0Hz frequency (cf. inset figure 3.22). In this way, when it is mapped into the intensity of the optical carrier, two sidebands appear at the modulating signal, one in each side of the optical carrier as indicated in figure 3.22.

One of the main issues when transmitting an optical DSB signal over the fiber is the DSB cancellation fading caused by chromatic dispersion [238], which is explained in the following. Considering a single-tone frequency $x_{RF}(t) = m\cos(2\pi f_{RF} t)$ modulating the intensity of an optical carrier. For simplicity, we assume that there is no frequency chirp. The instantaneous power $P(t)$ of the optical carrier is then given by

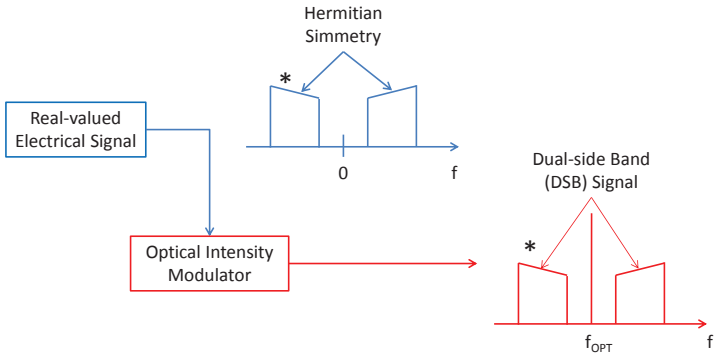

FIGURE 3.22: DSB optical signal as a result of the intensity modulation.

$$P(t) = |E(t)|^2 = P_0 \cdot (1 + m \cos \hat{a}Ąą(2\pi f_{RF} t)) \tag{3.59}$$

where P_0 is the average power of the optical carrier and $E(t)$ is the instantaneous field of the optical signal which is given by (2.19). Assuming small signal modulation regime ($m << 1$), the slow-varying envelope $A(t)$ of the optical signal can be written as

$$\begin{aligned} A(t) &= \sqrt{P_0 \cdot (1 + 2m \left(\exp(j2\pi f_{RF} t) + \exp(-j2\pi f_{RF} t)\right))} \\ &\approx \sqrt{P_0} \cdot (1 + m \left(\exp(j2\pi f_{RF} t) + \exp(-j2\pi f_{RF} t)\right)) . \end{aligned} \tag{3.60}$$

As explained in subsection 2.1.2, different spectral components travel at different speeds in the optical fiber because of the chromatic dispersion. A spectral component at $f_{opt} + f_{RF}$ after travelling a fiber of length L and chromatic dispersion D is phase-shifted by $\Phi_{D_{LSB}}(f_{RF}) = \pi c D L f_{RF}^2 / f_{opt}^2$ [222] relative to the optical carrier (LSB denoting left-sideband). Since $f_{RF} << f_{opt}$, the chromatic dispersion around f_{opt} can be considered to be linear, and we can assume that the spectral component at $f_{opt} + f_{RF}$ is phase shifted by $\Phi_{D_{RSB}}(f_{RF}) = -\pi c D L f_{RF}^2 / f_{opt}^2$.

Then, the complex envelope of the signal at the fiber output is

$$\begin{aligned} A(t) \approx \sqrt{P_0} \cdot (1 + m \left(\exp(j2\pi f_{RF} t + j\Phi_{D_{RSB}}(f_{RF})\right) \\ + \exp(-j2\pi f_{RF} t + j\Phi_{D_{LSB}}(f_{RF}))) . \end{aligned} \tag{3.61}$$

At reception, the electrical signal is obtained with a square-law photodetector and the received electrical current is proportional to

$$I_{elec}(t) \propto |E(t)|^2 \approx P_0 + 2\sqrt{P_0}\Re\{\exp(j2\pi f_{RF}t)\cdot(\exp(j\Phi_{D_{RSB}}(f_{RF})) + \exp(j\Phi_{D_{LSB}}(f_{RF})))\} \tag{3.62}$$

$$\approx P_0 + 2\sqrt{P_0}\Re\left\{\exp(j2\pi f_{RF}t)\cdot\left(\exp\left(j\frac{\pi cDLf_{RF}^2}{f_{opt}^2}\right) + \exp\left(-j\frac{\pi cDLf_{RF}^2}{f_{opt}^2}\right)\right)\right\} \tag{3.63}$$

$$\approx P_0 + 2\sqrt{P_0}\Re\left\{\exp(j2\pi f_{RF}t)\cdot 2\cos\left(\frac{\pi cDLf_{RF}^2}{f_{opt}^2}\right)\right\} \tag{3.64}$$

$$\approx P_0 + 4\sqrt{P_0}\cos(2\pi f_{RF}t)\cdot\cos\left(\frac{\pi cDLf_{RF}^2}{f_{opt}^2}\right) \tag{3.65}$$

The higher-order terms at $2f_{RF}$ in (3.62) caused by the beating between the two sidebands are neglected and the first term P_0 is a DC level that can be easily eliminated. Finally, the normalized amplitude transfer function of the optical DSB signal after travelling the fiber link is given by

$$H_F(f) \propto \left|\cos\left(\frac{\pi cDLf^2}{f_{opt}^2}\right)\right|. \tag{3.66}$$

Equation (3.65) shows that the tone at each sideband will beat with the optical carrier and it will add after the square-law photo-detector. If the phase-shift difference between the tone at the left and right-hand side is 180°, the output amplitude at the tone frequency will be zero. This causes several nulls in the link frequency response. The transfer function given in (3.66) is plotted in figure 3.23 (no chirp case, $\alpha_{MZM} = 0$) for $D = 16ps/(nm\times km)$, $f_{opt} = 193THz$ ($\lambda_{opt} = 1.55\mu m$) and $L = 100km$, showing the several nodes due to DSB cancellation. Considering a baseband OFDM signal with bandwidth B which is located at the frequency band $0 - BHz$, the overall transmission capacity is decreased.

So far, the modulation chirp was neglected. If a chirped MZM is considered with chirp parameter α_{MZM} (cf. subsection 2.2.2.2) the link frequency response is written as [239]

$$H_{F_{MZM}}(f) \propto \left|\cos\left(\frac{\pi cDLf^2}{f_{opt}^2}\right) - \alpha_{MZM}\cdot\sin\left(\frac{\pi cDLf^2}{f_{opt}^2}\right)\right|. \tag{3.67}$$

$H_{F_{MZM}}$ is plotted in figure 3.23 for $\alpha_{MZM} = 0$ (Equation (3.66)), $\alpha_{MZM} = -1$ and $\alpha_{MZM} = 1$. One can observe an advantage of having a negative chirp parameter : the first null is at 7.6GHz instead of 6.25GHz for the unchirped case and 4.4GHz for positive chirp. As a consequence, for baseband transmissions (starting from 0Hz), transmission capacity can be improved by imposing a negative chirp.

Furthermore, if a DML is considered, because adiabatic chirp is present, another parameter should be taken into account. As indicated in [240], this parameter is called f_c, and it is related to the adiabatic chirp parameter κ by $f_c = \kappa P_0$ [134]. Using the relations described in subsection 2.2.1.1, the f_c parameter can be written as a function of the physical parameter of the lasers as [240]

$$f_c = \frac{\Gamma\epsilon_{NL}}{2\pi eV}\cdot(I_b - I_{th}). \tag{3.68}$$

where Γ is the optical mode confinement factor within the active region, ϵ_{NL} is the non-linear saturation gain parameter, V is the volume of the active region, I_b and I_{th} are the bias and

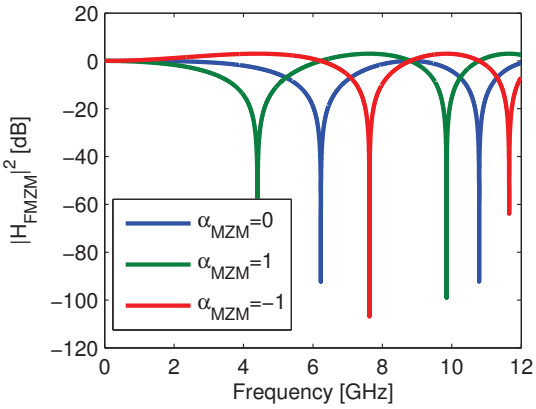

FIGURE 3.23: Frequency-response of the transmission of an optical IM/DD signal (DSB) over the fiber using a MZM.

threshold current respectively. These parameters were described in subsection 2.2.1.1. Then the link frequency response is given by [240]

$$H_{F_{DML}}(f) \propto \left|\cos\left(\frac{\pi cDLf^2}{f_{opt}^2}\right) - \alpha \cdot \left(1 - j\frac{f_c}{f}\right) \cdot \sin\left(\frac{\pi cDLf^2}{f_{opt}^2}\right)\right|. \tag{3.69}$$

Note that (3.67) is a particular case of (3.69) where $f_c = 0$ (MZMs do not have adiabatic chirp). Figure 3.24 (left) shows the link frequency response for several f_c values and fixed $\alpha = 3$, while figure 3.24 (right) shows the link frequency response for several α and fixed $f_c = 3GHz$. Same parameters as the one from figure 3.69 are assumed. We conclude that the f_c parameter plays a role in the deepness of the first node. It is interesting to note that higher values of f_c (higher adiabatic chirp) will result in a less profound node and even some gain is observed for $f_c > 3GHz$. The chirp parameter is directly related to the height of the secondary lobes. Due to chirp, some gain is observed at the secondary lobes, and the gain increases with the value of the chirp. The interest of chirped sources for IM/DD transmissions is studied in [241].

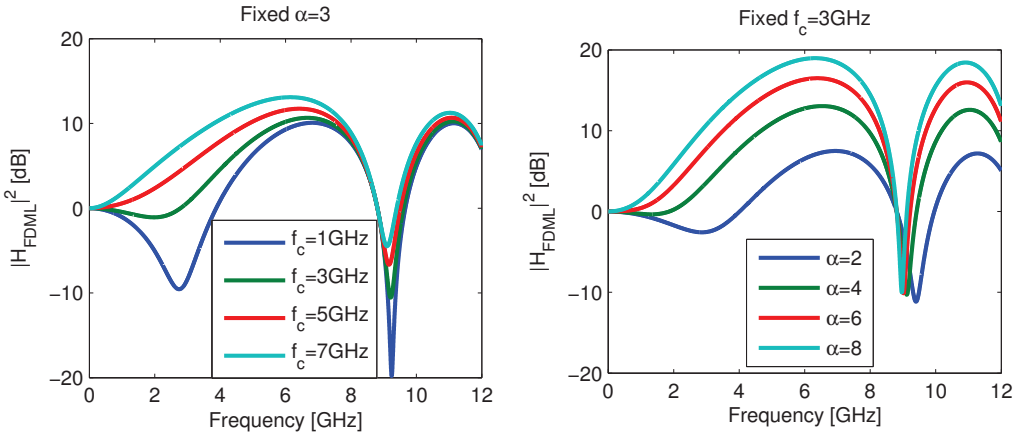

FIGURE 3.24: Frequency-response of the transmission of an optical DSB signal over the fiber using a DML for (left) fixed $\alpha = 3$ and varying f_c and (right) fixed $f_c = 3GHz$ and varying α.

The reader can refer to [134] for a very detailed explanation and comparison between the resulting frequency response of many types of intensity modulators.

Note that the analysis made in this part was made under the small-signal regime assumption. A large-signal analysis of the fiber frequency response is given in [242], for a MZM with arbitrary chirp.

Dispersion-induced Distortions Caused by Laser Frequency-chirp

Another type of performance degradation when using intensity modulators with frequency chirp is that the unwanted phase modulation that is generated by the modulator is transformed to intensity modulation by fiber chromatic dispersion. In other words, the chromatic dispersion causes a phase difference between phase-modulation side bands which becomes detectable after a certain transmission distance. As a consequence, the modulation depth of the intensity modulator should be decreased as the transmission reach increases. This is because a large modulation depth translates into large frequency chirp, and hence higher distortion. This is experimentally verified in [243]. An analytical description of this distortion is found in [244, 245].

3.3.3.2 SSB-based Optical OFDM

As mentioned in subsection 3.2.1, optical SSB modulation was first proposed to direct-detection single-carrier systems to reduce chromatic dispersion effects. The benefits of optical SSB modulation applied to OFDM is to get rid of the frequency fading caused by dispersion and the DSB cancelation effect. This is shown in this subsection.

The general form of an optical SSB-OFDM signal is shown in figure 3.25. The optical SSB-OFDM signal is centered at a frequency of $f_{RF}+f_{OPT}$, where $f_{RF} > B$, where B is the baseband bandwidth of the OFDM signal. At reception, the OFDM signal beats with the optical carrier is centered at a frequency of f_{RF}. An interference called Signal-to-Signal Beat Interference (SSBI) appears from 0Hz to $2B$. It is caused by the beating of the OFDM signal with itself, and it will be described analytically in the following. An efficient method for generating the optical SSB-OFDM signal is discussed in subsection 4.2.2.

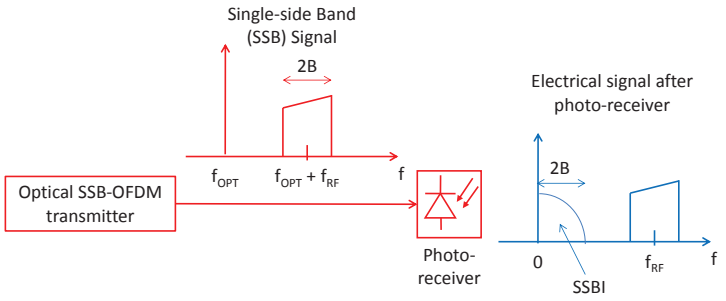

FIGURE 3.25: General form of an optical SSB-OFDM signal.

Let us consider that baseband OFDM signal $x_{OFDM}(t)$ given by (3.21) has unitary RMS value ($E[|x_{OFDM}(t)|] = 1$). Assuming a linear conversion between electrical and optical field, the optical SSB-OFDM signal is then defined as

$$x_{SSB}(t) = \sqrt{\alpha_{CSPR}} \cdot \exp\left(j2\pi f_{OPT} t\right) + \exp\left(j2\pi \left(f_{OPT} + f_{RF}\right) t\right) \cdot x_{OFDM}(t). \tag{3.70}$$

where α_{CSPR} is the ratio between the power of the optical carrier and the OFDM signal (Carrier-to-Signal Power Ratio (CSPR)). The signal at the output of the fiber affected by chromatic dispersion is given by (and expanding $x_{OFDM}(t)$ according to (3.21))

$$r_{SSB}(t) = \sqrt{\alpha_{CSPR}} \cdot \exp\left(j2\pi f_{OPT} t + j\phi\right) + \exp\left(j2\pi\left(f_{OPT} + f_{RF}\right)t + j\left(\phi + \Phi_D(f_{RF})\right)\right) \cdot \sum_{k=-N/2}^{N/2-1} X_k(t) \cdot \exp\left(j\frac{2\pi kt}{T} + j\Phi_D(k/T)\right). \quad (3.71)$$

where ϕ is the phase shift at the optical carrier caused by chromatic dispersion. At the receiver, the signal is detected by a square-law photodetector and the resulting electrical current is given by

$$I(t) = |r_{SSB}(t)|^2 = \underbrace{\alpha_{CSPR}}_{\text{carrier}\times\text{carrier beating}} + \underbrace{2\sqrt{\alpha_{CSPR}} \cdot \Re\left\{\exp(j2\pi f_{RF}t) \cdot \sum_{k=-N/2}^{N/2-1} X_k(t) \cdot \exp\left(j\frac{2\pi kt}{T} + j\Phi_D(k/T)\right)\right\}}_{\text{useful signal}} + \underbrace{\sum_{k_1=-N/2}^{N/2-1} \sum_{k_2=-N/2}^{N/2-1} X^*_{k_2}(t) X_{k_1}(t) \cdot \exp\left(j\frac{2\pi(k_1-k_2)kt}{T} + j(\Phi_D(k_1/T) - \Phi_D(k_2/T))\right)}_{\text{SSBI}} \quad (3.72)$$

The received electrical signal of (3.72) has three terms. The first one is a result of the beating of the optical carrier with itself. The second one is the useful signal. It is a result of the beating between the OFDM signal and the optical carrier. The received OFDM signal is a pass-band signal centered at f_{RF}. The third one is called SSBI. It has a spectral width of $2B$, and the PSD is maximum close to 0Hz and decreases linearly until $2B$. Compared to the DSB-optical signal, no fading is observed. A phase-rotation in each subcarrier appears, but it can be easily estimated and corrected.

In order to get rid of the SSBI, the straightforward solution is to choose $f_{RF} > 3B$ [246]. In this way, a frequency guard-band is inserted between the optical carrier and the OFDM signal, the SSBI does not interfere with the OFDM signal. Also, in [247], the author showed that by modulating only the odd-index subcarriers, the SSBI falls at the even-index subcarriers. This is observed from (3.72), where $k_1 - k_2$ is always even if k_1 and k_2 are odd. The drawback of these solutions is the bandwidth required by the photoreceiver, which is 4B. In order to decrease the bandwidth required at the photoreceiver, Peng *et al.* [248] demonstrated an optical SSB-OFDM transmission without the guard band using an iterative method to suppress SSBI.

It is important to note that the level of the SSBI (relative to the OFDM signal level) can be minimized by making α_{CSPR} as large as possible. This is intrinsically done in [120]. It is evident that the SSBI is also present in optical DSB-based OFDM transmission. However, since DSB-based transmission is inevitably intensity-modulation, the power of the optical carrier is generally much larger than the OFDM signal power ($\alpha_{CSPR} > 30dB$) and SSBI can be neglected.

The problem in increasing α_{CSPR} for SSB-based optical OFDM transmissions is that the receiver sensibility is sacrificed. This is because, for a fixed optical power, a higher value of the CSPR leads to lower powers of the useful OFDM signal, being more susceptible to noise. In other words, if the CSPR is high, most of the optical power is "wasted" on the optical carrier. The

author has shown in [249] that the receiver sensibility can be optimized by carefully adjusting the α_{CSPR} parameter. Moreover, in [247], the author shows that the optimum α_{CSPR} for the proposed optical SSB-OFDM scheme is 0dB.

3.3.3.3 Real-time implementation of high data-rate OFDM

A major bottleneck for the development of OFDM solutions for medium and long-range optical communications ($> 20km$) is the complexity of the OFDM modem, which makes it unattractive for implementation as compared to single-carrier OOK (cf. subsection 3.2.1). Commercially available ones that are used for RF communications have maximum bandwidth and data-rate in the range of 2GHz and 7Gbps respectively. Many efforts in showing the feasibility of optical OFDM transceivers have been made in the last few years for PON, where the bandwidth can go from 2.5GHz up to 10GHz.

Real-time Optical OFDM Implementation Using FPGA

The first end-to-end real-time optical OFDM demonstration was made in 2009 by Giddings [250]. It achieved a data-rate of 1.5Gbps over a 500m MMF-link, using a directly-modulated DFB. For the transmitter, the OFDM modulator includes the functions (cf. figure 3.26) S/P conversion, QAM-mapping, IFFT, add cyclic prefix, clipping and quantization, P/S conversion and DAC. The receiver performed the exact inverse operation except for clipping and quantization and added synchronization/channel equalization. The DSP part is implemented in FPGA as illustrated in figure 3.26. The DAC/ADC sampling speed of $f_s = 2Gsps$, using off-the-shelf components. For the IFFT/FFT implementation, the authors developed their own custom implementation, based on a highly pipelined architecture using extensive parallel processing stages for high-speed performance. Historically, the most common FFT algorithm is the Cooley-Tukey algorithm [251]. A simple and practical implementation in fixed-point arithmetic can be found in details in chapter 1.6.1 of [252]. An automatic code generation in Verilog for the Cooley-Tukey algorithm is provided by the Spiral tool [253]. An investigation of the performance of fixed-point implementation for the FFT is given in [254], using the Spiral tool. It explores a wide number of parameters and fixed-point precisions.

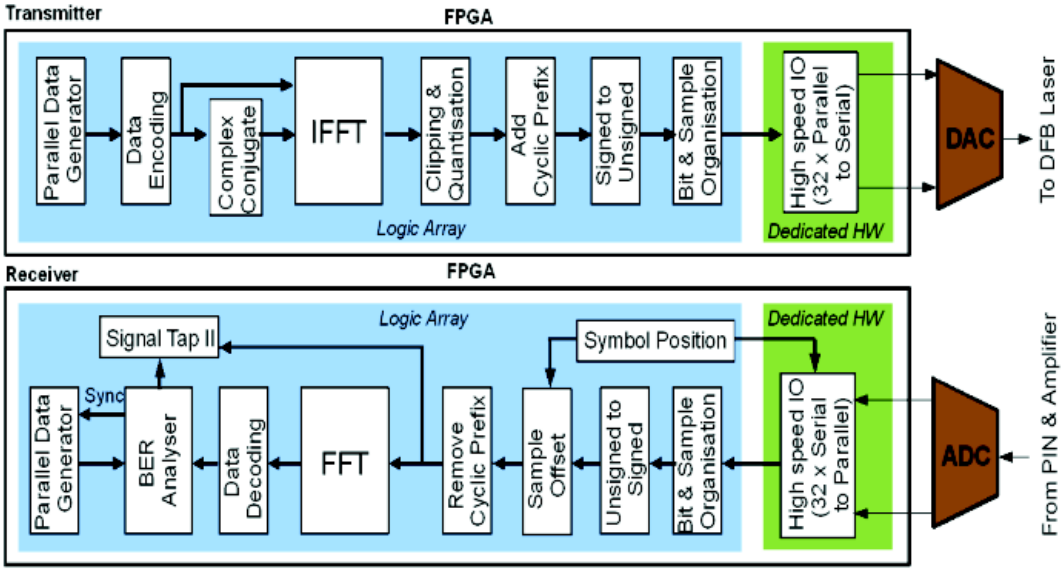

FIGURE 3.26: Real-time optical OFDM architecture using FPGA (Source [255]).

With increased DAC/ADC sampling speed $f_s = 4Gsps$ (but still off-the-shelf components), improved algorithms and system design, many real-time optical OFDM experiments followed, using the same basis as the first demonstrated OFDM transceiver [250], exhibiting increased transmission capacity and reach [56, 62, 255–262]. The latest results are reported in [62], demonstrating a dual-band OFDM transmission with a data-rate of 19.25Gbps over 25km SMF using a REAM intensity-modulator.

DSP implementation using ASIC technology

While FPGA-based implementations are practical to demonstrate the feasibility of real-time optical OFDM, they are not optimized for a given application. ASIC implementation allows to taylor the design to the considered application. Allowing for mass production, ASICs have the drawback of very high development costs.

A design study for ASIC implementation in terms of footprint and power consumption for high-speed optical OFDM transceivers was made by Bouziane and Milder [263, 264]. For each study, only the functions of QAM mapping/de-mapping, IFFT/FFT, clipping/scale and equalization are considered. The Verilog codes are generated by the Spiral tool [253] and processed by a standard 65nm CMOS cell-library.

In [263], the author considers a fixed sampling-rate of 28Gsps and two modulation formats - QPSK and 16-QAM - to enable data-rates of 21.8Gbps and 43.7Gbps respectively. Basically, the author investigates the required fixed-point precision for the 128-point IFFT/FFT operations for both Tx (Transmitter)/Rx (Receiver) and modulations formats. Evidently, the required fixed-point precision for 16-QAM is higher than for QPSK, resulting in higher footprint and power consumption. Once the precision is defined, it considers three different clock frequency values (therefore three different parallelization levels) in order to find the required power consumption and footprint for both Tx/Rx and modulation formats. A higher clock frequency would require less parallelization (lower footprint) but higher power consumption. A summary of the results of this work is shown in table 3.1.

Modulation Format	Minimum footprint / Maximum power consumption	Maximum footprint / Minimum power consumption
QPSK-Tx	$0.6mm^2$/0.4W	$1mm^2$/0.15W
QPSK-Rx	$1mm^2$/0.6W	$1.65mm^2$/0.25W
16-QAM-Tx	$0.75mm^2$/0.5W	$1.25mm^2$/0.2W
16-QAM-Rx	$1.75mm^2$/1.3W	$2.5mm^2$/0.4W

TABLE 3.1: Summary of results for ASIC implementation of 28Gsps optical OFDM [263].

A similar study is made in [264], but setting the data-rate fixed at 25Gbps, and varying the IFFT/FFT size and modulation formats. Concerning the number of points of the IFFT/FFT, higher the number of points, higher the power consumption and footprint. As the modulation formats are concerned, higher modulation formats tend to have better trade-off between footprint and power consumption, but higher fixed-point precision for the IFFT/FFT is required. Also, for a fixed data-rate, higher modulation formats enable the use of lower sampling-rates DACs/ADCs, hence lower clock frequencies for a given parallelization level.

State-of-the-art DACs/ADCs

A resolution of 6 bits is necessary so as to have less than 1dB SNR penalty for modulations up to 64-QAM as shown in [222]. Besides the resolution, the parameters that will have an impact on the system performances are the sampling speed (that should be at least twice the required bandwidth for the transmission), the SNR (or equally Effective Number of Bits (ENOB) which is $\approx SNR/6$), footprint and power consumption. It is necessary that the SNR provided by the

DAC and ADC do not cause significant SNR penalty. The SNR required by these components so that the SNR penalty (ΔSNR) is below a target value considering a SNR target (SNR_t) is written as

$$SNR_{DAC/ADC}[dB] = SNR_t[dB] - 10\log_{10}\left(10^{\frac{\Delta SNR[dB]}{10}} - 1\right). \tag{3.73}$$

For instance, considering a $SNR_t = 21.75dB$ (SNR necessary to achieve BER of 2.2×10^{-3} 64-QAM) and a SNR penalty of less than 1dB, the necessary DAC/ADC SNR is 27.6dB. As power consumption and footprint are concerned, evidently that we wish to have both as low as possible. Table 3.2 and 3.3 show a summary of the latest state-of-the-art of DACs and ADCs, respectively, that has been published in the last few years. The last items of each table are commercially available ones. We show that there are many technological possibilities for DAC and ADC implementation, with reasonable performance and power consumption.

Ref.	f_s	BW / Data-rate	Res.	SNR / ENOB	Foot-print	Power consump-tion	Tech.
[265]	56Gsps	26.9GHz	6 bits	5 bits ($f_{out} < 10Ghz$)	$0.6 \times 0.4mm^2$	0.75W	65nm CMOS
[266]	12Gsps	7.1GHz	8 bits	32.5dB ($f_{out} < 1.5Ghz$)	$0.6 \times 0.35mm^2$	0.19W	90nm CMOS
[267]	22Gsps	10Gbps	6 bits	-	$1.8 \times 2.5mm^2$	1.2W	$0.13\mu m$ SiGe BiCMOS
[268]	65Gsps	13GHz	8 bits	6.5bits ($f_{out} < 8GHz$)	-	0.75W	40nm CMOS

Table 3.2: State-of-the-art DAC technologies. Ref. : Reference, BW : Bandwidth, Res. : Resolution, Tech. : Technology.

Ref.	f_s	Res.	SNR / ENOB	Foot-print	Power consump-tion	Tech.
[269]	40Gsps	6 bits	4.5 bits ($f_{in} < 10Ghz$)	$4 \times 4mm^2$	1.5W	65nm CMOS
[270]	12Gsps	5 bits	25.1dB ($f_{in} < 6GHz$)	$0.44mm^2$	0.081W	65nm CMOS
[271]	16Gsps	6 bits	30.8dB ($f_{in} < 3GHz$)	$0.93 \times 1.58mm^2$	0.435W	65nm CMOS
[272]	24Gsps	6 bits	4.1 bits ($f_{in} < 12Ghz$)	$4x4mm^2$	1.2W	90nm CMOS
[273]	65Gsps	8 bits	5.7 bits ($f_{in} < 8Ghz$)	-	1.2W	40nm CMOS

Table 3.3: State-of-the-art ADC technologies. Ref. : Reference, Res. : Resolution, Tech. : Technology.

Comparison with Single-carrier OOK Modulation

In [274], a detailed comparison in terms of performance and power consumption between single carrier OOK and 16-QAM-OFDM for a fixed data-rate of 28Gbps is carried out.

Concerning the performance, it is shown that optical OFDM is capable of achieving a transmission distance of at least 35km SMF, while OOK modulation is limited to 15km SMF.

The power consumption of optical OFDM is found to be roughly 4 times the power consumption of the OOK modulation. However, an observation can be made. The author considers an OOK transceiver without Forward Error Correction (FEC). In recent standards for 10Gbps and beyond (e.g. XG-PON and 10G-EPON), FEC is mandatory to support the higher optical budgets [16, 23]. Taking into account this remark, the power consumption of an optical OFDM transceiver is estimated to be 2.4 times the power consumption of an OOK transceiver for SMF-links.

3.4 Summary of the Chapter

In this chapter, a review if the different optical receivers, single-carrier/multi-carrier transmission techniques and modulation formats applied to optical communication is presented.

The key conclusion of the optical receivers (direct-detection / coherent-detection) analysis is that, in spite of the fact that coherent receivers can perform better than direct-detection receivers, the high cost makes it unattractive for the considered application. This justifies our choice for direct-detection receiver architectures.

An important point reviewed in section 3.2 is the definition of the precision in the BER and SNR estimator as a function of the bits/symbols analyzed. This serves as reference for the upcoming experiments and simulations in order to have accurate results.

The features and impairments of OFDM for optical communications are analyzed in section 3.3. which is very important for the good comprehension of this thesis. As a conclusion, the fading caused by DSB cancellation will definitely decrease the capacity of the link for IM/DD transmission as the reach increases. The use of SSB-OFDM transmission avoids the frequency fading caused by chromatic dispersion and can indeed maximize the [bit-rate $\times$ reach] product of the OFDM transmission.

In subsection 3.3.3.3, an extended review of the available components required for building an OFDM modem is analyzed. The conclusion of this part is that OFDM modems for bandwidths up to 6GHz can be made with reasonable power consumption and footprint using CMOS technology. According to [274], power consumption considering 16-QAM-OFDM is still about 2.4 times higher than OOK modems (including FEC) for the same bit-rate, while reach is increased by at least twofold.

In section 3.2, a review of single-carrier modulation formats is presented. An experimental validation of the simulation platform built with the models presented throughout this thesis is made for OOK modulation, showing the good accuracy of the tool. This is a very important result because it shows that the performance of an optical system can be analyzed for a given optical transmitter (DML/MZM) and receiver using the simulation tool with precise results. Another important point of this chapter is that the precisions in the BER (equation (3.10)) and SNR (equation (3.16)) estimators are defined. They are used in chapters 4 and 5 to calculate the number of OFDM symbols required to give an accurate estimation of these parameters.

The impairments and features of OFDM for optical communications are analyzed in section 3.3, which is very important for the good comprehension of this thesis. As a conclusion, the fading caused by DSB cancellation will definitely decrease the capacity of the link for IM/DD transmission. This is more evident in section 1.3.5.1 where the state-of-the-art for IM/DD optical OFDM transmissions is presented. A negative transmitter chirp can increase system's capacity for baseband transmissions as compared to a positive and zero chirp transmission. The use of

SSB-OFDM transmission avoids the frequency fading caused by chromatic dispersion and can indeed maximize the [bit-rate × reach] product of the transmission.

In subsection 3.3.3.3, an extended review of the available components required for building an OFDM modem is analyzed. The conclusion of this part is that OFDM modems for bandwidths up to 6GHz can be made with reasonable power consumption and footprint using CMOS technology. According to [274], power consumption considering 16-QAM-OFDM is still about 2.4 times higher than OOK modems (including FEC) for the same bit-rate, while reach is increased by at least twofold.

Chapitre 4

Experimental Validation of the Algorithms and Simulation Platform

In the previous chapters, the basic building blocks, transmission techniques and modulation formats for optical communications systems were described. This study led to the development of a dedicated simulation platform to assess the performances of different optical components in different configurations of the optical system.

The simulation platform is developed in Rsoft Optsim in co-simulation with Matlab. In the simulation tool, each component is a black box with a number of inputs/outputs and a set of parameters to define it. A print-screen of the simulation tool is shown in figure 4.1 for the direct-OFDM modulation of a single-mode III/V laser. Each box represents a transfer function and eventually noise based on the models previously described in chapters 2 and 3. Note that the boxes for the semiconductor DML, MZM, propagation in the SMF and optical receivers are available as a part of the Optsim tool. The silicon photonics MZM, ring-resonator modulator, OFDM modulator and demodulator are implemented in Matlab as a part of the work realized during this thesis. The propagation through the fiber is simulated using the split-step Fourier method. The DML is simulated in Optsim by inputting the physical characteristics of the laser and solving the laser rate-equations (2.24), (2.25) and (2.26).

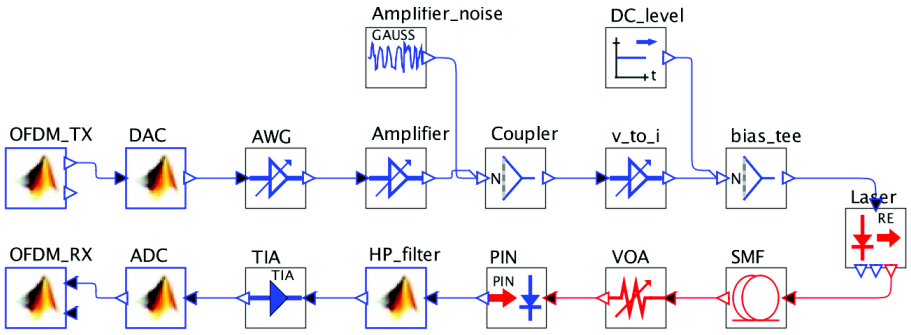

FIGURE 4.1: Simulation of optical communcation systems in RSoft Optsim and Matlab.

In order to evaluate the accuracy of the results provided by the simulation tool, an experimental validation using commercial-available components is presented in this chapter. Two optical transmitters are assessed - a III/V DFB at 1.55μm from 3S Photonics (model 1915LMA) and a $LiNbO_3$ optical IQ modulator from Photline (model MXIQ-LN-40). Three different transmission techniques are validated. First, 10Gbps single carrier OOK modulation is evaluated in terms of sensitivity and reach. Then, a 10GHz-bandwidth IM/DD optical OFDM with adaptive bit and power loading is assessed - the achievable data-rate and reach in both simulation and experiment are compared. When the optical IQ modulator is used as an intensity modulator,

only one of the two MZMs is used. The final analysis concerns SSB-OFDM modulation using an optical IQ modulator as optical transmitter.

The characteristics of these transmitters as well as common components for the experiments (SMF and optical receiver) are summarized in table 4.1. Further technical details of the optical and electrical components used in this chapter as well as particularities for the OFDM modem implementation in Matlab are described in appendix B. The chirp parameter α of the DML is estimated using the method explained in appendix A.3.

DML (3S Photonics 1915LMA)	
Threshold current	20mA
Optical output power ($I_b = 100mA$)	7.6dBm
-3dB bandwidth ($I_b = 100mA$)	17GHz
Chirp parameter (α)	2.8
RIN (typical)	-165dB/Hz (from 0.1GHz to 10GHz)
CW laser source (Tunics External-cavity Laser)	
Optical output power	10.5dBm
Linewidth	$< 100kHz$
Wavelength	$1.55\mu m$
Optical IQ modulator (Photline MXIQ-LN-40)	
V_π	7V
Optical insertion loss	5dB
-3dB bandwidth	20GHz
Residual chirp (α_{MZM})	< 0.1
Standard SMF	
Attenuation	0.2dB/km
Dispersion parameter	$16ps/(nm \times km)$
Optical receiver (Newfocus PIN+TIA 1554-B)	
Conversion Gain	750V/W
NEP	$33pW/\sqrt{Hz}$
-3dB bandwidth	12GHz

TABLE 4.1: Characteristics of the commercial components used in the experiments.

Except for the DML, the characteristics detailed in table 4.1 are given directly as input for the building blocks of the simulation tool. However, simulating the behavior of a given DML is not straightforward because its physical characteristics are unknown in principle. In this way, we use a numerical tool from RSoft to estimate the physical characteristics of the DML from the behavior parameters, which were obtained by characterization of the DML. This process is described in details in appendix A. The physical characteristics of the DFB from 3S Photonics are described in table A.4, which are used as input for the simulations.

The optical transmitters used in the experiments are state-of-the-art commercial components, therefore unsuitable to be placed at the ONU, for instance. They could serve as solutions for future PON in downlink direction. In order to fulfill the requirements for NG-PON2, 10Gbps with OOK modulation (for the use with WDM) or 40Gbps OFDM modulation technique are required. Reach should be at least 20km and serve at least 32 users (15dB attenuation without accounting the fiber), but it is desirable to achieve up to 100km SMF and 1000 users to be compliant with LR-PON.

4.1 Single-carrier OOK Modulation Validation

The general experimental set-up is depicted in figure 4.2. A Pseudo-Random Binary Sequence (PRBS) generator (ParBERT N4872A from Agilent) generates a 10Gbps OOK signal. The sequence length is $2^{15} - 1$.

When the DML is used as optical transmitter, the OOK signal is combined with a bias current of 100mA using a bias-tee. In the MZM case, a voltage source is connected to the modulator to adjust the bias voltage to the quadrature point. Modulation depth is $5V_{pp}$ ($100mA_{pp}$) in both cases. The fiber span is varied from 0km (Back-to-back (B2B) configuration) to 50km standard SMF. The received optical power is varied with a Variable Optical Attenuator (VOA).

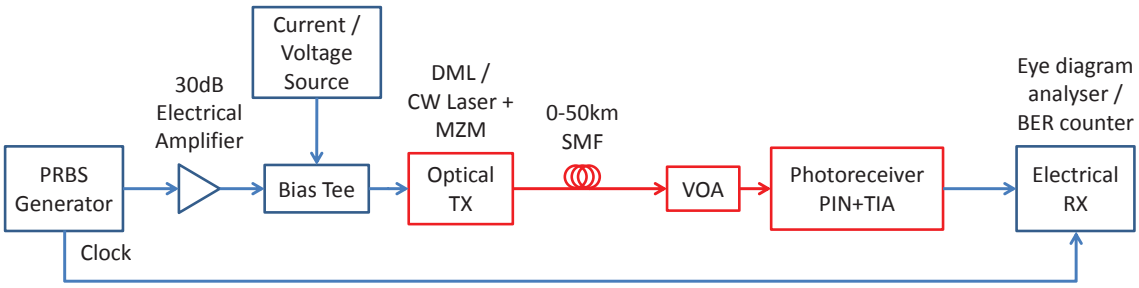

FIGURE 4.2: Experimental set-up for the OOK transmission.

In the simulation tool, in order to avoid very long simulation times, the BER is estimated from the Q-factor as indicated in (3.8) for 10^4 bits, and the received OOK signal is said "error-free" for BER $< 10^{-12}$. In the experiment, the BER at low values ($BER < 10{-}11$) is counted with at least 100 errors measured, which gives a precision of 10% in the BER estimator, while for higher values of the BER, a much higher number of errors is counted, and the precision is negligible.

4.1.1 Fundamental Limit of the [bit-rate x reach] Product

In the following, we evaluate the achievable [bit-rate × distance] product limited by chromatic dispersion for both types of optical modulators. This limitation is analyzed visually using an eye diagram analyzer and qualitatively by measuring the BER.

4.1.1.1 Case I - DML from 3S Photonics

First, the DML is considered. We observe that at 10km SMF, an error-free transmission is achievable. However, at 20km SMF, the signal gets considerably distorted and an error-free transmission is no longer possible ($BER > 10^{-4}$ in the experiment and $BER > 10^{-7}$ in the simulation tool). Figure 4.3 show the received eye diagram after 20km of SMF in the experiment and in the simulation platform, showing that the eye is very similar in both cases and it is almost completely closed.

Finally, we evaluated in the experiment the achievable bit-rate for an error-free transmission over 20km, 40km and 50km of SMF, which is shown in figure 4.4. The right-vertical-axis represents the product [bit-rate $\times\sqrt{reach}$]. It remains quasi-constant as the fiber length increases (less than 6% variation from the mean value), as predicted in subsection 2.1.2.3 for optical sources with spectral width below the modulation bandwidth. The product has a value of about $40Gbps \times \sqrt{km}$ which is higher than the prediction in [141] for $\alpha \approx 2.8$ of about $31Gbps \times \sqrt{km}$. For the latter, the computation assumes that the pulse broadening does not exceed 1/5 of the bit period ($\Delta T \leq 1/(5B)$). Relaxing this constraint to $\Delta T \leq 1/(4B)$ as assumed in [139], the

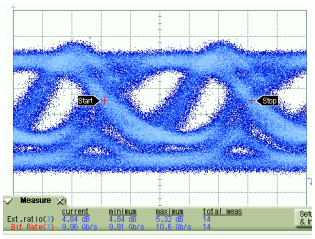

(a)

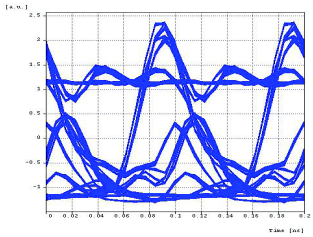

(b)

FIGURE 4.3: Eye diagram at 10Gbps after 20km SMF using a DML in (a) experiment and (b) simulation.

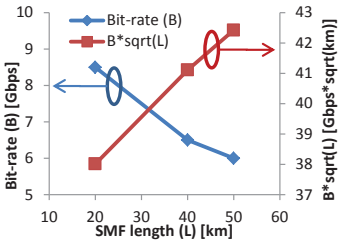

FIGURE 4.4: Achievable bit-rate as a function of the SMF length.

maximum bit-rate-square-root-distance predicted is increased to about $39Gbps \times \sqrt{km}$ which is closer to the experimental results.

4.1.1.2 Case II - MZM from Photline

Concerning the OOK transmission using the zero-chirped MZM, we were able to transmit over 50km SMF (maximum fiber length available in the laboratory) with no errors. Even after 50km of SMF, the eye diagram is wide open as illustrated in figure 4.5. By using the simulation tool, the maximum transmission distance for 10Gbps data-rate for the MZM case is evaluated. Figure 4.6 shows the minimum BER (computed from the Q factor) for several fiber lengths from 80-140km. For an "error-free" transmission, the reach is about 80-90km, in accordance with the predicted value in subsection 2.1.2.2.

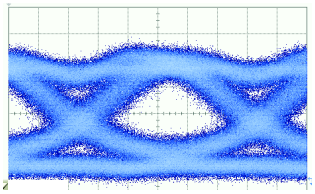

(a)

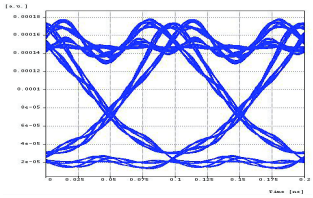

(b)

FIGURE 4.5: Eye diagram at 10Gbps after 50km SMF using a MZM in (a) experiment (b) simulation tool.

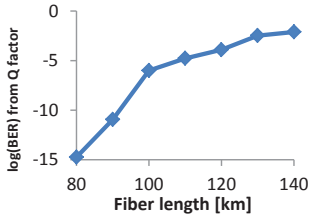

FIGURE 4.6: BER from Q-factor as a function of the SMF length.

4.1.2 Sensitivity Penalty Due to Chromatic Dispersion

The performance of our OOK transmission system are evaluated by analyzing the BER as function of the received optical power. The sensitivity is defined as the average received optical power required to achieve a BER of 10^{-9}.

The extinction ratio for the DML case is 7dB, while for the external modulator is 8.5dB. The finite extinction ratio results in a sensitivity penalty of 1.8dB and 1.3dB respectively (as indicated by (3.9)).

Figure 4.7 shows the BER versus the received optical power for the DML and MZM configurations and table 4.2 summarizes the experimental and simulated results. A sensitivity difference ranging from 1.25 to 1.5dB is noted in each case. While a sensitivity penalty for the DML case at 10km varies from 1.75dB between experiment and simulation, a good agreement for the sensitivity penalties is found in the MZM case (less than 0.5dB difference).

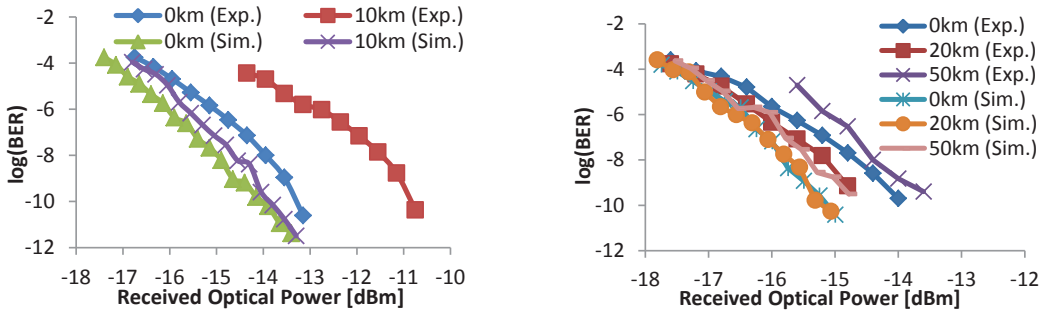

(a) DML (b) MZM

FIGURE 4.7: BER as a function of the received optical power.

Case	S. (Exp.)	S. (Sim.)	ΔS 10km (Exp.)	ΔS 10km (Sim.)	ΔS 20km (Exp.)	ΔS 20km (Sim.)	ΔS 50km (Exp.)	ΔS 50km (Sim.)
DML	-13.5dBm	-14.75dBm	2.2dB	0.5dB	-	-	-	-
MZM	-14.25dBm	-15.75dBm	-	-	-0.5dB	0	0.5	0.25

TABLE 4.2: Summary of the sensitivity and penalties due to chromatic dispersion in both DML and MZM cases. S. : Sensitivity, ΔS : Sensitivity penalty.

4.2 Multi-carrier OFDM Validation

For the optical OFDM experiments/simulations presented in the following subsections, the OFDM signal is generated and demodulated off-line using Matlab. It is defined in a classic manner as described in subsection 3.3.1. The OFDM symbol configuration is specified in each case. Before loading the samples to the Arbitrary Waveform Generator (AWG), a clipping with clipping ratio with $k = 3$ is performed.

The OFDM samples are downloaded to the AWG Tektronix AWG70000 for the digital-to-analog conversion. The Digital Sampling Oscilloscope (DSO) used is the DSA72004C to capture the analog data, and sends the digital samples to the computer for off-line demodulation. Both AWG and DSO sample at $f_{s_{DAC}} = f_{s_{ADC}} = 25Gsps$. The clock from the DAC and ADC are locked between each other to avoid SFO impairment.

For the simulation set-up, the high-frequency roll-off and the noise from the electric components are added throughout the link. The noise PSD of the received signal given in RMS value relative to Volts is calculated using

$$N_{PSD_k} = \sqrt{\frac{|H_k|^2}{SNR_k \cdot 2N_{DATA}/N}} \tag{4.1}$$

where H_k is the coefficient for the frequency response of the k^{th} subcarrier, SNR_k is the SNR of the k^{th} subcarrier, N_{DATA} and N are the number of data and total subcarriers.

4.2.1 Adaptive Optical OFDM with IM/DD Transmission using Commercial E/O Coverters

In order to maximize data-rate given the frequency-fading of the intensity-modulated signal caused by chromatic dispersion, a bit and power loading algorithm is used. The OFDM symbol configuration used in the experiments/simulations for both transmitters is detailed in table 4.3. The real-valued OFDM signal is generated using the Hermitian symmetry property of the FFT

(cf. subsection 3.3.1.6). Note that the actual cyclic prefix length is $N_{CP}/2$. The other $N_{CP}/2$ are attributed to the cyclic suffix to give a margin in the FFT window synchronization as explained in appendix B.1.

FFT Size	$N = 256$
Cyclic prefix+suffix samples	$N_{CP} = 4$
Subcarrier spacing	$\Delta f = f_{s_{DAC}}/N = 97.65MHz$
Number of data carriers	$N_{DATA} = 101$
OFDM bandwidth	$B = f_{s_{DAC}} \cdot N_{DATA}/N = 10GHz$

TABLE 4.3: OFDM symbol configuration for the optical IM/DD link with adaptive bit and power loading.

The number of OFDM symbols per acquisition in the experiment is 4000. For the simulations, it is reduced to 1000 because of the larger memory required.

The simulation and experimental procedure for setting-up the bit and power algorithm is the following. A first transmission of QPSK symbols is made to evaluate the SNR per subcarrier. The SNR is calculated from the EVM using (3.13). The optimum bit and power distribution is calculated according to the algorithm described in appendix C.3. The BER target is 2.2×10^{-3}. The total data-rate B is calculated using the following equation

$$B = \frac{\sum b_k \cdot f_{s_{DAC}}}{N + N_{CP}} \tag{4.2}$$

where b_k is the number of bits carried by the k^{th} subcarrier and $f_{S_{DAC}}$ is the DAC sampling-rate. A second transmission with the bit and power allocation applied is performed to verify the achieved BER.

4.2.1.1 Case I - DML from 3S photonics

We analyze first the IM/DD optical OFDM performance with the DML as the optical transmitter. The experimental set-up is depicted in figure 4.8.

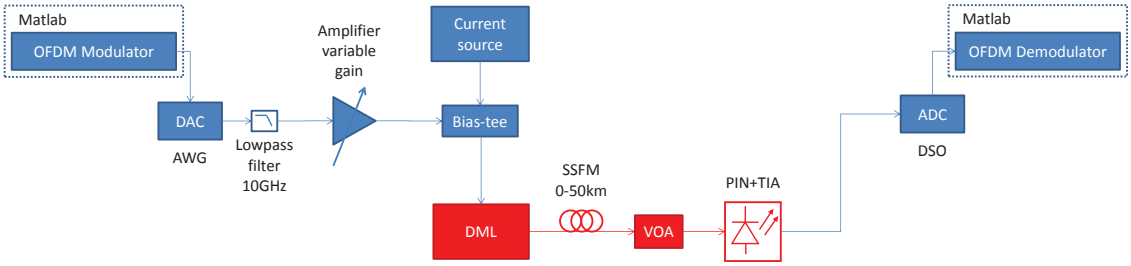

FIGURE 4.8: General experimental set-up for the adaptive IM/DD optical OFDM with commercial DML for uplink.

For this experiment, the modulation depth of the modulator is optimized according to the fiber span length. As explained earlier, a high modulation depth introduces considerable chirp in the modulated optical signal, which interacts with chromatic dispersion and degrades the SNR [243]. The peak-to-peak modulation currents are $100mA_{pp}$ (B2B), $80mA_{pp}$ (10-20km), $63mA_{pp}$ (30km) and $50mA_{pp}$(40-50km). The bias current is 80mA. Before the optical receiver, a VOA is used to adjust the received optical power.

Figure 4.9 shows the achievable data-rate at a received optical power of -6dBm for both experiment and simulation. In practice, the received optical power at the ONU is generally lower

than that. However, since the transmitter performance is evaluated, it is necessary to consider a high value of the received optical power so that photo-receiver noise is low. The form of the curve is very similar in both simulation and experimental results but an offset is observed. This is investigated by observing the SNR distribution and noise PSD (calculated from (4.1)) predicted in simulation and obtained in the experiment, illustrated in figure 4.10. We note that noise power is enhanced in the lower frequencies in the experiment, which is not accurately predicted in the simulation platform, causing the achievable data-rate to be actually lower than predicted by simulations.

The exact reason for the low-frequency noise enhancement is unknown for the moment. It can be verified that it comes from one of the optical components, because this noise enhancement is not seen in the electrical B2B transmission (cf. figure B.6). From appendix B.7, the electrical part of the link contributes for a 2dB SNR penalty in the region between 4-6GHz, and negligible otherwise.

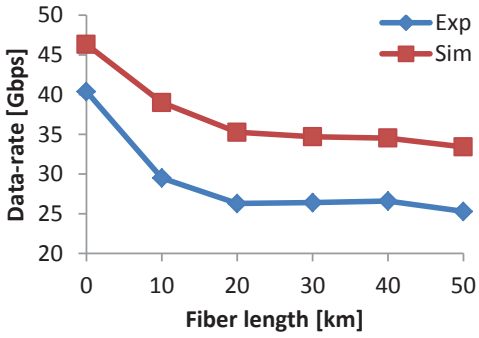

FIGURE 4.9: Achievable data-rate as a function of the fiber length for the DML, received $P_{opt} = -6dBm$.

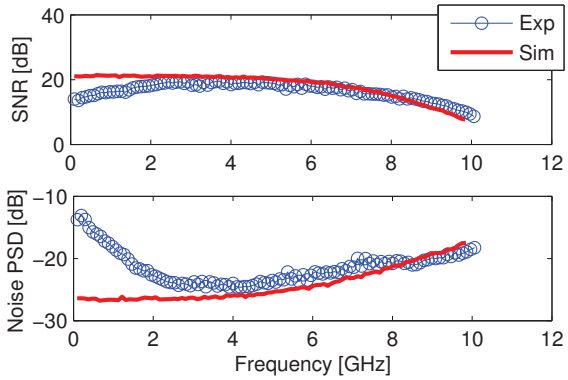

FIGURE 4.10: SNR and noise PSD per subcarrier in optical B2B and received $P_{opt} = -6dBm$.

Moreover, figure 4.11 shows the achievable bit-rate as a function of the received optical power for B2B, 20km and 50km fiber span length. A good agreement between experimental and simulated results is observed for lower received optical power, where thermal noise from the receiver dominates. At a data-rate of 20Gbps, a sensitivity penalty of 3dB is measured at 20km and 50km as a consequence of the lower electric power driving the DML. The achieved BER in any case is lower than 2.2×10^{-3}. At a received optical power of -6dBm, the transmission achieves a spectral efficiency of 4.1bps/Hz, 2.8bps/Hz and 2.5bps/Hz in optical B2B, 20km and 50km of SMF.

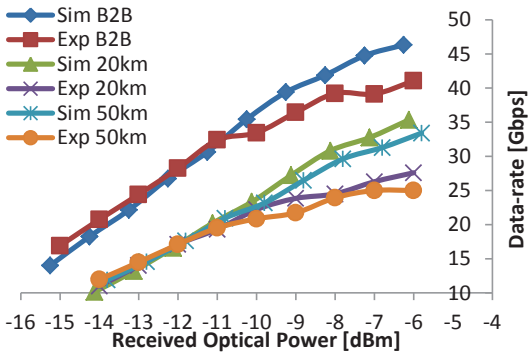

FIGURE 4.11: Achievable bit-rate as a function of the received optical power for optical B2B, 20km and 50km of SMF, using a commercial DML as transmitter.

4.2.1.2 Case II - MZM from Photline

In the following, the optical IM/DD OFDM performance with the MZM as the optical transmitter is assessed. The experimental set-up is depicted in figure 4.12.

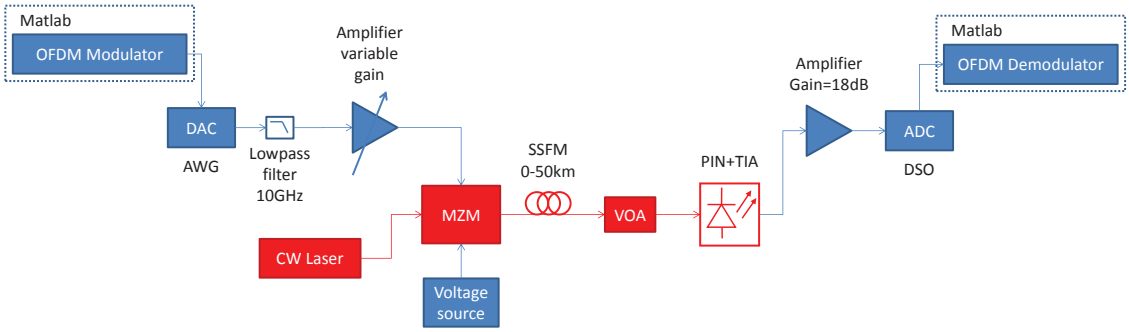

FIGURE 4.12: General experimental set-up for the adaptive IM/DD optical OFDM with commercial $LiNbO_3$ MZM for uplink.

In this experiment, the electric signal amplitude modulating the MZM is fixed to approximately $8V_{pp}$, and the MZM is biased at quadrature. Figure 4.13 shows the achievable data-rate as a function of the fiber span length for a received optical power of -8dBm. The achievable data-rate is above 40Gbps in any case, showing a minor degradation at the transmission distance increases. The variations in the experimental data-rate may be attributed to minor biasing drifts for the MZM, because it was not controlled automatically. If the SNR precision is taken into account, a $\Delta SNR = 0.38dB$ confidence interval is calculated from (3.16). In optical B2B, this translates in an interval between 42.1Gbps and 43.3Gbps in the experimental data-rate, showing to be a precise measure.

Moreover, figure 4.14 displays the frequency response, SNR per subcarrier and bit allocation for the B2B and 50km case after the bit and power loading. We observe that at 50km the bandwidth is limited to about 8GHz as a consequence of the frequency fading caused by the DSB cancellation. But the power left by the nulled subcarriers is re-distributed to the other efficient data subcarriers. This is the reason why a slightly SNR improvement is seen up to 4GHz at 50km compared to the optical B2B transmission.

At a received optical power of -8dBm, a SNR degradation of about 3dB compared to the electrical B2B measures in appendix B.7 is calculated, which comes mostly from non-linear degradation of the MZM and thermal noise from the receiver.

Finally, figure 4.14 shows the data-rate as a function of the received optical power, showing a very good agreement between simulation and experimental results. The measured BER in any case is below 2.2×10^{-3}, and no significant sensitivity penalty is observed below 30Gbps.

As a conclusion, the MZM performs better than the DML because of the lower chirp, which affects both the frequency response of the link and allows to have a higher modulation depth as the transmission distance increases.

4.2.2 Optical SSB-OFDM Transmission using Commercial E/O Coverters

As explained in subsection 3.3.3.2, optical SSB modulation can be applied to eliminate the frequency fading caused by chromatic dispersion and DSB cancellation. Because optical filtering is not a viable option for the considered application for the reasons explained in subsection 1.3.5.1, an efficient implementation of the optical SSB-OFDM transmitter is considered, which was first proposed in [126]. The schematic view of the transmitter is shown in figure 4.16.

A complex OFDM signal is generated. Ideally, all subcarriers carry data, but, in practice, a few subcarrier in the edges can be set to zero for oversampling. A RF-tone with frequency

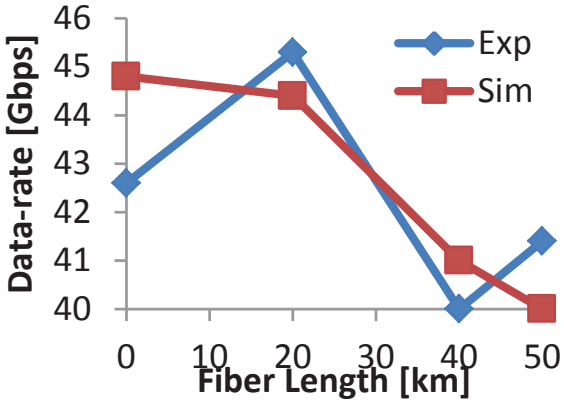

FIGURE 4.13: Achievable data-rate as a function of the fiber length for the MZM, received $P_{opt} = -8dBm$.

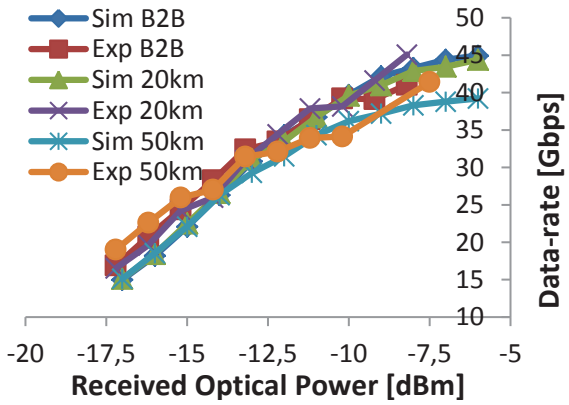

FIGURE 4.14: Data-rate as a function of the received optical power for the MZM.

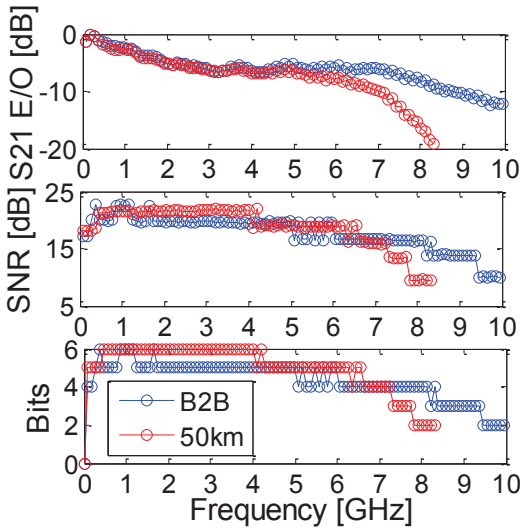

FIGURE 4.15: Experimental results - frequency response, SNR and bits per subcarrier, MZM as optical transmitter in optical B2B and 50km SMF, received $P_{opt} = -8dBm$.

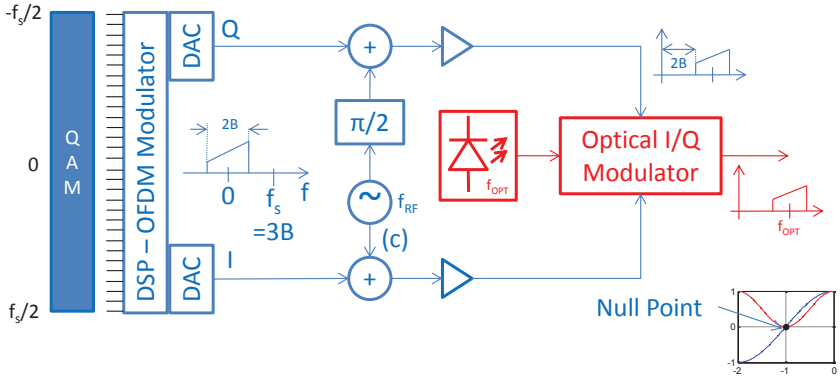

FIGURE 4.16: Schematic view of the SSB-OFDM transmitter proposed in [126].

$f_{RF} = 3B$, where B is the baseband bandwidth of the OFDM signal, is added to the OFDM signal with a phase shift of $\pi/2$ between in-phase and quadrature arms. The RF frequency is chosen with the purpose of eliminating the SSBI as explained in subsection 3.3.3.2. It drives an optical IQ modulator in the null intensity biasing point. In this way, the electrical field of the modulated signal is translated linearly to the optical field of the optical carrier as indicated by the transfer function in (2.42). A virtual optical carrier is formed at $f_{opt} + f_{RF}$.

This architecture has the advantage of being colorless and having a single laser source for generating the optical signal, contrary to [122]. In addition, it avoids the use of broadband RF mixers, simplifying the transmitter. Also, the possibility of using silicon photonics to tightly integrate the electro-optical components of this transmitter is a great asset for the considered application. A silicon photonics implementations of the optical I/Q modulator is analyzed in subsection 5.2, in which the sensitivity penalty associated to the silicon modulator impairments is calculated. For that purpose, an experimental validation of the optical SSB-OFDM simulation routine is done using the commercial optical IQ modulator from Photline to assess the accuracy of the simulation.

4.2.2.1 Experimental/Simulation Set-up

The experimental set-up for the optical SSB-OFDM transmission is depicted in 4.17.

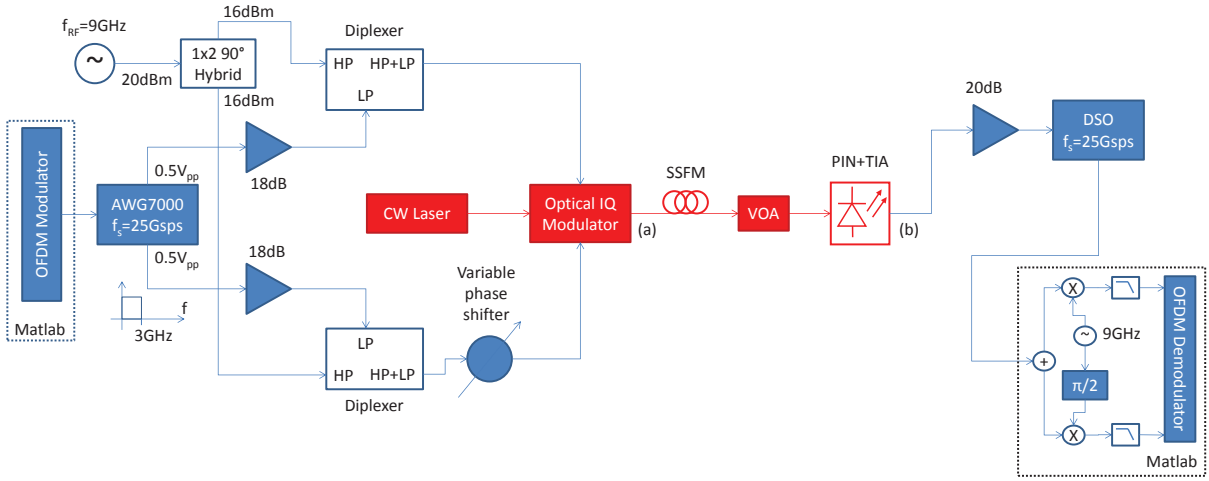

FIGURE 4.17: Experimental set-up for the optical SSB-OFDM transmitter with analog RF-tone insertion. HP :High-pass ; LP :Low-pass.

The OFDM symbol configuration is shown in table 4.4. The increase in the number of cyclic prefix samples as compared to the previous IM/DD OFDM experiment is due to the relative time misalignment between I and Q channels, which can be in the order of a few samples. The method explained in subsection 3.3.2.3 is used to correct residual IQ imbalances, with 2000 probe OFDM symbols before the 4000 data OFDM symbols per acquisition. The modulation format is the same for every subcarrier - QPSK (11.5Gbps) or 16-QAM (23Gbps).

Note that the useful OFDM baseband bandwidth of 3GHz (or 6GHz complex bandwidth) is far below the total available bandwidth of the AWG. The bandwidth limitation for this experiment comes from the photoreceiver (12GHz) and the diplexer. The diplexer is used to effectively add together the RF and baseband OFDM signal. It has two input ports : 1) A low-pass (LP) input with 2.8GHz cut-off frequency which is connected to the baseband OFDM signal ; and 2) high-pass (HP) input with pass-band from 5.5GHz to 12GHz which is connected to the 9GHz-RF tone.

Modulation format	QPSK or 16-QAM (same for every subcarrier)
FFT Size	$N = 256$
Cyclic prefix+suffix samples	$N_{CP} = 8$
Subcarrier spacing	$\Delta f = f_{s_{DAC}}/N = 97.65MHz$
Number of data carriers	$N_{DATA} = 60$
OFDM bandwidth	$B = f_{s_{DAC}} \cdot N_{DATA}/(2N) = 3GHz$

TABLE 4.4: OFDM symbol configuration for the optical SSB-OFDM experiment/simulation.

The CSPR is computed to be about 6dB and the modulating peak-to-peak voltage is about $8V_{pp}$. The CSPR could not be optimized to 0dB because of the limited OFDM power in the RF amplifier output. The optical output power of the optical IQ modulator is -10dBm, which limits the reach of the transmission. Before the photoreceiver, a VOA is placed to adjust the received optical power. The down-conversion to baseband is made numerically in Matlab, with the CFO parameter previously estimated (cf. subsection 3.3.2.3) and applied to the receiver LO frequency in the program.

A total of 2.4×10^5 complex symbols per acquisition are analyzed, which results 4.8×10^5 bits with QPSK modulation. According to subsection 3.2, this gives a good accuracy on the BER estimation at the BER target of 2.2×10^{-3}, either by direct count of the error bits (3% precision) or calculating it from the SNR (BER uncertainty below 4×10^{-5}). The BER value given is the worst case between the direct count and estimated from SNR.

In the simulation platform, because of the relatively large computational time to run the simulations, only 500 data OFDM symbols were generated per acquisition. In this case, the BER is estimated from the SNR. The rest of the simulation parameters are the same as the ones from the experiment.

4.2.2.2 Results and Discussion

A key utility of the simulation platform is to calculate the penalty associated to the electrical components of the link. For that purpose, a first simulation run is performed without accounting the high frequency roll-off and noise from the electrical part of the link. Considering QPSK modulation, a 2dB sensitivity penalty is calculated in optical B2B at a BER of 2.2×10^{-3} for QPSK modulation. In [275], the author shows that a pre-emphasis technique can minimize penalty due to high-frequency roll-off.

The optical spectrum in point (a) and the electric spectrum in point (b) of figure 4.17 obtained in the experiment are shown in figure 4.18. In the optical spectrum, one can note a secondary attenuated optical carrier at the left side. This is mostly due to phase imbalance between I and Q arms of the optical modulator. The influence of this secondary tone is negligible since a power ratio of 25dB compared to the main optical carrier is observed. In the electric spectrum, we can properly observe the SSBI between 0 and 6GHz, and the OFDM signal centered at $f_{RF} = 9GHz$.

Prior to comparing simulation and experimental results, the effectiveness of the optical IQ imbalance and CFO correction are analyzed in the experiment.

As discussed in subsection 3.3.2.3, the IQ imbalance arises from phase, amplitude or time misalignment. Since both MZMs from the optical modulator are identical, amplitude and time misalignment are originated mostly from the AWG and the driving electrical components. Phase imbalance is caused by non-ideal $\pi/2$ phase shift of the analog RF carrier between in-phase and quadrature components, or non-ideal $\pi/2$ between the two MZMs of the optical modulator. It

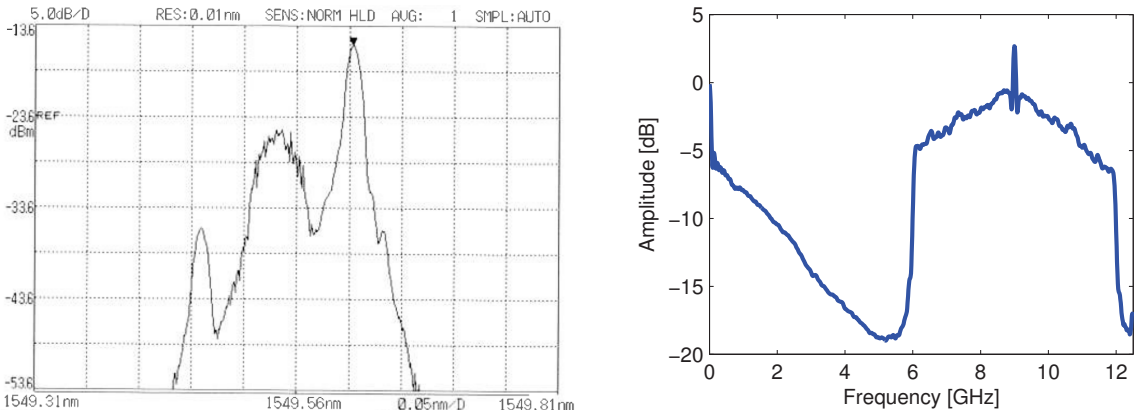

(a) (b)

FIGURE 4.18: Optical and electric spectrum in points (a) and (b) of the experimental set-up described in figure 4.17.

is corrected with the method described in subsection 3.3.2.3. Figure 4.19 displays the SNR per subcarrier before and after the IQ imbalance, showing a clear improvement of up to 6dB.

The presence of IQ imbalance is also evident from figure 4.20, where the QPSK constellation of the 15^{th} subcarrier before the correction is displayed - because the IQ imbalances cause interference between positive and negative index subcarriers, the received symbol in a given subcarrier is a sum of the actual data symbol and the interferer symbol, multiplied by a complex gain.

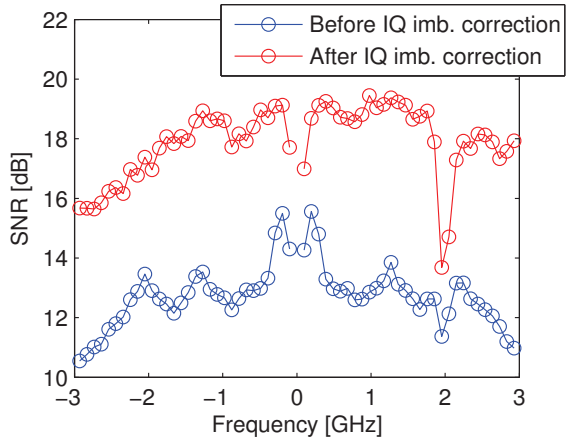

FIGURE 4.19: SNR per subcarrier before and after the IQ imbalance correction.

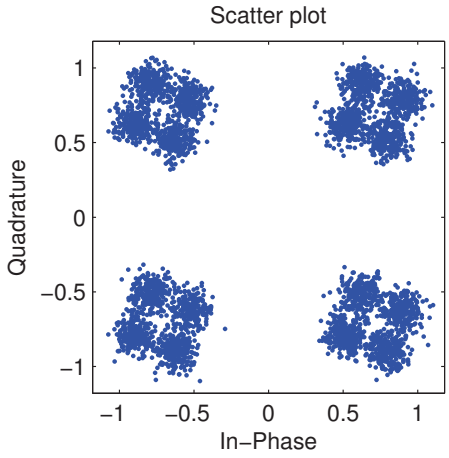

FIGURE 4.20: Received constellation before IQ imbalance correction.

The CFO impairment is also analyzed. The evidence of the presence of CFO is that, without correction, the EVM of the OFDM symbols increase in time as shown in figure 4.21. This is because the CFO impairment adds a phase shift in each subcarrier which increases in time as explained in subsection 3.3.2.3. This is observed in the received QPSK constellation of the last OFDM symbol without CFO correction in figure 4.22. Even after channel equalization, the QPSK symbols appears to be rotated. The CFO is correctly corrected - this is evident from figure 4.21 where the mean EVM per OFDM symbol changes very little in time compared to the case without CFO correction.

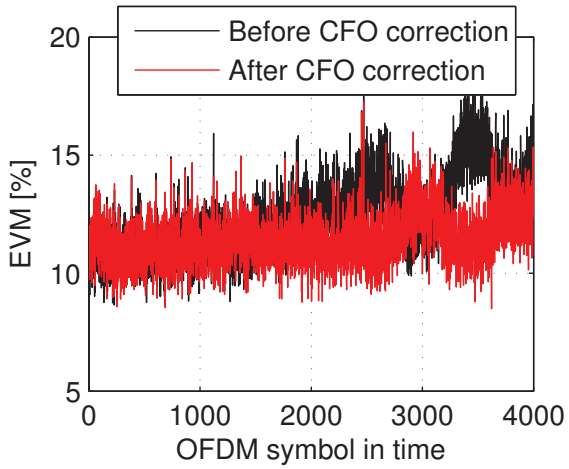

FIGURE 4.21: Mean EVM per OFDM symbol before and after CFO correction.

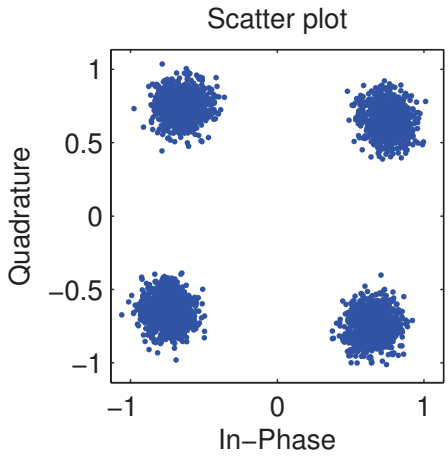

FIGURE 4.22: Received constellation on the 30^{th} subcarrier before CFO correction.

Finally, we compare the experiment performance against the predicted ones by the simulation platform. Figure 4.23 depicts the frequency response (S21 E/O) and SNR per subcarrier from the experiment and that predicted by simulation for a received optical power of -10dBm in optical B2B. A good agreement is observed. It should be noted that one of the sidebands experiences higher roll-off than the other one as a consequence of the fact that the received electric OFDM signal is centered at 9GHz as illustrated in figure 4.18(b).

Moreover, the BER for QPSK modulation as a function of the received optical power is illustrated in figure 4.24 for both B2B and 20km SMF cases, where a sensitivity of -16.5dBm for a BER of 2.2×10^{-3} is found. A minor disagreement between experiment and simulation is observed at higher received optical powers, as a consequence an over-estimation of the SNR in the simulation platform as illustrated in figure 4.23. However, the experimental and simulated results match very well at lower received optical powers, where the dominating noise is the thermal noise from the receiver. Furthermore, a 16-QAM transmission is successfully achieved with a BER lower than 7.8×10^{-4} for a received power of -10dBm. Received 16-QAM constellation is shown in figure 4.25.

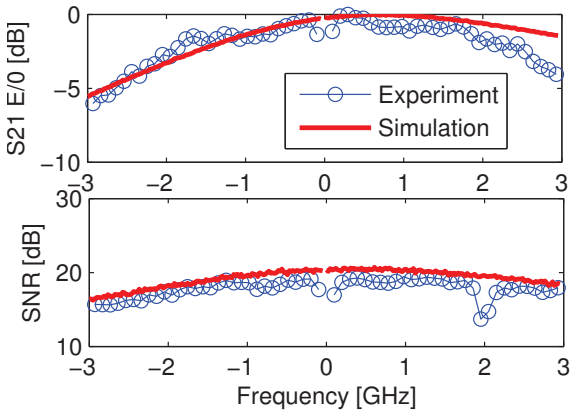

FIGURE 4.23: Frequency response (S21 E/O) and SNR per subcarrier for the optical SSB-OFDM validation.

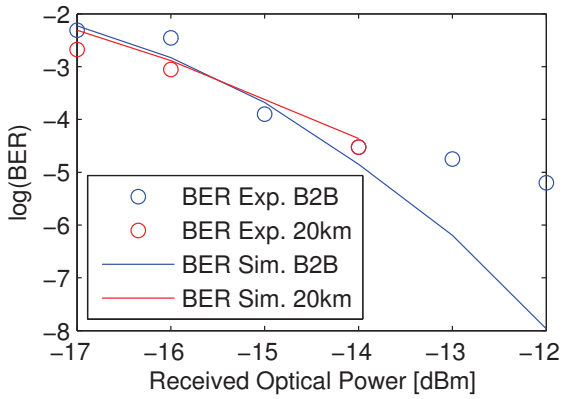

FIGURE 4.24: BER as a function of the received optical power (QPSK) for the optical SSB-OFDM validation.

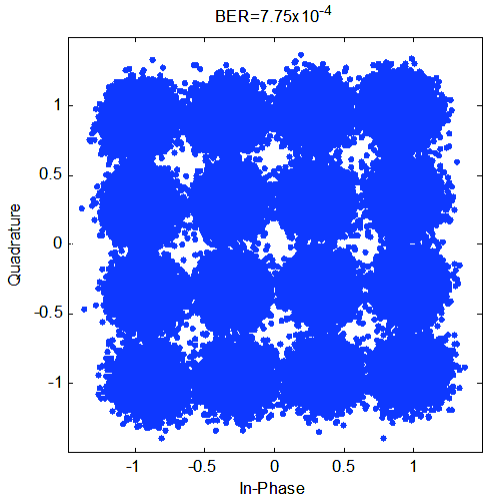

FIGURE 4.25: Received 16-QAM constellation at a received optical power of -10dBm, in optical B2B.

4.3 Summary of the Chapter

The simulation platform based on the building blocks described in chapter 2 is successfully validated using commercial available components for three different transmission techniques - single-carrier OOK, optical IM/DD (DSB-based) OFDM with bit and power loading and optical SSB-OFDM. In addition, for each transmission technique, two different optical transmitters - DML and MZM - are validated.

The results of this chapter show that the simulation platform provides accurate results for evaluating different optical links in different configurations. This serves as a basis for the following chapter, where silicon photonics transmitters are analyzed, and beyond this thesis as a powerful tool for future work on optical communications systems.

The adaptive IM/DD optical OFDM experiments demonstrated in this chapter show to achieve state-of-the-art performance (cf. table 1.5). A data-rate higher than 40Gbps (over 10GHz bandwidth) in optical B2B was achieved with both transmitters, but the performance over the fiber were much better for the MZM due to lower chirp. In this case, a data-rate of 40Gbps was demonstrated after at least 50km SMF for received optical powers higher than -8dBm.

The data-rate for the optical SSB-OFDM transmission was limited to 23Gbps (16-QAM) due to the bandwidth limitation of the devices and the low optical output power of the transmitter.

Chapitre 5

Experiments and Simulation of OFDM on Silicon Photonics Transmitters

This chapter reports the experimental demonstrations and simulations of silicon photonics-based transmitters modulated using OFDM modulation technique.

In the first part, silicon intensity modulators are considered for the uplink direction. We explore :

- Hybrid III/V-on-silicon DMLs (Experiments)
  - Longitudinally multimode Fabry-Perot (FP) laser
  - Single-mode laser with a double-ring filtering structure
  - DBRs laser
- Silicon modulators
  - Silicon ring-resonator modulator (Experiment/Simulation)
  - Mach-Zehnder Modulator (MZM) (Simulation)

In the first section, the methodology for characterization of the devices and general OFDM set-up is described. Then, particularities for each device are detailed in the following sections, and the results are presented and discussed. Many aspects of the transmission are analyzed, such as channel frequency response, SNR, bit and power distribution, BER and sensibility for $> 10Gbps$ data-rate. The objective in the simulations (ring-resonator and MZM) are twofold : 1) quantify the sensitivity penalty for optical links up to 100km SMF and 2) compare the sensitivy required for a 10Gbps 16-QAM-OFDM between both devices and a $LiNbO_3$ intensity modulator.

In the second part, a silicon photonics implementation of an optical IQ modulator for 40Gbps SSB-OFDM suitable for downlink PON is described. The sensitivity penalty due to silicon modulator impairments compared to the "ideal" $LiNbO_3$ modulator is calculated by means of simulation.

Please refer to the appendices A and B for the technical description of the electrical and optical components used in the experiments and later modeled in our simulation. This includes particularities for the OFDM modem implementation in Matlab. The penalty associated to the electrical components of the link was also evaluated by comparing the optical transmission results with the electrical B2B performance reported in the appendix B.7.

5.1 Adaptive Optical OFDM using Silicon Photonics Intensity Modulators

5.1.1 Methodology for Setting-up the Experiments

A detailed characterization of each employed silicon optical transmitter is performed, prior to the optical OFDM experiments. The characterizations include DC, AC and non-linear assessment of the device.

In the set of characterizations and experimental set-up described below, the lasers and silicon ring modulator are driven using high-frequency RF probes placed directly on the wafer. An example picture is shown in figure 5.1, for the hybrid III/V-on-silicon DBR laser. The tests were made at room temperature without any temperature control.

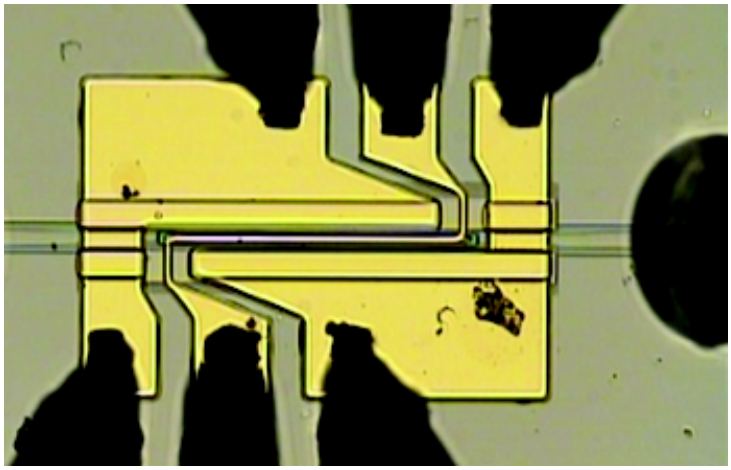

FIGURE 5.1: Picture example of RF proves driving directly the III/v-on-silicon DBR laser.

5.1.1.1 DC Characterization

The DC (static) characterizations for the hybrid lasers include a measure of the optical power coupled to the fiber and voltage as a function of the injected current. The experimental set-up for the DC characterization of the hybrid DML is shown in figure 5.2(a). For each case, the emission spectrum is also measured with an optical spectrum analyzer.

For the silicon ring resonator modulator, the spectral response of the modulator is assessed by connecting a tunable laser source to its input, sweeping the wavelengths across the C-band and measuring the optical output power in each wavelength, for several reverse bias voltages as illustrated in figure 5.2(b). Then, the optical output power as a function of the applied voltage is measured for a fixed wavelength.

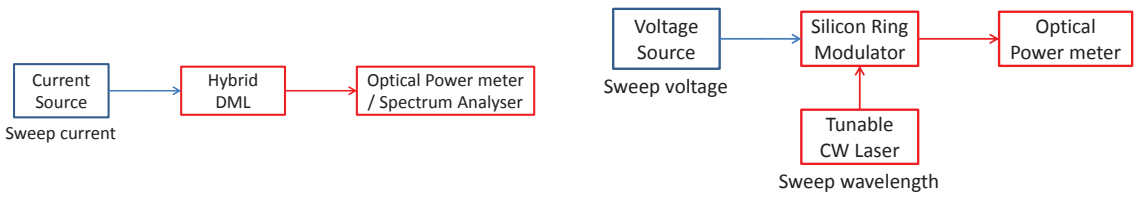

FIGURE 5.2: Experimental set-up for the DC characterization of the (a) hybrid DML and (b) silicon ring-resonator modulator.

5.1.1.2 AC Characterization

In order to determine the E/O modulation bandwidth of the silicon photonics transmitters, an AC characterization bench is set-up. The general experimental set-up using a 40GHz Vector Network Analyser (VNA) from Agilent with an E/O module is depicted in figure 5.3 for both DML and silicon ring modulator.

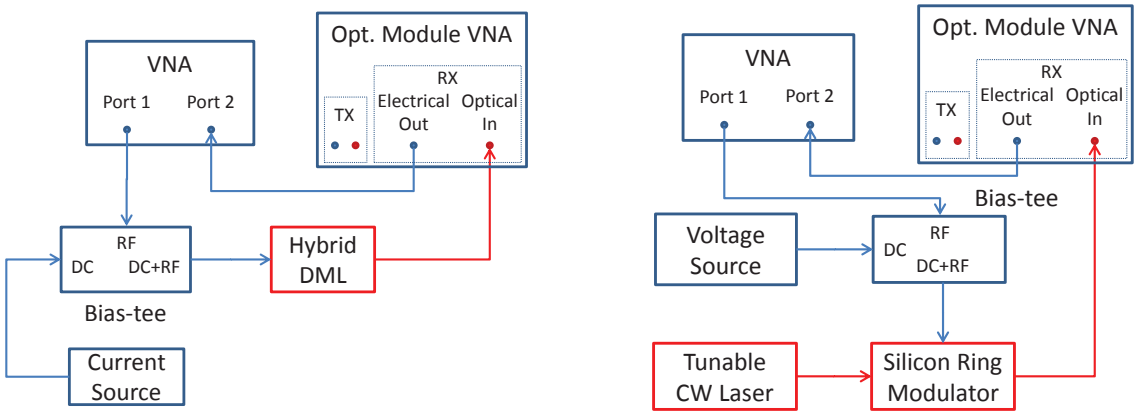

FIGURE 5.3: Experimental set-up for the AC characterization of the (a) hybrid DML and (b) silicon ring-resonator modulator.

For the hybrid DMLs, there is an intrinsic bandwidth limitation due to the rate in which photons are generated from the electron-hole recombinations, as explained in subsection 2.2.1. In addition, bandwidth can also be reduced due to RC parasitic caused by the electrical contact geometry of the device, and the electrical components of the link. In order to differentiate these two sources of bandwidth limitation, we consider a simplified RC circuit frequency response H_{RC} multiplying the frequency response of the DML

$$H_{T_{B2B}}(f) = H_{AM}(f) \times H_{RC}(f) = H_{AM}(f) \cdot \frac{1}{\sqrt{1 + (2\pi\tau_{RC})^2}} \tag{5.1}$$

where $\tau_{RC} = R \times C$ is the time constant for the RC circuit and $H_{AM}(f)$ is the frequency response to small-signal modulation of the DML defined in (2.29). In this way, the measured frequency response of the DML small-signal modulation is fitted with (5.1) to find the τ_{RC} parameter that best matches the measured frequency response with (5.1). The optimization algorithm used for the fitting is found in [276].

5.1.1.3 Non-linearity Measurements set-up

The linearity of the optical modulator is an important feature for OFDM modulation because as shown in subsection 3.3.2.2, a non-linear device degrades the signal quality (the SNR), limiting the maximum achievable modulation order of the transmission. The linearity of the silicon photonics transmitters are evaluated by measuring the input Third-Order Interception Point (IP3) and the 1dB Compression Point (CP1dB).

The input IP3 is measured by modulating the DUT by a two-tone RF signal (with close input frequencies f_1 and f_2 and power P_1 and P_2). For simplicity, we consider that $P_1 = P_2 = P_{RF}$ so that the power at f_1 and f_2 are equal. Then, the input IP3 is defined as the input power at f_1 for which the output power at f_1 is equal to the output power at $2f_2 - f_1$ (or $2f_1 - f_2$).

A simple experimental set-up to measure IP3 is shown in figure 5.4. The RF power P_{RF} should be lower than the compression point in the DUT (in the linear range of operation of the DUT) and higher than the noise floor of the electrical spectrum analyser. So as to have accurate measures, the power at $2f_2 - f_1$ should be at least 10 times higher than the noise floor.

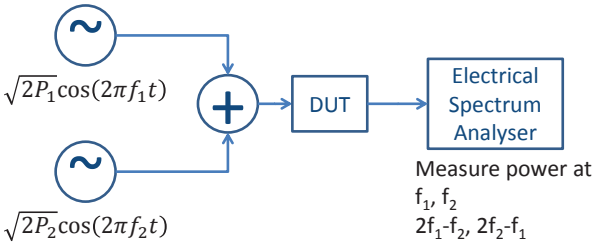

FIGURE 5.4: Simple experimental set-up for non-linear measurements.

In dBm units, the power at f_1 (P_{OUT_1}) and $2f_2 - f_1$ ($P_{OUT_{21}}$) are then given by

$$P_{OUT_1}[dBm] = P_{RF}[dBm] + K_1. \tag{5.2}$$

$$P_{OUT_{21}}[dBm] = 3P_{RF}[dBm] + K_{21}. \tag{5.3}$$

It can be shown that the parameters K_1 and K_{21} are related to the parameters of the non-linear equation (3.54) (G_1 and G_3) introduced in subsection 3.3.2.2 by $K_1 = 10\log_{10}(G_1)$ and $K_{21} = 10\log_{10}(3G_3/4)$. The input RF power at the IP3 is finally given by

$$P_{IIP3}[dBm] = \frac{K_1 - K_{21}}{2}. \tag{5.4}$$

Graphically, the input IP3 represents the interception point between the two curves given in (5.2) and (5.3) as illustrated in figure 5.5(a). In order to have a more accurate estimation of the input IP3, several points can be measured (for different P_RF values). Different measuremeasurement points should lead to the same input IP3 value if the measures are made in the linear range of the DUT (below the gain compression point).

For the CP1dB measurement, we consider now a single-tone at the DUT's input. So we set $P_1 = P_{RF}$ and $P_2 = 0$. Then, the output power at f_1 is measured as a function of the input power P_RF until the gain of the *DUT* decreases by 1dB as shown in figure 5.5(b). Based on the previously reported non-linear equation model (3.54), a relationship between the input CP1dB and IP3 can be established, which is given by (3.56).

5.1.1.4 General OFDM Experimental Set-up

OFDM Signal Generation

For each experiment and simulations, the OFDM signal is generated off-line using Matlab. Particularities of the OFDM modem implementation are detailed in appendix B. The FFT size is always $N = 256$. According to [277], a larger number of subcarriers can improve the system's capacity when using bit and power loading due to a finer granularity decomposition of the available spectrum, which makes the OFDM system to adapt better to the frequency-dependent response of the channel. In addition, for a higher number of subcarriers, the cyclic prefix overhead is lower (if considering a fixed number of samples for the cyclic prefix) as explained in subsection 3.3.1.3. However, the DSP complexity is increased with the FFT size[278], because more parallel channels are necessary to generate the OFDM signal. The value of 256 is found to be a good

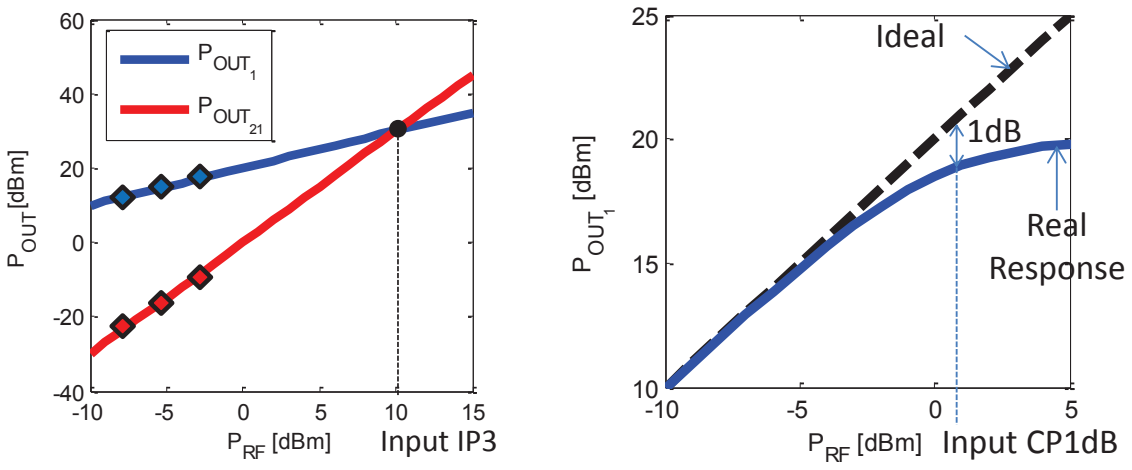

(a) IP3 (b) CP1dB

FIGURE 5.5: Example of graphical representation of the (a) IP3 and (b) CP1dB.

trade-off between performance and DSP complexity. The OFDM symbol is defined in a classic manner as explained in subsection 3.3 :

1. The incoming serial data is divided into parallel channels, corresponding to the number of data subcarriers ($N_{DATA} \leq (N/2-1)$), indexed from 1 to N_{DATA} ;
2. The bits are encoded using QAM ;
3. The subcarriers from N_{DATA}+1 to $(N/2-1)$ are set to zero ;
4. Another $(N/2-1)$ subcarriers (indexed from $-(N/2-1)$ to -1) are appended as the complex conjugate of the aforementioned $(N/2-1)$ subcarriers to respect Hermitian symmetry and form a real-valued OFDM signal. The first subcarrier at 0Hz (of index 0) and the leftmost subcarrier (of index $-N/2$) are not used at all ;
5. An IFFT is performed with a total size of N ;
6. The samples are converted from parallel-to-serial ;
7. Cyclic prefix and suffix are added with 2 samples each ($N_{CP} = 4$, overhead of 1.5% for $N = 256$) ;
8. A digital clipping with clipping ratio of $k = 3$ is performed before loading the samples to the DAC.

The effective bandwidth of the OFDM signal is given by $B = f_{s_{DAC}} \cdot N_{DATA}/N$, where $f_{s_{DAC}}$ is the DAC sampling rate. In every experiment, an oversampling of the OFDM signal is done by setting the number of data carriers is lower than the total number of available subcarriers ($N_{DATA} < (N/2-1)$) to ease the antialiasing filter requirements. In real applications with proper optimization of the antialiasing filter, the DAC sampling can be reduced close to the Nyquist frequency $2B$.

For each experiment and simulation, particularities for the optical OFDM set-up are detailed, and the transmission parameters are discussed. The experimental procedure for the bit and power loading set-up is the same as described in subsection 4.2.1 for commercial transmitters.

For these experiments, the reference 10MHz signal of the DSO is connected to the input reference of the AWG to avoid SFO impairment.

Electrical Power Loss due to Impedance Mismatch

In the hybrid III/V-on-silicon lasers used in this work, the input impedance is not adapted to 50Ω. The impedance mismatch causes a reduction in the electrical power effectively delivered to the charge (the laser). It is calculated using the reflection coefficient

$$\Gamma_R = \frac{Z_{laser} - 50}{Z_{laser} + 50} \tag{5.5}$$

where Z_{laser} is the laser resistance. Then, the effective electrical power $P_{elec_{laser}}$ delivered to the laser is given by

$$P_{elec_{laser}} = P_{in} \cdot (1 - |\Gamma_R|^2) \tag{5.6}$$

where P_{in} is the output electrical power of the RF amplifier before the laser. The peak-to-peak modulating current is written as

$$I_{pp} = 2 \cdot \sqrt{\frac{PAPR_{OFDM} \cdot P_{elec_{laser}}}{Z_{laser}}} \tag{5.7}$$

where $PAPR_{OFDM}$ is the PAPR of the OFDM signal. If clipping with a clipping ratio k is applied, the PAPR is $PAPR_{OFDM} = k^2$.

5.1.2 Hybrid III/V-on-Silicon Fabry-Perot Laser

In this first experiment, we assess OFDM modulation performance by using a hybrid III/V-on-silicon Fabry-Perot laser. The structure of the laser is described in subsection 2.2.1.4, and illustrated in figure 2.18(a).

The hybrid laser is fabricated at CEA-Leti using molecular bonding (with a thin layer of SiO_2 between the III/V material and the Si waveguide). The cavity is formed by two DBR mirrors. One of the DBR mirrors is designed to have high reflectivity ($> 90\%$) and the other one with about 50% reflectivity. The optical mode is transferred from the III/V material to the silicon waveguide through adiabatic tapers with high efficiency ($> 95\%$). Because the DBR mirrors are designed to reflect the entire gain-spectrum of the active-region, a Fabry-Perot laser is defined. A surface grating coupler is used to couple the light from silicon waveguide of the laser into the optical fiber. The design and fabrication of the hybrid Fabry-Perot lasers are detailed in [153].

5.1.2.1 DC Characterization of the Hybrid FP Laser

Several Fabry-Perot lasers were fabricated and fully characterized. We report below the characterization of a sample with typical behavior. Figure 5.6 shows the optical power coupled to a MMF and the measured voltage versus injected current. The threshold current is about 90mA and an optical power of 1mW is measured at a bias current of 220mA, resulting in a slope efficiency of $SE = 7.7 \times 10^{-3} mW/mA$ as defined in (2.28). An over etching of the grating coupler accounted for a MMF coupling loss of about 7dB instead of 3dB for nominal grating coupler to fiber loss. The slope of the laser voltage versus current indicates a contact resistance of 6Ω.

The laser emission spectrum is shown in figure 5.7 at a bias current of $I_b = 220mA$. It indicates an optical bandwidth (-20dB) of approximately 3nm, with the main longitudinal mode at 1582.5nm and a mode spacing of 0.33nm. According to the chromatic dispersion analysis with broadband laser sources in subsection 2.1.2.1, this would limit the OFDM subcarrier bandwidth at approximately 52MHz after 100km of standard SMF, as indicated in (2.16). This can be adjusted by properly choosing the number of subcarriers.

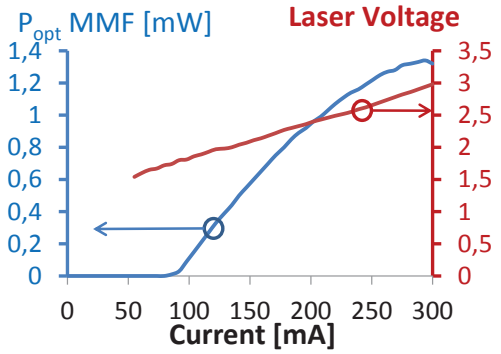

FIGURE 5.6: Optical output power coupled to MMF and laser voltage as a function of the applied current.

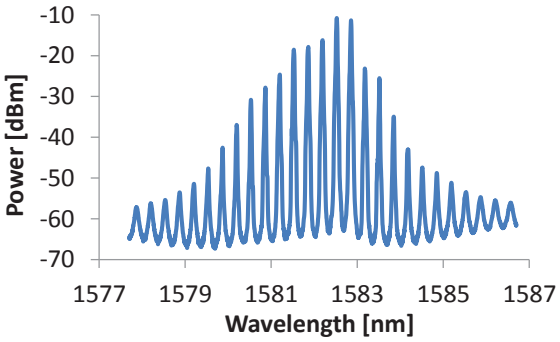

FIGURE 5.7: Hybrid Fabry-Perot laser emission spectrum ($I_b = 220mA$).

5.1.2.2 AC Characterization of the Hybrid FP Laser

The frequency response to small-signal modulation of the hybrid III/V-on-silicon laser is assessed, by using a VNA with an optical receiver module (cf. figure A.1). A -3dB bandwidth of 4.6GHz at a bias current of 220mA is reported in figure 5.8. In order to measure the contribution of the RC parasitic to the bandwidth limitation, a fitting with (5.1) is performed. Besides the RC time constant τ_{RC}, the other unknown variables are the relaxation oscillation frequency Ω_R and damping rate Γ_R of (2.29). In figure 5.8, the result of the fitting operation is shown in red with a good agreement. Using the resistance previously extracted from the slope of the voltage versus current curve, a capacitance of 9pF is extracted from this measure, and -3dB bandwidth of the hybrid FP laser without the RC contribution is measured to be 5.5GHz as illustrated in the green curve of figure 5.8. This study shows that the modulation bandwidth can be effectively enhanced by proper optimization of the electric contact geometry. The measured overall bandwidths (with RC parasitic contribution) at bias currents of 200mA and 240mA are respectively 4.5GHz and 4.8GHz. As explained in subsection 2.2.1.2, the -3dB bandwidth of the DML f_{3dB} is proportional with the square-root of the bias current ($f_{3dB} \propto \sqrt{I_b}$).

The PSD of the RIN at a bias current of 220mA is also evaluated by connecting an electric spectrum analyzer at the output of the photoreceiver (after electric amplification). The measure is shown in figure 5.9, where a clear enhancement around the relaxation oscillation frequency is observed, peaking at approximately -125dBm/Hz.

5.1.2.3 Non-Linearity Characterization of the Hybrid FP Laser

In the following subsection, the non-linearity of the hybrid III/V-on-silicon laser is assessed using the procedure reported in subsection 5.1.1.3 for the IP3 and CP1dB measurements.

The input IP3 is evaluated by generating a two-tone signal (f_1 and f_2) centered at 1GHz and separated by 42MHz. The two tones are generated by a RF source SMJ100A from Rhode & Schwartz driving directly the laser with a bias current of 220mA. The measured IP3 from the source is negligible as compared to the IP3 of the hybrid laser. The measurement results are displayed in figure 5.10(a). An input IP3 of approximately 35dBm electrical is measured.

For the CP1dB assessment, a single tone at 1GHz is generated using the same RF source than above. The same set-up than above is used, but with the addition of a 18dB-gain RF amplifier placed before the hybrid laser. The CP1dB of the RF amplifier is negligible as compared with the one of the hybrid FP laser. The electric power modulating the laser is increased at the RF source until the 1dB compression point is reached. Figure 5.10(b) displays the results, indicating an input CP1dB of about 24dBm electrical.

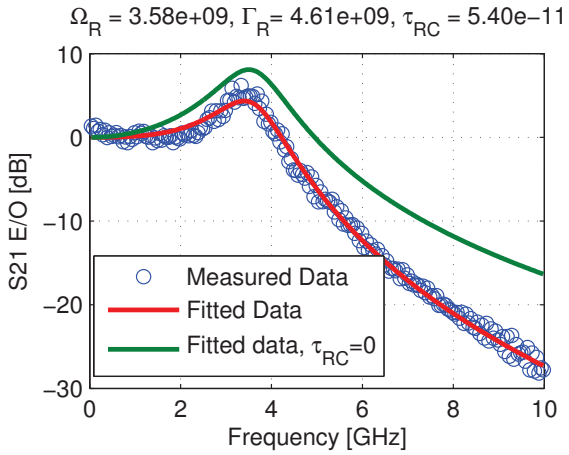

FIGURE 5.8: Frequency response to small-signal modulation of the hybrid FP ($I_b = 220mA$).

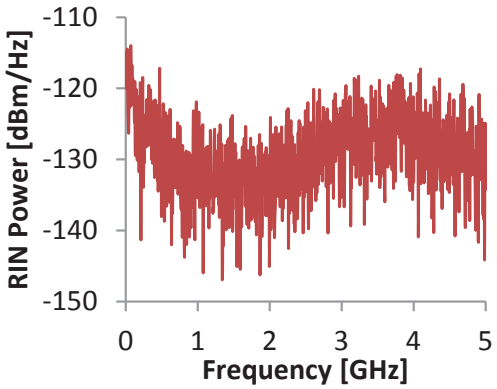

FIGURE 5.9: Measurement of the PSD of the RIN of the hybrid FP ($I_b = 220mA$).

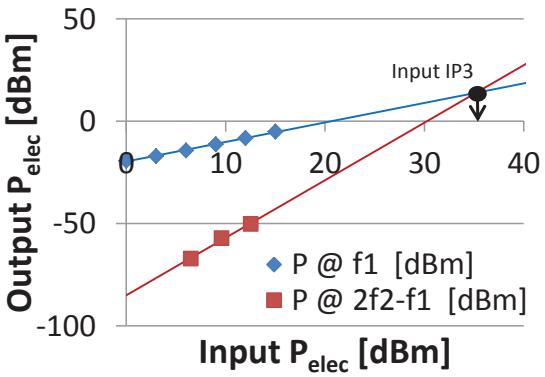

(a) Input IP3=35dBm

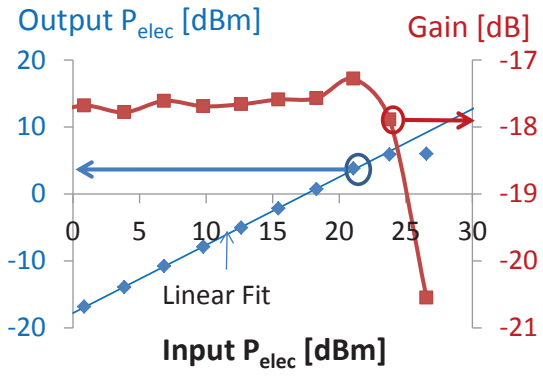

(b) Input CP1dB=24dBm

FIGURE 5.10: Linearity assessment of the hybrid FP laser ($I_b = 220mA$), (a) IP3 and (b) CP1dB.

The input IP3 and CP1dB are shown to be better than previously reported lasers for OFDM modulation [115, 279], but with lower slope efficiency. The non-linearity measurements indicate that the input electric power modulating the laser can be set as close as possible to the compression point without non-linear degradation. At high modulation depths, the signal quality degrades as a consequence of the clipping because the modulating signal goes below the threshold condition for the laser, or above the saturation optical power of the laser.

5.1.2.4 OFDM Experimental Set-up for the Hybrid FP Laser

Figure 5.11 illustrates the optical OFDM transmission using the hybrid FP laser. It is defined in a classic manner as described in subsection 5.1.1.4. The only difference is that the digital clipping is not performed as it was not implemented at the time of the experiment.

Table 5.1 lists the transmission parameters for this experiment. In practice, because of the limited bandwidth of the hybrid laser, the OFDM signal bandwidth is limited to 4GHz (with 42 data subcarriers). Subcarriers above this frequency do not have enough SNR to carry any data. The DAC sampling-rate was kept to 24Gsps to avoid high-frequency roll-off by the DAC and ease the anti-aliasing low-pass filter requirements. In a practical system with proper design, a

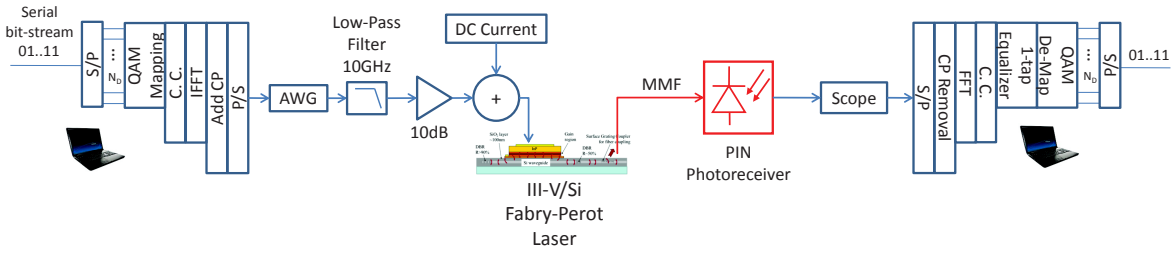

FIGURE 5.11: Experimental set-up for the direct-OFDM modulation of the III/V-on-Silicon Fabry-Perot laser.

DAC close to 8Gsps could be used, together with an antialiasing filter with passband from DC to 4GHz.

The peak-to-peak modulating current given in table 5.1 takes into account the power loss due to the impedance mismatch. For this laser ($Z_{laser} = 6\Omega$), the impedance mismatch results in a power loss of 62% as indicated by (5.6). Because no clipping is applied in this experiment, the average PAPR of the OFDM signal is $PAPR_{OFDM} \approx 16$.

Number of OFDM symbols per acquisition	5000
AWG (sampling rate)	Tektronix AWG7122C ($f_{s_{DAC}} = 24Gsps$)
Subcarrier spacing	$\Delta f = f_{s_{DAC}}/N = 93.75MHz$
Number of data carriers	$N_{DATA} = 42$
OFDM bandwidth	$B = f_{s_{DAC}} \cdot N_{DATA}/N = 4GHz$
AWG output peak-to-peak voltage	$1V_{pp}$ (Zeroing mode OFF)
Bias current	220mA
Peak-to-peak current modulating the laser	$110mA_{pp}$
Optical output power in MMF	1mW
Photoreceiver (conversion gain)	NewFocus 1554-B ($600V/W$)
DSO (sampling rate)	Tektronix DSA72004C ($f_{s_{ADC}} = 25Gsps$)

TABLE 5.1: Parameters for the direct-OFDM modulation of the hybrid III/V-on-silicon Fabry-Perot laser.

5.1.2.5 Results and Discussion of the OFDM experiment using the Hybrid FP Laser

Figure 5.12 illustrates the normalized received electric spectrum before the DSO in electrical and optical B2B with the OFDM bandwidth limited to 4GHz (42 data subcarriers). The power fading in the highest frequencies caused by the electric components is compensated by the enhancement of the frequency response around the relaxation oscillation frequency of the hybrid laser.

The SNR per subcarrier before and after the bit and loading are shown in figure 5.13. Each circle in the figures corresponds to a single subcarrier. The SNR degradation due to the electric part of the link is negligible according to the electric B2B measurements presented in appendix B.7. The staircase effect in the SNR per subcarrier after the bit and power loading is typical when using this technique (cf. appendix C). This is because, for each modulation format, the relative power is adjusted to achieve the target BER. As a consequence, for subcarriers carrying the same modulation format, the SNR is about the same.

The number of bits (constellation order) and relative power per subcarrier are shown in figure 5.14. The highest modulation format is 32-QAM around 1.25GHz, which corresponds

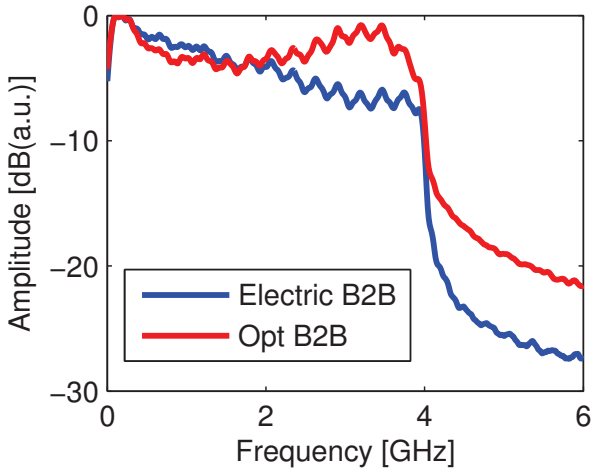

FIGURE 5.12: Received spectrum before the DSO for the electric B2B, optical B2B and 250m MMF.

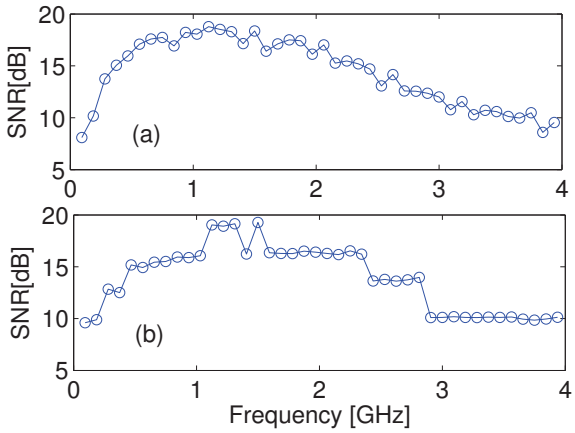

FIGURE 5.13: SNR per subcarrier (a) before and (b) after bit and power loading.

to about 19dB and SNR in optical B2B. Received 32-QAM and QPSK constellations for the 13^{th} and 40^{th} subcarrier, respectively, are shown in figure 5.15(a). The achievable data-rate is 12.6Gbps without accounting the 7% FEC overhead. The number of bits per acquisition is 6.8×10^5, indicating a good precision in the BER estimator for the target BER (cf. subsection 3.2.1.2). The BER per subcarrier is shown in the last line of figure 5.14, which is taken as the worst value between the BER calculated from the SNR and the counted from the error bits. It shows a total BER of 1.7×10^{-3}. Furthermore, it is interesting to analyze the noise PSD calculated using (4.1), as illustrated in figure 5.16. It is given in dBm/Hz, relative to electrical mW and normalized to the ADC bandwidth. By comparing the measured noise PSD in the OFDM transmission with the measured RIN in figure 5.9, it suggests that the RIN is the limiting noise in the transmission.

The uncertainty of the measured capacity is verified. The SNR uncertainty is given in (3.16). Considering 5000 OFDM symbols, an uncertainty value for the SNR per subcarrier of 0.35dB as calculated in . Taking into account this uncertainty, the lower and upper bounds on the measured capacity in optical B2B is a 12.5 and 12.9Gbps, respectively, indicating a good precision in the measurements.

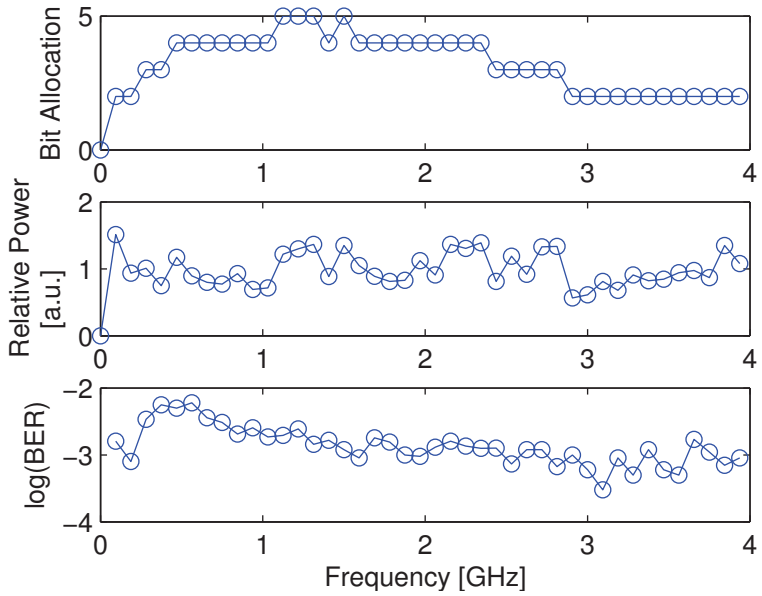

FIGURE 5.14: Bit allocation, relative power and BER per subcarrier after the bit and power loading.

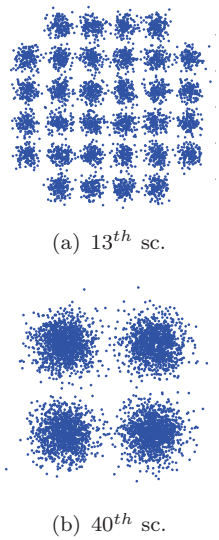

(a) 13^{th} sc.

(b) 40^{th} sc.

FIGURE 5.15: Received constellations in the (a) 13^{th} and (b) 40^{th} sc.

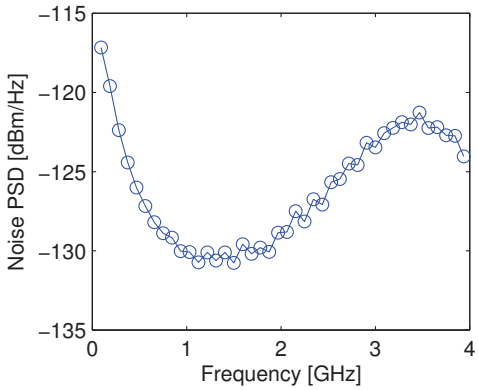

FIGURE 5.16: Noise PSD in the B2B and 250m MMF case.

5.1.3 Single-mode Tunable Hybrid III/V-on-Silicon laser with Double-ring Structure

Tunable lasers are a requirement for the transmitter for future generations of passive optical networks. In subsection 1.3.1.1, a brief state-of-the-art on tunable silicon photonics lasers was presented. III/V-lab has developed a particular architecture, based on a double-ring resonator structure in each side of the active region to filter the side-modes and make the laser single-mode. At the same time, wavelength tunability can be achieved by integrating resistive heaters on top of the rings and heating them up. The temperature variation translates into an effective index variation, which changes the resonance wavelength of the ring resonators. A schematic view of the hybrid laser was shown in figure 1.9.

The hybrid laser is fabricated in the CEA-Leti using a wafer bonding technique, with silica as the bonding layer between the III/V material and the silicon. A complete description of the structure is given in [39]. A top view picture of the sample is depicted in figure 5.17, which shows the heaters in both sides of the gain section for tuning the laser to the desired wavelength. A grating coupler is used to collect the light out from the silicon waveguide with a SMF. The direct OOK modulation up to 10Gbps over of 25km SMF was reported by[44] . The reach was

mainly limited by chromatic dispersion. In this work, we evaluate the performance of direct OFDM modulation of this hybrid laser.

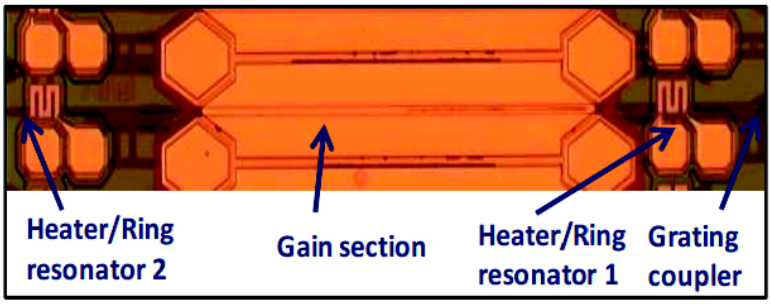

FIGURE 5.17: Top view picture of the Hybrid III/V-on-silicon laser with double ring structure used for OFDM modulation (Source [39]).

5.1.3.1 DC Characterization of the Tunable Hybrid Laser

Figure 5.18 shows the laser optical power coupled to the SMF as a function of the injected current. The kinks observed in the optical power versus current curve are mainly due to mode hops caused by the thermal detuning between the main longitudinal mode and the pass-band of the ring resonator filter. This should not affect AC operation because the variations in the injected current (by the modulating signal) are fast enough so that the laser-junction temperature does not vary. The threshold current is about 40mA and the maximum optical output power (coupled in the waveguide) is close to 0.12mW (-9dBm) at approximately 100mA and 180mA. The slope of the voltage versus current curve indicates a laser resistance of 7.3Ω.

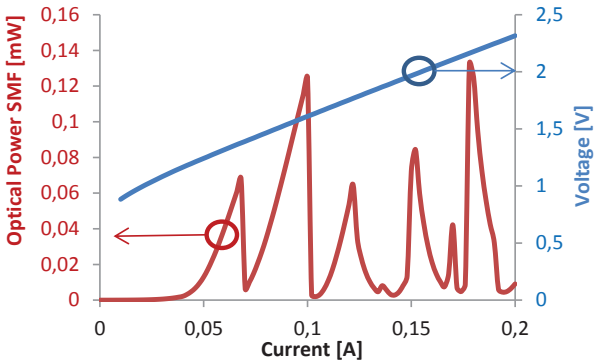

FIGURE 5.18: Optical power and voltage as a function of the injected current for the single-mode hybrid laser with double ring structure.

The tuning current of the heaters on top of the rings are adjusted to that single-mode operation around 1542.5nm is achieved. Figure 5.19 shows the optical spectrum in the laser output, showing a SMSR higher than 30dB. The SMSR reported here is limited by the dynamic range of the measurement equipment - a SMSR higher than 50dB is reported in [39].

5.1.3.2 AC Characterization of the Tunable Hybrid Laser

The small-signal frequency response of the tunable hybrid laser is assessed using the set-up illustrated in figure 5.3(a). The bias current used is 100mA. The result is reported in figure 5.20. A relaxation oscillation frequency of about 5GHz and -3dB bandwidth of 7.5GHz are measured. The value of the parasite capacitance could not be extracted using the previous

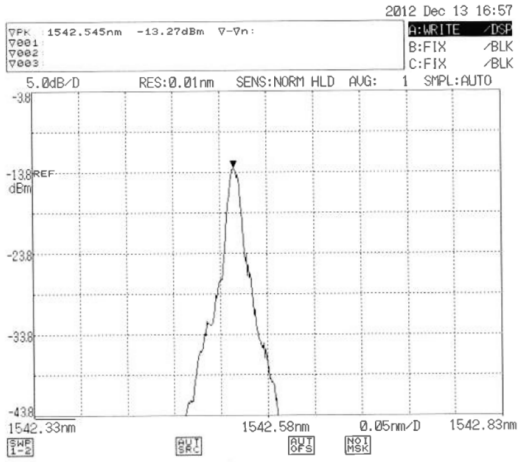

FIGURE 5.19: Optical spectrum of the hybrid III/V-on-silicon laser with double ring-resonator structure ($I_{bias} = 100mA$).

method described in subsection 5.1.1.2 because the bandwidth limitation imposed by the RC parasitic is negligible as compared to the modulation bandwidth of the laser itself.

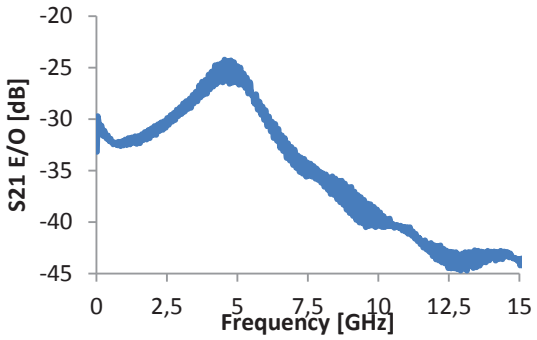

FIGURE 5.20: Frequency response to small-signal modulation of the hybrid III/V-on-silicon laser with double ring-resonator structure ($I_{bias} = 100mA$).

5.1.3.3 Non-linear Characterization of the Tunable Hybrid Laser

To assess the non-linearity of the tunable hybrid laser, the set-up is the same as the one depicted in figure 5.4 except for a 30dB electric amplifier and a variable attenuator to vary the modulating depth of the hybrid laser. The bias current is 100mA.

The IP3 is measured with a two tones RF signal centered at 2GHz and spaced apart from 25MHz. We checked out that the source and RF amplifier IP3 are negligible as compared to the one of the hybrid laser. The gain curve for the tone at f_1 and $2f_2 - f_1$ are displayed in figure 5.21(a), which results in an input IP3 of 23dBm. The CP1dB is measured with a single tone at 2GHz. The gain curve is displayed in figure 5.21(b). It indicates an input CP1dB of about 18dBm. This hybrid laser structure shows to be less linear than the hybrid Fabry-Perot laser presented before.

5.1.3.4 OFDM Experimental Set-up for the Tunable Hybrid Laser

The experimental set-up for the adaptive OFDM modulation of the hybrid laser with double-ring resonator structure is depicted in figure 5.22 and the main parameters are listed in table 5.2.

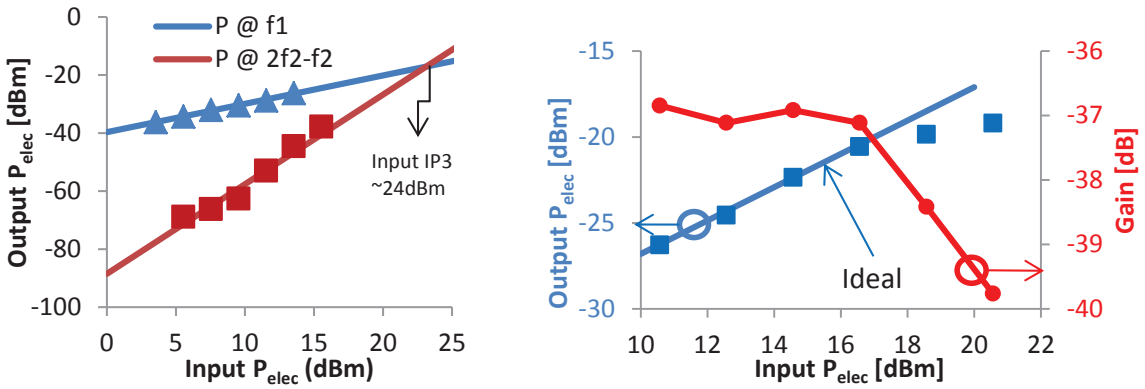

(a) Input IP3=24dBm (b) Input CP1dB=18dBm

FIGURE 5.21: Linearity assessment of the hybrid tunable laser with double ring structure ($I_b = 100mA$), (a) IP3 and (b) CP1dB.

For this experiment, two cases are considered : with EDFA (optical B2B and 20km SMF) and without EDFA (optical B2B only). In the set-up, there are two differences between the two cases : 1) Without the EDFA, the electrical gain before modulating the laser is set to 11dB, whereas with the EDFA it is set to 12dB ; 2) AVOA is placed before the photoreceiver to adjust received optical power when EDFA is used, otherwise the output of the laser is connected directly to the photoreceiver.

Number of OFDM symbols per acquisition	4000
AWG (sampling rate)	Agilent M8190A ($f_{s_{DAC}} = 12Gsps$)
Subcarrier spacing	$\Delta f = f_{s_{DAC}}/N = 46.87MHz$
Number of data carriers	$N_{DATA} = 95$
OFDM bandwidth	$B = f_{s_{DAC}} \cdot N_{DATA}/N = 4.5GHz$
AWG output peak-to-peak voltage	$700mV_{pp}$
Bias current	100mA
Peak-to-peak current modulating the laser	$90mA_{pp}$ (w/out EDFA) and $100mA_{pp}$ (with EDFA)
Optical output power in SMF	$0.125\mu W$ (-9dBm)
Photoreceiver (conversion gain)	NewFocus 1554-B ($600V/W$)
DSO (sampling rate)	Tektronix DSA72004C ($f_{s_{ADC}} = 25Gsps$)

TABLE 5.2: Parameters for the direct-OFDM modulation of the hybrid III/V-on-silicon laser with double ring structure.

Note that the OFDM signal bandwidth $B = 4.5GHz$ this is far below the laser bandwidth of 7.5GHz. The poor performance of the AWG (high frequency roll-off, estimated to be 12dB at 4.5GHz, and noise) and the RIN enhancement above this frequency combined with the low optical launched power contribute for that.

5.1.3.5 Results and Discussion of the OFDM Experiment using the Tunable Hybrid Laser

For the link frequency response, a frequency roll-off about 8dB is observed at 4.5GHz in optical B2B. The channel frequency response has a 1.8dB additional attenuation at about 4GHz after 20km of SMF compared to the optical B2B. The SNR per subcarrier is shown in figure

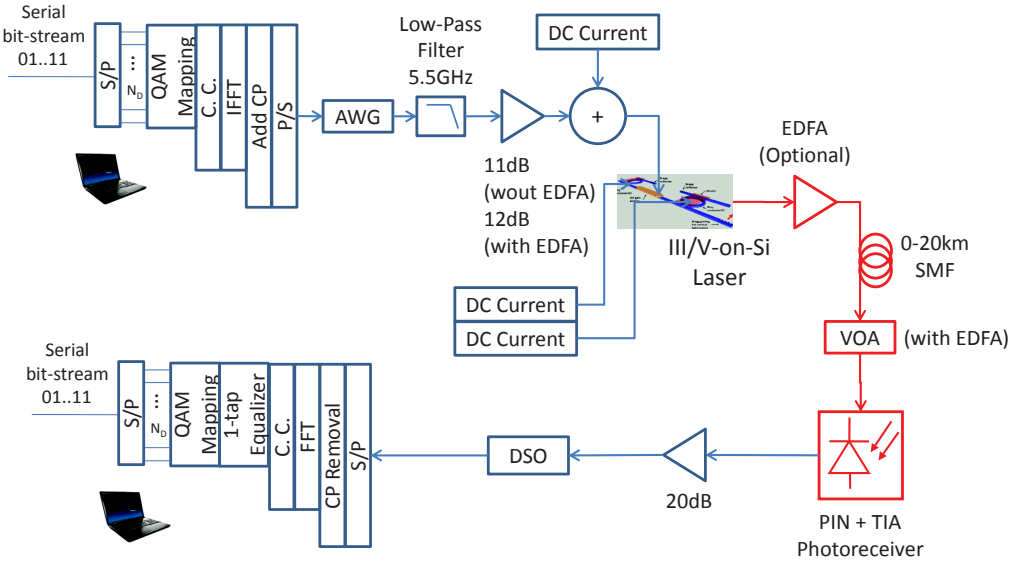

FIGURE 5.22: Experimental set-up for the direct-OFDM modulation of the hybrid laser with double-ring resonator structure.

5.23 (a) before and (b) after the bit and power loading, for the optical B2B with and without EDFA and the 20km case. When no EDFA is used, the received optical power is -9dBm. In the case the EDFA is used, the output power of the EDFA in optical B2B measured with a power meter is -2dBm. However, using an optical spectrum analyzer, we measured a net gain of 2.4dB, which indicates the poor performance of the EDFA adding considerable ASE noise into the optical signal. Also, some degradation is expected because no optical filter is used before the photoreceiver. In 20km SMF, the optical output power of the EDFA is 1.2dBm with a net gain of 5.6dB, and the received optical power is approximately -0.7dBm. The measured SNR per subcarrier shows little change in the three cases. It peaks at approximately 15dB in the lower frequencies and decreases to about 8 to 10dB in the higher frequencies, depending on the configuration.

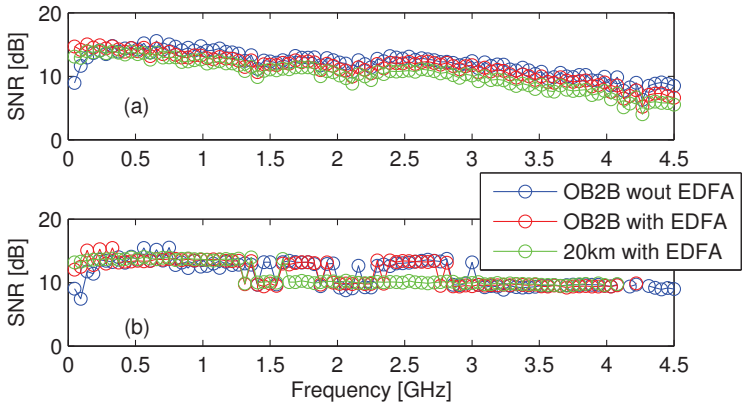

FIGURE 5.23: SNR per subcarrier of the OFDM transmission using the hybrid tunable laser with double-ring structure (a) before and (b) after bit and power loading.

Moreover, figure 5.24 displays the bit and power allocation in the three configurations considered as well as the BER per subcarrier. In optical B2B the highest constellation achieved is 16-QAM in a few subcarriers below 1GHz, with a SNR of approximately 16dB. In the 20km

case, the SNR is degraded and the maximum achievable constellation is 8-QAM, showing a SNR of approximately 13dB. Received constellations for the 5^{th} subcarrier in optical B2B with EDFA (16-QAM) and 20km SMF (8-QAM) are shown in figure 5.25.

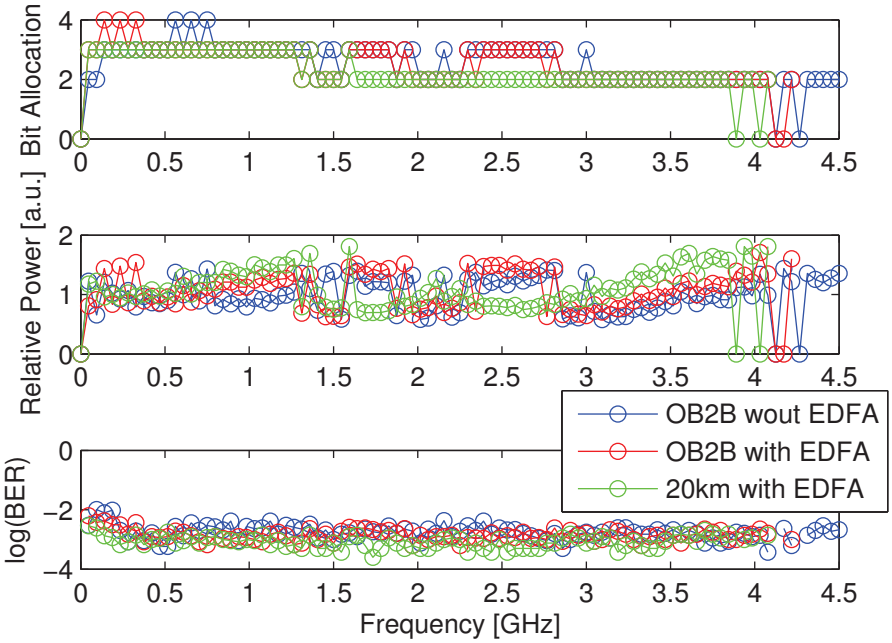

FIGURE 5.24: Number of bits, relative power and measured BER per subcarrier of OFDM transmission using the hybrid tunable laser with double-ring structure after bit and power loading.

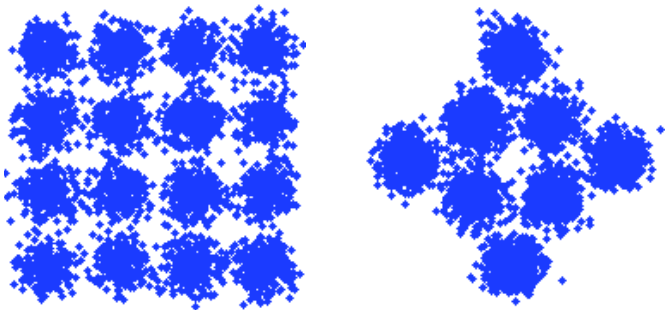

(a) Optical B2B (b) 20km SMF

FIGURE 5.25: Received constellations for the 5^{th} subcarrier in (a) optical B2B with EDFA, 16-QAM and (b) 20km SMF, 8-QAM.

The data-rate and total BER are summarized in table 5.3. The number of bits per OFDM symbol in the worst case (9.2Gbps) is 7.96×10^5. The value of the BER per subcarrier is taken as the worst value between the BER obtained from the SNR and the actual counted BER.

To finish with, figure 5.26 displays the achievable data-rate as a function of the received optical power. It shows that the EDFA causes a 5dB sensibility penalty for data-rates higher than 10Gbps. We conclude that the very low optical power provided by the laser limits the transmission performance. In order to extend the reach, a better performing optical amplifier should be used.

	Received Optical Power	Data-rate	Total BER
Optical B2B w/out EDFA	-9dBm	11.2Gbps	2.1×10^{-3}
Optical B2B with EDFA	-2dBm	10.3Gbps	1.6×10^{-3}
20km SMF with EDFA	-0.7dBm	9.2Gbps	9.4×10^{-4}

TABLE 5.3: Summary of achievable data-rate and total BER for the adaptive OFDM modulation of the hybrid III/V-on-silicon laser with double ring structure.

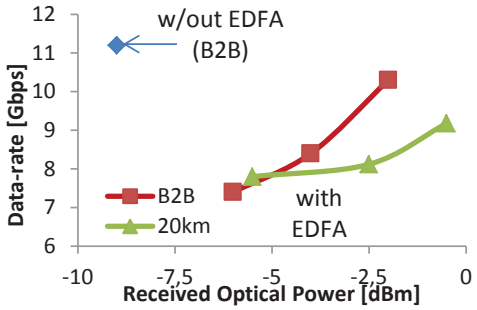

FIGURE 5.26: Achievable data-rate as a function of the received optical power for the direct OFDM modulation of the hybrid laser based on a double-ring structure.

5.1.4 Hybrid III/V-on-Silicon DBR

In this part, we consider a laser structure similar to the one used in subsection 5.1.2. The difference is that the DBR mirrors are only partially etched so that the reflectance bandwidth of the mirrors is narrower. Ideally, only a single longitudinal mode should be reflected back to the cavity to make single-mode lasers.

A very detailed description of the laser structure can be found in [155]. The only difference from that hybrid laser to the one it was used in this experiment is the length of the active region which is 950μm-long against 400μm-long for the one reported in [155]. We will show later that because the length of the cavity is longer, the mode-spacing of the longitudinal modes (FSR) is lower and there are two main longitudinal modes that are amplified in the cavity. However, this is not a limiting factor for the OFDM modulation.

5.1.4.1 DC Characterization of the Hybrid DBR Laser

The DC characterization of the particular sample used in this experiment is described in the following. Figure 5.27 shows the optical power coupled to the SMF and voltage as a function of the injected current. The threshold current is below 35mA and the slope efficiency is about 0.012mW/mA. The series resistance of the laser is 17Ω, calculated from the slope of the voltage versus current curve. The optical power coupled into the SMF is 1.6mW at a 170mA bias current. The relatively low SMF-coupled optical power (as compared to 10mW-coupled power provided by bulk III/V lasers) can be attributed to the high insertion losses of the surface grating coupler, estimated to be 8.5dB. Two factors account for that, as compared to typical loss of 3dB : 1) The grating couplers were optimized for coupling into an MMF, resulting in 3-dB additional losses for coupling into SMF, and 2) An additional Nitride layer was added for encapsulating the laser, but the gratings design did not take into account this additional layer. One can note that the expected SMF coupled power when using optimized gratings could therefore exceed 6mW.

The laser emission spectrum at 170mA is measured with an optical spectrum analyzer and it is displayed in figure 5.28. We can effectively observe two main longitudinal modes which are spaced apart from 0.5nm.

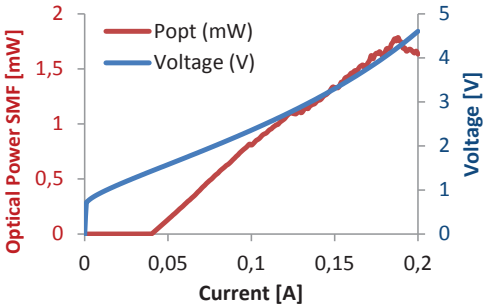

FIGURE 5.27: Optical output power coupled to SMF and laser voltage as a function of the applied current.

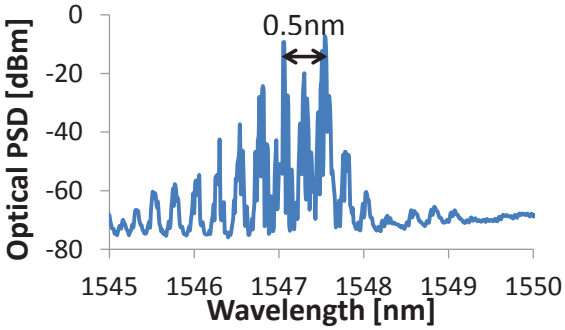

FIGURE 5.28: Hybrid DBR laser emission spectrum ($I_b = 170mA$).

5.1.4.2 AC characterization of the Hybrid DBR Laser

We further assessed the frequency response to small signal modulation of the hybrid DBR laser at 170mA injected current. A-3dB modulation bandwidth of 5.5GHz is extracted from the measure in optical B2B as shown in figure 5.29(a). By fitting the measured frequency response with (5.1), a parasitic capacitance of 2.24pF is extracted from this measure, resulting in a bandwidth reduction from 6.8GHz to 5.5GHz as indicated in the green curve of figure 5.29(a).

Furthermore, the frequency response of the 20km and 50km SMF-link with the direct modulation of the hybrid DBR laser is assessed. The results are illustrated in figure 5.29(b). The initial idea was to evaluate the frequency chirp parameter of the laser [134]. This can be done by finding the laser chirp parameter α that best fits the measured frequency response of the hybrid laser over the SMF-link with (3.69) [134]. Note that this method is described in detail in appendix A.3, and an example is shown for the commercial DFB from 3S Photonics, indicating an accurate estimation of α. However, the frequency response predicted by (3.69) does not fit well the measurements. This is possibly because (3.69) is obtained assuming a laser with single longitudinal mode. Therefore, it was not possible to accurately estimate the chirp parameter of the hybrid DBR laser using this method. At 20km SMF, a null in the frequency response is observed at around 5GHz, which will limit the OFDM signal bandwidth in this case. A 7-dB dip is seen from 0 to 2.5GHz in the 50km SMF case.

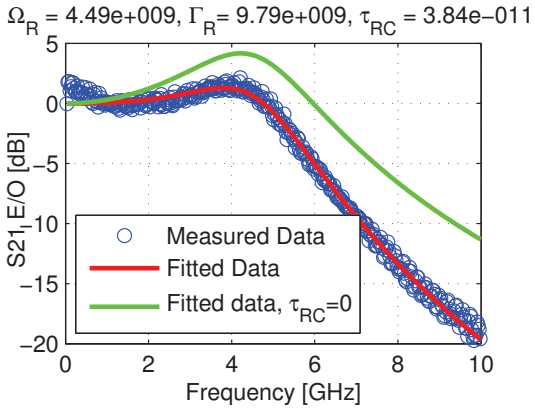

(a)

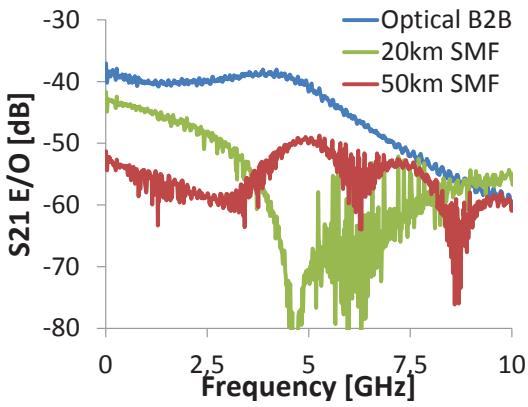

(b)

FIGURE 5.29: Frequency response to small signal modulation of the hybrid DBR laser ($I_b = 170mA$), (a) extraction of the parasitic capacitance and (b) comparison optical B2B, 20km SMF and 50km SMF.

5.1.4.3 Non-linear Characterization of the Hybrid DBR Laser

The IP3 is measured with the set-up described in figure 5.4 with a bias current of 170mA, added a 30dB electric amplifier placed after the RF source. The electrical power modulating the laser is varied by changing the output power of the RF source. The two-tone signal (f_1 and f_2) is centered at 1GHz and the two tones are spaced apart from 80MHz. Figure 5.30(a) shows the measurements results, indicating an input IP3 of approximately 26.5dBm. For the CP1dB evaluation, a single-tone at 1GHz modulating the laser is generated. As illustrated in figure 5.30(b), the input CP1dB is computed to be approximately 20.6dBm. As the OFDM signal RMS modulation power of the laser is further set to 8.5dBm (this will be detailed later in this section), negligible penalty due to laser non-linear distortion is expected. This is verified through simulation using the non-linear model described in subsection 3.3.2.2.

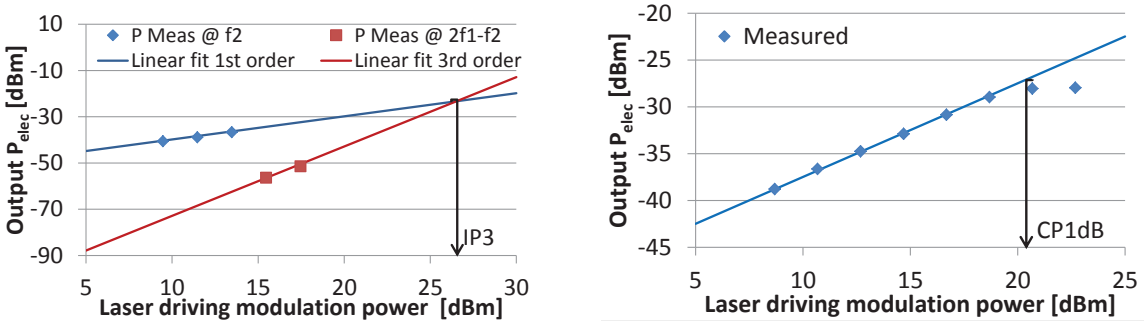

(a) Input IP3=26.5dBm

(b) Input CP1dB=20.6dBm

FIGURE 5.30: Linearity assessment of the hybrid DBR laser ($I_b = 170mA$), (a) IP3 and (b) CP1dB.

The hybrid DBR laser shows to be more linear than the previous hybrid laser with double ring resonator structure, but less linear than the hybrid Fabry-Perot presented in subsection 5.1.2. However, because of the better efficiency and higher bandwidth, better performance are expected. Note that the CP1dB and IP3 measured values are in the same order of magnitude of commercially available III/V lasers [115] and better than previously reported 1550nm-VCSEL used for OFDM modulation [279].

5.1.4.4 Single-carrier OOK Modulation of the Hybrid DBR Laser

Before setting-up the OFDM experimental set-up, we have evaluated the eye diagram of the direct OOK modulation of the hybrid DBR laser as a simple benchmark. Figure 5.31 depicts the experimental set-up for the direct-OOK modulation of the hybrid DBR laser. In optical B2B, up to 13Gbps was achieved with an open eye diagram (cf. figure 5.32(a)). As explained in subsection 2.1.2, chromatic dispersion in fiber accounts for a limitation of the [bit-rate × reach] product. It can be approximated by [139]

$$B_{max} \cdot L \approx \frac{1}{D \cdot \Delta\lambda} \tag{5.8}$$

where B_{max} is the maximum bit-rate, L is the fiber length, D is the chromatic dispersion parameter and $\Delta\lambda$ is the spectral width of the spectral source. This is different from (2.16) because, in this case, $\Delta\lambda$ accounts for the maximum spectral width of the optical source rather than its RMS value. For L=*20km*, D=*16ps/nm.km* and $\Delta\lambda = 0.5nm$ (cf. figure 5.19), we have $B_{max} \approx 6.25Gbps$. Effectively the eye diagram closes from 6Gbps to 8Gbps after 20km of fiber as illustrated in figure 5.32(b)-(d).

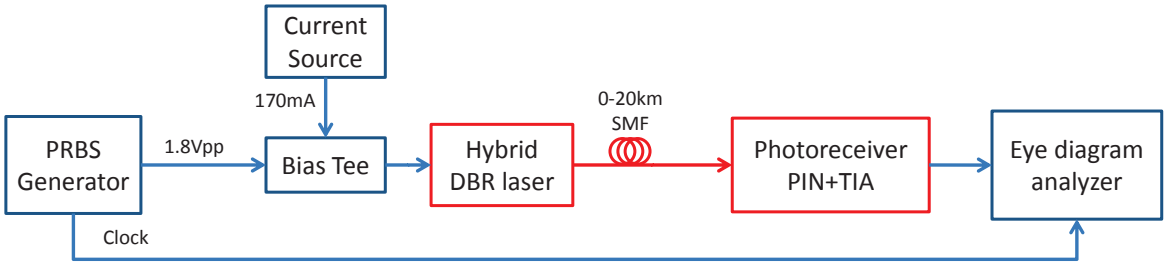

FIGURE 5.31: Experimental set-up for the direct-OOK modulation of the hybrid DBR laser.

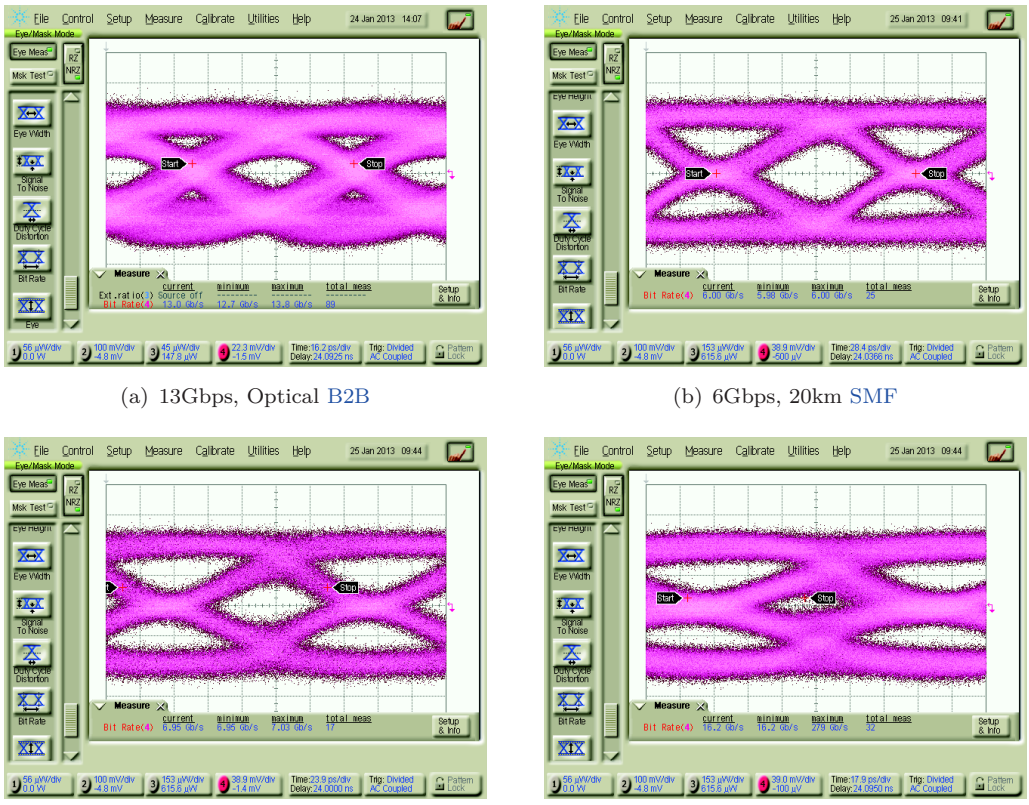

(a) 13Gbps, Optical B2B

(b) 6Gbps, 20km SMF

(c) 7Gbps, 20km SMF

(d) 8Gbps, 20km SMF

FIGURE 5.32: Measure eye diagrams for direct OOK modulation of the hybrid DBR laser, (a) 13Gbps, optical B2B ; (b) 6Gbps, 20km SMF ; (c) 7Gbps, 20km SMF ; (d) 8Gbps, 20km SMF.

5.1.4.5 OFDM Experimental Set-up for the Hybrid DBR Laser

The experimental set-up for the direct-OFDM modulation of the hybrid DBR laser is shown in figure 5.33. The OFDM symbol configuration is the same as the one described in section 5.1.1.4. Table 5.4 gives the parameters specific for this experiment with the hybrid DBR laser.

A Variable Electrical Attenuator (VEA) combined with a 30dB Electrical Amplifier (EA) are used to set the electric gain of the OFDM signal to 18dB (in 0-40km of SMF) and 16dB (50km). The peak-to-peak voltage of the OFDM signal in the electric attenuator output is $4V_{pp}$ ($3.15V_{pp}$) at 0-40km (50km) configuration. The lower modulation depth in 50km SMF is a consequence of the dispersion-induced distortions in chirped optical signals as studied in [243].

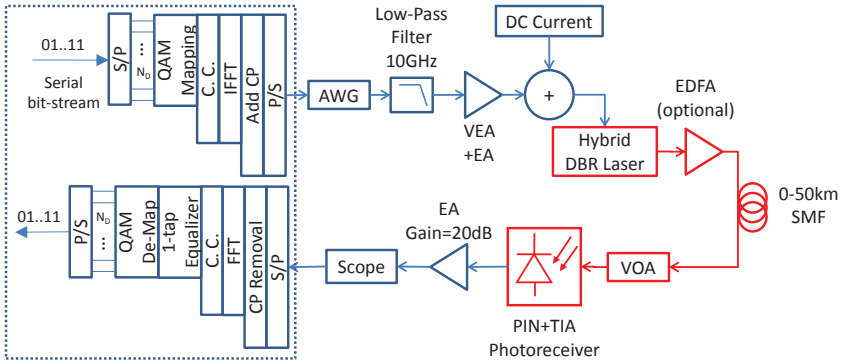

FIGURE 5.33: Experimental set-up for the direct-OFDM modulation of the hybrid DBR laser.

Number of OFDM symbols per acquisition	4000
AWG (sampling rate)	Tektronix AWG7122C ($f_{s_{DAC}} = 24Gsps$)
Subcarrier spacing	$\Delta f = f_{s_{DAC}}/N = 93.75MHz$
Number of data carriers	$N_{DATA} = 66$
OFDM bandwidth	$B = f_{s_{DAC}} \cdot N_{DATA}/N = 6.25GHz$
AWG output peak-to-peak voltage	$0.5V_{pp}$ (Zeroing mode ON)
Bias current	170mA
Peak-to-peak current modulating the laser	$120mA_{pp}$ (0-40km) and $90mA_{pp}$ (50km)
Optical output power in SMF	1.6mW
Photoreceiver (conversion gain)	NewFocus 1554-B ($600V/W$)
DSO (sampling rate)	Tektronix DSA72004C ($f_{s_{ADC}} = 25Gsps$)

TABLE 5.4: Parameters for the direct-OFDM modulation of the hybrid III/V-on-silicon DBR laser.

5.1.4.6 Results and Discussions of the OFDM Experiment using the Hybrid DBR Laser

A set of measurements is reported for the optical B2B case (with received optical power of -2.3dBm) and 50km SMF (with received optical power of -8.8dBm) in figure 5.34, without EDFA.

The first line shows the link frequency response ($H(f)$), showing a roll-off of 12dB at 6GHz in optical B2B configuration. After 50km, this roll-off is compensated with the gain experienced by the optical signal as a consequence of the interaction between dispersion and chirp [241]. This is agrees with the measure of the electro-optic frequency response with the fiber illustrated in figure 5.29(b). The second and third lines display the SNR per subcarrier after the bit and power loading and the number of bits per subcarrier. We observe that at 50km SMF a few subcarriers around 3GHz are turned off since due to low SNR as a consequence of the fading. The maximum constellation in optical B2B (50km SMF) is 32-QAM (8-QAM), corresponding to a SNR of about 19dB (13dB). We evaluated that, in optical B2B, the SNR penalty due to the electrical part of the link (DAC/ADC, amplifiers and filter) is negligible up to 2GHz, around 2dB from 2 to 4.5GHz and less than 1dB beyond 4.5GHz. This is calculated by analyzing the electrical B2B performance in appendix B.7 and using (B.2). The data-rate in optical B2B is 21.5Gbps and after 50km SMF is 12.4Gbps.

The last line of figure 5.34 shows the BER per subcarrier calculated from SNR and measured from the error bits showing a good agreement. This indicates that the assumption of AWGN is valid and that the number of bits sent per acquisition is enough to accurately estimate the

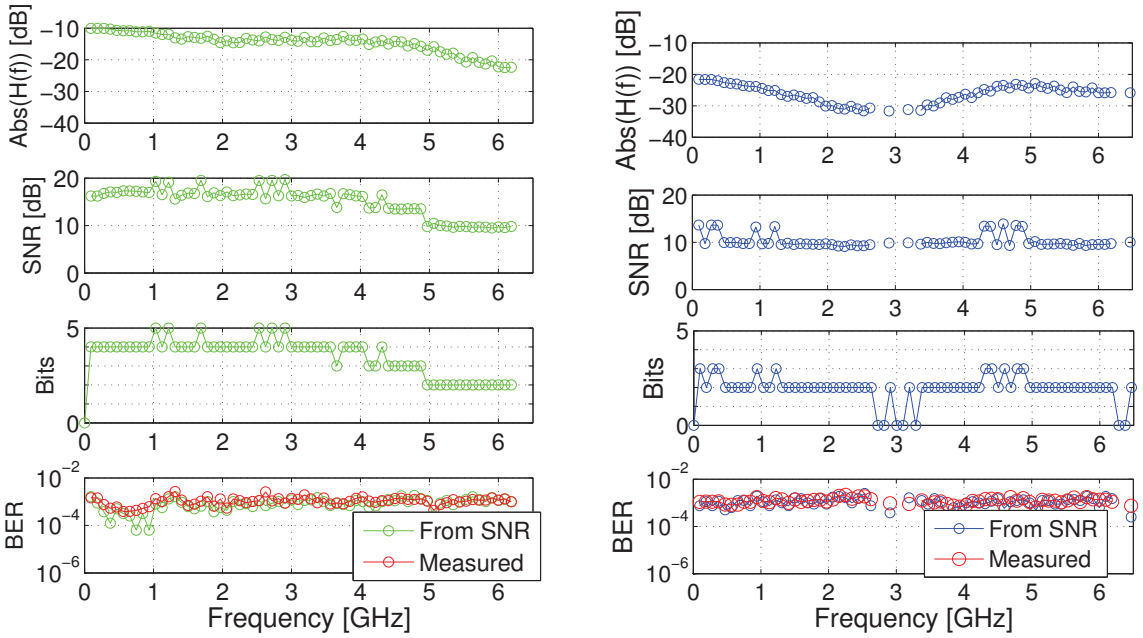

(a) Optical B2B ($P_{opt} = -2.3dBm$) (b) 50km SMF ($P_{opt} = -8.8dBm$)

FIGURE 5.34: Transmission results for the direct-OFDM modulation of the hybrid DBR laser after bit and power loading.

BER. The total BER is 9×10^{-4} in optical B2B and 1.2×10^{-3} in 50km SMF configuration. Received constellations for the 11^{th} subcarrier in optical B2B (32-QAM) and 1^{st} subcarrier in 50km SMF configuration (8-QAM) shown in figure 5.35.

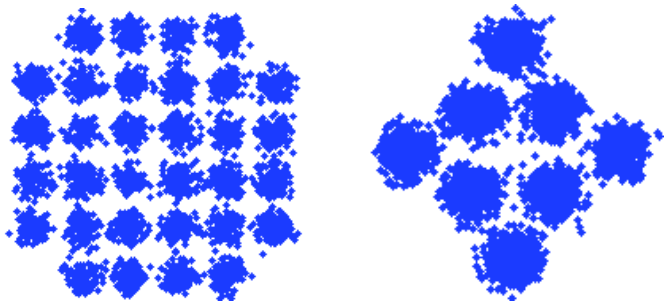

(a) Optical B2B (b) 50km SMF

FIGURE 5.35: Received constellations in (a) optical B2B with EDFA, 11^{th} subcarrier, 32-QAM and (b) 50km SMF, 1^{st} subcarrier, 8-QAM

We analyze the achievable data-rate as a function of the received optical power without the use of the EDFA. The results are depicted in figure 5.36, which shows a sensitivity for 10Gbps of -13dBm (optical B2B). It shows a 1.8dB sensitivity penalty for data-rates higher than 10Gbps at 50km SMF. An interest remark is that the sensitivity penalty is higher for 20km SMF (approximately 3.2dB), because of the higher attenuation of the frequency response above 3GHz as indicated in figure 5.29(b).

At 50km SMF, a [bit-rate × reach] product of $620 Gbps \times km$ is measured, which is about five times the [bit-rate × reach] product of the single-carrier OOK modulation, limited by chromatic dispersion. This demonstrates the effectiveness of OFDM to mitigate dispersion.

In order to extend optical budget, an EDFA is placed at the laser output. The optical gain is set to 10dB in optical B2B (corresponding to a launched power of 12dBm) while it is set 7.5dB for 20-50km of SMF (corresponding to a launched power of 8.5dBm). A summary of the achievable optical budget (including fiber) for data-rates higher than 10Gbps with and without EDFA is listed in table 5.5.

	B2B	20km SMF	50km SMF
W/out EDFA	14.5dB	11.3dB	12.7dB
With EDFA	23dB	17dB	18.5dB

TABLE 5.5: Summary of the achievable optical budget with the direct OFDM modulation of the hybrid III/V-on-silicon DBR laser with and without EDFA.

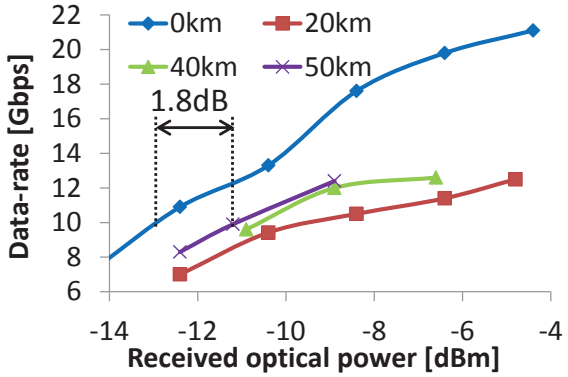

FIGURE 5.36: Data-rate as a function of the received optical power without EDFA for the hybrid DBR laser.

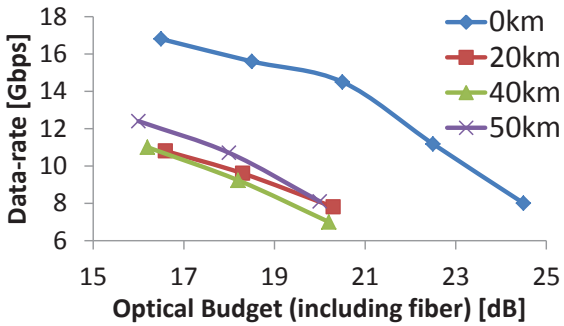

FIGURE 5.37: Data-rate as a function of the optical budget with EDFA for the hybrid DBR laser.

5.1.5 Silicon Ring-Resonator Modulator

Another very popular type of silicon-based modulator is the microring structure. A very detailed description of this type of modulator is given in subsection 2.2.3.2.

In this part, the transmission performance of an optimized optical OFDM link using a silicon microring modulator is studied. Compared to silicon MZM, it has generally a lower footprint and lower power consumption, which are two desirable characteristics for transmitters at the ONU. In addition, lower optical insertion losses are achieved with this structure. The disadvantage is that local temperature should be finely controlled to avoid drifting of the resonance wavelength of the resonator and ensure proper operation.

In the first part, the experimental work is described. Due to the high coupling losses into and out of the silicon chip, the reach was limited to 20km. In the second part, we use the simulation platform to evaluate the transmission capacity of the OFDM transmission using the ring modulator at longer SMF-span lengths. It starts by computing the SMF-link frequency response with the proposed model in an undercoupling and overcoupling condition. Then, the capacity penalty associated with the fading caused by chromatic dispersion up to 100km is evaluated.

5.1.5.1 Experimental Demonstration

Silicon Ring Modulator Characteristics

The interferometric structure used in this experiment is fabricated in a 220nm/100nm rib waveguide in a 200mm-diameter SOI wafer in the CEA-Leti clean-rooms. The ring has $200\mu m$ diameter and 150nm gap between the input waveguide and the ring resonator. The rib waveguide has a width of 400nm and a height of 120nm, which ensures single-mode operation. The waveguide is defined by partially etching the silicon using lithography.

The junction is based on a lateral PN structure, and the cross section of the active region is shown in figure 5.38(a). The center of the junction is shifted by 100nm from the center of the waveguide in the N-doped region direction to maximize overlap between the depletion zone and the optical mode. The target doping is $5 \times 10^{17} cm^{-3}$ for both P and N regions, but measured to be slightly lower than that. The heavily-doped regions are defined $1\mu m$ spaced from the waveguide for both the P-doped and N-doped regions to avoid high propagation losses, with a target doping of $10^{19} cm^{-3}$. The doped regions are defined by ion implantation (Boron for the P-doping and Phosphorous for the N-doping) and rapid thermal annealing to active the dopants. The contact between the electrodes and the heavily doped regions is done using Tungsten. The electrode is formed with AlCu deposition and etching using a hard mask.

The input/output into the chip is done using 1D grating couplers. A picture of the device is shown in figure 5.38(b).

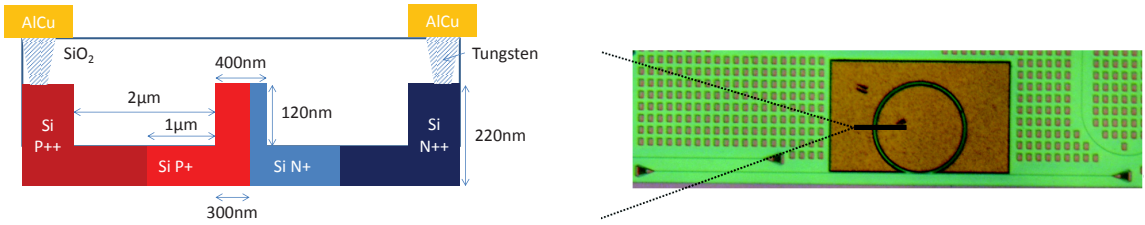

(a) Cross-section active region

(b) Microscopic picture

FIGURE 5.38: Structure of the ring modulator used for OFDM modulation.

DC Characterization of the Silicon Ring Modulator

For the DC characterization of the device, we checked out that the input light into the sample is polarized in the TE direction, maximizing coupling efficiency regarding the state of polarization. Figure 5.39 shows the transmitted spectrum around the resonance wavelength 1547.8nm for several inverse bias voltages. Figure 5.40 depicts the transmission at a fixed wavelength of $\lambda_{opt} = 1547.8nm$ as a function of the applied inverse voltage, which corresponds to the resonant wavelength λ_{res} at about $V_0 = -1.75V$.

Around $1.55\mu m$, a FSR of 1nm is measured, resulting in a group index of approximately 3.8. The DC contrast (ratio between minimum and maximum optical output power) is 13.5dB at 0V and increases up to 24.5 at -10V. This indicates that the ring approaches the critical coupling as the inverse bias voltage decreases. It also suggests that the ring is in the undercoupled condition (cf. definition in subsection 2.2.3.2). The off-resonance insertion losses are 12.5dB. Figure 5.40 indicates a contrast of 17dB at the wavelength of 1547.8nm. In a resonant structure, the $V_\pi L_\pi$ product can be calculated using the following equation

$$V_\pi L_\pi = V \cdot \frac{FSR \cdot \pi R}{\Delta\lambda} \tag{5.9}$$

where $\Delta\lambda$ is the resonance wavelength shift when a voltage V is applied. This equation is obtained from the $V_\pi L_\pi$ definition in (2.45) and using $\Delta n_{eff} = \lambda_{opt} \cdot \Delta\lambda / (FSR \cdot 2\pi R)$. Considering the fact that the PN junction in located only 86% of the ring resonator, The $V_\pi L_\pi$ varies from 2.6V.cm at -2V to approximately 3.9V.cm at-10V.

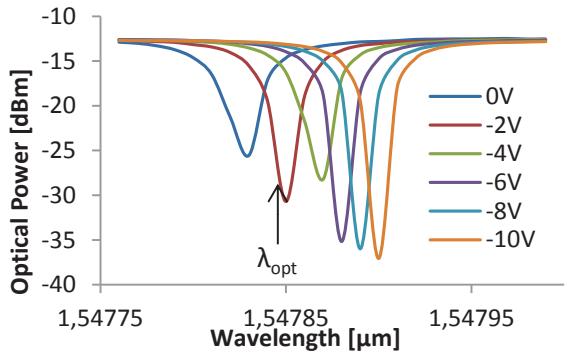

FIGURE 5.39: Spectral response of the ring modulator for several applied voltages.

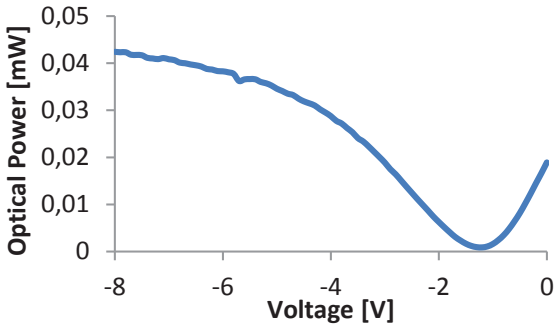

FIGURE 5.40: Transmitted optical power as a function of the applied voltage at $\lambda_{opt} = 1547.8nm$.

AC Characterization of the Silicon Ring Modulator

For the AC characterization, the bias voltage is -2.25V, which corresponds an optical output power of 40% (-4dB) below the maximum of the transmission. In each AC measure, the operating wavelength λ_{opt} is chosen at the resonance wavelength λ_{res} for an applied voltage $V_0 = -1.75V$. It is around $\lambda_{opt} = 1547.8nm$, but it can vary from a few tens of pm due to local temperature variations. Figure 5.41 shows the electro-optic frequency response for several biasing points with a RF modulating power of -2dBm ($0.5V_{pp}$ peak-to-peak voltage). The biasing point is represented in % relative to the maximum transmission point which is 12.5dB below the optical input power. As expected from figure 5.41, lower biasing points result in higher modulation efficiencies (in low frequencies). However, the -3dB modulation bandwidth increases from 2.4GHz in 9% biasing to approximately 3.6GHz in 42% biasing. The estimated Q factor (using $Q = FWHM/\lambda_{opt}$) at -2V is between 40000-50000, which results in a photon-lifetime bandwidth of 3.8GHz.

The frequency response of the link including 40km of SMF is displayed in figure 5.42 (subtracting the response of the modulator in optical B2B). It indicates an almost flat frequency response up to 6GHz. Because of the very low optical output power of the modulator, it was not possible to evaluate the link response to small-signal modulation for longer fiber-span lengths.

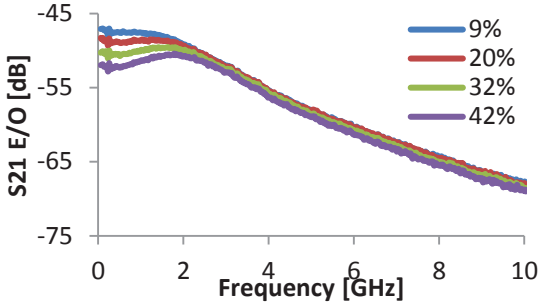

FIGURE 5.41: E/O frequency response to small-signal modulation of the silicon microring modulator.

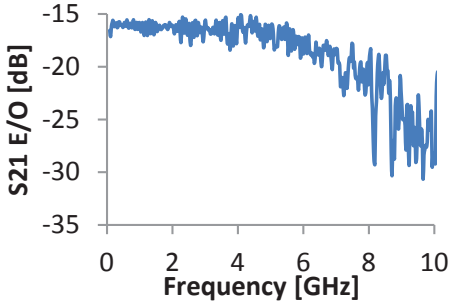

FIGURE 5.42: E/O frequency response of the 40km-SMF link, subtracting the optical B2B response.

Non-linear Characterization of the Silicon Ring Modulator

The non-linear characteristic of the modulator is analyzed by modulating the ring with a single tone signal at $f_{RF} = 125MHz$ with a fixed RF power of 8dBm (using a 10dB electric amplifier), similar to the set-up described in figure 5.4, but with $P_2 = 0$. The two-tone RF signal was not used in this measure due to unavailability of the RF source at the time of the experiment. The

CP1dB could not be measured because the RF power modulating the ring is limited due to the fact that it is not adapted to a 50Ω charge (estimated to be ≈ 25Ω), causing excessive reflection back to the electric amplifier. The RF power of 8dBm is the maximum modulating power allowed to ensure that the electric amplifier is not damaged. The results are displayed in figure 5.43. The Third-order Harmonic Distortion (HD3) is the ratio between the RF power at f_RF and at $3f_{RF}$. The most linear region and with higher output power is between 30-45% of the biasing point.

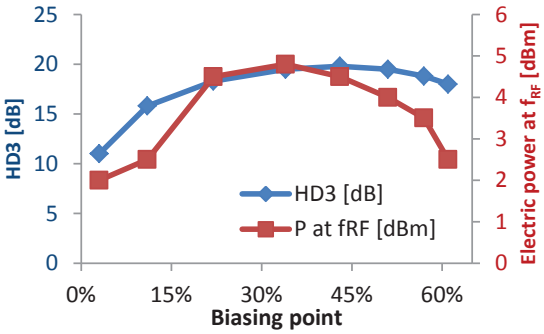

FIGURE 5.43: HD3 and RF power at the photoreceiver output for the ring modulator with a single tone at $f_{RF} = 125MHz$.

OFDM Experimental Set-up for the Silicon Ring Modulator

The experimental set-up for the optical OFDM modulation of the silicon microring modulator is shown in figure 5.44 and table 5.6 summarizes the parameters of the OFDM transmission.

Number of OFDM symbols per acquisition	4000
AWG (sampling rate)	Tektronix AWG70000 ($f_{s_{DAC}} = 12.5Gsps$)
Subcarrier spacing	$\Delta f = f_{s_{DAC}}/N = 48.9MHz$
Number of data carriers	$N_{DATA} = 81$
OFDM bandwidth	$B = f_{s_{DAC}} \cdot N_{DATA}/N = 4GHz$
AWG output peak-to-peak voltage	$0.5V_{pp}$
Bias current	$\approx -2V$ (31%)
Peak-to-peak voltage modulating the ring	$2.9V_{pp}$
CW laser optical power	10.5dBm
CW laser wavelength	$1.55\mu m$
Optical output power in SMF	-7.1dBm
Photoreceiver (conversion gain)	NewFocus 1554-B ($750V/W$)
DSO (sampling rate)	Tektronix DSA72004C ($f_{s_{ADC}} = 12.5Gsps$)

TABLE 5.6: Parameters for the OFDM modulation of the ring-resonator modulator.

The electric gain before the modulator is set to 10dB, resulting in a peak-to-peak voltage of $1.58V_{pp}$ in the amplifier output. Due to microwave reflection from the ring-resonator modulator, the effective modulating voltage V_s of the ring is the sum of the output voltage V_0 from the amplifier and the reflected signal $V_s = V_0 + V_r$. This can be calculated using the measured complex S_{11} parameter through the relation $V_s = V_0 \cdot [1 + |S_{11}| \exp(jArgS_{11})]$. The effective modulation voltage of the ring-resonator modulator is calculated to be $V_s = 2.9V_{pp}$.

Note that the modulation depth is not optimized. This is because the fact that the input impedance to the ring modulator is not adapted to 50Ω, which causes the input electric signal to be reflected almost completely. Thus the modulation depth is limited to avoid damaging the

RF driver before the modulator. The optimum biasing point is found to be approximately 31% below the maximum transmission point, in accordance with non-linear characteristics of the modulator in figure 5.43.

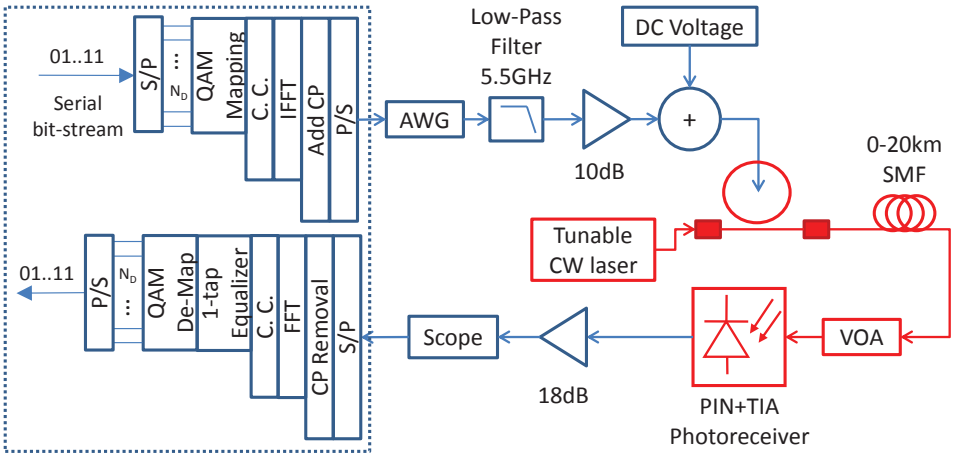

FIGURE 5.44: Experimental set-up for the optical OFDM experiment using the ring-resonator modulator as optical transmitter.

Results and Discussions of the OFDM Experiment using the Silicon Ring Modulator

The SNR per subcarrier before and after the bit and power loading is shown in figure 5.45 and figure 5.46 for the optical B2B (received optical power of -7.1dBm) and 20km SMF (received optical power of -11.3dBm) respectively. By comparing it to the electric B2B performance shown in appendix B.7, it can be shown that the penalty due to the electric components of the link is negligible.

Figure 5.47 shows the channel frequency response ($H(f)$), bit and power allocation as well as the BER per subcarrier (measured and calculated from SNR) for the optical B2B and 20km case. The SNR degradation after 20km is uniquely due to the lower received optical power since the link frequency response is unaltered (14dB roll-off at 4GHz) as illustrated in the first line of figure 5.47. Note the excellent performance of the modulator, achieving up to 64-QAM constellation in optical B2B (22dB SNR) and up to 32-QAM after 20km SMF (with 19dB SNR). These results are achieved without any optical amplifier in the link. The total data-rate and total BER measured (which has the same value as the one computed from the SNR) are 16.8Gbps/1.7×10^{-3} in optical B2B and 11.7Gbps/1.2×10^{-3} after 20km SMF. Note that the BER per subcarrier measured from the generated bits has a higher variance than the one computed from the SNR, but the total BER among the subcarriers converges to the same value in both cases. Received constellations for the 12^{th} subcarrier in optical B2B (64-QAM) and the 1^{st} subcarrier after 20km SMF (32-QAM) are shown in figure 5.48, demonstrating the good quality of the transmission.

Finally, figure 5.49 shows the achievable data-rate as a function of the received optical power for which the total BER is systematically below 2.2×10^{-3}. Negligible sensitivity penalty is observed for data-rates higher than 10Gbps. Transmission performance is limited by the high coupling losses into and out of the chip. In practice, an optical amplifier is required. Due to the relatively low bandwidth required for the OFDM signal, the transmission up to 100km is expected to be possible without degrading the achievable data-rate as the link frequency response is unaltered.

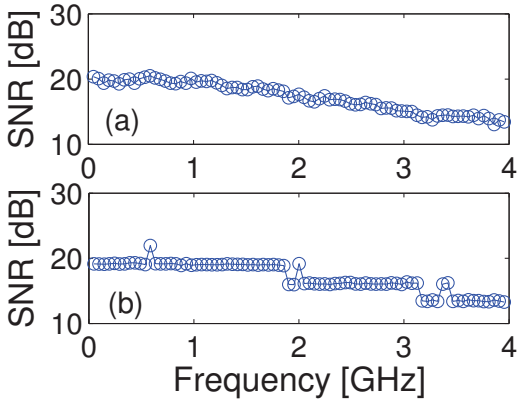

FIGURE 5.45: SNR per subcarrier (a) before and (b) after bit and power loading, in optical B2B.

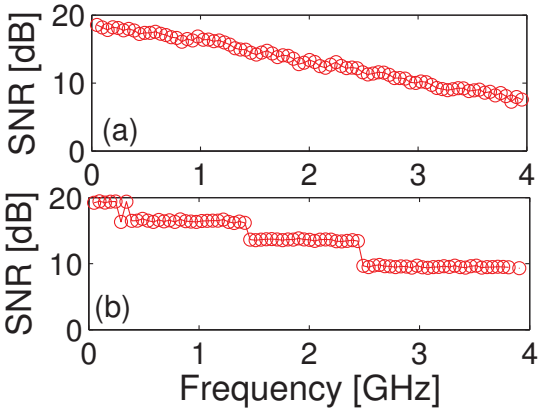

FIGURE 5.46: SNR per subcarrier (a) before and (b) after bit and power loading, in 20km SMF.

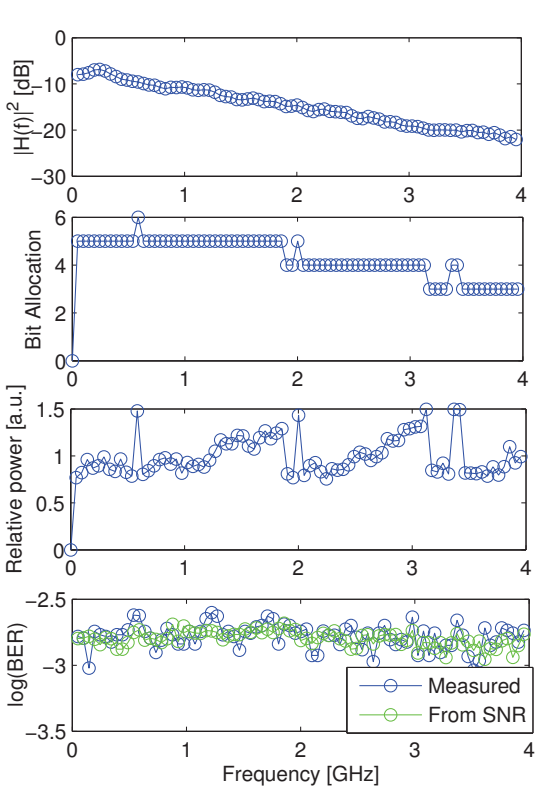

(a) Optical B2B

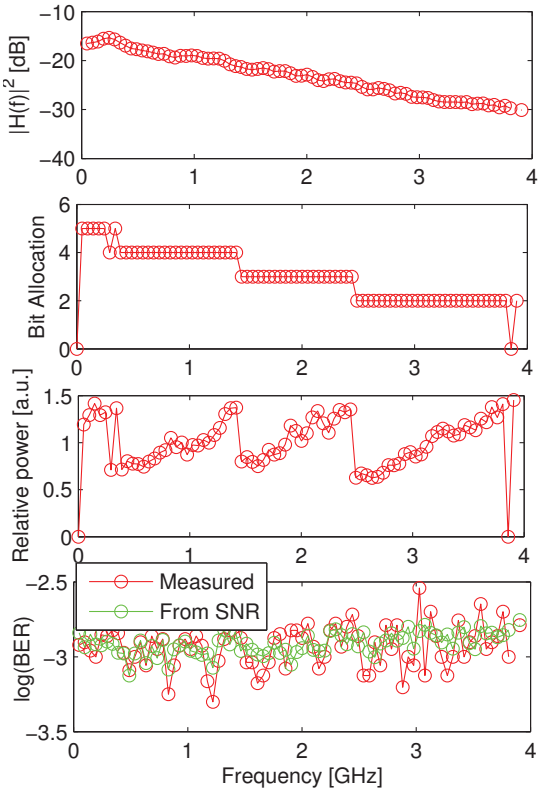

(b) 20km SMF

FIGURE 5.47: Channel frequency response ($H(f)$), bit and power allocation and BER per subcarrier in (a) Optical B2B ($P_{opt} = -7.1dBm$) and (b) 20km SMF ($P_{opt} = 11.3dBm$).

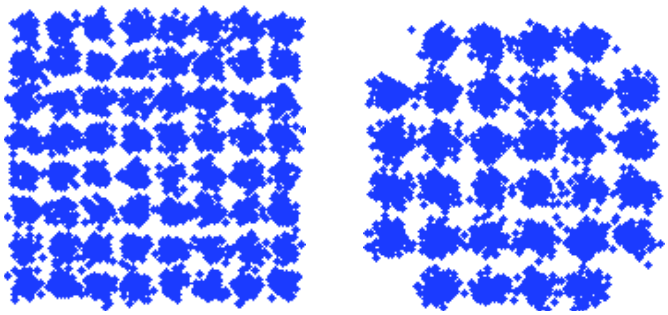

(a) Optical B2B (b) 20km SMF

FIGURE 5.48: Received constellations in (a) optical B2B, 12^{th} subcarrier, 64-QAM and (b) 20km SMF, 1^{st} subcarrier, 32-QAM

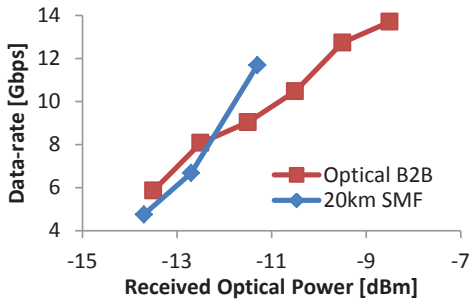

FIGURE 5.49: Achievable data-rate as a function of the received optical power for the adaptive OFDM modulation of the ring modulator.

5.1.5.2 Simulation

Because of the high coupling losses in and out of the chip, we were unable to assess the OFDM performance using the ring-resonator modulator at higher SMF lengths. By means of simulation, the transfer function and the required sensitivty for the OFDM transmission using the ring-resonator modulator is evaluated up to 100km SMF. The silicon ring-resonator modulator model is simulated using a Matlab routine according to the model presented in 2.2.3.2.

Numerical Evaluation of the Frequency Response of the SMF-Link using the Silicon Ring Modulator

In the following, the frequency response of the SMF link considering an optical carrier modulated with a silicon ring-resonator modulator is evaluated. This depends on the frequency chirp introduced by the silicon ring modulator. This analysis is important because it impacts on the performance of the OFDM signal transmission over the fiber as discussed in subsection 3.3.3.1. A positive and high value of the chirp limits the achievable bandwidth because the first null of the transmission is closer to DC for a given fiber span length. The previous presented dynamic model for the ring modulator is considered. We considered a fixed Q factor of 19000, which results in a photon lifetime -3dB bandwidth of 10GHz.

Two coupling conditions are considered, and another two conditions on the operating wavelength λ_{opt} are studied, totalizing four study cases :

- Undercoupled
  - $\lambda_{opt} = \lambda_{res}$ at $V_0 = 0V$
  - $\lambda_{opt} = \lambda_{res}$ at $V_0 = -8V$
- Overcoupled

– $\lambda_{opt} = \lambda_{res}$ at $V_0 = 0V$
– $\lambda_{opt} = \lambda_{res}$ at $V_0 = -8V$

The coupling coefficient and absorption loss in the ring are chosen such that, at V_0 voltage applied, 10% of the intensity passes through the ring. The resulting parameters for the simulation are detailed in table 5.7 for a ring radius of $R = 10\mu m$. For illustration purposes, figure 5.50 depicts the spectral response of the proposed models for the ring modulators in the undercoupled condition, for both values of V_0.

	Undercoupling, $V_0 = 0V$	Undercoupling, $V_0 = -8V$	Overcoupling, $V_0 = 0V$	Overcoupling, $V_0 = -8V$
α_{abs}	25dB/cm	29dB/cm	13dB/cm	15dB/cm
κ_1	0.136	0.139	0.189	0.175

TABLE 5.7: Ring resonator parameters used for computing the frequency response to small-signal modulation with chromatic dispersion.

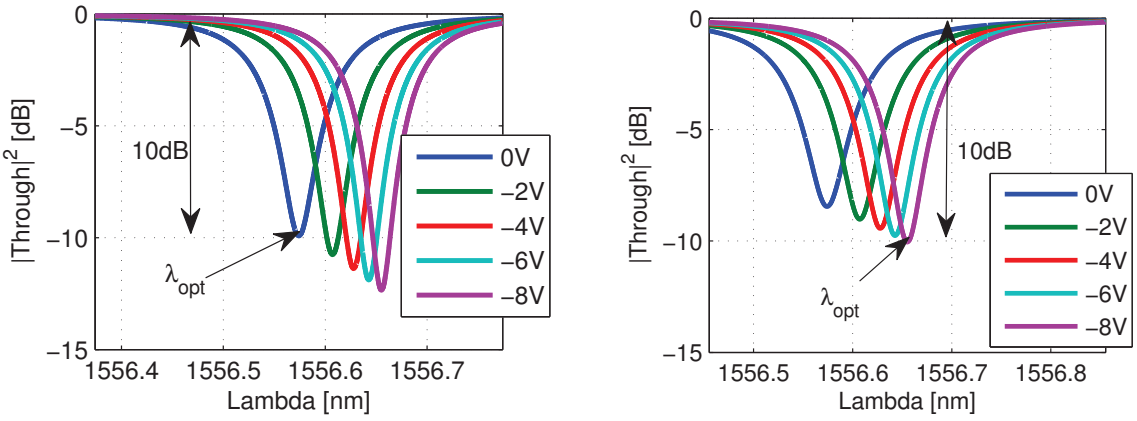

(a) $\lambda_{opt} = \lambda_{res}$ at $V_0 = 0V$ (b) $\lambda_{opt} = \lambda_{res}$ at $V_0 = -8V$

FIGURE 5.50: Spectral response of the proposed microring modulator model in undercoupled condition used to evaluate the frequency response of a SMF-link with λ_{opt} at resonance.

The frequency response of the ring-resonator modulation over a 100km-SMF link ($D = 16ps/nm \times km$) is evaluated, three biases are considered (-2V, -4V and -6V) and the modulation amplitude is 0.01V. Figure 5.51(a) and (b) show the simulation results for the undercoupled case considering $V_0 = 0V$ and $V_0 = -8V$, respectively. Figure 5.52(a) and (b) illustrate the overcoupled case results for $V_0 = 0V$ and $V_0 = -8V$, respectively. The frequency response in optical B2B is first calculated and then subtracted from the frequency response in the presence of the 100km-SMF span.

An interesting observation is that there is one case, the overcoupled condition with $\lambda_{opt} = \lambda_{res}$ at $V_0 = -8V$ that gives better results over the four cases, which may be a result of negative frequency chirp. In this specific case, the highest bandwidth and even some gain up to 4GHz is observed. A general conclusion is that the undercoupled condition results in lower bandwidth regardless the position of λ_{opt}. This may be a result of a higher frequency chirp in this condition.

Note that the simulated frequency response of the link does not fit well the general frequency response to small-signal modulation with chromatic dispersion provided by (2.30). This is why it was not possible to estimate an equivalent chirp parameter. A possible reason for that is because the frequency chirp of the ring-resonator modulator cannot be described as the classical definition for DMLs and MZMs given in equation (2.30). As explained in [204], this may be

caused by oscillations in the phase of the output signal when the ring goes from the "on" state to the "off" state.

As a future work, one can consider evaluating analytically the frequency response to small-signal modulation of the ring modulator with chromatic dispersion.

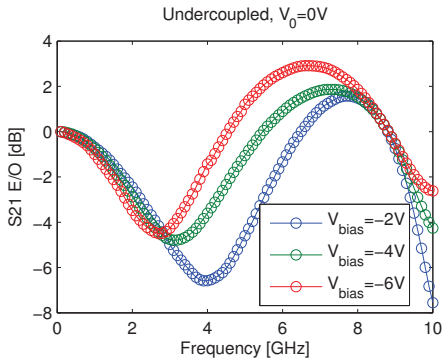

(a) $\lambda_{opt} = \lambda_{res}$ at $V_0 = 0V$

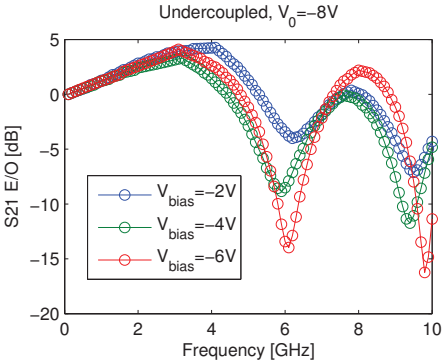

(b) $\lambda_{opt} = \lambda_{res}$ at $V_0 = -8V$

FIGURE 5.51: Frequency response, undercoupled condition in 100km-SMF with (a) $V_0 = 0V$ and (b) $V_0 = -8V$.

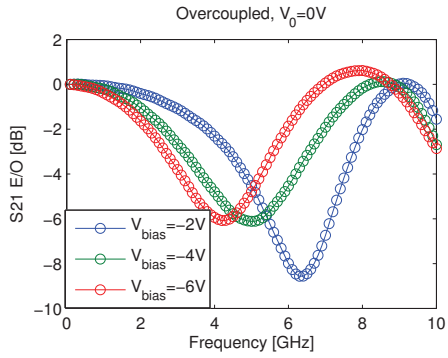

(a) $\lambda_{opt} = \lambda_{res}$ at $V_0 = 0V$

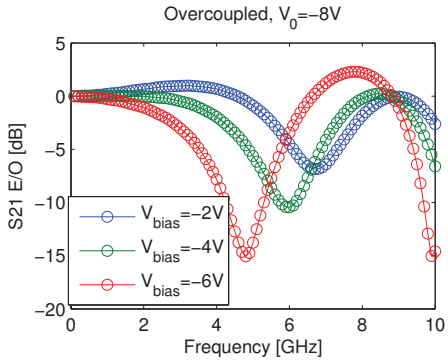

(b) $\lambda_{opt} = \lambda_{res}$ at $V_0 = -8V$

FIGURE 5.52: Frequency response, overcoupled condition in 100km-SMF with (a) $V_0 = 0V$ and (b) $V_0 = -8V$.

OFDM Simulation Set-up and Results for the Silicon Ring Modulator

For this analysis, the OFDM symbol configurations is the same as described in subsection 5.1.1.4, except for the number of cyclic prefix samples which is decreased down to $N_{CP} = 2$.

The main simulation parameters are summarized in table 5.8. Note that the modulation format per subcarrier is fixed to 16-QAM. The number of OFDM symbols per simulation run is 500, which gives a SNR uncertainty of 0.07dB according to (3.16), resulting in BER uncertainty below 10^{-4} for the target BER. In the simulation, to ensure convergence of the Euler's method for the dynamic simulation of the ring, the OFDM signal is oversampled by a factor of 16 by increasing fourfold the FFT size, resulting in a simulation bandwidth of 40GHz and a time step of 25ps. The number of data subcarriers is 127 over an OFDM bandwidth of 2.5GHz.

The objective is to evaluate the sensitivity for the four cases analyzed in table 5.7, and the sensitivity penalty due to the SMF up to 100km. The ring modulator parameters are the same as above. We consider that, for $V_0 = 0V$ and $V_0 = -8V$, the junction is biased at -2V and -6V, respectively, to enhance modulation efficiency. The insertion losses at these bias voltages are 3.35dB and 7.35dB, respectively.

OFDM signal baseband bandwidth	$B = 2.5GHz$
Subcarrier spacing	$\Delta f = 2B/N = 19.5MHz$
Modulation format per subcarrier	16-QAM
Data-rate (w/out accounting cyclic prefix)	10Gbps
OFDM symbols per simulation run	1000
Simulation bandwidth (time-step)	$B_{sim} = 40GHz$ ($t_{step} = 1/B_{sim} = 25ps$)
Wavelength	$1.55\mu m$
SMF dispersion parameter	$D = 16ps/(nm \times km)$
SMF propagation loss	$0.2dB/km$
Photoreceiver conversion gain	750V/W
Photoreceiver NEP	$20pA/\sqrt{Hz}$

TABLE 5.8: Simulation parameters for the performance evaluation of optical OFDM using silicon ring-resonator modulator.

The first analysis is to find the optimum peak-to-peak driving voltage to maximize the receiver's sensitivity. Figure 5.53 depicts the BER for 16-QAM as a function of the receiver optical power for several driving voltages, in an undercoupling condition and $\lambda_{opt} = \lambda_{res}$ at $V_0 = 0V$. It shows an optimum driving voltage of $3V_{pp}$. It should be noted that lower driving voltages can be obtained by increasing the Q factor of the ring (which gives better modulation efficiency) at the expense of modulation bandwidth. Using this drive voltage, the sensitivity for a BER of 2.2×10^{-3} for the four cases considered (Undercoupled (UC) and Overcoupled (OC), for $V_0 = 0V$ and $V_0 = -8V$) is depicted in figure 5.54. A specific case, the overcoupled condition with $V_0 = -8V$, presents negative sensitivity power penalty. This agrees with the predicted frequency responses of the previous subsection. As indicated in figure 5.52(b), a gain is observed up to 3GHz, which leads to an improved sensitivity at 100km. All the other cases have positive sensitivity penalty, mainly due to the frequency fading up to 2.5GHz observed in figure 5.51 and figure 5.52(a).

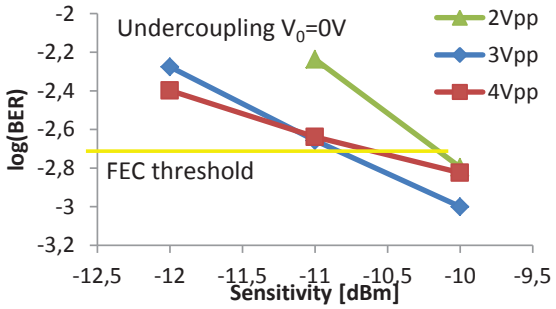

FIGURE 5.53: Optimization of the ring modulator driving voltage for the undercoupled condition.

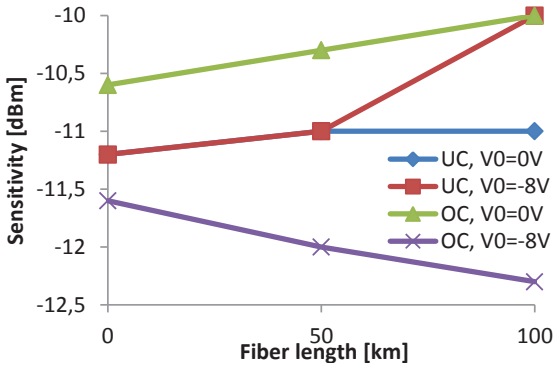

FIGURE 5.54: Sensitivity ($BER = 2.2 \times 10^{-3}$) as a function of the fiber length.

5.1.6 Silicon MZM

In this subsection, the transmission performance of a silicon MZM employing OFDM modulation is assessed. We had no possibility to evaluate experimentally the performance of the MZM modulators for the OFDM transmission because of the unavailability of the samples during the course of the thesis. Instead, we assessed their potential for the OFDM transmission

using our simulation platform. The simulations were fed with the silicon MZM model proposed in subsection 2.2.3. It is compared to an "ideal" $LiNbO_3$ MZM.

Note that the feasibility of OFDM modulation up to 16-QAM in silicon MZM was already demonstrated in [182] but limited to 1.7Gbps (with 500MHz bandwidth). The purpose of this analysis is to compute the sensitivity penalty caused by imperfections of the silicon MZM.

5.1.6.1 Numerical Evaluation of Chirp in Silicon MZM with Single-arm Modulation

In section 3.3.3.1, we show that by intentionally adding negative chirp to the modulated optical signal, the [bandwidth × reach] product can be improved. Assuming that the silicon MZM is modulated in only one arm, the output optical signal has considerable chirp as indicated by the phase transfer function illustrated in figure 2.35.

Equation (2.39) reports the relation between the chirp in a MZM α_{MZM} and the ratio between the driving voltages in the two arms of the modulator r_{MZM}. This assumes a $LiNbO_3$ modulator in which 1) the change in the refractive index of the waveguide is linear with the applied voltage as indicated in (2.32) and 2) the waveguide absorption does not vary with the applied voltage. As a consequence, a first consideration is that the MZM chirp (2.39) does not apply to silicon-based devices.

One could calculate the chirp in a silicon MZM considering two arbitrary modulation voltages between the two arms by using (2.57) (field transfer function of the silicon MZM) and replacing it in (2.38) (general chirp equation). In this work, we use a numerical approach. First, by using the simulation tool, the frequency response of the silicon MZM model driven in a single-arm in a 100km SMF-link is evaluated. In the simulation platform, a Matlab routine is used to simulate the silicon MZM model. The length of the device is set to 4mm and the junction is biased at -3V, corresponding to approximately the quadrature point. Small-signal modulation is assumed as the peak-to-peak voltage driving the modulator is $0.01V_{pp}$.

The α_{MZM} parameter is estimated by fitting the numerical results for the frequency response of the link with (3.67). Figure 5.55 displays the simulated frequency response over the 100km SMF-link, with two biasing points $\phi_0 = 0$ and $\phi_0 = \pi$ (cf. silicon MZM transfer function in (2.57)). The results show that the chirp in a silicon MZM based on the proposed model can be effectively calculated using (2.39) as for the $LiNbO_3$ modulators, in spite of the non-linear nature of the transfer function and the absorption variation with the applied voltage.

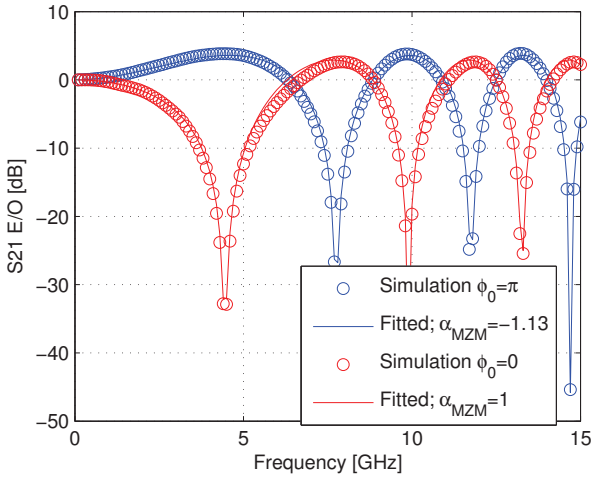

FIGURE 5.55: Chirp evaluation in silicon MZM driven in a single-arm.

5.1.6.2 OFDM Simulation Set-up and Results using the Silicon MZM

For this analysis, the OFDM symbol configuration and simulation parameters are the same as the ones used for the silicon ring-resonator modulator simulation (subsection 5.1.5.2) - 10Gbps 16-QAM-OFDM. The only difference is that the simulation bandwidth is decreased to 10GHz ($t_{step} = 100ps$). In this way, the number of OFDM symbols per run is increased to 1000 to improve precision on the BER estimator.

The modulation depth is measured in terms of the Optical Modulation Index (OMI), which is given by

$$OMI = \frac{V_{RMS}}{V_\pi} \tag{5.10}$$

where $V_{RMS} = \sqrt{E\left[|x_{OFDM}[n]|^2\right]}$ is the RMS value of the OFDM signal modulating the MZM. In the case of the $LiNbO_3$, the V_π is set to 5V. For the silicon MZM, the length is set to 4.7mm so that the V_π is the same as the $LiNbO_3$ at a voltage of -5V.

In both cases, the biasing point is chosen so that the chirp is negative ($\phi_0 = \pi$ in the silicon MZM case). First, the optimum OMI is evaluated to maximize receiver sensitivity at a BER of 2.2×10^{-3}. A low OMI decreases the received peak-to-peak voltage for a given received optical power, reducing the sensitivity. On the other hand, high values of the OMI cause severe non-linear degradation. Therefore, an optimum value must be found. As illustrated in figure 5.56, the receiver sensitivity is maximized for an OMI of 0.14 for the "ideal" $LiNbO_3$ modulator and 0.1 for the silicon MZM. The $LiNbO_3$ achieves a higher sensitivity of 3.75dB as compared to the silicon MZM at the optimum value of the OMI for each modulator. If the same OMI of 0.1 is considered, a sensitivity difference of 2.85dB is observed. This lower sensitivity may be attributed to the non-linear nature of the silicon MZM.

An interesting remark is that, at 0km, the sensitivity is in the same order of magnitude of the silicon ring-resonator-modulator (depending on the ring configuration, it may be slightly higher or lower), indicated in figure 5.54. This suggests that, in accordance with [209], that the non-linearity degradation introduced by the junction dominates over the non-linear transfer function of the ring.

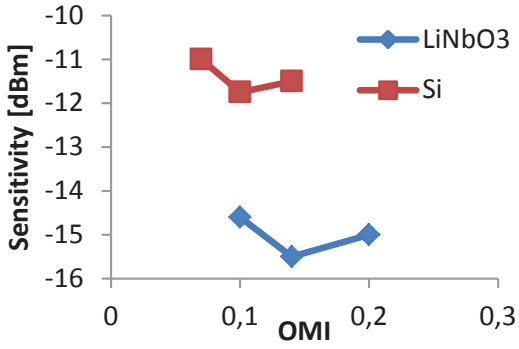

FIGURE 5.56: Sensitivity of the 16-QAM-OFDM signal at a BER of 2.2×10^{-3} as a function of the OMI for the silicon and $LiNbO_3$ MZMs.

Then, the transmission performance in 50km and 100km SMF is assessed using an OMI of 0.14 for the $LiNbO_3$ and 0.1 for the silicon MZM. The simulation results are displayed in figure 5.57. It shows a slightly negative sensitivity penalty for the $LiNbO_3$ case, while for the silicon MZM a negative power penalty of approximately -0.25dB and -1dB in 50km and 100km SMF, respectively. The negative power penalty is expected as a result of the negative chirp induced

by the modulators. The higher negative power penalty of silicon MZM is attributed to the lower modulation depth, which reduces dispersion-induced distortions of chirped signals [243].

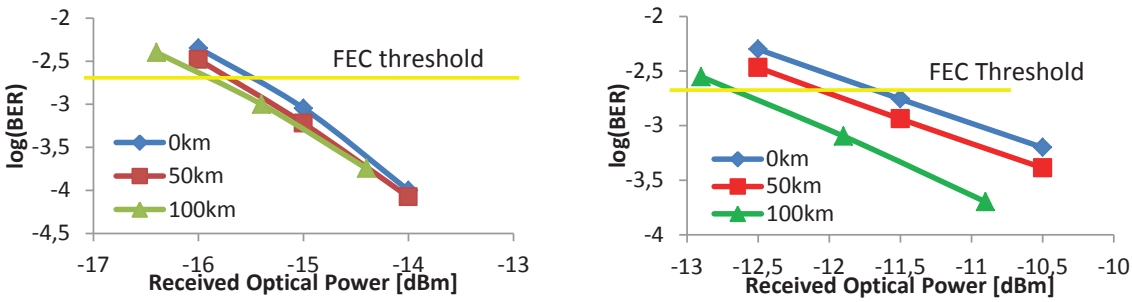

(a) $LiNbO_3$ (b) Silicon MZM

FIGURE 5.57: BER of the 16-QAM-OFDM signal as a function of the received optical power for the (a) $LiNbO_3$ and (b) silicon MZMs, for 0, 50km and 100km SMF.

5.2 Optical SSB-OFDM using a Silicon Photonics Transmitter

Transmitters based on silicon photonics technologies are an interesting solution for decreasing the cost per unit of the CO transmitter as well for such a large-volume application. Due to its high integration capability, this technology is attractive for building complex transmitters that would normally require several discrete components such as the optical SSB-OFDM transmitter introduced in subsection 4.2.2. As mentioned in subsection 2.2.3.1, silicon optical IQ modulators have already been demonstrated using single-carrier modulation [179, 280].

As compared to $LiNbO_3$, optical modulation using silicon for advanced modulation formats which require high linearity is more challenging. As explained earlier, the electro-optic effect in silicon by the free-carrier plasma effect is not linear. In addition, the electron/hole concentration variation necessary to change the refractive index of the waveguide varies also the absorption coefficient. In interferometric structures such as a MZM, this can cause a power imbalance between both arms, leading to a non-ideal push-pull operation.

5.2.1 Numerical Evaluation of Residual Chirp in Push-Pull Silicon MZM

The residual chirp in push-pull silicon MZM has already been addressed by a few authors. For example, in [281], the author shows that a residual chirp of -0.8 in a push-pull MZM is measured. This was mainly due to the asymmetrical splitting of the device (31 : 69 instead of 50 : 50). The author calculates that a residual chirp of -0.2 is found considering ideal splitting, which is caused by the difference in the modulation efficiency and absorption between both arms. In spite of that, near zero chirp operation with push-pull silicon MZMs is reported in [73, 280, 282, 283].

Using the same method described in subsection 5.1.6.1, the residual chirp in silicon MZM based on the model described in subsection 2.2.3.2 is evaluated numerically. The driving scheme for the push-pull silicon MZM is illustrated in figure 2.36. The modulation amplitude is set to $V_{pp} = 0.01V$. Figure 5.58 displays the evaluated frequency response over a 100km-SMF-link together with the fitting results with (3.67). The residual chirp is evaluated to be $\alpha_{MZM} \approx 0.087$.

5.2.2 Silicon Optical IQ Modulator Integrated Circuit

A schematic of the integrated modulator is depicted in figure 5.59. The optical carrier is coupled through a classic grating coupler. The light is split in two branches, each one dedicated

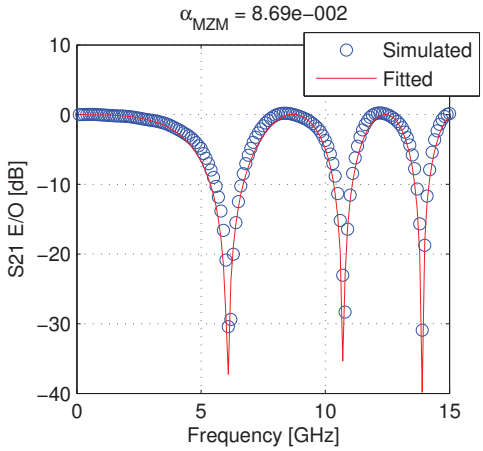

FIGURE 5.58: Chirp evaluation on a silicon MZM driven in push-pull, resulting in $\alpha_{MZM} \approx 0.087$.

to an independent MZM. The upper MZM is driven by the in-phase data and the bottom MZM with the quadrature data, both in a push-pull configuration. In order to properly set the biasing point of the MZM, a useful solution to avoid insertion losses is to integrate resistive heaters in top of the waveguide [284]. In this way, the refractive index varies as a function of the temperature, which in its turn is varied by applying an electric current. The $\pi/2$ phase-shift between I and Q arms can also be finely adjusted with a resistive heater. The modulated optical signal is coupled out using a grating coupler.

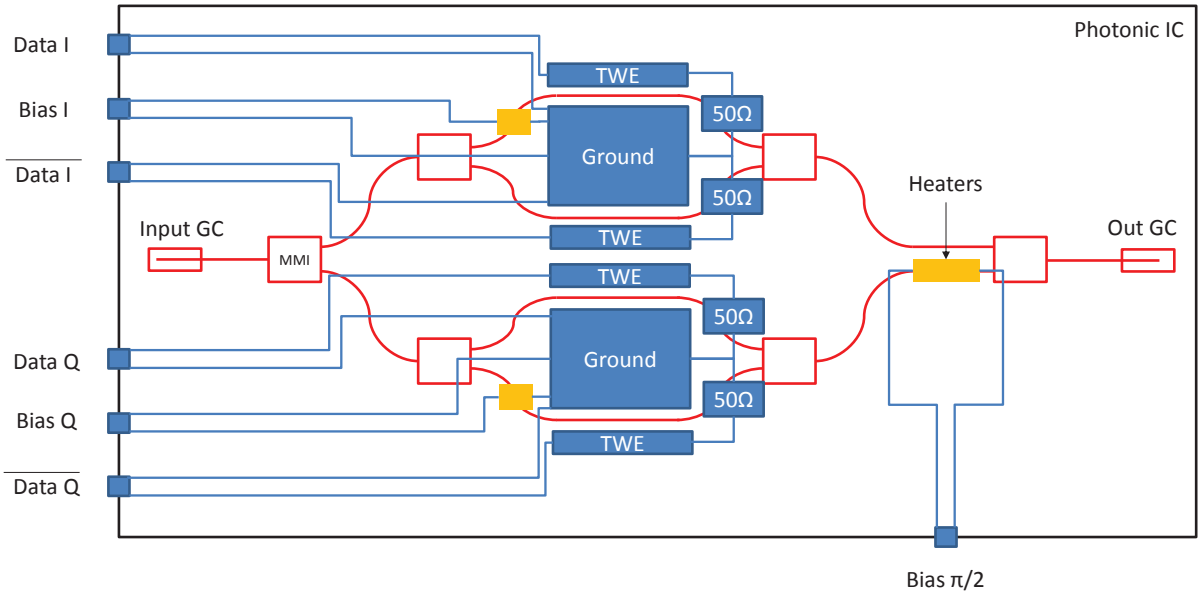

FIGURE 5.59: Schematic of the photonic integrated circuit for the optical IQ modulator. GC : Grating coupler ; TWE : Travelling-wave electrode ; MMI : Multimode Interferometer.

5.2.3 Simulation of the Transmission Performance

In this part, the sensitivity penalty and achievable optical budget for an optical SSB-OFDM transmission implemented with a silicon optical IQ modulator is evaluated in comparison with

a $LiNbO_3$ modulator. The silicon MZM is based on the previous presented model for the active region in subsection 2.2.3.2.

5.2.3.1 Simulation Set-up for the Optical SSB-OFDM with Silicon Photonics Transmitter

The simulation parameters are displayed in table 5.9. A baseband bandwidth of 5.5GHz is set for a modulation format of 16-QAM, resulting in a data-rate higher than 40Gbps accounting the 1.5% overhead due to the cyclic prefix and 7% FEC overhead. Neither quantization nor clipping is added to the OFDM signal. The CSPR is set to the optimum value of 0dB [247]. The SNR uncertainty range for the 500 OFDM symbols is 0.07dB, resulting in a very accurate BER estimation from the SNR.

A silicon MZM with length 4.7mm and propagation loss of 15dB/cm is considered, which gives a V_π of 5V at an applied voltage of 5V, with the proposed model. For comparison, a $LiNbO_3$ MZM with the same V_π and insertion loss is considered. Because the optical modulator is necessarily biased at the null intensity point, the insertion loss of the device is directly proportional to the OMI, which is defined in (5.10), as indicated by the transfer function of the optical IQ modulator in (2.42). On the other hand, high values of the OMI induce non-linear distortion to the signal. This is the trade-off between insertion losses and non-linear distortion of the optical IQ modulator. An optical amplifier in the transmitter output is added to overcome high insertion losses of the device.

The direct detection receiver comprises an APD, a TIA followed by a high pass filter and a RF down-conversion circuit (2 mixers, a LO, a $\pi/2$ phase-shifter and two low-pass filters) to convert the IF signal to baseband. The APD parameters were extracted from state-of-the-art SiGe APDs which were described in subsection 2.3.4. The TIA parameters were taken from the component presented in [285], which is fabricated in 90nm CMOS and designed for 40Gbps OOK receivers. No imperfections such as power and phase imbalance are assumed in the electrical down-conversion circuit.

Modulation format	16-QAM
FFT Size	$N = 256$
Cyclic Prefix Samples	$N_{CP} = 4$
OFDM Symbols per run	500
Baseband OFDM Bandwidth	5.5GHz
Simulation Bandwidth	44GHz ($t_{step} = 22.7ps$)
CW laser Power	13dBm
CW laser Wavelength	1550nm
EDFA Gain	22dB
EDFA Noise Figure	8dB
EDFA Saturation Power	17dBm
Fiber Chromatic Dispersion	$16ps/(nm \times km)$
Fiber Loss	0.2dB/km
APD Conversion Gain	$M \times R_d = 10A/W$
APD Dark Current	$I_d = 1\mu A$
APD Excess Noise Factor	$F_A = 10$
TIA Gain	$2k\Omega$
TIA NEP	$22pA/\sqrt{Hz}$

TABLE 5.9: Simulation parameters for the performance evaluation of optical SSB-OFDM transmitters.

5.2.3.2 Sensitivity Penalty Analysis of the SSB-OFDM Simulation with the Silicon Photonics Transmitter

In a first analysis, we compare the sensitivities of the transmission using the "ideal" transmitter ($LiNbO_3$) and the silicon photonics one without the use of the EDFA. Figure 5.60 shows the 16-QAM sensitivity for achieving a BER of 2.2×10^{-3}, as a function of the OMI. For low OMI, both transmitters have same sensitivity. A much higher sensitivity penalty for the silicon photonics transmitter is observed as the OMI increases (5.5dB against 1dB for the $LiNbO_3$ modulator, at an OMI of 0.28) because of the non-linear degradation imposed by the silicon transmitter. As a consequence, the OMI is set to 0.14 to keep the sensitivity penalty below 1dB. Considering propagation losses of 15dB/cm, the output optical power of the modulator is -14dBm (27dB total insertion losses), but without taking into account additional coupling losses.

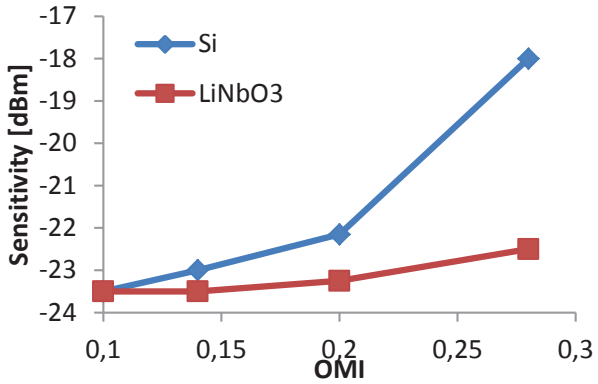

FIGURE 5.60: Sensitivity ($BER = 2.2 \times 10^{-3}$) as a function of the OMI for the silicon and $LiNbO_3$ transmitter, in optical B2B, 16-QAM.

5.2.3.3 Optical Budget of the Optically Amplified SSB-OFDM Link Simulation with the Silicon Photonics Transmitter

In a second analysis, we consider using an optical amplifier to boost the signal before launching it into the fiber. The optical fiber non-linearity, namely the Kerr Effect, is taken into account in the simulations by using a complete split-step Fourier method. Figure 5.61 shows the BER as a function of the optical budget for several optical launched powers considering 100km SMF, for both transmitters. The launch power is varied by placing a VOA at the EDFA output. By increasing the optical launched power by ΔP_{OPT}, the increase in the optical budget is $\Delta P_{OPT} - \Delta S_{NL}$, where ΔS_{NL} is the sensitivity penalty due to fiber non-linearity at a given BER. The optimum launched power is the maximum optical power so that $\Delta S_{NL} < \Delta P_{OPT}$, resulting in an improvement of the optical budget. The silicon modulator shows to be less robust against fiber non-linearity because the optimum launched optical power is 4dBm against 6dBm for the $LiNbO_3$ modulator for a BER of 2.2×10^{-3}. This is probably because of the increase in the out-of-band spectrum due to the silicon modulator non-linearity and residual phase modulation. In this study case, an EDFA with 18dB and 20dB gain would be required for the silicon and $LiNbO_3$ modulators, respectively.

Finally, using the values of the OMI and launched optical power described in table 5.10, the achievable optical budget is evaluated for both transmitters in optical B2B, 50km and 100km of SMF. The necessary RMS driving voltages are also given in table 5.10.

The results are shown in figure 5.62 and summarized in table 5.11. The first observation is that, comparing the optical B2B sensitivities with and without EDFA, the sensitivity penalty

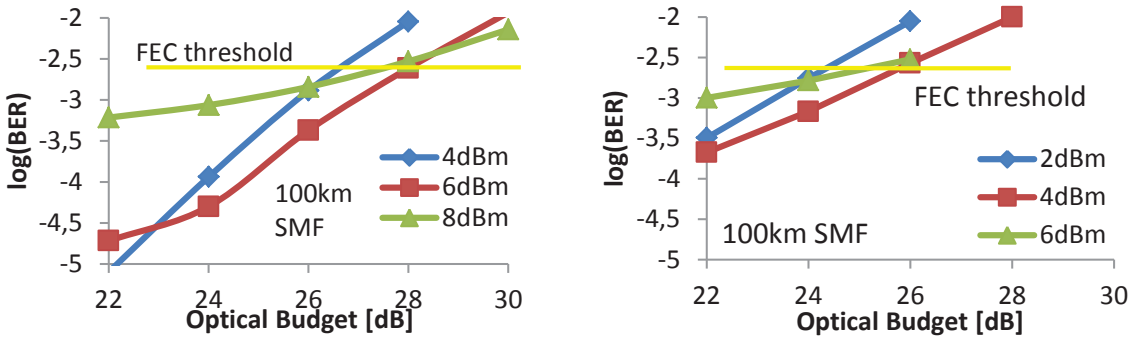

(a) $LiNbO_3$ (b) Silicon

FIGURE 5.61: BER as a function of the achievable optical budget for sseveral launched optical powers, (a) $LiNbO_3$ modulator and (b) silicon modulator.

	OMI	V_{RMS} of modulating signal (OFDM+tone)	Optical launched power
Silicon	0.14	$0.7V_{RMS}$	4dBm
$LiNbO_3$	0.14	$0.7V_{RMS}$	6dBm

TABLE 5.10: Optimized simulation parameters for the SSB-OFDM performance assessment.

due to ASE noise is negligible. The maximum achievable optical budget for a $BER = 2.2 \times 10^{-3}$ for the silicon modulator is 3dB lower than "ideal" $LiNbO_3$ modulator, because of the 2dB lower launched power 1dB sensitivity penalty. However the optical budget penalty is 0.5dB lower (at 100km SMF) for the silicon modulator due to the lower launched power into the fiber.

	Optical Budget (B2B)	Optical budget penalty at 50km	Optical budget penalty at 100km
Silicon	26.5dB	0.5dB	1dB
$LiNbO_3$	29.5dB	0.8dB	1.5dB

TABLE 5.11: Summary of the results in terms of optical budget and optical budget penalty due to fiber non-linearity for the optical SSB-OFDM transmission.

5.3 Summary of the Chapter

In this chapter, the silicon-photonics-based solutions for uplink OFDM-PON as enabling technologies for future PONs were demonstrated for the first time. This study has shown that silicon-photonics transmitters enable OFDM technique achieving data-rates up to 10Gbps with good spectral efficiency, improving the capacity thanks to the efficient high-order modulation. OFDM has shown not only to compensate for the relatively low bandwidth of the devices, but also to be robust against dispersion.

A summary of the experimental results is shown in table 5.12 in terms of the achievable data-rate, spectral efficiency (in optical B2B), sensitivity ($> 10Gbps$) and maximum reach demonstrated. As a comparison, the hybrid III/V-on-silicon lasers achieved slightly lower spectral-efficiency than the commercial DFB laser from 3S photonics as described in subsection 4.2.1.1. This is a consequence of the bandwidth-limitation of the hybrid DBR laser. It achieved $3.4bps/Hz$ and $2bps/Hz$ in optical B2B and 50km SMF, respectively, while the commercial laser showed $4.1bps/Hz$ and $2.5bps/Hz$, respectively.

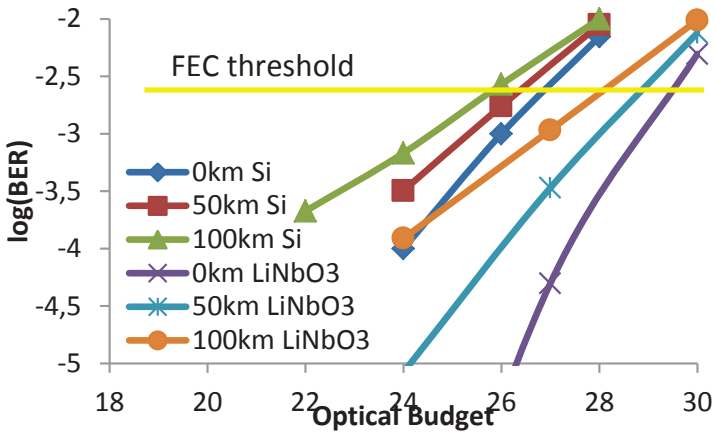

FIGURE 5.62: BER as a function of the optical budget for optimized parameters of the optical SSB-OFDM transmission for the silicon and $LiNbO_3$ modulators.

In terms of data-rate, these solutions show to be compliant for future generations of PON, however further improvement on the optical budget is required to fulfill the requirements of future PONs. Note that optical budget/reach were limited due to the low optical power launched to the fiber. In the hybrid DBR laser experiment, reach was limited to the SMF spool available in the laboratory. The low optical output power of the devices can be attributed to the high coupling losses into the fiber ($> 6.25dB$ per coupler), which can be reduced by optimizing the design of the grating couplers (to achieve typical coupling losses of 3dB). Optical budget/reach can also be improved by using optical amplifiers at the receiver (CO) and using more sensitive photoreceivers (APDs), for instance.

Optical transmitter	Data-rate (B2B)	Spectral efficiency (B2B)	Sensitivity (Optical budget) $> 10Gbps$	SMF length (L_{max})	Data-rate (L_{max})
Hybrid FP laser	12.6Gbps	3.2bps/Hz	-	-	-
Hybrid single-mode laser (2-ring structure)	11.2Gbps	2.5bps/Hz	-9dBm	20km (with EDFA)	9.2Gbps (with EDFA)
Hybrid DBR laser	21.5Gbps	3.4bps/Hz	-13dBm (14.5dB/23dB EDFA)	50km	12.4Gbps
Ring-resonator modulator	16.8Gbps	4.2bps/Hz	-11dBm (4dB)	20km	11.7Gbps

TABLE 5.12: Summary of the experimental results for uplink OFDM-PON using silicon photonics transmitters.

The hybrid DBR laser used in this work had two main longitudinal modes. Under this circumstance, OFDM enabled a fivefold improvement in the [bit-rate × reach] product. Tunability can be achieved by using integrated heaters on top of the DBR mirrors as already demonstrated in similar structures [42]. This is a requirement for transceivers for future PON. In addition, using the same structure but shorter active regions, single-longitudinal mode lasers have been recently demonstrated [155].

The silicon ring-resonator modulator shows to be an attractive solution for the proposed application due to the low insertion losses, small footprint and low driving voltage. Because the chirp in such a modulator is generally lower than for DMLs, lower sensitivity penalty as the

reach increases can be expected. However, it requires an additional component (CW laser) as compared to DMLs which may increase the cost of the transceiver.

The driving voltages for the hybrid III/V-on-silicon lasers vary from $2.5V_{pp}$ to $4V_{pp}$. This is slightly higher than CMOS driving circuits can provide (about $2V_{pp}$). The driving voltages can be reduced, for instance, by 1) decreasing the coupling losses out of the chip which improves modulation efficiency ; or 2) designing impedance-matched electrical contacts to reduce electrical power loss. At the same time, the ring-resonator modulator required a lower driving voltage of $1.6V_{pp}$. The bandwidths considered are below 6.25GHz, which is feasible with existing DACs/ADCs as detailed in subsection 3.3.3.3. For example, a 12Gsps DAC with 190mW [266] and a 12Gsps ADC with 81mW [270] with reasonable performance were already demonstrated, with relatively low footprint.

Using the simulation platform and the previously proposed model in section 2.2.3.2, we evaluated that a silicon MZM has 2.85dB lower sensitivity than the $LiNbO_3$ modulators, in a 10Gbps 16-QAM-OFDM transmission, mainly because of the non-linear transfer function. Simulation results have shown that the silicon ring-resonator modulator can achieve same sensitivity as the silicon MZM, or even better in some cases, depending on the ring resonator parameters. As a conclusion, in spite of the sensitivity degradation caused by the junction non-linearity, these devices may enable efficient high-order modulation. In addition, negative chirp can be induced to improve sensitivity of SMF-links up to 100km.

The final study concerning an integrated silicon photonics transmitter for optical SSB-OFDM reveals that the silicon modulator has increased sensitivity penalty for the same modulation depth and it is weaker against fiber non-linearity, in the case an optical amplifier is used. A study case shows a 3dB lower achievable optical budget as compared to the $LiNbO_3$. However, it still can accommodate 128 users after 20km, or reach 100km SMF but serving fewer subscribers.

General Conclusions and Future Work

Conclusions of this Thesis

The feasibility of **OFDM** technique using **silicon photonics** transmitters has been put forward in this thesis. The application considered is the **future generations of PON**. The optical transmitters considered are hybrid III/V-on-silicon sources and silicon modulators. The objective of this study is to propose a transmitter with 1) a high **spectral efficiency** and **resilience against chromatic dispersion**, provided by the OFDM technique; and 2) with **low-cost per unit**, provided by the mass-production and E/O integration capability of silicon photonics. For that purpose, a **simulation platform** was developed based on theoretical models of the building blocks of an optical communication system. The **experimental work** allowed to **validate** these models, and to **evaluate the performances** of silicon photonics transmitters using OFDM modulation.

To begin with, it was essential to understand the **motivations** behind the work. This was presented in the first chapter. The main motivation for upgrading existing PON is the **growing bandwidth requirements** driven by HD media services and cloud computing. At the same time, the CO should **serve more users** and optical transceivers for both CO and mainly ONU should be as **low-cost** as possible. An alternative to decrease the operating and capital expenditures is to define networks with extended reach/split-ratio, the LR-PON. In summary, future generations of PON should provide an **aggregated data-rate of 40Gbps/10Gbps in downlink/uplink** (or even 40Gbps in uplink if symmetric data-rates are considered), **reach from 20-100km** and **serve 32-1000 users**. In spite of the recent standardization of TWDM for the NG-PON2, many proposed solutions in the literature based on WDM, TWDM, FDM and OFDM were presented, in order to improve the data-rate/reach/split-ratio beyond NG-PON2. The advantages and disadvantages in each case were analyzed. As a conclusion, to **fulfill** the **requirements** for future generation of PONs, **silicon photonics**-based **optical OFDM** is investigated in this work.

One of the main motivations for using OFDM over single-carrier techniques is the robustness against the fiber chromatic dispersion. This is analyzed in subsection 2.1.2 - the **fundamental [bit-rate $\times$ reach] product** limitation for **single-carrier OOK** due to dispersion was defined **analytically**. In the same chapter, the principle of operation of electro-optical and opto-electrical components was studied in detail. **Models** for **silicon photonics modulators** (MZM and ring) are **developed** and **validated** with experimental results, showing a good accuracy. This chapter serves as a **reference** for chapters 4 (experimental validation of the simulation platform) and 5 (OFDM experiments/simulation using silicon optical transmitters).

After a **description** of **OFDM**, the main **features** and **impairments** are identified in chapter 3. The optical channel model for the direct-detection OFDM is divided in two main groups - IM/DD (DSB-based) and SSB-based. The transfer function of the optical link shows

that the transmission capacity in the DSB-based case can be degraded as the SMF reach increases. This is because of the **frequency fading** imposed by the chromatic dispersion - the so called **DSB cancellation** effect. It can be **avoided** by eliminating one of the sidebands as shown in the **SSB modulation** case, at the expense of higher complexity for optical transmitter.

An important part of the work performed during this thesis was the development of a dedicated **simulation platform**. The purpose is to evaluate different optical **transmission techniques** in different **link configurations**. To assess the **accuracy** of the **simulation results**, an experimental test-bed is built using **commercial available components** - a commercial DML and MZM are considered as optical transmitters. The validation of the simulation platform is reported in chapter 4. Three different transmission techniques are analyzed, namely

- 10Gbps single-carrier OOK ;
- 10GHz IM/DD optical OFDM with bit and power loading ;
- 3GHz Direct-detection optical SSB-OFDM.

The conclusion is that the experimental results confirm that the simulation platform gives **very accurate** results. It serves as a **support** for the simulations of the following chapter. More than 40Gbps was demonstrated with the 10GHz IM/DD adaptive OFDM link, with both commercial DML and MZM. The MZM exhibits better [bit-rate × reach] product due to lower chirp. The optical SSB-OFDM data-rate is limited to 23Gbps due to bandwidth limitations of the optical link components.

An experimental test-bed dedicated to **on-chip testing** was developed to study the transmission performance of direct-OFDM modulation of **hybrid III/V-on-silicon lasers** in the fifth chapter. Targeting **uplink PON**, more than 10Gbps sustainable data-rate was demonstrated over three different structures : Fabry-Perot, Single-mode tunable lasers with double-ring filtering and DBR. In the first two, transmission reach was limited by the very low optical power coupled to the optical fiber. Due to an improved design leading to a higher optical output power and modulation bandwidth for the DBR, a **data-rate higher than 10Gbps** is demonstrated over a **50km-SMF link** ($620 Gbps \times km$ [bit-rate × reach] product) without any optical amplification. At the same, OOK modulation using the same device had a limited [bit-rate × reach] product of $125 Gbps \times km$. The spectral efficiency was 17% lower than the commercial DML because of the limited bandwidth of the hybrid DBR laser. It can further be made tunable by integrating resistive heaters in top of DBR mirrors, which is important for being considered for next-generations of PON. This represents one of the most important results of this thesis.

The feasibility of optical **OFDM** on silicon optical modulators have also been assessed. Efficient OFDM modulation up to **64-QAM** of a **ring-resonator modulator** is experimentally demonstrated. It shows a data-rate **higher than 10Gbps** over **20km of SMF** without optical amplification, while the modulator bandwidth was limited to 3.4GHz.

Because of many factors, the optical budget achieved with these experiments was low. A high coupling loss in (in the case of the external modulators) and out of the chip was observed, in the order of 6-10dB per grating coupler, which is higher than the typical value of 3dB. Through **optimization** of the **grating couplers** design, one can expect **lower insertion losses**. In addition, one can consider using more **sensitive photo-receivers** (APDs). In the case of the modulator, a solution for increasing the output optical power is to monolithically **integrate a SOA** before the modulator output [106].

An important observation from these experiments is that the OFDM **bandwidths** used are relatively low ($< 6.25 GHz$). From the analysis of subsection 3.3.3.3, an ASIC implementation of the OFDM **modem** (FFT/IFFT operations) is feasible with power consumptions **lower than 0.4W** for both transmitter and receiver [264]. In addition, this would require **DACs/ADCs** sampling rates close to 12.5Gsps, which is shown to be **feasible** with **relatively low power consumption** components ($< 200 mW$) (cf. subsection 3.3.3.3). The **required modulation depths** are also **close** to the ones provided by **CMOS driving circuits**.

Simulations have shown that the silicon intensity **modulators enable** transmission over **100km** SMF with **negative sensitivity penalty**, using 16-QAM-OFDM efficiently over a 2.5GHz bandwidth. In addition, the results showed that (considering a ring modulator with Q=19000) **ring modulators** can achieve nearly same sensitivity than silicon MZMs with **lower driving voltages**. A **silicon photonics** implementation of the **optical IQ modulator** for the SSB-OFDM modulator is investigated. A study case shows an achievable **optical budget** of **3dB lower** than the **"ideal"** $LiNbO_3$ modulator. A key conclusion from the simulations is that the **intrinsic non-linearity** of the silicon modulators **degrade the sensitivity** of the photoreceiver as **compared** to $LiNbO_3$ modulators. This degradation can be **minimized** by **optimizing** the **modulation depth** at the transmitter. The sensitivity penalty is quantified to be from 1dB to 3dB according to the study cases presented in this work.

The general conclusion of this work is that **silicon photonics** transmitters **enable** advanced and **efficient** modulation formats using the OFDM technique. An important **legacy** of this thesis is the **simulation platform** developed during this work. It is a powerful and accurate tool to evaluate the transmission capacity, optimize system's parameters and identify limitations in optical OFDM transmission systems, considering arbitrary transmitter/receivers.

Future Work

In spite of the fact that promising achievements in high-speed DSPs implementation for optical OFDM have been demonstrated in the last few years, further development is still required. **ASIC implementation** of the OFDM modem is for the moment limited to theoretical analysis (cf. subsection 3.3.3.3). Future research should consider implementing **physically** these circuits. In addition, the **integration** with **DACs/ADCs** as well as the **driving circuits** should be demonstrated as a preliminary step for **electro-optical** integration using silicon photonics.

An order of magnitude of the power consumption of the electrical part of the optical OFDM link (DSP, DAC and ADC) is reported in this work. However, a deeper analysis component by component of the global **power consumption** should be made, as it is a **crucial** point for the OFDM **implementation**.

Silicon-photonics transmitters are analyzed in this thesis. As a future research direction and to demonstrate the full-feasibility of an integrated transceiver, optical OFDM with **silicon-based photoreceivers** should be investigated to allow the integration between transmitter and receiver.

As the silicon photonics components are concerned, their evolution in the last few years is notable. However, as shown in this work, the coupling into the photonic chip is an issue because of the high insertion losses, which limits both reach and split-ratio if no optical amplifiers are used. To address PON, research directions on **efficient coupling structures**, **compatible** with **simple fabrication process** and **high packaging reliability** could be addressed.

Through numerical simulations of a silicon MZM model, results indicate that optical SSB-OFDM modulation can be enabled by **silicon optical IQ modulators**. Future work can consider **fabricating** the device and **testing** it in an **optical OFDM** link.

Annexe A

Modeling of a DML

The purpose of this appendix is to provide a numerical model for a single-mode directly modulated laser. Such a numerical model is built from the laser physical parameters defined in subsection 2.2.1. The numerical resolution of the laser rate equations (2.24), (2.25) and (2.26) is performed using the simulation tool RSoft Optsim. The physical parameters of the DML necessary for the modeling by the simulation tool are :

- Volume of the Active region (V) ;
- Photon lifetime in the cavity (τ_p) ;
- Photon output rate at the output facet ($v_g \alpha_{mir}$) ;
- Carrier density at Transparency (N_T) ;
- Differential gain ($sigma_g$) ;
- Derivative of optical gain against number of photons (dG/dP) - It is the derivative of the net stimulated emission gain as function of the number of photons $dG/dP = -\epsilon_{NL}\Gamma v_g \sigma_g \cdot (N - N_T)/V$;
- Non-radiative coefficient, spontaneous radiative recombination coefficient and Auger recombination coefficient (A_{nr}, B and C) ;
- Spontaneous emission factor (β_{sp}) ;
- Linewidth enhancement factor (α) - equally called chirp parameter ;
- Field confinement factor (Γ) ;
- Group index of the active waveguide (n_g) ;
- Fiber coupling efficiency.

In order to define the physical parameters of a given DML, a software called "Best-Fit Laser Toolkit" from RSoft is used. It enables to define them from a set of measured characteristics of the laser, such as :

- Bias current of the laser (I_b) - Current at which the set of measurements are made ;
- Laser Threshold Current (I_{th}) ;
- Output optical power (P_{OPT}) when laser is biased at I_b ;
- Relaxation Oscillation Frequency (Ω_R) ;
- Overshoot at the relaxation oscillation frequency in dB - The difference between the gain in the low-frequency band and at the relaxation oscillation frequency. It is related to the damping-rate at the relaxation oscillation frequency Γ_R mentioned in (2.29) ;
- Quasi-static frequency chirp above threshold - it is related to the adiabatic chirp coefficient κ defined in (2.30) ;
- Linewidth ($\Delta\nu$) ;
- RIN - Average Relative Intensity Noise in dB/Hz, defined in a start/stop frequency.

These behavior parameters are described in subsection 2.2.1.2. Note that if some of the physical parameters are known or estimated, they can be fixed to their known values. All the modeling process is done at room temperature (20°).

The commercial laser used in this work is a DFB 1915LMA prototype from 3S photonics. In the following, the set of characterizations performed to define the physical characteristics as requested by the software "Best-Fit Laser Toolkit" are reported. The set of characterizations are made at room temperature, controlled by a Newport laser controller.

A.1 DC Characterization

The measured output optical power was plotted as a function of the bias current in figure 2.11. Table A.1 summarizes the DC characteristics of the DML.

Measured characteristic	Value
I_{th}	24.5mA
P_{opt} at I_b=100mA	5.75mW
Slope Efficiency	0.075mW/mA

TABLE A.1: DC characteristics of the DML from 3S Photonics.

A.2 AC Characterization

The experimental set up to measure the frequency response to small signal modulation of the laser is shown in figure A.1. A 40GHz-VNA with an optical module is used. The port 1 of the VNA is connected to the AC port of the bias tee, while the electrical output of the laser controller is connected to the DC port of the bias tee. The optical output of the laser is connected to the optical receiver (RX) of the optical module of the VNA. The RX electrical output is then connected to the port 2 of the VNA. A frequency sweep from 0-40GHz is performed, with an electrical modulating power of 0dBm (corresponding to a peak to peak modulation current of $12mA_{pp}$).

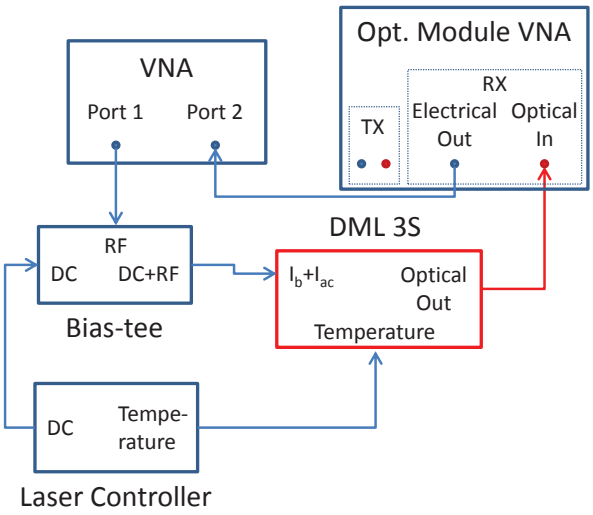

FIGURE A.1: Experimental procedure to measure the frequency response to small signal modulation of the laser.

In order to find the exact value and damping rate of the relaxation oscillation frequency of (2.29), a numerical fitting using the Nelder-Mead algorithm is used, similarly to what is done in [134]. As explained in subsection 5.1.1.2, an equivalent RC circuit frequency response

multiplying to the laser frequency response is considered to take into account the attenuation of the several cables, bias tee and laser parasitic capacitance at high frequencies. The total frequency response of the link is given in (5.1). Figure A.2 shows the measurements and fitting results for $I_b = 100$ and table A.2 summarizes the results.

In order to find the exact value and damping rate of the relaxation oscillation frequency of (2.29), a numerical fitting using the Nelder-Mead algorithm is used, similarly to what is done in [134]. To take into account the attenuation of the several cables, bias tee and laser parasitic capacitance at high frequencies, we further consider an equivalent RC circuit frequency response multiplying to the laser frequency response. The total frequency response is defined as

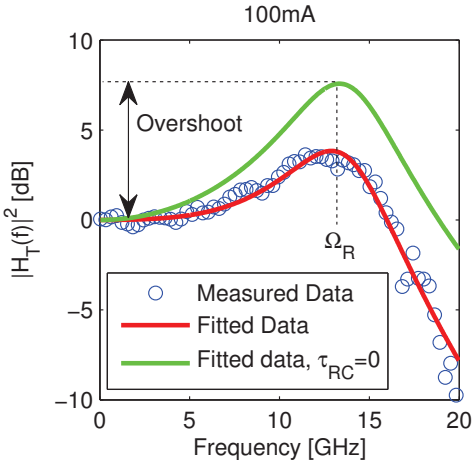

FIGURE A.2: Frequency response measurement of the 3S DFB laser at $I_b = 100mA$, fitted data with and without RC circuit contribution.

I_b	Ω_R	Γ_R	τ_{RC}	f_{3dB} (without RC circuit contribution)
60mA	10.8GHz	1.4×10^{10}	14.3ps	17GHz
80mA	12.7GHz	1.6×10^{10}	14.6ps	19.6GHz
100mA	13.7GHz	1.9×10^{10}	14.2ps	21GHz

TABLE A.2: Summary of the fitted AC characteristics of the 3S photonics DML.

A.3 Linewidth Enhancement Factor (Chirp Parameter) Measurements

As explained in subsection 3.3.3.1, the frequency response of the DML in the presence of chromatic dispersion is altered by the chirp characteristics of the DML. Observing (3.69), it depends on the chirp parameter α and another parameter called f_c related to Γ and ϵ_{NL} through (3.68).

The chirp parameter α and f_c of the laser can be estimated by measuring the small-signal frequency response of the DML over a non-negligible SMF length ($> 10km$). Then, the α and f_c parameters are estimated by finding the values that best fit (3.69). The fitting can be done using an optimization algorithm. This procedure is well detailed in [134]. The total frequency response of the link is written as

$$H_{T_{SMF}}(f) = H_{AM}(f) \times H_{RC}(f) \times H_{F_{DML}}(f) \tag{A.1}$$

where $H_{RC}(f)$ and $H_{F_{DML}}(f)$ are defined in (5.1) and (3.69), respectively. In order to isolate $H_{F_{DML}}(f)$, the frequency response in optical B2B is measured and subtracted from the one with the fiber.

Figure A.3 reports the measurements of the transfer function $H_{F_{DML}}$ over three different fiber lengths when the laser is biased at $I_b = 100mA$; the fitted data show excellent agreement. For the fitting the dispersion parameter $D = 16ps/(nm \times km$ is used. Table A.3 gives the fitted parameters fc and chirp for the three fiber lengths. In our numerical model, the mean value of the fitted parameters $\alpha = 2.8$ and $f_c = 3.77GHz$ are used.

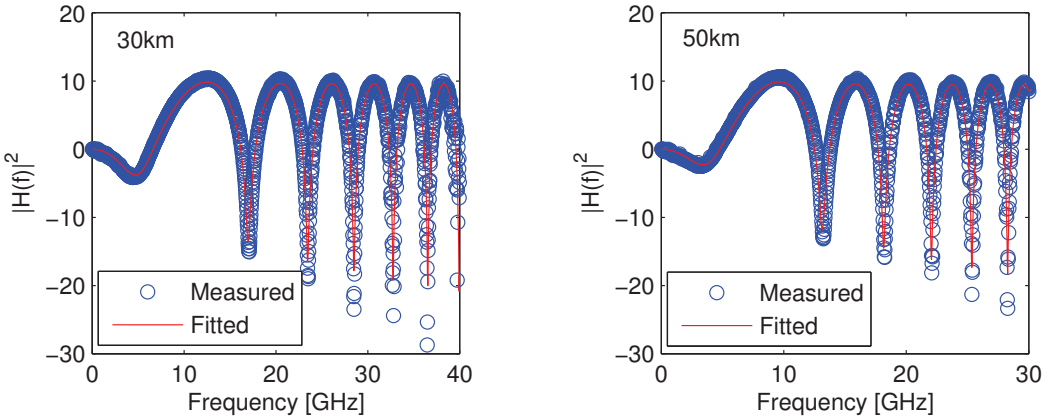

(a) 30km (b) 50km

FIGURE A.3: Frequency response to small signal modulation of the 3S photonics DFB with the optical fiber (Ib=100mA) and fitting results.

SMF length	α	f_c
30km	2.82	3.85GHz
50km	2.78	3.7GHz

TABLE A.3: Summary of the fitted laser chirp characteristics.

A.4 Fitting the Physical Parameters of the DML

Table A.4 summarizes the fixed and fitted physical parameters found by the software, using as input the measured characteristics described in tables A.1, A.2 and A.3 and detailed in the previous subsections. The average RIN is -165dB/Hz (from 0.1 to 10GHz), which is the typical value given by the manufacturer. The value of the non-linear saturation parameter ϵ_{NL} is found by using the estimated value of f_c and the fitted values for the field confinement factor Γ and volume of the active region V as indicated in (3.68).

We note that the obtained linewidth after the parameter fitting is quite inferior to the typical linewidth values for the DFB laser. This may be a result of an underestimation of the spontaneous emission rate β_{sp} of the laser (cf. [139]). The low value of the linewidth does not compromise our simulation results because the phase noise do not have a considerable impact on the transmission performance even if the DML used had a relatively large value for the linewidth (10MHz for instance), for the applications considered in this work.

	Value	Typical values
Fixed Parameters		
Spontaneous radiative recombination coefficient (B)	$10^{-16}m^3/s$	$10^{-16}m^3/s$; [244, 286, 287]
Auger recombination coefficient (C)	$3 \times 10^{-41}m^6/s$	$3 \times 10^{-41}m^6/s$; [244, 286, 287]
Linewidth enhancement factor (α)	2.8	$2.8 < \alpha < 8$; [54, 134, 139, 286, 287]
Fitted parameters (results)		
Volume of the active region (V)	$5.76 \times 10^{-17}m^3$	$1.2{\times}10^{-18}m^3 < V < 2{\times}10^{-17}m^3$; [54, 244, 287, 288]
Photon lifetime (τ_p)	1.48ps	3.6ps [288] ; 1.69ps [287], 1.94ps [244]
Mirror losses (α_{mir})	$2715m^{-1}$	$4000m^{-1}$ [244]
Carrier concentration in transparency (N_T)	$1.4 \times 10^{24}m^{-3}$	$10^{24} < N_T < 1.5 \times 10^{24}$; [54, 139, 244, 286, 287]
Differential gain (σ_g)	$3 \times 10^{-20}m^2$	$2 \times 10^{-20} < \sigma_g < 9.9 \times 10^{-20}$ [54, 139, 244, 286, 287]
Non-radiative coefficient (A_{nr})	$9.25 \times 10^{-8}s^{-1}$	10^{-8} [287], 10^{-9} [244]
Spontaneous emission factor (β_{sp})	4×10^{-6}	10^{-5} [244, 287]
Confinement factor (Γ)	0.4	$\Gamma < 0.45$ [54, 139, 244, 286, 287]
Group index (n_g)	3.7	$3.55 < n_g < 4$; [54, 244, 286, 287]
Non-linear saturation parameter (ϵ_{NL})	$7.2 \times 10^{-24}m^3$	$3 \times 10^{-24}m^3 < \epsilon_{NL} < 7.4 \times 10^{-23}m^3$; [139, 244, 287, 288]
Fiber coupling efficiency	30%	38% [288]
Resulting characteristics after fitting		
Linewidth ($\Delta\nu$)	0.1MHz	1-10MHz ; [139]

TABLE A.4: Physical parameters obtained from fitting for the 3S Photonics DML numerical model.

A.5 Verifying the Fitted Physical Parameters of the DML

From the defined set of physical parameters, the Rsoft Optsim tool can numerically solve the rate equations (2.24), (2.25) and (2.26). One can then check that the modeled behavior of the laser matches the measurements. We will further use this model to simulate transmission links making use of the commercial laser.

The simulated DC and AC (optical B2B) simulated behaviors were reported in figures 2.13 and 2.14, respectively, of this work. The frequency response of the DML over a SMF-link is simulated. Figure A.4 displays the simulation results for 30km and 50km. It should be noted that the estimated f_c parameter is not used as an input to the model. It depends on the physical parameters as indicated in (3.68), which are found by the software through fitting with other measured characteristics of the DML. Therefore, we observe an accurate estimation of the physical parameters related to the f_c parameter. The large-signal behavior of the proposed model is simulated and compared with the experimental results for OOK and OFDM modulation is sections 4.1 and 4.2.1.1, respectively.

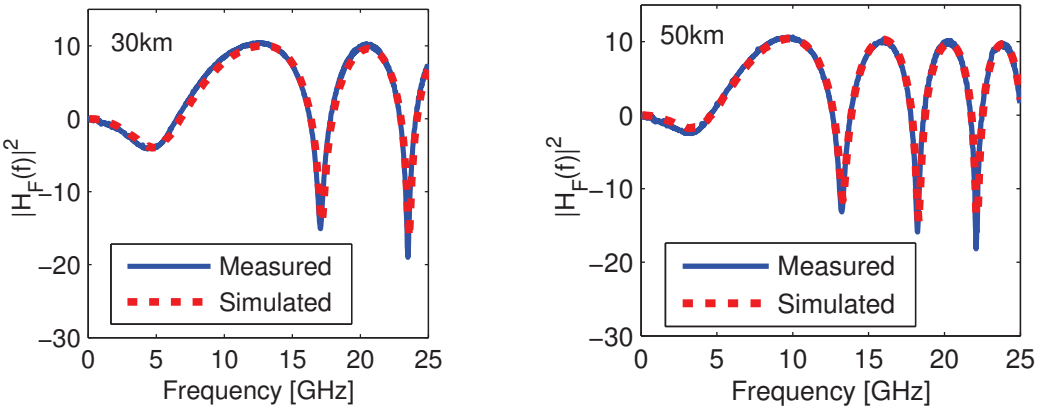

(a) 30km (b) 50km

FIGURE A.4: Frequency response to small signal modulation of the 3S photonics DFB with the optical fiber ($I_b = 100mA$) and simulated from the numerical model.

Annexe B

Description of the Experimental Set-up

In this appendix, we detail the OFDM modem implementation in Matlab, and the equipment used in this work. In the last part, the electrical B2B performance with the AWGs and DSOs used in this work are analyzed. This is relevant for this work in order to calculate the transmission penalty associated with the electoral equipment.

B.1 OFDM Modulator

The OFDM modulator is scripted using Matlab. The input parameters for the OFDM modulator are :

- Baseband bandwidth (BW) ;
- FFT Size (N_{FFT}) ;
- Cyclic prefix samples (N_{CP}) ;
- Hermitian Symmetry on OFDM signal (HS) ;
- Number of OFDM symbols per frame ($N_{symbols}$) ;
- Number of bits per subcarrier (b) ;
- Relative power per subcarrier (p) ;
- DAC sampling frequency ($f_{s_{DAC}}$) ;
- Clipping ratio (k).

From the input parameters, the following parameters are derived :

- Subcarrier spacing : $\Delta f = f_{s_{DAC}}/N_{FFT}$;
- Number of data carriers : if $HS = 1$, then $N_{DATA} = floor(BW/\Delta f)$, else $2 \times floor(BW/\Delta f)$. Floor is the rounding down to the nearest integer function ;
- Total number of bits per frame : $number\_of\_bits = N_{symbols} \times \sum b$;
- Number of samples per OFDM symbol : $N_{samples} = N_{FFT} + N_{CP}$
- Total number of samples : $N_{total} = N_{samples} \times N_{symbols}$

Evidently the baseband bandwidth should be less than the half of the DAC sampling frequency ($BW < f_{s_{DAC}}/2$). The HS variable is Boolean and indicates if the output signal is real (by applying Hermitian Symetry) or complex. The number of bits b and relative power per subcarrier p are a vector of length N_{DATA}. The sum of the elements of p divided by N_{DATA} should be equal to 1 ($1/N_{data} \times \sum p$).

The block diagram for the OFDM modulator is depicted in figure B.1. In the transition between the different blocks in the diagram, the data size is given (in line × column format). It is defined in a classic manner as described in section 3.3. The only difference is that a cyclic suffix is added to the OFDM symbol of length $N_{CP}/2$ (in this way, the cyclic prefix length

is $N_{CP}/2$). This is because the detected OFDM window at the receiver can deviate from one sample before or after the first sample of the ideal window. As illustrated in figure B.2, if the detected OFDM window is shifted from one sample at forward direction, ISI occurs if no cyclic suffix is added. The cyclic suffix provides a margin of $N_{CP}/2$ in the detected OFDM window at the receiver, at the expense of lower robustness against dispersive effects of the channel because the cyclic prefix length is halved.

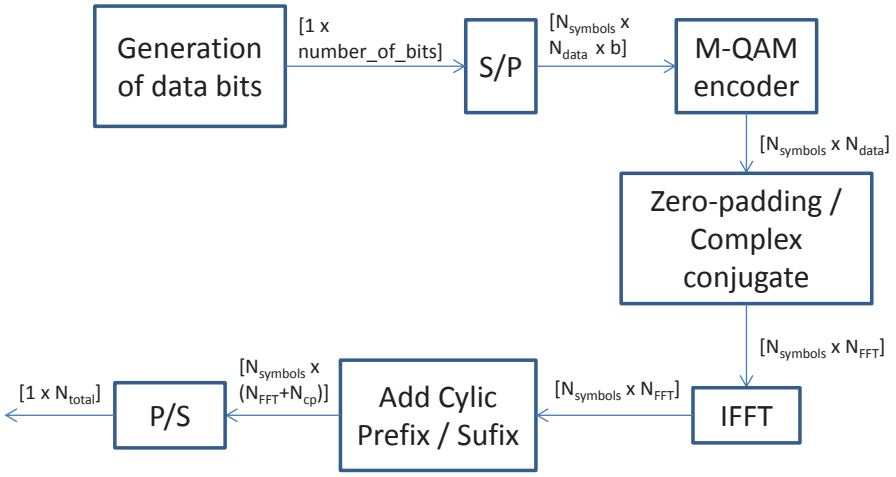

FIGURE B.1: Block diagram for the OFDM modulator implemented in Matlab.

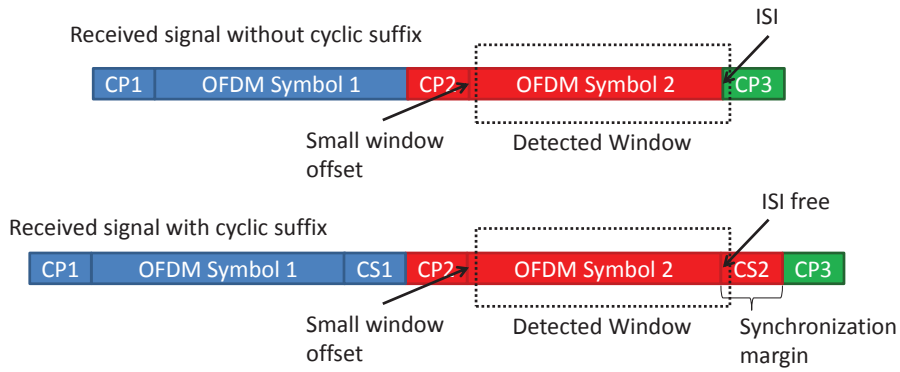

FIGURE B.2: Principle of the cyclic suffix for eliminating ISI due to residual synchronization errors.

B.2 Arbitrary Waveform Generator (AWG)

The AWG performs the digital-to-analog conversion. In general, the OFDM signal is generated in Matlab and downloaded into the AWG through an Ethernet cable or USB, with automated scripts in Matlab. The features of an AWG include number of bits, maximum sampling rate and electric bandwidth. Throughout this thesis, different AWGs were used, depending of the availability of the equipment at the time of the demonstrations. They are described in table B.1. The AWG 7122B from Tektronix has either 2 channels at a maximum sampling rate of 12Gsps each and a bandwidth of 5.6GHz per channel, or an interleaved mode with one channel at 24Gsps. In the interleaved mode, there is an option called "Zeroing" which extends the bandwidth to 9.6GHz, at the expense of the output peak-to-peak voltage which is reduced twofold (from $1V_{pp}$ to $0.5V_{pp}$).

Manufacturer / Model	Number of bits	Output Level	Sampling rate	-3dB bandwidth
Tektronix / 7122B	10	$1V_{pp}$ ($0.5V_{pp}$ IL/Zeroing)	2×12Gsps (1×24Gsps IL)	5.6GHz (9.6GHz IL/Zeroing)
Tektronix / 70000	10	$0.5V_{pp}$	2×12.5Gsps	11.1GHz
Agilent / M8190A	12	$0.7V_{pp}$	2×12Gsps	5GHz

TABLE B.1: Specifications of the different AWG used in this work. IL : Interleaved mode.

B.3 Electric Amplifiers, Attenuators and Filters

In the AWG output, a low-pass filter is generally placed to filter image bands generated by the digital-to-analog conversion process. The cut-off bandwidth is adapted to the OFDM signal bandwidth - it is chosen so that the roll-off at high frequencies is minimized.

Two amplifiers have been used in the experiments. The first one is DR-AN-20-HO from Photline. It has a typical gain of 30dB and 20GHz bandwidth. It is generally used as the driver for the optical transmitter. The second one is the 100BP from SHF, with 18dB of typical gain and 25GHz bandwidth, which is generally placed as a pre-amplifier before the DSO. In each experiment, special attention is made so that the output electric signal is not saturated. We verified that signal degradation due to non-linearity and noise is negligible for these components.

In order to optimize the modulation depth of the optical transmitter, a 18GHz variable electric attenuator with a 1dB step is placed in front of the driver amplifier. In this way, the overall electric gain can be adjusted to maximize transmission performance.

B.4 Optical Components

The optical link starts with the optical transmitter. The characteristics of the DML (1915LMA from 3S photonics) is described in appendix A. The optical IQ modulator is the MXIQ-LN-40 from Photline. It has a V_π of 7V, an E/O bandwidth of about 20GHz and $\alpha_{MZM} < 0.1$. Figure B.3 shows the experimental set-up to drive the DML and optical IQ modulator.

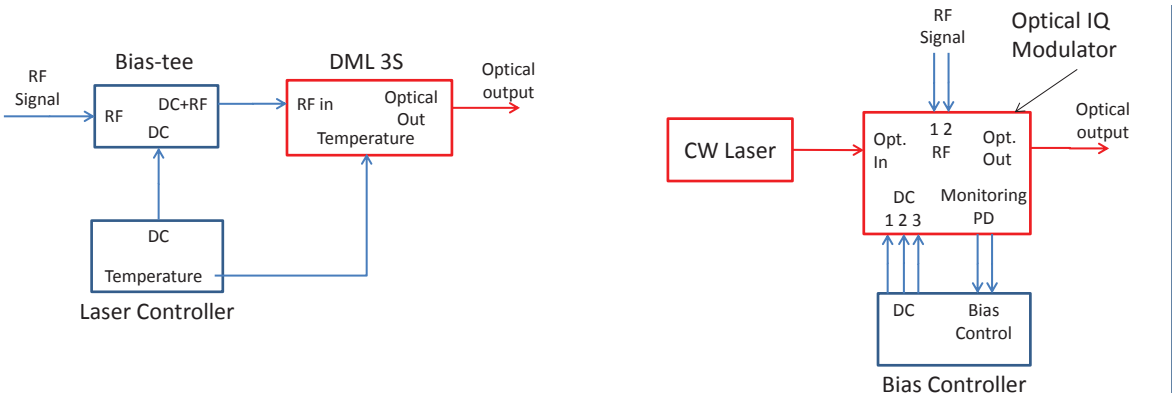

(a) DML (b) MZM

FIGURE B.3: Experimental setup for the optical transmitters used in this work.

For the DML, a laser controller is used to control the temperature and provide the bias current. A bias-tee is placed before the RFinput of the laser to combine both RF signals and DC

current. The optical IQ modulator has three bias voltages inputs : for both arms and to adjust the relative $\pi/2$ phase shift for both arms. The bias voltages are provided by a bias controller. In the modulator, a part of the optical signal from MZMs is detected by a monitoring photodiode and sent to the controller to automatically adjust the bias for the MZM operating point desired. The CW laser is provided with a narrow linewidth ECL with maximum optical output power of 10.5dBm.

The SMF used has standard values of 0.2dB/km attenuation and $D = 16ps/(nm \times km)$ dispersion parameters. The fiber span varied from 10km to 50km length. A VOA is placed before the photoreceiver to adjust the received optical power. The photoreceiver is a PIN photodiode integrated with a TIA, model 1554-B from NewFocus, with 12-GHz bandwidth and $20pA/\sqrt{Hz}$ NEP. Two versions of the photoreceiver were used, one with $600V/W$ conversion gain and another with $750V/W$, but the NEP was the same for both versions.

B.5 Digital Sampling Oscilloscope (DSO)

The DSO is in charge of performing the analog-to-digital conversion. The analog signal is captured by the oscillator and sent to the computer through an Ethernet or USB cable. The DSO used in this work is from Tektronix, model DSA72004C. It has equally 8 bits resolution, 20GHz bandwidth and up to 100Gsps sampling-rate. The minimum ENOB is announced to be 5.5bits, resulting in a SNR of 33dB.

B.6 OFDM demodulator

At the demodulator, the ADC sampling frequency ($f_{s_{ADC}}$) should be specified. The, the following variables can be derived :

- Oversampling ratio : $r_{OS} = f_{s_{ADC}}/f_{s_{DAC}}$;
- Acquisition length in samples : $N_{acq} = 2 \times N_{total} \times r_{OS}$.

The acquisition length is two times the total number of samples to assure that the entire frame is captured. The block diagram for the OFDM demodulator is shown in figure B.4.

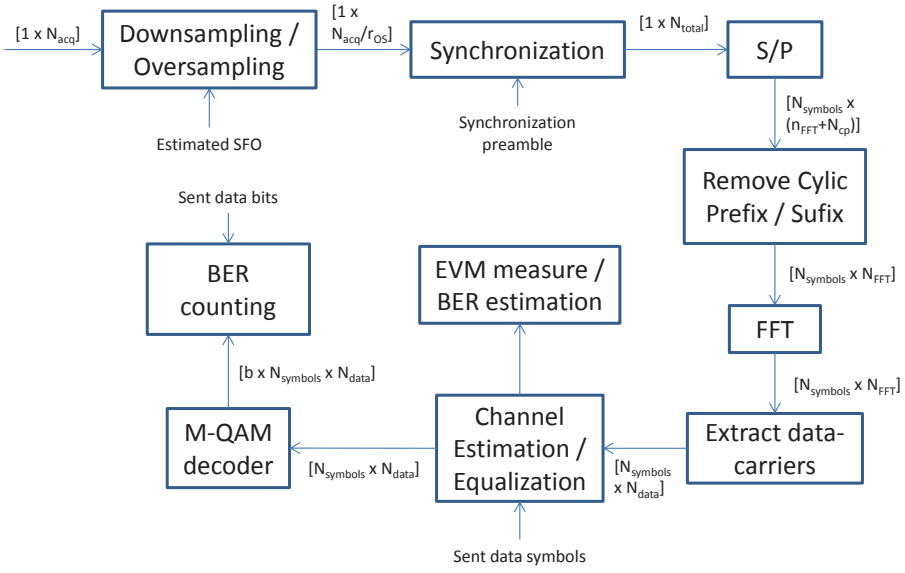

FIGURE B.4: Block diagram for the OFDM demodulator implemented in Matlab.

The received signal is downsampled or oversampled (depending if r_{OS} is higher or lower than 1) by $1/r_{OS}$ to fit the sampling frequency of the DAC. The oversampling function is performed

using spline interpolation as this gives more accurate results. If SFO correction is applied, the actual oversampling ratio is $1/r_{OS} + \xi$, where $\xi = 1 - f_s'/f_s$ is the SFO parameter (and f_s' is the sampling frequency offset) previously estimated using the method described in subsection 3.3.2.3. In certain cases, the clock of DAC and ADC are locked between each other, then SFO correction is not necessary.

In order to find the first sample of the frame, a synchronization using the cross-correlation function is performed. Assuming $r[n]$ are the received samples and $s[n]$ are the sent samples, the cross correlation function is defined by

$$(s[n] * r[n])[m] = \sum_{n=0}^{N_p-1} s[n] \cdot r[m+n] \tag{B.1}$$

where N_p is the length of the correlation product, with $N_p \leq N_{total}$ and $0 \leq m < N_{total}$. Longer correlation products require more computational memory, but are more robust against noise. The value used in this work is $N_p = 4 \times N_{symbols}$ which shows to be a good trade-off between complexity and robustness to noise. This method works very well in off-line demonstrations, but it is unattractive for real-time implementation due to high complexity. A very popular algorithm for OFDM timing synchronization is the Schimdt and Cox algorithm [236], which has relatively low complexity for real-time implementation. Moreover, an interesting and very low-complex approach has been proposed in [289], using only subtraction operations and Gaussian windowing. It has been demonstrated in real-time using FPGAs.

The channel coefficients are estimated by the maximum likelihood method as described in subsection 3.3.1.4. The entire OFDM symbols within a frame are used for estimation (an average is made) in order to minimize estimation noise. In real-time implementations, as the optical link is considered to be static, averaging can be made over a sufficient amount of time to reduce overhead due to channel estimation and estimation noise.

A very comprehensive tutorial in algorithms for real-time DSP is given in [290], including synchronization, channel estimation and clock recovery algorithms.

B.7 Evaluation of Electric B2B Performance

An important aspect on the optical OFDM transmission is that the electric part of the link should be as performing as possible with the purpose of minimize transmission penalty. In this way, the transmission performance is rather limited by the optical part of the link.

In order to evaluate the quality of the transmission, a few experiments in electric B2B configuration were performed. Important features of this transmission to be analyzed are the high-frequency roll-off and the SNR per subcarrier. The set-up is quite simple : it consists of the AWG, low-pass filter at 10GHz and DSO. Both AWGs from Tektronix are analyzed, the 7122B sampling at 24Gsps and the 70000 sampling at 25Gsps. The DSO samples at 25Gsps and the clock from AWG and DSO are connected to avoid SFO.

The results are shown in figures B.5 and B.6 for the 7122B and 70000, respectively. With the 7122B, a rather poor SNR for frequencies higher than 2GHz is observed - it decreases from 19dB (maximum 32-QAM) to about 13dB at 10GHz (maximum 8-QAM) due to imperfection of the AWG. AWG 70000 exhibits better performance, with a measured SNR of 20dB at 8GHz, which decreases to about 16dB at 10GHz.

Finally, the SNR penalty ΔSNR_{elec_k} in the k^{th} subcarrier caused by the electric components can be calculated with the following equation

$$\Delta SNR_{elec_k} = 10 \log_{10} \left(\frac{1}{SNR_{elec_k} - SNR_{oe_k}} \right) \tag{B.2}$$

where SNR_{elec_k} is the SNR in electric B2B in linear scale and SNR_{oe_k} is the SNR in optical B2B in linear scale. If $SNR_{elec_k} \approx SNR_{oe_k}$, the transmission performance is rather limited by the electric components of the link, while if $SNR_{elec_k} >> SNR_{oe_k}$, the SNR penalty caused by electric components is negligible.

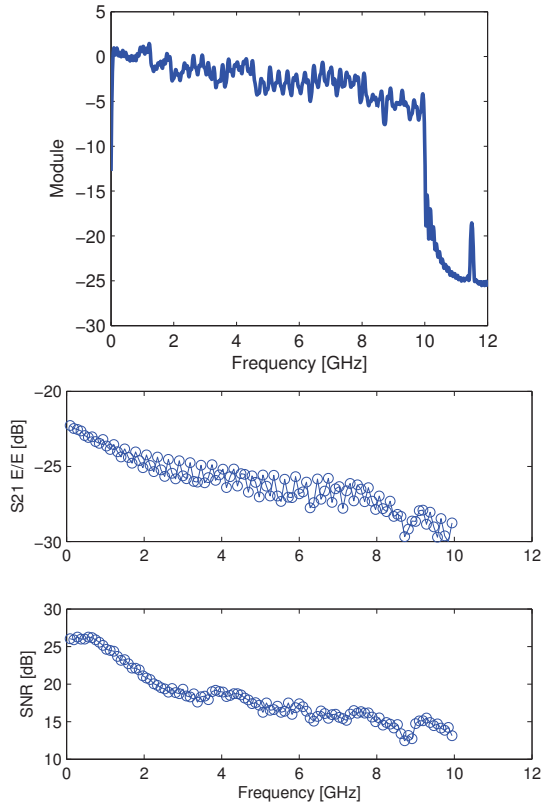

FIGURE B.5: Electrical B2B performance, AWG 7122B.

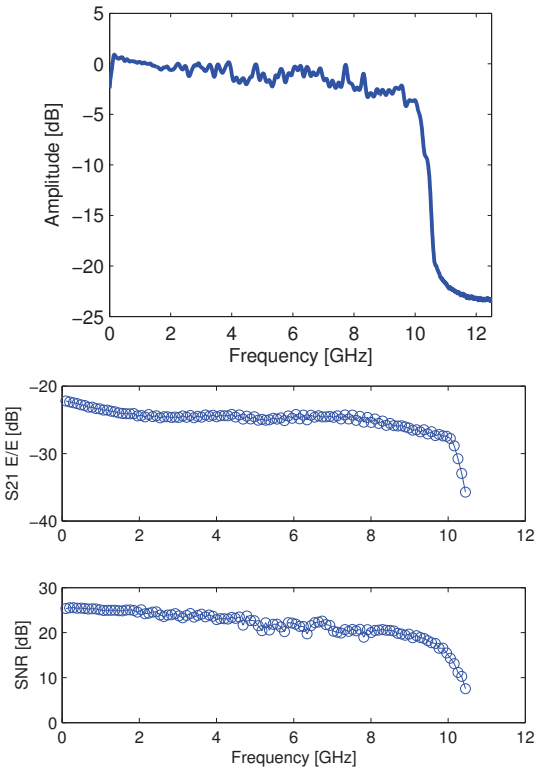

FIGURE B.6: Electrical B2B performance, AWG 70000.

Annexe C

Bit and Power Loading Algorithm

This appendix describes the bit and power loading algorithm used in this thesis. In the first part, we present the optimum solution for the bit and power loading problem, which is the water-filling algorithm. Since the water-filling algorithm cannot be used in practice because it results in non-integer number of bits per subcarrier, a near-optimum solution is proposed. Before describing the algorithm, we define a very accurate approximation for the BER as a function of the SNR for any constellation. This approximation is used in the near-optimum algorithm described in the final section.

C.1 Classical Bit and Power Loading Problem

For an AWGN channel, the number of bits that can be transmitted for maximizing capacity as a function of the SNR, according to the Shannon-Hartley theorem is

$$b = \log_2\left(1 + \frac{SNR}{\Gamma_{gap}}\right) \tag{C.1}$$

where Γ_{gap} is commonly called the SNR gap [291]. It is the ratio between the SNR required to achieve the maximum (Shannon) capacity, and the SNR needed to achieve a target BER_t. It is given in [291] by

$$\Gamma_{gap} = \frac{1}{3} \cdot \left(Q^{-1}\left(\frac{SNR_t}{2}\right)\right)^2 \tag{C.2}$$

where Q^{-1} is the inverse of the Q function (tail probability of the normal distribution). For QAM schemes (with even number of bits) with any error correction code, and an error probability target of 2.2×10^{-3}, the SNR gap is $\Gamma_{gap} = 5dB$.

Let us consider an OFDM symbol with N_{DATA} data subcarriers, where SNR_k is the SNR of the k^{th} subcarrier when unit power is applied. The bit and power loading problem consists in maximizing the number of bits transmitted per OFDM symbol $R = \sum_{k=0}^{N_{DATA}-1} b_k$, where b_k is the number of bits per subcarrier, by choosing an optimum power distribution p_k among the subcarriers

$$\max_{p_k} = \sum_{k=0}^{N_{DATA}-1} \log_2\left(1 + \frac{p_k \cdot SNR_k}{\Gamma_{gap}}\right) \tag{C.3}$$

with the added condition on the overall transmitted power

$$\frac{1}{N_{DATA}} \sum_{k=0}^{N_{DATA}} p_k = 1 \tag{C.4}$$

since the power per OFDM symbol allocated is finite. The power constraint is based on the assumption that the mean energy of an OFDM symbol is normalized to 1, written as

$$1/N_{DATA} \sum_{k=0}^{N_{DATA}-1} b_k \left|X_k\right|^2 = 1. \tag{C.5}$$

The optimum solution for the bit and power loading algorithm is given by the classical water-filling solution [292]. It states that the subcarriers should have a constant level given by $p_k + \Gamma/SNR_k$. Figure C.1 shows an output example of application of the water-filling algorithm for 31 subcarriers and $\Gamma = 1$. The subcarriers for which the inverse of the SNR ($1/SNR_k$) is higher than the constant value $p_k + \Gamma/SNR_k$ (subcarriers 5, 16, 27 and 28) have their power set to 0 ($p_k = 0$). This example shows that, low SNR subcarriers, are set to 0 ($p_k = 0$), while the power is instead reallocated in subcarriers with higher SNR.

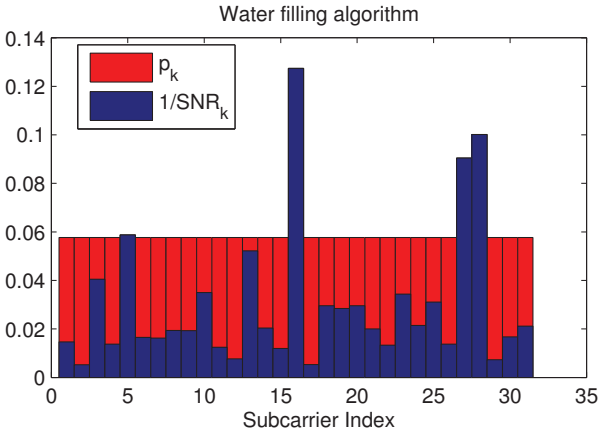

FIGURE C.1: Typical output of the water-filling algorithm.

While this solution gives the optimum combination of p_k to maximize data-rate, it cannot be applied in practice since it gives non-integer values for the number of bits per subcarriers. Near-optimum solutions have been proposed by Chow [223] and Campello [224]. Basically, after calculating the optimum number of bits per subcarrier, it is rounded to the nearest integer value. The rounding operation shifts the achievable BER from the target value. This can be solved by adapting the relative power per subcarrier to adjust SNR so as to achieve the target BER. It is proven to achieve near-optimum solution [223].

In this work, we propose a similar solution to the one proposed by Chow [223]. For odd-bit constellations, we chose to use cross-QAM constellations since they perform better in AWGN channels than rectangular QAM-channels as mentioned previously in in subsection 3.2.2.2. Those constellations were illustrated in figure 3.9(d) and 3.9(f). The difference of the proposed algorithm as compared with the previous ones is that we use better approximations for the bit error probability (or equivalently the SNR gap) for the odd-bit constellations. Additionally, as stated in [293], we can achieve optimum performance by turning off the subcarriers (setting $p_i = 0$) which canâĂŹt carry more than 1 bit due to low SNR, and allocate the power left to the other subcarriers. In this way, we assume that the minimum number of bits that can be carried by one subcarrier is 2 (QPSK modulation).

C.2 Coding of Constellations

The objective of this part is to define a general equation for the BER as a function of the SNR for any constellation. For that, two parameters for each constellation should be defined. In the following part, we consider symbols having an average energy equal to one.

The first parameter is the minimum distance d_{min} between two adjacent points of the constellation. It is given in second column of table C.1 for all the constellations.

The second parameter is related to the coding of the bits over the symbols of the constellation. An alphabet using Gray coding achieves the best BER performance for AWGN channels. It is a type of coding for which, from an adjacent constellation symbol differ by only one bit. In this way, for Gray-coded constellations, the BER can be approximated from the Symbol Error Rate (SER) for low values of the BER.

Perfectly Gray coding is possible for constellations with even number of bits per symbol, but impossible for the other ones (except BPSK). In [218], Smith introduced a new dimensionless parameter called G_p (Gray penalty). It is the average number of bits by which two adjacent symbols from the constellation differ. With perfect Gray coding, we have $G_p = 1$. Odd-bit constellations with G_p closer to 1 perform better in AWGN channels. The optimum coding for odd-bit constellations ($M > 32$) is given in [218] and for $M = 8$ in [294]. Then, the Gray penalty for each constellation is given third column of table C.1.

Modulation Order (M-QAM)	d_{min}	G_p	N_{av}
$M = 2^{2k} (k \in \mathbb{N}^*)$	$\sqrt{\frac{3}{2\cdot(M-1)}}$	1	$4\left(1 - \frac{1}{\sqrt{M}}\right)$
$M = 8$	$\frac{1}{\sqrt{3+\sqrt{3}}}$	10/8 [294]	3
$M = 32$	$\sqrt{\frac{48}{31M-32}}$ [218]	7/6 [218]	$4 - 6/\sqrt{2M}$ [218]
$M = 2^{2k+1} (k \in \mathbb{N}^*; k \geq 3)$	$\sqrt{\frac{48}{31M-32}}$ [218]	$1 + 1/\sqrt{2M} + 1/3M$ [218]	$4 - 6/\sqrt{2M}$ [218]

TABLE C.1: BER calculation parameters for M-QAM constellations.

Then, the BER probability for a given M-QAM constellation can be approximated by [218]

$$P_b(M) \approx G_p \cdot \frac{N_{av}}{2\log_2 M} \cdot \operatorname{erfc}\left(d_{min} \cdot \sqrt{SNR}\right) \tag{C.6}$$

where N_{av} (given in fourth column of table C.1 for each constellation) is the average number of nearest neighbours for a symbol in the constellation. It should be noted that exact BER computations for even-bit QAM constellations [295] and odd-bit QAM constellations [294] can be found in the literature, but they are very complex and unpractical. The accuracy of (C.6) is evaluated through monte-carlo simulations as illustrated in figure C.2(a) (even-bit QAM) and figure C.2(b) (odd-bit QAM). It gives a good approximation for BER in the range of 2.2×10^{-3}. Since the BER is approximated for the SER as mentioned previously, a difference between the analytical equation and monte-carlo simulations for low values of SNR is observed.

C.3 Algorithm Description

For each constellation, the bit error probability given in (C.6) is considered rather than the upper-bound approximation given in the previously mentioned algorithms [291].

The algorithm is described below. Considering N_{DATA} subcarriers, the algorithm takes as an input the SNR per subcarrier ($SNR(i)$) and a target BER target (BER_t). The output of the

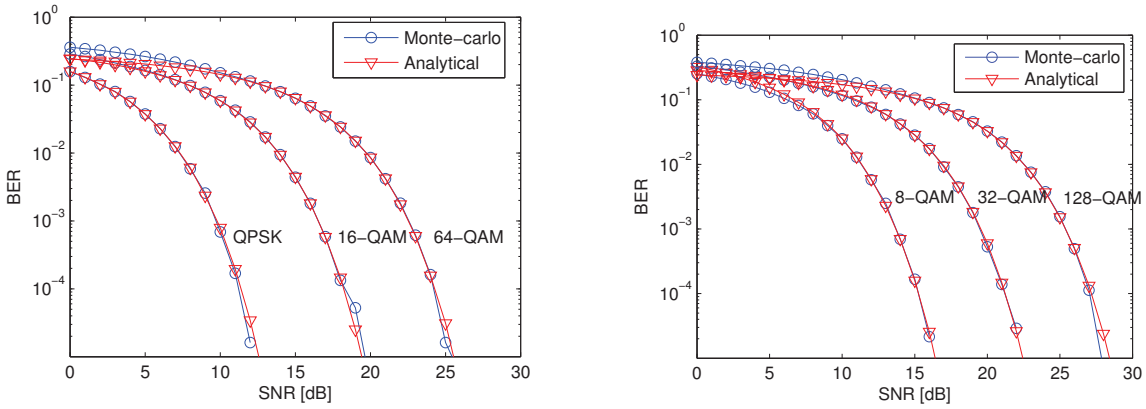

(a) Even-bit QAM (b) Odd-bit QAM

FIGURE C.2: BER vs SNR for QAM constellations, Monte-Carlo simulations and analytical.

algorithm is the optimum number of bits ($b(i)$) and relative power per subcarrier ($p(i)$). At the beginning, the relative power per subcarrier is initialized to 1 for all the subcarriers. Basically, it consists of three mains steps. Algorithmically, this procedure can be described as follows.

– First step - Setting to zero low-SNR subcarriers.

1. Order $SNR(i)$ from the smallest to the highest value $SNR_{ord}(i)$, and the corresponding subcarrier index $ord_{index}(i)$.
2. Set $i = 1$.
3. Calculate the number of bits $b(i)$ that the subcarrier of index $ord_{index}(i)$.can carry with relative power $p(i)$ At each step, round b to the nearest integer. If $b(i) \geq 2$ go to next step. If $b < 2$ and $i = N_{DATA}$, stop algorithm and declare bad channel. Else, set $p(i) = 0$. Redistribute the power among the other subcarriers so that $\sum p(j)/N_{DATA} = 1, 1 \leq j \leq N_{DATA}$. Increase $i = i + 1$ and star-over step 3.
4. Set $N_{used} = i$ and set $index_{used}$ as a vector containing the index of the used subcarriers in ascending order.

– Second step - Compute couple ($b(i)$, $p(i)$) per subcarrier.

5. For $j = 1$ to N_{used}, do steps 6 to 8.
6. Define subcarrier index $i = index_{used}(j)$. Build look-up table of error probability versus modulation order M as following

$$P_b(M) = G_p(M') \cdot \frac{N_{av}(M')}{2\log_2 M} \cdot \operatorname{erfc}\left(d_{min}(M') \cdot \sqrt{p(i) \cdot SNR(i)}\right) \tag{C.7}$$

for $2^{1.5} < M$ and $M' = 2^{round(\log_2 M)}$. The G_p, N_{av} and d_{min} parameters are defined in table C.1 for every $M > 4$.

7. Find in the look-up table the position M_{real} for $\min(|P_b(M) - BER_t|)$ and define

$$b_{real}(i) = \log_2(M_{real}) \tag{C.8}$$

$$b(i) = \text{round}(b_{real}(i)) \tag{C.9}$$

$$dif(i) = b(i) - b_{real}(i). \tag{C.10}$$

8. Calculate $p(i)$ as follows

$$p(i) = \frac{1}{SNR(i)} \cdot \left(\frac{1}{d_{min}\left(2^{b(i)}\right)} \cdot \text{erfc}^{-1}\left(\frac{BER_t \cdot 2 \cdot 2^{b(i)}}{G_p\left(2^{b(i)}\right) \cdot N_{av}\left(2^{b(i)}\right)} \right) \right)^2. \tag{C.11}$$

– Third step - Adapting bit and power distribution so that $1/N_{data} \sum p(i) = 1$.

9. Calculate $P_{tot} = 1/N_{data} \sum p(i)$.
10. If $P_{tot} > 1$ go to 11, else go to 15.
11. Find i for $\max(dif(i))$. If $b(i) = 2$, do $b(i) = 0$ and $p(i) = 0$, else do $b(i) = b(i) - 1$, recalculate $p(i)$ from (C.11) and update $dif(i) = b(i) - b_{real}(i)$.
12. Recalculate $P_{tot} = 1/N_{data} \sum p(i)$.
13. Repeat 11 to 12 until $P_{tot} < 1$.
14. Go to 19.
15. Find i for $\min(dif(i))$. Do $b(i) = b(i) + 1$ and recalculate $p(i)$ from (C.11).
16. Recalculate $P_{tot} = 1/N_{data} \sum p(i)$.
17. If $P_{tot} > 1$ do $b(i) = b(i) - 1$ and recalculate $p(i)$ from (C.11), else update $dif(i) = b(i) - b_{real}(i)$.
18. Repeat 15 to 17 until $P_{tot} > 1$.
19. Normalize $p(i) = p(i) \cdot (N_{DATA} / \sum p(i))$.

The algorithm ensures that, theoretically, the achieved BER is below the BER target. It is observed that as the number of data subcarriers increases, the closer we get to the optimum solution [277]. It is also based on the assumption that the SNR increases linearly with power, which is not always the case. This can be solved by multiple iterations until the BER converges to the BER target.

A Matlab routine was developed to validate our algorithm. The simulation script consists in two parts. Firstly, a probe signal is generated and used for estimating the SNR per subcarrier. Two arbitrary multipath channels were generated. After convolution with the arbitrary multipath channels, white Gaussian noise is added to the signal. Then, the algorithm calculates the optimum bit and power allocation per subcarrier. The OFDM signal is re-generated using the bit and power allocation previously calculated, and the SNR and BER per subcarrier are computed. The parameters are $N = 128$ (where $N_{DATA} = 63$, the DC subcarrier is set to 0 and the 64 subcarriers left are set as the complex conjugate of the aforementioned subcarriers to form a real-valued OFDM signal), $N_{CP} = 16$ and $BER_t = 2.2 \times 10^{-3}$. The cyclic prefix length is enough to ensure no ISI from the multi-path channels. For SNR estimation, 10000 OFDM symbols are generated and for counting BER after bit and power loading, over 100000 OFDM symbols are generated.

Figure C.3 shows the simulation output for the two arbitrary channels. It indicates that the algorithm has successfully computed a bit and power distribution so that the achieved BER is as near as possible of the BER target. The SNR after the bit and power loading has a staircase aspect since it is defined as the symbol energy to noise ratio. If the SNR per subcarrier is normalized by the number of bits per subcarrier, we get the bit energy to noise ratio, and the solution resembles to the water filling solution as the resulting bit energy to noise ratio is approximately constant.

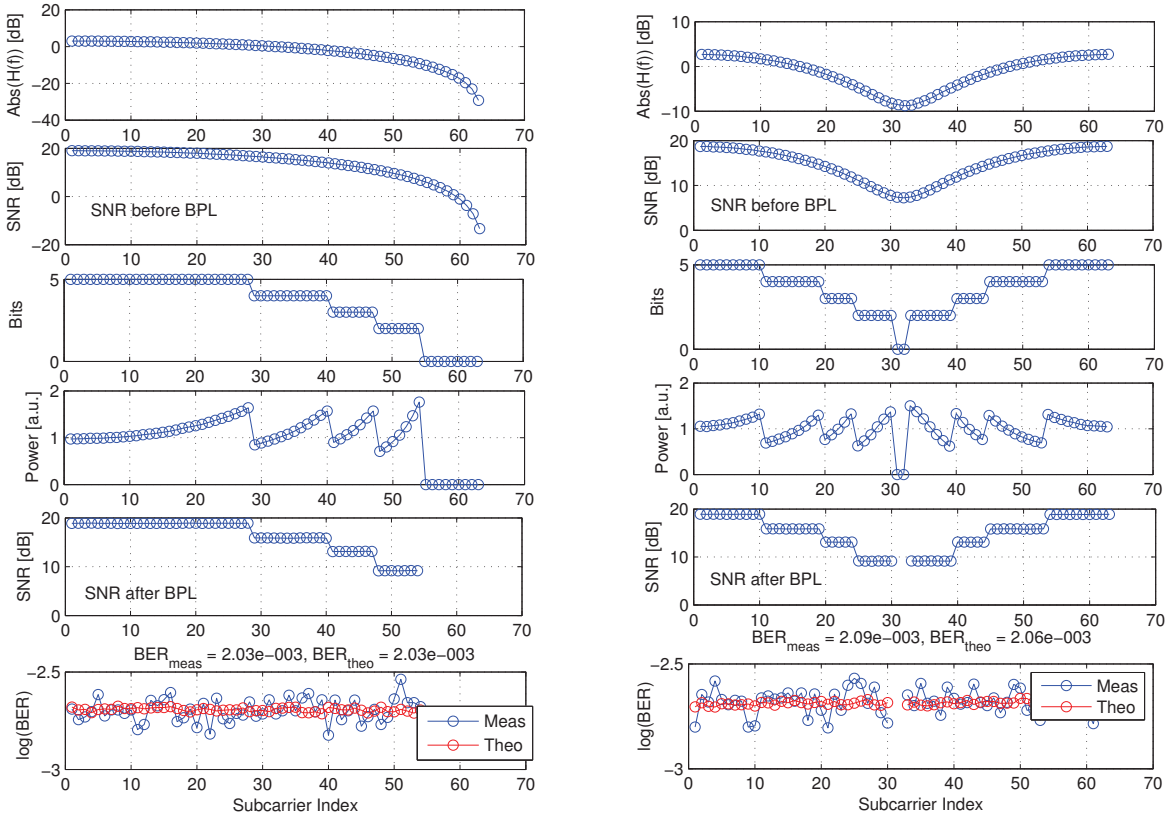

(a) Example 1

(b) Example 2

FIGURE C.3: BER vs SNR for QAM constellations, Monte-Carlo simulations and analytical. BPL : Bit and Power Loading, Meas : BER counted from error bits, Theo : BER calculated from SNR.

Annexe D

Résumé en français

D.1 Introduction Générale et Contexte

Contexte

Depuis l'invention d'internet, nous vivons une révolution numérique qui a complètement changé notre mode de vie. Grâce à internet, les utilisateurs jouissent de nombreux services : ils peuvent, par exemple, regarder des vidéos en très haute définition en temps réel, ou accéder à leurs données personnelles stockées en "cloud" de façon nomade, entre autres.

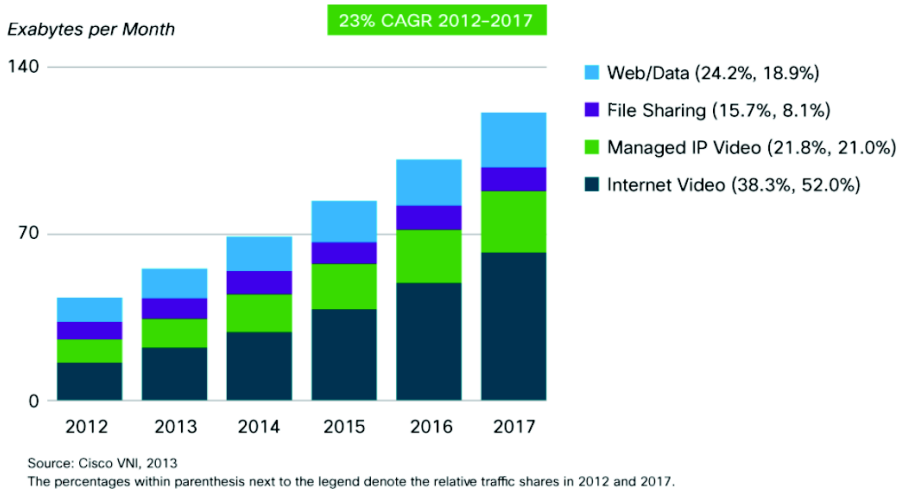

FIGURE D.1: Bande passante et services demandés par utilisateur au cours du temps (source [25]).

La figure D.1 donne l'évolution au cours du temps de la bande passante requise par utilisateur, et une prévision jusqu'à 2015 [25]. Historiquement, les services à très haut débit sont assurés par des réseaux en câbles de cuivre (*Digital Subscriber Line* (xDSL)). Le succès de ce type de réseaux a rendu possible un certain nombre d'applications comme la vidéo à haute définition (HDTV) et le *cloud computing*. Cependant, en raison de l'atténuation élevée dans le câble cuivre, la bande passante des technologies xDSL est en pratique limitée à 50Mbps (cf figure D.1).

D'après les prévisions détaillées dans le rapport [25] et illustré en figure D.1, la bande passante par utilisateur dépassera 250Mbps après 2015. Pour répondre à cette évolution, le déploiement des réseaux d'accès optique a commencé, de manière discrète au début des années 2000, puis très rapidement depuis. Il a en effet subi une très grande croissance vers la moitié

des années 2000 avec la popularisation des services à très haut débit. L'état de déploiement des réseaux FTTH/B (*Fiber-to-the-Home/Building*) est cependant très différent d'un pays à l'autre. Le leader mondial est le Japon, où plus de 90% de la population est couverte par la fibre, et à peu près 60% des foyers couverts sont abonnés [3].

Les réseaux passifs optiques

Les réseaux FTTH/B peuvent être déployés suivant plusieurs architectures différentes. L'architecture la plus connue est celle dite de "réseau optique passif" (*Passive Optical Network* (PON)). Un schéma d'un PON classique est illustré en figure D.2. Il est constitué d'un *Central Office*, qui se charge de distribuer les données du monde extérieur vers un groupe de N utilisateurs. Une simple fibre optique (dite branche) fait le lien entre le *Central Office* et le réseau de distribution optique (*Optical Distribution Network* (ODN)). Ce dernier permet de diviser le signal optique en N signaux identiques, par l'utilisation d'un diviseur de puissance optique passif. Ces signaux sont ensuite acheminés vers les différents utilisateurs servis par chacune des branches. La voie descendante est le chemin du *Central Office* vers les utilisateurs. Le chemin contraire est appelé voie montante.

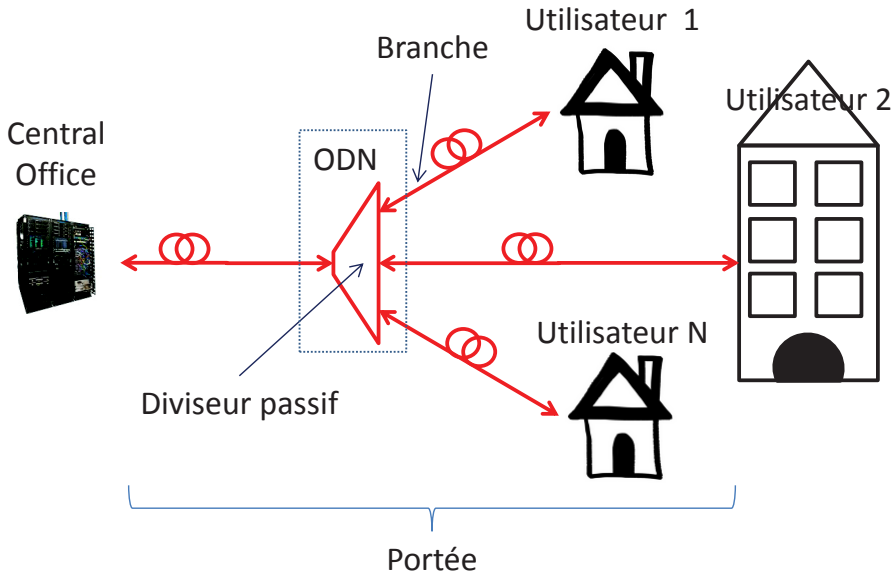

FIGURE D.2: Schéma d'un réseau optique passif (PON).

Dans le sens descendant, puisque tous les signaux optiques des différents utilisateurs sont envoyés vers chacun des utilisateurs, une discrimination est nécessaire. Elle peut être réalisée dans le domaine temporel (une fenêtre temporelle est allouée à chacun des utilisateurs), dans le domaine des longueurs d'onde ou fréquentiel (une longueur d'onde optique ou une fréquence RF est allouée à chacun des utilisateurs). Dans le sens montant, les utilisateurs se partagent également l'accès à la fibre de la même manière (partage temporel, fréquentiel ou en longueur d'onde).

Technologies actuelles et besoins futurs

La première question adressée par cette thèse est relative à la capacité des technologies actuelles à répondre aux besoins prédits en débit.

Le dernier standard publié en 2010 est le XG-PON [16]. Le tableau D.1 résume ses caractéristiques en termes de débit agrégé (débit total prenant en compte tous les utilisateurs de la branche), de nombre d'abonnés par branche et de portée. Prenant en compte le débit agrégé

maximum et le nombre d'utilisateurs, le débit théorique maximum par abonné est d'environ 300Mbps, mais en pratique limité à 10 fois moins.

Débit agrégé	10Gbps (voie descendante) / 2.5Gbps (voie montante)
Nombre minimum d'utilisateurs	32
Portée	20km to 60km

TABLEAU D.1: Résumé des principales caractéristiques du standard XG-PON.

Le standard XG-PON utilise la technique de multiplexage dans le domaine temporel (*Time Division Multiplexing* (TDM)), et représenté en figure D.3. Cette technique est considérée plus simple à implémenter que les techniques de multiplexage en fréquence ou en longueurs d'onde. Le plus gros inconvénient est lié aux performances requises pour les émetteurs-récepteurs optiques chez les utilisateurs. Ces derniers doivent en effet générer/démoduler un signal au débit agrégé du lien (appelé aussi débit série), c'est à dire à 10Gbps et 2.5Gbps pour le XG-PON, respectivement en réception et en transmission, alors que le débit effectif par utilisateur est nettement inférieur ($< 100Mbps$).

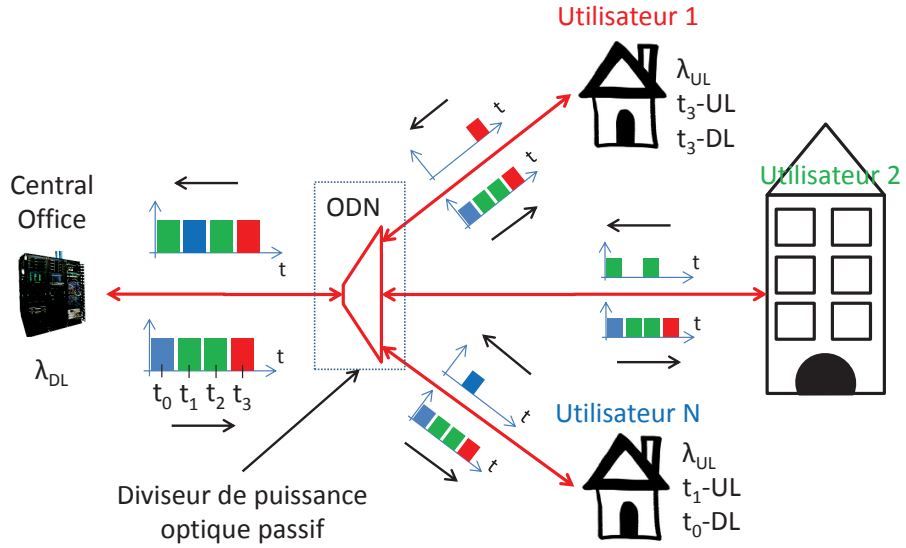

FIGURE D.3: Schéma représentatif de la technique de multiplexage en temps (TDM).

La technique de modulation définie dans le XG-PON est celle d'*On-Off Keying* (OOK). Dans cette modulation, le bit 1 est représenté par un niveau haut de puissance optique, et le bit 0 par un niveau bas. Pour un débit de 10Gbps, la bande passante requise avec une modulation OOK est de l'ordre de 7GHz. Il est à noter que plus la bande passante est élevée, plus la portée de la transmission sur fibre optique est réduite, du fait de la dispersion chromatique de la fibre. Par exemple, à 10Gbps avec une porteuse optique à $1.55\mu m$, la transmission dans une fibre monomode (*Single-mode fiber (SMF)*) standard est limitée à moins de 10km [1], si un laser modulé en directe est utilisé comme émetteur.

Le format de modulation et technique de modulation définis par le XG-PON limitent les performances du système. Une nouvelle technologie est nécessaire, permettant des débits et portées accrues. Le groupe d'étude FSAN (*Full Service Access Networks*) a récemment (2012 [20]) défini un ensemble de solutions pour répondre à ces besoins, appelé *Next-Generation of Passive Optical Networks : Stage 2* (NG-PON2). Le tableau D.2 résume les principales exigences des futurs systèmes NG-PON2 [20].

1. Considérant une source optique avec chirp en fréquence $\alpha = 3$ (typique des lasers modulés en directe).

Débit agrégé	40Gbps (voie descendante) / 10Gbps (voie montante)
Débit durable par utilisateur	1Gbps
Nombre minimum d'utilisateurs	64-256
Portée	40km to 60km

Tableau D.2: Spécification des technologies compatibles avec NG-PON2.

Un autre groupe de solutions est considéré par quelques auteurs - *Long-Reach* PON (LR-PON) [12]. Dans cette architecture, chaque ODN doit servir plus de 1000 utilisateurs, et avoir une portée allant jusqu'à 100km. L'objectif est de de pouvoir fusionner le réseau d'accès et métropolitain. En conséquence, les coûts d'installation et opérationnels sont minimisés.

Objectifs et méthodologie de la thèse

Cette thèse a pour objectifs

1. de proposer des solutions de transmissions optiques répondant aux besoins des réseaux d'accès optique futurs, avec un produit [débit × portée] bien conformes aux objectifs énoncés au tableau D.2 ;
2. de proposer des solutions bas-coût basées sur la technologie photonique silicium.

Pour améliorer les produits [débit × portée] des transmissions, l'utilisation d'une technique de transmission multi-porteuse est proposée. Le principe de base est de diviser le signal mono-porteuse (série) en plusieurs signaux de plus faibles bandes passantes. Ces signaux sont portés et envoyés en parallèle par plusieurs sous-porteuses. Le signal est donc plus robuste contre la dispersion temporelle de la fibre (du fait de plus faibles bandes passantes par sous porteuse), alors que le débit est le même. La durée d'un symbole est multipliée par le nombre de sous-porteuses. En particulier, la technique multi-porteuse *Orthogonal Frequency Division Multiplexing* (OFDM) est largement connue dans le domaine RF. Cette technique permet une utilisation très efficace du spectre disponible par rapport aux techniques classiques (FDM), puisque les sous-porteuses se chevauchent entre elles, comme illustré dans la figure D.4. Le principe de l'orthogonalité assure qu'il n'y aura pas de *crosstalk* entre les elles. En plus, le modem peut être implémenté avec un processeur numérique de signaux.

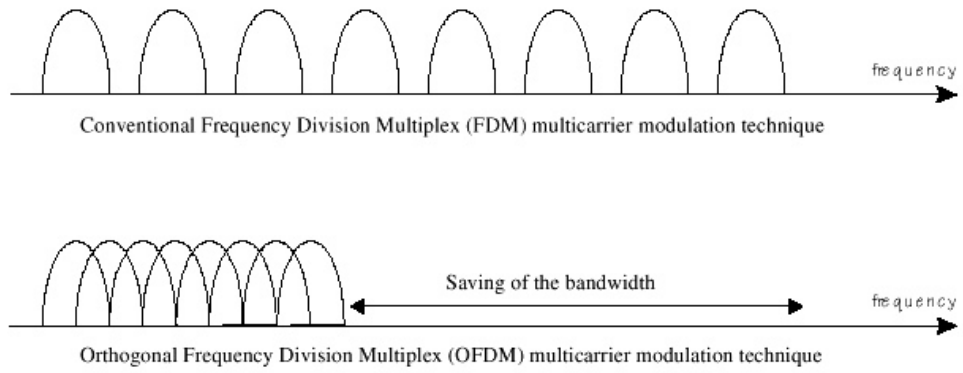

Figure D.4: Avantage de l'OFDM par rapport aux techniques FDM classiques - meilleure efficacité spectrale.

La technologie Photonique sur Silicium permet de réaliser dispositifs optiques et électro-optiques avec les procédés de fabrication CMOS sur substrat silicium. Aujourd'hui, la majorité de fonctions passives optiques ont déjà été démontrés sur silicium. Les dispositifs actifs exigent

parfois d'autres matériaux (par exemple du Germanium pour les photodétecteurs, et des matériaux III/V pour les lasers) mais la fabrication reste toujours compatibles avec du CMOS. Les performances sont en général très satisfaisantes, alors que la taille des composants est plus petite que celle de composants commerciaux. La photonique sur silicium est donc très adaptée pour des applications exigeant de la production en masse comme le PON. L'intégration optique avec les circuits électroniques peut encore alléger le coût par pièce des composants.

Technologie TWDM pour le NG-PON2

Pendant le déroulement de cette thèse, en avril 2012, la technologie hybride de multiplexage temporel et en longueurs d'onde (*Time and Wavelength Division Multiplexing* (TWDM)) a été choisie comme solution primaire pour le NG-PON2 [29]. Dans cette solution, le débit agrégé est augmenté 4 fois en empilant 4 longueurs d'ondes provenant du XG-PON. Le principe d'opération est donné dans la figure D.5.

Chaque longueur d'onde peut servir plusieurs utilisateurs employant du TDM. Compatibilité avec le réseau existant est assurée en plaçant le multiplexer/démultiplexeur de longueur d'ondes (*WDM Mux/Demux*) au *Central Office*. Chaque utilisateur reçoit toutes les longueurs d'ondes de la voie descendante. Un filtre optique adaptatif permet de sélectionner la bonne longueur d'onde. Pour la voie montante, l'émetteur doit être capable de générer toutes les longueurs d'ondes allouées pour cette voie.

Malgré ce fait, beaucoup d'auteurs prétendent que ce choix a été prématuré parce qu'il reste beaucoup de détails techniques qui n'ont pas de réponse. Par exemple, le démarrage aveugle et le réglage "furtif" de la longueur d'onde n'ont pas encore de solution. En plus, l'utilisation de la modulation OOK ne permet pas d'améliorer le produit [débit × portée] si une solution LR-PON est envisagée.

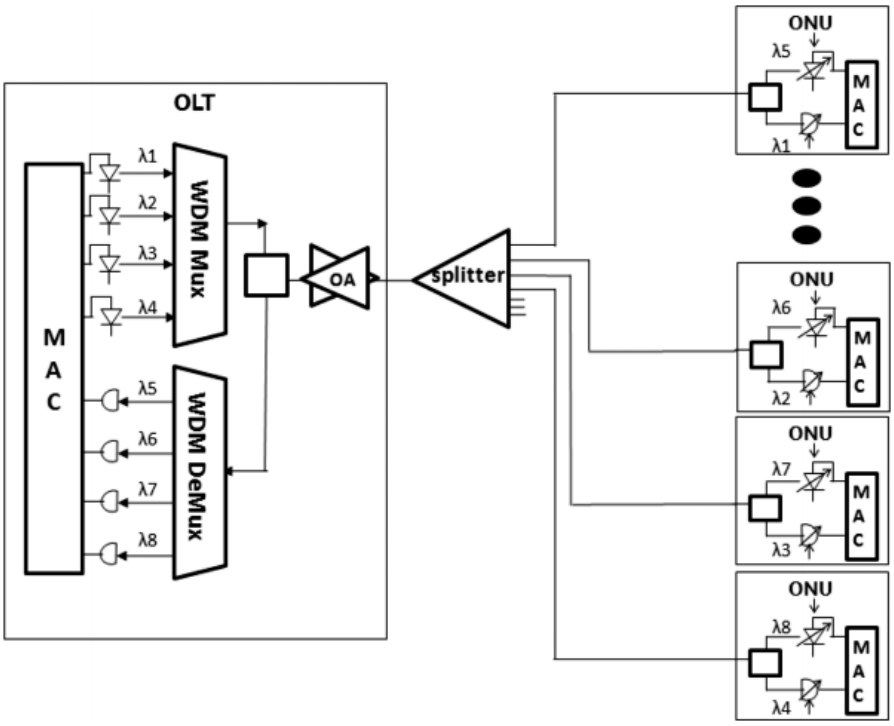

FIGURE D.5: Technologie de multiplexage en temps et longueur d'ondes proposée pour le NG-PON2. OA : Amplificateur Optique ; ONU : Utilisateurs. (Source [29]).

D.2 Etat-de-l'art

Depuis la standardisation du XG-PON en 2010, plusieurs groupes d'études ont commencé à travailler sur la prochaine génération de réseau d'accès, le NG-PON2. Quelques auteurs proposent des schémas de multiplexage alternatifs. En plus, des formats de modulations complexes sont aussi considérés. En général, ils peuvent être implémentés quel que soit le schéma de multiplexage. En parallèle, des composants à bas coût basés sur nouvelles technologies (comme la photonique sur silicium) sont étudiés pour le PON.

Techniques de multiplexage

Afin de résoudre le problème de la technique TDM - l'utilisation inefficace de la bande disponible - le multiplexage en fréquence (FDM) a été proposé [101]. Le principe de base est illustré dans la figure D.6. Dans cette technique, la bande passante disponible est divisée en slots fréquentielles. La largeur de bande par utilisateur est allouée dynamiquement selon la demande. Un circuit de conversion RF et un processeur numérique de signaux est nécessaire chez les utilisateurs pour générer et démoduler les signaux RF.

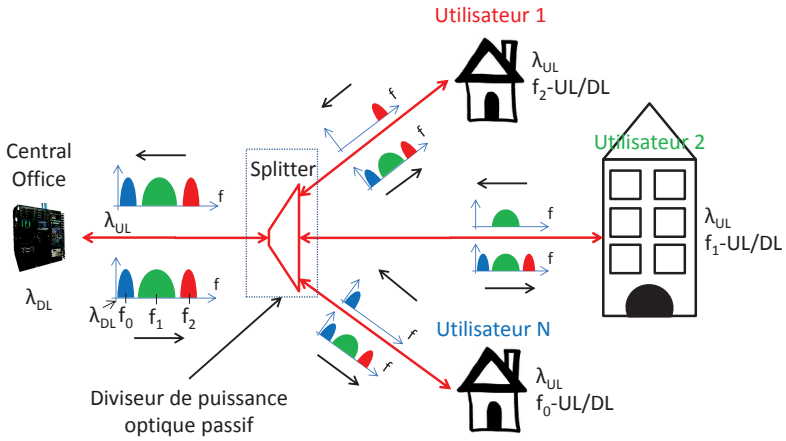

FIGURE D.6: Schéma représentatif de la technique de multiplexage en fréquence (FDM).

L'auteur dans [101] montre qu'un simple circuit électronique de 500MHz est suffisant pour fournir un débit durable par utilisateur de 1Gbps. Ceci est le principal avantage de ce schéma - le couple émetteur-récepteur à faible bande passante. En conséquence, le coût des composants est minimisé et la portée peut être améliorée. Cependant, la voie montante est plus difficile à réaliser. Afin d'éviter l'interférence entre deux utilisateurs adjacents, deux solutions sont possibles. 1) Le signal optique est envoyé par le *Central Office* (dans ce cas les abonnées d'un même branche ont strictement la même longueur d'onde). L'inconvénient est que le budget optique nécessaire est doublé ; 2) Si le signal optique est généré par les abonnées, ils doivent avoir forcement des longueurs d'ondes différentes. Ceci rend le système plus cher et plus difficile de l'agrandir.

Comme mentionné dans la section précédente, le multiplexage en longueur d'onde (WDM) permet aussi d'améliorer les performances du système et ainsi d'atteindre les spécifications du NG-PON2. Cependant, l'utilisation du WDM exige des composants qui, pour le moment, sont chères et pas adaptés pour cette application. Beaucoup d'efforts dans cette direction est faite [31]. En général, il est du sens commun que le WDM sera présent dans les futures générations des réseaux d'accès, combiné avec d'autres formes de multiplexages.

Transmission point-à-point avec des composants photoniques sur silicium

Le premier couple émetteur-récepteur basé sur la technologie photonique sur silicium pour le PON a été démontré en 2010 [69]. Cependant, aucune transmission sur la fibre monomode n'a été

faite sur ce travail. Depuis, des nombreuses travails ont montré la faisabilité de la transmission longue distance ($> 20km$) pour le réseau d'accès [44, 72–74, 182]. Le tableau D.3 présente un résumé des principaux travails.

Reference	Technique	Emetteur Silicium	Débit	Portée
[44]	OOK Mono-porteuse	Laser hybride III/V	10Gbps	25km
[72]	OOK Mono-porteuse	Modulateur en anneau	10Gbps	70km
[73]	OOK Mono-porteuse	Modulateur Mach-Zehnder	11Gbps	80km
[74]	OOK Mono-porteuse	Modulateur en anneau	12.5Gbps	80km
[182]	OFDM	Modulateur Mach-Zehnder	4.38Gbps	50km

TABLEAU D.3: Etat de l'art des transmissions longue-distance pour le PON futures utilisant des composants photoniques sur silicium.

Dans [44], une transmission de 10Gbps jusqu'à 25km utilisant la modulation directe d'un laser hybride III/V sur silicium a été démontré. La structure de base du laser est un guide d'onde III/V collé sur un guide d'onde silicium. Le guide III/V fournit le gain optique nécessaire pour le laser, alors que le guide silicium supporte toutes les fonctions passives. La portée dans ce cas est limitée par le chirp en fréquence élevé du laser combiné avec la dispersion temporelle de la fibre.

Pour améliorer la portée de la transmission, des nombreux travails utilisant des modulateurs externes sur silicium ont été réalisés [72–74]. Il existe plusieurs mécanismes de modulation de la lumière utilisant le silicium. Le plus classique est l'effet plasma qui a été observé par Soref en 1987 [164]. Il se trouve qu'une variation dans la concentration de porteurs libres (électrons - ΔN ou trous ΔN en cm^{-3}) dans le silicium se traduit par une variation de l'indice de réfraction (Δn) et d'absorption ($\Delta \alpha$). A $\lambda = 1.55\mu m$, ils sont reliés par les équations

$$\Delta n = -8.8 \times 10^{-22} \Delta N - 8.5 \times 10^{-18} \Delta P^{0.8} \tag{D.1}$$

$$\Delta \alpha_{abs} = 8.5 \times 10^{-18} \Delta N + 6 \times 10^{-18} \Delta P. \tag{D.2}$$

La variation dans les concentrations d'électrons et trous peut se faire en intégrant une jonction PN au guide d'onde Silicium, entre autres. En termes de performance, les modulateurs externes peuvent avoir un chirp très faible, ou même un chirp négatif. En conséquence, le produit [débit $\times$ portée] est amélioré. Par exemple, avec de la modulation OOK, un débit plus de 10Gbps est émis avec une portée de 80km [72–74]. Très récemment, la faisabilité de la technique OFDM avec un modulateur Mach-Zehnder sur silicium est démontrée [182]. Cependant, à cause de la faible bande-passante du composant, le débit est limité à 4.4Gbps, pour une bande du signal OFDM de 2.5GHz (modulation *Quadrature Phase-Shift Keying* (QPSK)).

D.3 Principes de l'OFDM

La technique de modulation multi-porteuse classique (FDM) a été inventée dans les années 50 pour les systèmes de communication radio. Le principe de base est de diviser le signal série très large bande en N signaux à bande passante très étroite, chacun portée par une sous-porteuse différente. De cette façon, la durée temporelle d'un symbole temporelle est élargie d'un facteur égale au nombre de sous-porteuses $T = Nt_s$, où $t_s = 1/B$ est la période du signal mono-porteuse équivalent de bande passante B. En conséquence, il est plus robuste contre la dispersion temporelle, alors que le débit est tenu constant.

Le principe de génération et démodulation d'un signal FDM classique est illustré dans la figure D.7. Pour éviter l'interférence entre les canaux adjacents, une bande de garde en fréquence

est rajoutée. Ceci rend le signal FDM inefficace parce qu'il occupe une bande passante plus grande que le signal mono-porteuse avec le même débit.

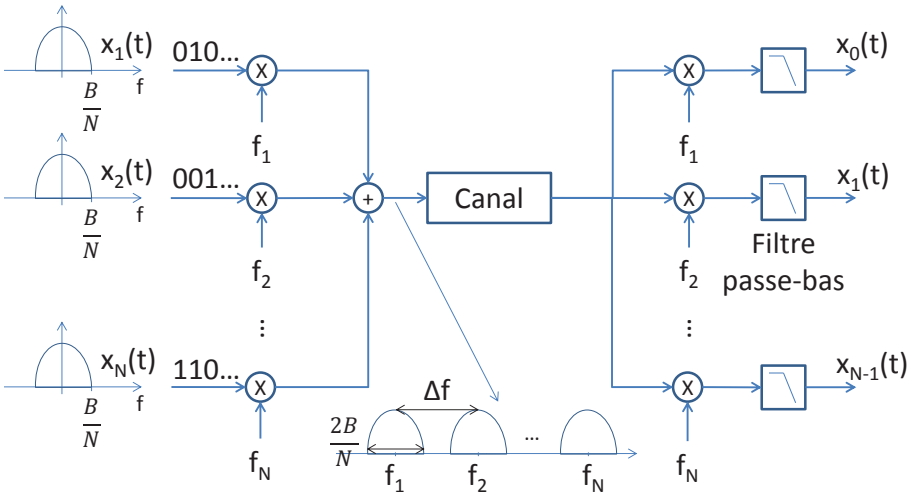

FIGURE D.7: Génération et démodulation d'un signal FDM classique.

Cependant, il peut être montré que, même si deux canaux adjacents se chevauchent entre eux, l'interférence est éliminée si le principe d'orthogonalité est respecté. C'est le principe de base de l'OFDM. Supposons un signal FDM générique avec une bande de garde Δf entre deux sous-porteuses adjacentes

$$x_{FDM}(t) = \sum_{k=1}^{N} X_k(t) \cdot \exp\left(j2\pi k\Delta f t\right) \tag{D.3}$$

où $X_k(t)$ est le signal de la $k^{ème}$ sous-porteuse. Le principe de l'orthogonalité dit que deux signaux x(t) et y(t) sont orthogonaux si et seulement si la condition suivante est respectée

$$\langle x(t)|y(t)\rangle = \int_0^T x(t) \cdot y^*(t)dt = 0. \tag{D.4}$$

Utilisant l'équation D.4, il peut être montré que si la condition suivante

$$\Delta f = m\frac{1}{T} = m\frac{B}{N}; m \in \mathbb{Z} \tag{D.5}$$

est respectée, les sous-porteuses sont orthogonales entre elles. Prenant m=1, l'écart entre deux sous-porteuses adjacentes est $\Delta f = B/N$. En conséquence, la bande passante du signal OFDM est la même que le signal mono-porteuse équivalent.

Caractéristiques

- Implémentation utilisant un processeur numérique de signaux (*Digital Signal Processor* (DSP)) : le signal OFDM peut être généré/démodulé avec une opération de transformée de Fourier. Avec la popularisation des applications numériques, des algorithmes très efficaces pour réaliser la transformée de Fourier ont été développés, notamment la transformée de Fourier rapide (*Fast Fourier Transform* (FFT)). Après la génération du signal OFDM numérique, un convertisseur numérique-analogique (*Digital-to-Analog Converter* (DAC)) fait la conversion au domaine analogique (et vice-versa pour la démodulation).
- Pas d'interférence entre les symboles (*Inter-symbol Interference* (ISI)) : en général, la dispersion temporelle du canal optique n'affecte qu'une très petite partie du symbole

OFDM. L'ISI peut être complètement éliminé utilisant une forme d'intervalle de garde appelé préfixe cyclique.
– Egalisation linéaire du canal : puisque le signal OFDM reçu n'a pas d'ISI, un symbole OFDM reçu est égal à lui-même multiplié par un coefficient complexe (correspondant au gain complexe du canal de transmission). De cette façon, l'égalisation peut être réalisée avec un modèle "single-tap".

Modulation numérique / Allocation adaptatif de bit et puissance

En général, le format de modulation utilisé dans chaque sous-porteuse est appelé multi-niveau. Dans ce cas, un symbole dans le temps représente plusieurs bits, améliorant ainsi son efficacité spectrale. Il est avantageux de moduler au même temps l'amplitude et phase des sous-porteuses. Dans ce contexte, un symbole est représenté par un numéro complexe. Les formats de modulation d'amplitude et phase les plus connus sont appelés *M-Quadrature Amplitude Modulation* (M-QAM), où $M = 2^b$ est lié au nombre de bits b que chaque symbole porte (appelé aussi l'ordre du format de modulation). En particulier, pour M=4, la modulation est appelé *Quadrature Phase Shift-Keying* (QPSK) parce que seulement la phase de la sous-porteuse est modulée. La façon la plus connu de représenter un tel format de modulation est le diagramme de constellation, où tous les symboles sont tracés dans le plan complex. Les diagrammes de constellation pour les modulations QPSK, 8-QAM and 16-QAM sont donnés dans la figure D.8.

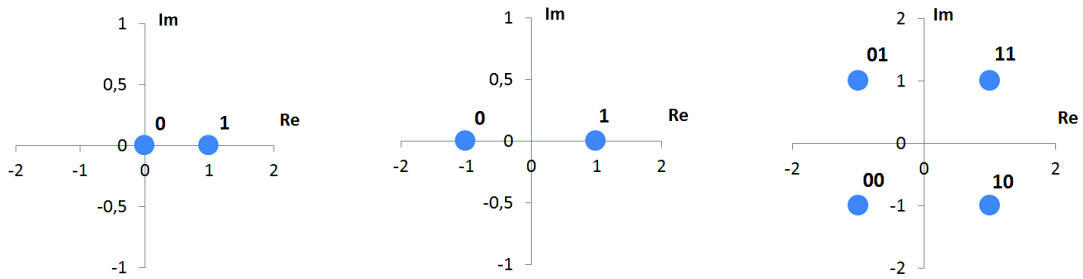

(a) M=2 OOK (b) M=2 BPSK (c) M=4 QPSK

FIGURE D.8: Diagrammes de constellations pour plusieurs types de modulation QAM.

Il est évident qu'une modulation QAM de plus grand ordre exige un niveau de rapport signal à bruit (*Signal-to-Noise Ratio* (SNR)) plus grand pour atteindre un taux d'erreur binaire (*Bit Error Rate* (BER)) donné. En raison de plusieurs caractéristiques du lien de transmission optique, comme par exemple la sélectivité en fréquence causée soit par le canal, soit par les composants, le SNR peut avoir une variation très important parmi les sous-porteuses du signal OFDM. L'inconvénient est que les sous-porteuses de très faible SNR pénalisent le BER total si les sous-porteuses ont toutes le même ordre de modulation fixe. Pour combattre cet effet, une technique d'allocation de bits et puissance est employée. Elle consiste en déterminer l'ordre de modulation de chaque sous porteuse d'après le SNR pour atteindre un BER cible. Du fait que le nombre de bits attribué est entier, la puissance relatif de chaque sous-porteuse est adaptée pour s'approcher au maximum du BER cible. Ceci permet d'optimiser le débit de la transmission d'après les conditions du lien. Ce type d'OFDM est appelé "adaptatif".

OFDM pour les communications optiques

Le type d'OFDM optique le plus simple est appelé *Intensity-Modulated/Directly-Detected* (IM/DD). Un schéma représentatif est montré dans la figure D.9. Dans l'émetteur, un modulateur d'intensité optique est utilisé, où le signal électrique est proportionnel à la puissance du signal optique modulé. Ceci peut être par exemple, un laser modulé en directe ou un modulateur

Mach-Zehnder polarisé en quadrature. En conséquence, le signal électrique modulant doit être réel. Au récepteur, une simple photodiode fait la conversion linéaire entre intensité optique et le signal électrique.

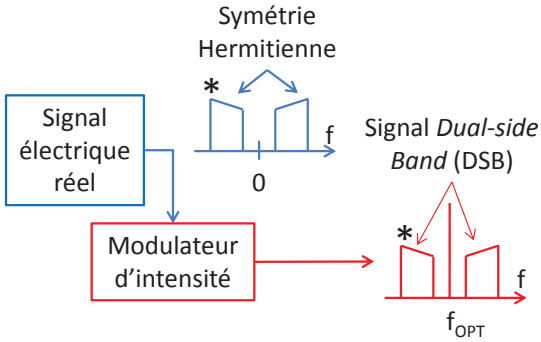

FIGURE D.9: Schéma du lien OFDM optique avec IM/DD.

La réponse en fréquence du lien optique IM/DD dépende de plusieurs caractéristiques du milieu de transmission, ainsi que de l'émetteur optique. Elle peut être écrite analytiquement par

$$H_{F_{DML}}(f) \propto \left|\cos\left(\frac{\pi c D L f^2}{f_{opt}^2}\right) - \alpha \cdot \left(1 - j\frac{f_c}{f}\right) \cdot \sin\left(\frac{\pi c D L f^2}{f_{opt}^2}\right)\right|. \tag{D.6}$$

où c est la vitesse de la lumière, DL est la dispersion cumulée de la fibre, f_{opt} est la fréquence de la source optique, α et f_c sont deux paramètres liés au chirp en fréquence du modulateur d'intensité optique.

Un exemple de réponse en fréquence d'un lien IM/DD est montré dans la figure D.10. Deux longueurs de fibre monomode avec une valeur de dispersion standard à $1.55\mu m$ sont considérées, ainsi qu'une source optique sans chirp. En effet, l'inconvenant de ce type d'OFDM optique est la très forte atténuation dans certains plages de fréquence, dépendant de la longueur de la fibre. Ceci est une conséquence du fait que le signal optique en sortie du modulateur en intensité est *Dual-side band* (DSB). La capacité du lien est donc réduite avec la portée de la transmission. Néanmoins, nous montrerons par la suite que les performances sont toujours supérieures à une modulation OOK mono-porteuse.

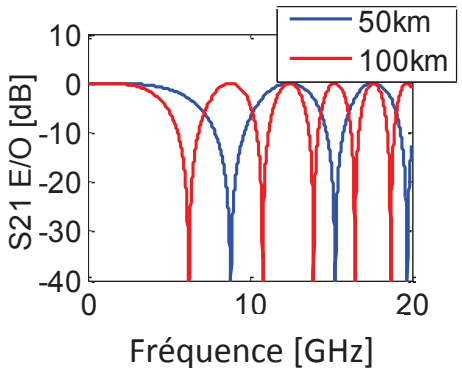

FIGURE D.10: Réponse en fréquence d'un lien IM/DD, source optique sans chirp et valeurs standards de dispersion à $1.55\mu m$.

D.4 Démonstrations expérimentales / Simulations d'OFDM avec des émetteurs Photoniques sur Silicium

Dans la section précédente, les avantages de la technique OFDM ont été énumérés. Cette technique de transmission peut effectivement améliorer les performances du lien de transmission optique pour répondre aux besoins des réseaux d'accès optique futures. Comme mentionné précédemment, le modem OFDM peut être implémenté avec un DSP utilisant la technologie ASIC (*Application Specific Integrated Circuits*) par exemple, qui est compatible avec le procédé de fabrication CMOS. En conséquence, la combinaison entre cette technique de transmission avec des composants photoniques sur Silicium est très avantageuse. L'intégration électro-optique peut au même temps réduire le coût de fabrication du transceiver, ainsi que réduire la consommation de puissance.

Dans cette partie, les principaux résultats de transmission utilisant comme technique de transmission l'OFDM et des émetteurs optiques compatibles avec du CMOS sont décrits et commentés. Les performances de transmission sont évaluées en termes de débit maximal atteint, portée de transmission, profondeur de modulation requise, sensibilité optique, entre autres.

La méthodologie de cette étude est représentée dans la figure D.11. Tout d'abord, une plateforme de simulation a été développée afin de valider les algorithmes mises en place, et d'évaluer les performances dans certain cas. Un banc expérimental a été mise en place ensuite. Dans un premier temps, les émetteurs optiques sur étagère ont été évalués. Dans un deuxième temps, le lien optique avec des composants photoniques est développé. Ils seront détaillés dans la suite. Des modèles théoriques pour les modulateurs externes sur Silicium sont implémentés sur la plateforme de simulation. Ces modèles sont validés avec des données expérimentales.

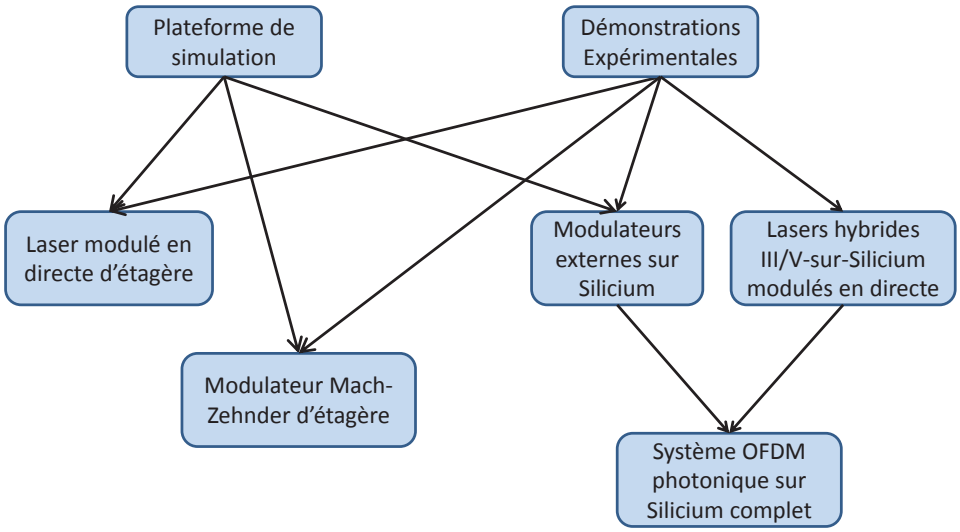

FIGURE D.11: Méthodologie d'évaluation du lien optique OFDM / photonique sur Silicium.

Description de la plateforme de simulation

La plateforme de simulation a été développée avec le logiciel de simulation système appelé Optsim en co-simulation avec Matlab. Le projet est composé de plusieurs blocs qui représentent des modèles simples ("*lumped models*") des composants du lien optique. Une capture d'écran d'un projet de simulation est donnée en figure D.12. Chaque bloc contient une fonction de transfert entre entrée et sortie et éventuellement du bruit rajouté. Les composants sont caractérisés par un ensemble de paramètres pour reproduire son comportement.

Les composants optiques classiques (amplificateurs / filtres électriques, lasers semi-conducteurs, modulateurs $LiNbO_3$, photodiodes, entre autres) sont disponibles comme part du logiciel de simulation. Le comportement des lasers III/V est simulé utilisant la méthode d'Euler pour résoudre numériquement ses équations. La propagation dans la fibre monomode est calculée avec la méthode *Split-step Fourier*. La contribution de cette thèse pour la plateforme de simulation a été le développement des blocs Matlab pour le modem OFDM et les modulateurs photoniques sur Silicium.

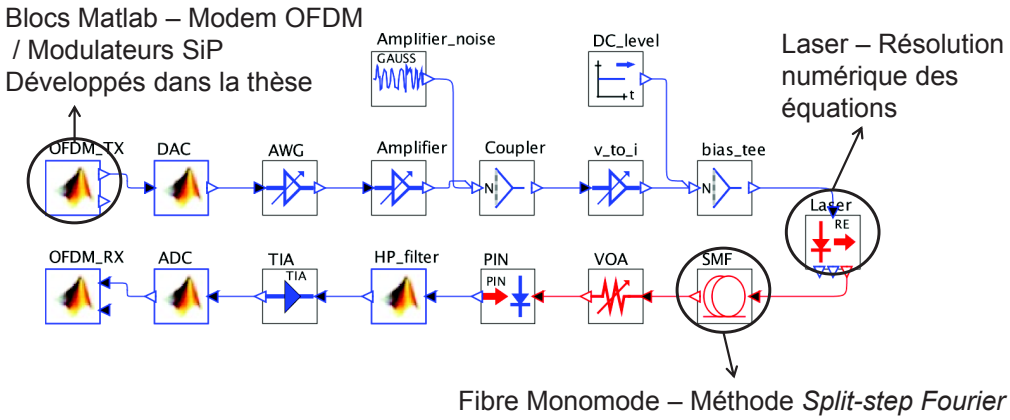

FIGURE D.12: Exemple de projet de simulation sur Optsim.

Mise en place du banc expérimentale

Un schéma général des démonstrations expérimentales réalisées dans cette thèse est représenté dans la figure D.13. Il est important de rappeler que, vu que l'émetteur dans le côté utilisateur est plus sensible en termes de coût, nous focaliserons dans la voie montante. Le débit cible est de 10Gbps avec une portée d'au moins 40km.

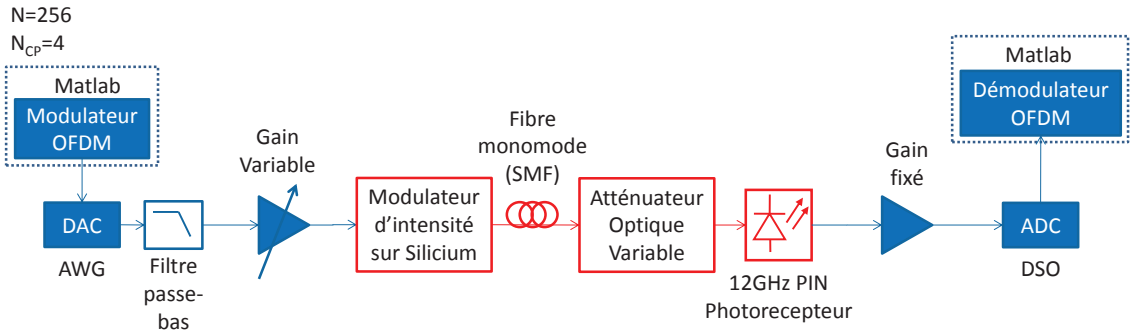

FIGURE D.13: Mise en place général du banc expérimental.

Le signal OFDM est définit en Matlab. Le nombre de sous-porteuses utilisés est $N = 256$, avec $N_{CP} = 4$ échantillons de préfixe cyclique. Afin de générer un signal électrique réel, la moitié des sous-porteuses sont fixés comme le complexe conjugué de l'autre moitié. Le nombre effectif de sous-porteuses de données N_{data} dépendent de l'émetteur utilisé. Les échantillons sont chargés dans un générateur de formes d'ondes (*Arbitrary Waveform Generator* (AWG)) pour réaliser la conversion au domaine analogique, avec un taux d'échantillonnage f_s. La bande passante du signal OFDM est donné par

$$B = \frac{N_{data}}{N + N_{CP}} \cdot f_s. \tag{D.7}$$

L'AWG est suivi d'un filtre passe-bas, pour éliminer les images parasites résultant de la conversion numérique-analogique ; et un amplificateur électrique avec un gain variable pour optimiser la profondeur de modulation selon l'émetteur. Utilisant des probes haute-fréquence, les modulateurs d'intensité sur silicium sont modulés avec le signal électrique analogique. Le lien optique inclut une fibre monomode, un atténuateur optique variable et un photorécepteur pour faire la conversion au domaine électrique. La numérisation est faite avec un Scope Numérique (*Digital Sampling Scope* (DSO)), et le signal numérique est envoyé vers un ordinateur pour démodulation en Matlab.

Avant la mise en place de la transmission OFDM, une caractérisation complète du dispositif photonique est réalisée. Ceci inclut la caractérisation en régime continu (DC) et fréquentielle (petit-signaux et non-linéarité). Ensuite, le lien OFDM optique est mis en place. Dans un premier temps, un signal OFDM de teste avec la modulation QPSK en toutes sous-porteuses est envoyé pour mesurer le SNR par sous-porteuse. Avec un BER cible de 2.2×10^{-3}, la distribution de bits et puissance parmi les sous-porteuses est calculée. Le BER peut être réduit à moins de 10^{-14} avec des codes correcteurs d'erreurs.

Les types de modulateurs d'intensité optique sur silicium considérés dans cette thèse sont décrits dans la figure D.14. Tous ces dispositifs ont été fabriqués au CEA-Leti. Dans la suite, les démonstrations expérimentales avec chacun de ces composants et les principaux résultats de simulation sont présentées et expliquées.

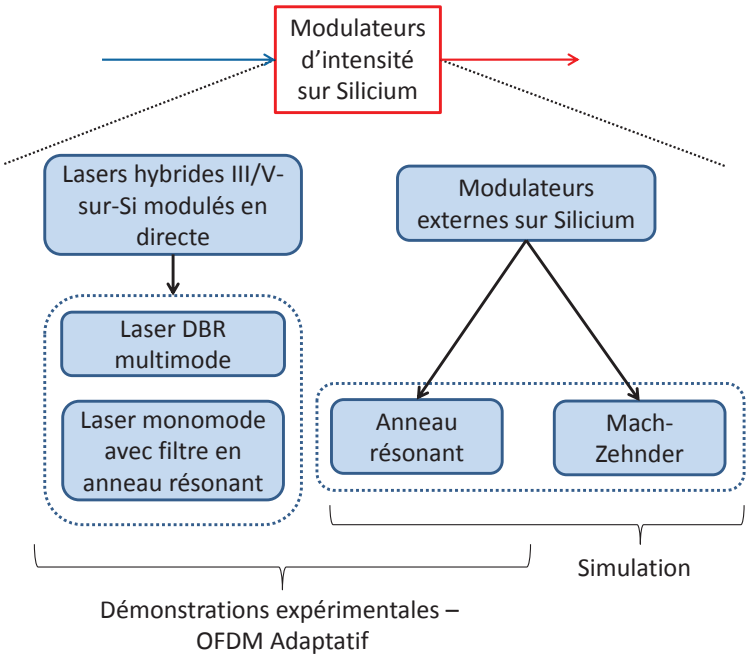

FIGURE D.14: Vue générale des modulateurs d'intensité optiques considérés dans cette thèse. DBR : *Distributed Bragg Reflector*.

D.4.1 Démonstration Expérimentale de l'OFDM Adaptatif avec un Laser Hybride en configuration DBR Multimode

Architecture du laser hybride multimode en configuration DBR

L'architecture du laser hybride III/V-sur-Silicium en configuration DBR utilisé pour évaluer la transmission OFDM est montrée en figure D.15. Une description complète du laser est faite

en [153]. Il est important de distinguer que l'aspect multimodal de ce laser fait référence aux plusieurs modes longitudinaux (expliqué dans la suite) et pas aux modes spatiaux.

Comme mentionné précédemment, un guide d'onde III/V est superposé avec un guide Silicium. Le guide d'onde III/V fournit le gain optique, alors que le guide d'onde Silicium supporte toutes les fonctionnalités passives. Dans un aller-retour dans la cavité, le mode optique est complètement transféré du guide d'onde Silicium vers le III/V utilisant des transformateurs de mode adiabatiques. La cavité est formé avec un miroir de Bragg dans chaque côté de la région actif. Ils ont deux fonctions. Tout d'abord, ils réfléchissent le signal optique pour créer la rétroaction requise pour l'effet laser. Comme montré dans la figure D.15, un des miroirs de Bragg a une très forte réflectivité ($> 90\%$), alors que de l'autre côté la réflectivité n'est que de 50% pour permettre la lumière de quitter la région actif. En plus, ils jouent comme des filtres optiques. Avec un design robuste, des lasers avec un seul mode longitudinal peuvent être développés [155]. La lumière est couplée dans la fibre monomode utilisant un coupleur en réseau de surface.

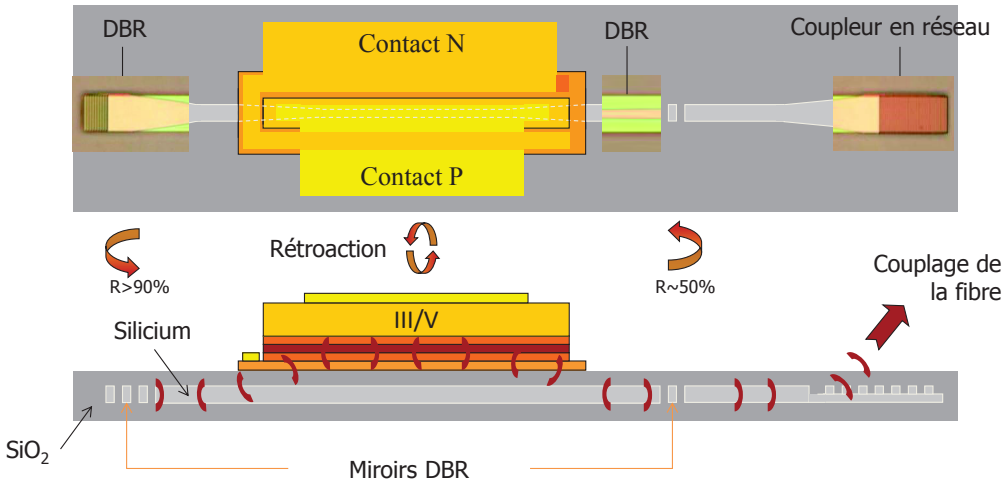

FIGURE D.15: Architecture du laser hybride III/V-sur-Silicium en configuration DBR.

Caractérisation du laser hybride multimode en configuration DBR

En particulier, l'échantillon que nous avons testé n'avait pas un seul mode longitudinal. Ceci est due à la passe-bande relativement large des miroirs de Bragg, occupant deux mode longitudinaux de la cavité.

La puissance optique en sortie du laser est de 1.6mW à un courant de polarisation de 170mA. Le courant de seuil est de 90mA environ. La figure D.16 donne le spectre d'émission du laser. Nous pouvons observer deux modes longitudinaux principaux, séparés de 0.5nm, autour de 1547nm. La bande-passante de modulation petit-signal est mesurée à 5.5GHz avec un courant de polarisation de 170mA.

Résultats de la transmission OFDM / comparaison avec la modulation OOK du laser hybride multimode en configuration DBR

Avant de la mise en place du lien OFDM optique, une évaluation du produit [débit × portée] avec de la modulation OOK mono-porteuse a été réalisé. A cause du spectre d'émission relativement très large, la technique de transmission mono-porteuse est très limitée. En effet, à une portée de 20km de fibre monomode, le débit OOK est limité à 7Gbps, résultant dans un produit [débit × portée] de $140 Gbps * km$. Cette technique de transmission ne répond pas aux débits requis pour les générations futures de réseau d'accès optique.

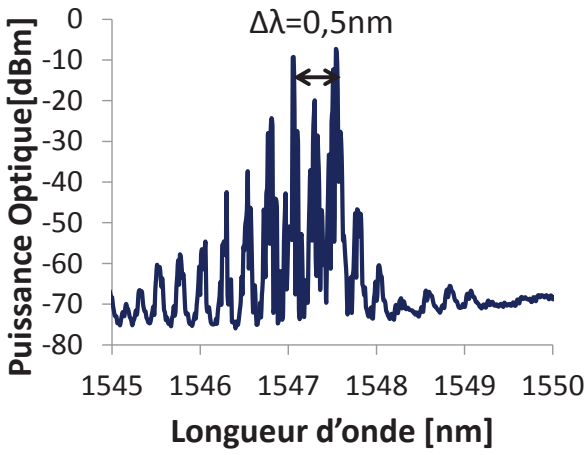

FIGURE D.16: Spectre optique du laser hybride III/V-sur-Silicium en configuration DBR multimode à 170mA de courant de bias.

La bande passante du signal OFDM a été choisie à 6.25GHz, due à la limitation en bande passante de modulation directe du laser. La profondeur de modulation est optimisée à $4V_{pp}$ ($3.15V_{pp}$) environ à 0km SMF (50km SMF). En B2B (*back-to-back*) optique (0km de fibre), un débit maximum de 21.5Gbps a été démontré. L'efficacité spectrale (rapport entre débit et bande passante du signal) donne une mesure quantitative de la qualité de la transmission, elle est donc évaluée à 3.5bps/Hz environ (bien au-dessus de 1bps/Hz de la modulation OOK). Le SNR et nombre de bits per sous-porteuse de la transmission en B2B est montré dans la figure D.17(a). Un SNR maximum de 19dB est atteint, supportant une modulation 32-QAM (5 bits per symbole). A 50km de fibre monomode, le SNR maximum chute à 13dB (3 bits / symbole), comme montré dans la figure D.17(b), en raison de l'atténuation en fréquence typique des liens IM/DD. En conséquence, le débit total est réduit à 12.4Gbps. Le BER total dans tous les cas est au-dessous du BER cible de 2.2×10^{-3}.

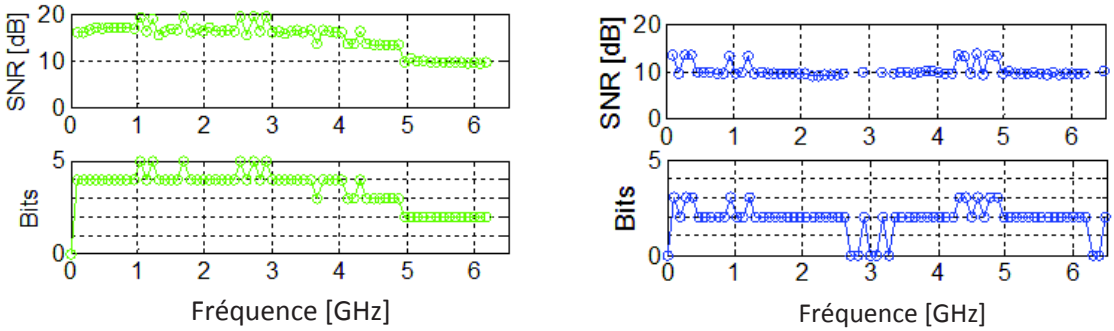

(a) B2B optique ($P_{opt} = -2.3dBm$)

(b) 50km SMF ($P_{opt} = -8.8dBm$)

FIGURE D.17: SNR et nombre de bits par sous-porteuse de la transmission OFDM adaptatif avec le laser hybride III/V-sur-Silicium en configuration DBR multimode.

La figure D.18 montre le diagramme de constellation des symboles reçus pour la sous-porteuse de plus grand SNR, à 0 et 50km de fibre. Les symboles reçus sont groupés autour des positions des symboles envoyés, ce qui démontre la bonne qualité du signal reçu.

Le tableau D.4 résume les principaux résultats de cette étude. La technique OFDM a permis une amélioration de 5 fois dans le produit [débit × portée] comparé à la technique monomode OOK. Il peut répondre aux exigences des réseaux d'accès futures.

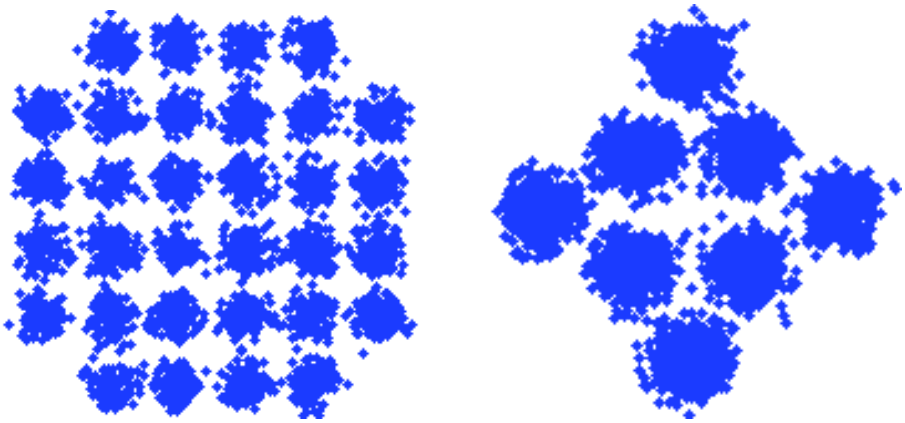

(a) B2B optique, 32-QAM (b) 50km SMF, 8-QAM

FIGURE D.18: Diagramme de constellation reçue pour la sous-porteuse de meilleur SNR.

	Débit à 0km	Portée maximale	Débit à la portée maximale	[Débit × portée]
Monoporteuse OOK	13Gbps	20km	7Gbps	$140 Gbps * km$
OFDM (bande-passante = 6.25GHz)	21.5Gbps	50km	12.4Gbps	$620 Gbps * km$

TABLEAU D.4: Résumé des résultats des transmissions optiques utilisant le laser hybride III/V-sur-Silicium en configuration DBR multimode.

D.4.2 Démonstration Expérimentale de l'OFDM Adaptatif avec un Laser Hybride Monomode avec des Filtres en Anneaux Résonants

Dans le cadre des technologies WDM pour les réseaux d'accès optique futures, une des solutions possibles pour la voie montante est de placer un laser accordable chez l'abonné. Comparé à une solution centralisée, où le signal optique est envoyé par le *Central Office* et re-modulé chez l'abonné, l'avantage est d'avoir une puissance optique en sortie du *transceiver* plus élevé et de supprimer les réflexions parasites. Ceci rend l'implémentation du système plus simple et élimine la nécessité d'avoir un amplificateur optique chez l'utilisateur. Cependant, les sources laser accordables du commerce d'aujourd'hui sont relativement chères. En conséquence, elles ne peuvent pas être considérées pour cette application.

Dans ce contexte, plusieurs groupes d'études se sont engagés à l'étude des sources lasers accordables sur Silicium [38, 39]. En particulier, une gamme d'accordabilité de 45nm dans la bande C a été démontrée dans [39], avec un rapport de suppression de modes secondaires (*Side-mode Suppression Ratio* (SMSR)) plus grand que 40dB. Pour rappel, un débit de modulation de 10Gbps OOK avec une portée de 25km de fibre monomode a été atteint avec cette même structure [44], limité par la dispersion chromatique de la fibre. Dans cette thèse, la technique de transmission OFDM a été évaluée avec ce laser.

Architecture du laser hybride monomode avec des filtres en anneaux résonants

Le schéma de base de ce laser hybride III/V-sur-Silicium est montré dans la figure D.19. Le principe de la région actif est le même que le laser précédent. La différence est que des filtres en anneau résonants sont placés des deux côtés de la région active, avant les miroirs de Bragg. Des structures résistifs (*heaters*) sont placées au-dessus des anneaux. Lorsque un courant électrique est appliqué aux électrodes, l'indice de réfraction du silicium est varié à travers de l'effet thermo-optique. En conséquence, les longueurs d'onde de résonance des anneaux bougent. Lorsque les

longueurs d'onde de résonance des deux anneaux sont alignées, le signal optique les traverse et ils sont réfléchis par le miroir de Bragg.

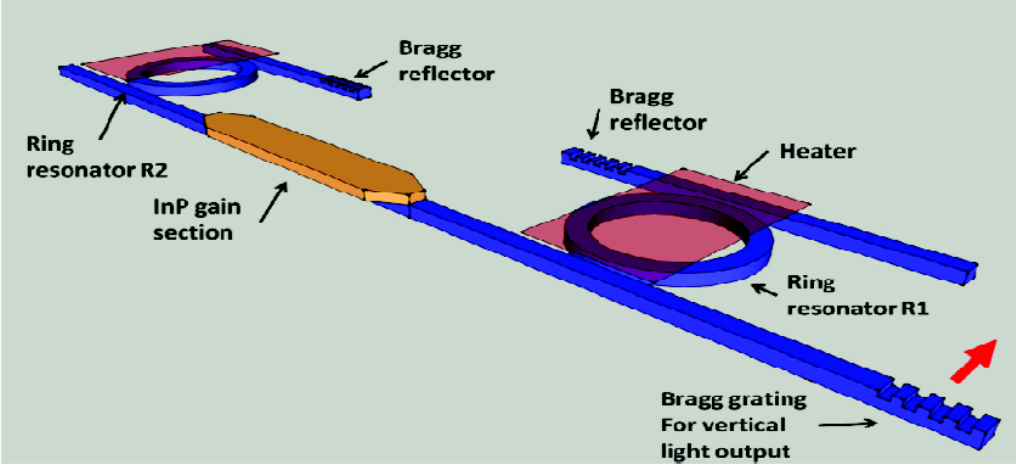

FIGURE D.19: Architecture du laser hybride III/V-sur-Silicium monomode avec des filtres en anneaux résonants. Source [39].

Caractérisation du laser hybride monomode avec des filtres en anneaux résonants

Tout d'abord, une caractérisation statique a été réalisée. Afin d'atteindre opération monomode, le courant de polarisation a été fixé à 100mA. Ensuite, les courants électriques dans chaque *heater* sont réglés de tel façon qu'un seul mode longitudinal soit émis. Le spectre d'émission typique est montré dans la figure D.20, avec une longueur d'onde d'émission à 1542nm. Le SMSR mesuré a été de 30dB, mais limité par l'équipement de mesure. La puissance optique couplée dans la fibre monomode (*Single-mode fiber* (SMF)) dans cette configuration est de -9dBm environ.

Il est important de comprendre comment la modulation rapide fonctionne dans ce laser. La figure D.21 montre la puissance optique dans la fibre monomode en fonction du courant optique injecté dans la région active. Il est possible de voir plusieurs sauts de modes. Ceci est une conséquence de l'augmentation de la température locale de la région active du laser. Les modes d'émission sont décalés et quittent la région de passe-bande des filtres en anneaux. Etant donné que le processus de chauffage de la cavité est de l'ordre de 1ms, une modulation rapide de >10kHz ne cause pas de sauts de modes parce que la cavité n'a pas le temps pour chauffer. La bande-passante de modulation directe de ce laser à 100mA est de 7.5GHz.

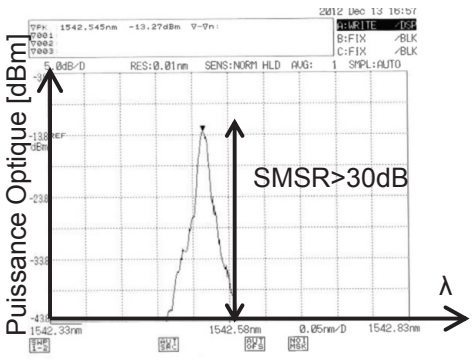

FIGURE D.20: Spectre d'émission du laser hybride monomode avec courant de bias de 100mA.

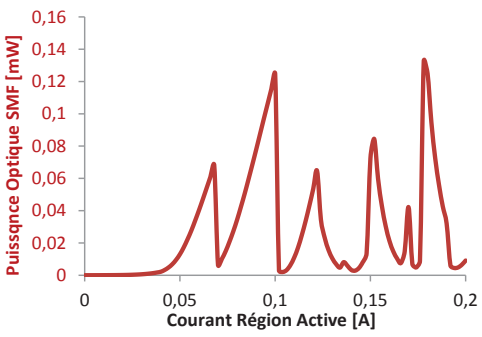

FIGURE D.21: Courbe de puissance optique couplée dans SMF versus courant électrique injecté dans la région active.

Résultats de la transmission OFDM avec le laser hybride monomode avec des filtres en anneaux résonants

Pour la transmission OFDM, la bande passante du signal électrique a été fixé à 4.5GHz. Notez que la bande passante est bien au-dessous de la bande passante de modulation directe du laser. Pour cette expérience, cette limitation vient plutôt du générateur de forme d'onde électrique. La profondeur de modulation est réglée à $2.5V_{pp}$.

En B2B optique (0km de fibre), un débit maximum de 11.5Gbps a été démontré. Le SNR et nombre de bits per sous-porteuse de la transmission en B2B est montré dans la figure D.22. Un SNR maximum de 16dB est atteint, supportant une modulation 16-QAM (4 bits per symbole). La constellation des symboles reçus pour cette modulation est montrée en figure D.23. L'efficacité spectrale est bien au-dessous de celle atteint par le laser hybride DBR précèdent. La non-linéarité du laser combiné avec la faible puissance optique couplé dans la fibre peuvent expliquer cette chute de performance.

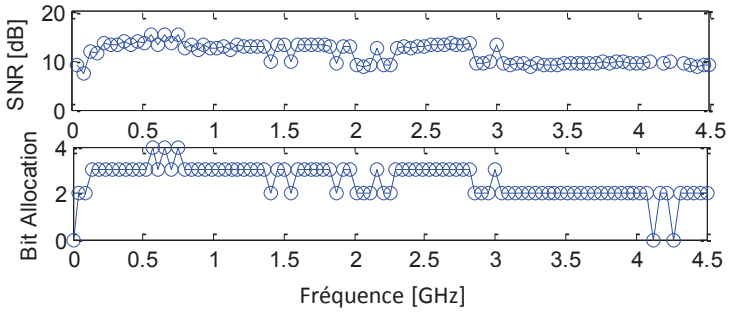

FIGURE D.22: SNR et nombre de bits par sous-porteuse de la transmission OFDM adaptatif en B2B optique avec le laser hybride monomode.

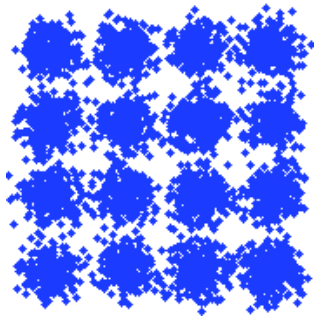

FIGURE D.23: Constellation 16-QAM reçue de la $12^{ème}$ sousporteuse.

Pour évaluer la performance de la transmission à travers de la fibre, un amplificateur optique a été placé en sortie du laser. La puissance optique lancée sur la fibre est d'environ 1dBm. Par contre, due au bruit de l'amplificateur, la portée est limitée à 20km de fibre avec un débit de 9.2Gbps. Dans ce cas, différemment de la transmission OOK reporté en [44], la portée a été limitée par la faible puissance optique en sortie du laser. Une amélioration des pertes dans la région active et de la structure de couplage dans la fibre permettra d'étendre la portée.

D.4.3 Démonstration Expérimentale de l'OFDM Adaptatif avec un Modulateur Silicium en Anneau Résonant

Dans les deux sections précédents, la technique de transmission OFDM a été évalué utilisant deux lasers hybrides modulé en directe à l'émission. Comme une alternative, des modulateurs externes peuvent être considérés. Malgré les pertes d'insertion plus importantes, ils introduisent en général moins de chirp en fréquence, ce qui améliore le produit [débit × porté] de la transmission. En 2013, la technique OFDM a été démontré compatible avec des modulateurs Mach-Zehnder sur silicium [182]. Cependant, le débit atteint a été limité par la faible bande-passante du dispositif ($< 5Gbps$). En particulier, des modulateurs en configuration anneaux résonants sont plus compacts et exigent une profondeur de modulation en tension plus petite comparée aux modulateurs MZM.

Pour la première fois, une démonstration expérimentale de la technique de modulation OFDM utilisant un modulateur en anneau sur silicium est réalisée. Dans la suite, l'architecture et caractérisation du dispositif ainsi que les résultats de simulation sont décrits.

Architecture du modulateur en anneau sur Silicium

Le modulateur silicium utilisé dans cette expérience est basé sur la déplétion de porteurs libres dans le guide d'onde silicium. Une jonction PN est intégrée dans le guide. En appliquant une tension inverse, les porteurs libres sont chassés du milieu du guide. Ceci conduit à une variation de l'indice de réfraction du guide, comme indiqué sur l'équation de Soref (équation (D.1) et (D.2)). En conséquence, la longueur d'onde de résonance est décalée.

La section transversale du modulateur est montrée dans la figure D.24(a). Le guide d'onde en configuration arête a une largeur de 400nm, une hauteur totale de 220nm, avec une profondeur de gravure de 120nm. Ces dimensions assure opération monomode en mode TE. La jonction est décalée de 100nm par rapport au centre du guide, pour maximiser l'efficacité de modulation. La valeur cible de dopage pour le P et N est de $5 \times 10^{-17} cm^{-3}$. Afin de réduire la résistance d'accès, le guide est remonté des deux côtés de la structure, à une distance de $2\mu m$ du guide d'onde. Une image microscopique du dispositif est montrée dans la figure D.24(b). L'anneau a un diamètre de $200\mu m$ et un écart de 150nm entre le guide d'entrée et l'anneau.

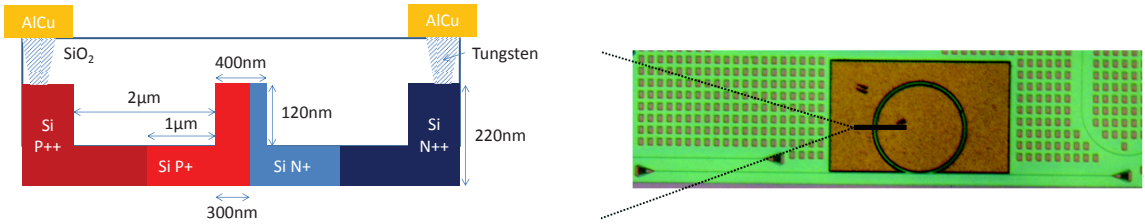

(a) Section transversale.

(b) Image microscopique.

FIGURE D.24: Structure du modulateur anneau sur silicium utilisé pour la transmission OFDM.

Caractérisation du modulateur en anneau sur Silicium

La figure D.25 donne la réponse spectrale de l'anneau pour plusieurs valeurs de tension appliquées. Nous pouvons observer le décalage de la longueur d'onde en fonction de la tension appliqué. La longueur d'onde d'opération λ_{opt} est fixée à 1548nm environ, comme indiqué sur la figure. De cette façon, la puissance optique en sortie du modulateur varie avec la tension appliquée, comme indiqué sur la figure D.26.

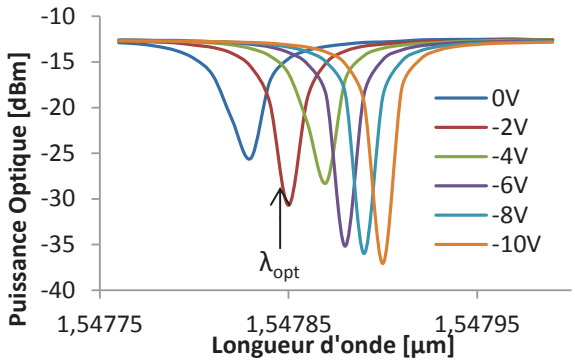

FIGURE D.25: Réponse spectrale du modulateur en anneau.

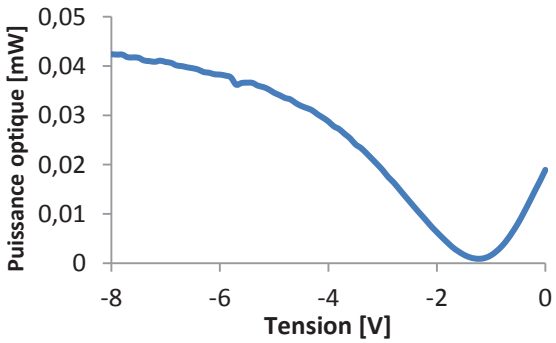

FIGURE D.26: Puissance optique vs tension à λ_{opt} du modulateur en anneau.

La tension de bias de -2.5V a été choisie pour maximiser le gain et au même temps minimiser les non-linéarités. La bande passante de modulation de l'anneau à ce point est de 3.4GHz. Il y a deux facteurs qui contribuent pour cette limitation 1) la capacité parasite de la jonction

ainsi que la résistance de la voie d'accès et 2) le temps de vie des photons dans la cavité. Une optimisation dans le design de la structure permettra d'améliorer la bande passante.

Résultats de la transmission OFDM avec le modulateur en anneau sur Silicium

Etant donné la bande passante de modulation de l'anneau de 3.4GHz, une modulation OOK serait limité à 5Gbps environ. La technique de transmission OFDM adaptatif est implémentée pour améliorer le débit.

La bande passante du signal OFDM est fixé à 4GHz. La profondeur de modulation est fixée à $1.6V_{pp}$, plus petite que celle des lasers hybrides modulés en directe. En B2B optique, la puissance optique maximale reçu est de -7dBm. Le débit atteint est de 16.8Gbps, qui résulte dans une efficacité spectrale de plus de 4bps/Hz. Le SNR maximum est d'environ 22dB, ce qui rend possible la transmission d'une modulation 64-QAM. En raison de la très faible puissance optique en sortie de modulateur, la portée a été limitée à 20km SMF, avec un débit atteint de 11.7Gbps. Dans tous le cas, le BER total est au-dessous du BER cible de 2.2×10^{-3}. Les résultats de la transmission (SNR et nombre de bits par sous-porteuse) pour les deux cas (0km et 20km), ainsi que la constellation de la sous-porteuse de meilleure SNR sont donnés en figure D.27.

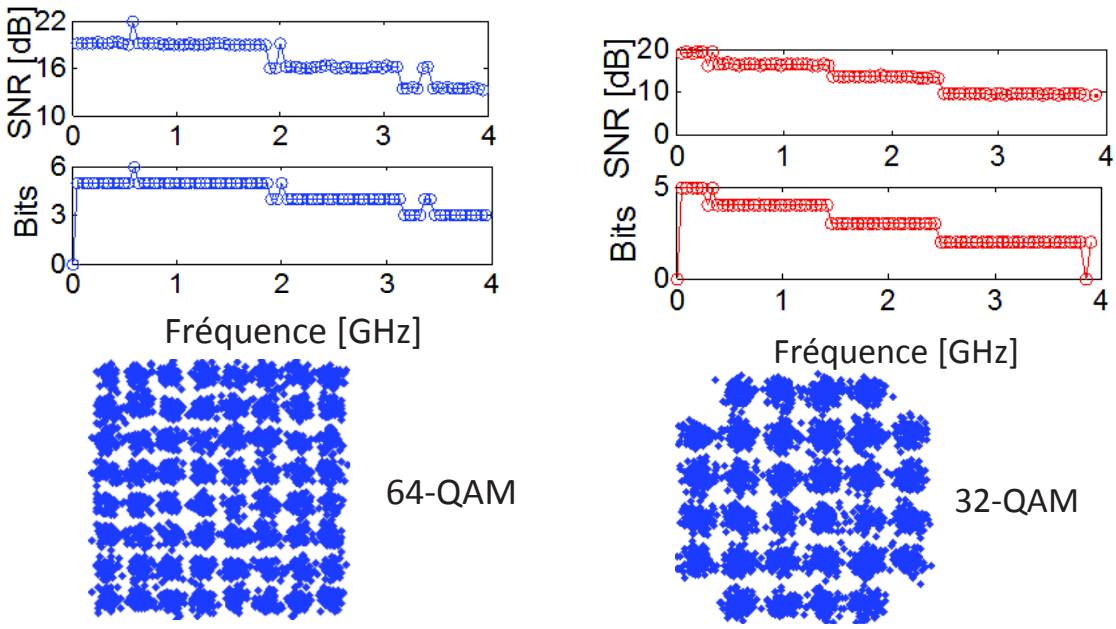

(a) B2B optique.

(b) 20km.

FIGURE D.27: SNR et nombre de bits par sous-porteuse (en dessus), constellation reçue de la sous-porteuse de meilleur SNR (au-dessous) de la transmission OFDM adaptatif avec le modulateur en anneau sur Silicium (a) en B2B optique et (b) 20km SMF.

D.4.4 Principaux résultats de simulation

Le comportement de la région active d'un modulateur Silicum en déplétion de porteurs (jonction PN) a été modélisé. Ce modèle, qui prend en compte la variation de l'indice effectif et d'absorption en fonction de la tension appliquée, a été validé expérimentalement utilisant deux dispositifs disponibles. Ensuite, ce modèle a été appliqué dans deux structures interférométriques bien connus - Mach-Zehnder et anneau résonant - pour construire le modèle complet du modulateur silicium. Le modèle MZM est statique, alors que celui de l'anneau prend en compte

le temps de vie de photons dans la cavité. Le modèle dynamique est régi par les équations décris dans [204].

Les modèles sont intégrés dans la plateforme de simulation en utilisant des blocs Matlab, afin d'évaluer un lien complet OFDM optique. Pour cette évaluation, un signal OFDM 10Gbps avec le da modulation 16-QAM dans toutes les sous-porteuses (2.5GHz de bande passante) est définit. Plusieurs comparaisons entre les deux modulateurs en silicium ainsi que le modulateur classique $LiNbO_3$ ont été réalisées. La performance de transmission sur la fibre monomode jusqu'à 100km a été évalué. Les principaux résultats sont les suivants :

- Le modulateur Mach-Zehnder en silicium a atteint une sensibilité (puissance optique requise pour atteindre le BER cible de 2.2×10^{-3}) 3dB inférieur à celle du MZM en $LiNbO_3$. Ceci est attribué à la réponse non-linéaire de la jonction avec la tension appliqué.
- La sensibilité entre le modulateur en anneau et le MZM en silicium a été très similaire. Ce résultat est très représentatif parce que cela montre que la non-linéarité de la jonction est dominante sur la non-linéarité de la réponse abrupte de l'anneau résonant. La sensibilité peut être améliorée en optimisant le design de la jonction.
- Dans les deux cas de modulateurs en silicium, de la modulation optique avec du chirp négatif a été atteint. En conséquence, la sensibilité avec le la fibre optique a été amélioré jusqu'à 1dB à 100km de fibre, comme montré dans la figure D.28 pour le MZM en silicium.

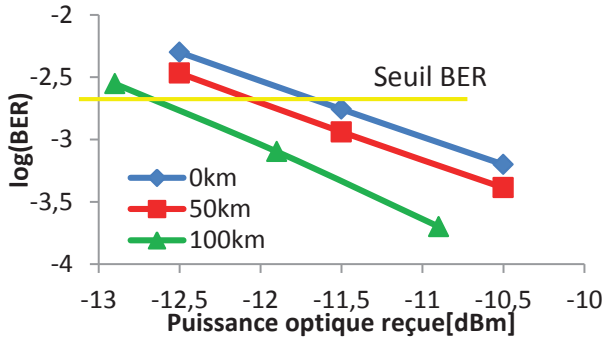

FIGURE D.28: BER simulé en fonction de la puissance optique reçue pour le MZM en silicium, pour plusieurs longueurs de fibre.

D.5 Conclusions et Perspectives

Les travaux décrits dans cette thèse couvrent l'étude théorique, simulation et implémentation expérimentale d'un lien OFDM optique avec des émetteurs Photonique sur Silicium. L'utilisation de cette technique de transmission peut fournir la performance requise pour les prochaines générations des réseaux d'accès optique. En plus, en étant compatible avec le procédé de fabrication CMOS, des solutions bas-coût par unité sont désormais possibles.

Dans l'ensemble des démonstrations expérimentales reportées dans cette thèse, les exigences des prochaines générations des réseaux d'accès optique sont remplis en termes de débit / portée. Cependant, à cause de la faible puissance optique en sortie de ces composants, le budget optique est encore faible pour répondre à ces besoins. Des optimisations dans le dispositif de couplage et/ou l'utilisation des amplificateurs optiques peuvent améliorer le budget optique. Nous avons démontré en effet des liens point-à-point, mais la bande passante disponible peut effectivement être partagée en fréquence / temps. Ces composants donnent aussi la possibilité d'employer des techniques WDM pour augmenter la capacité du réseau.

La conclusion générale de ce travail est que les émetteurs photoniques sur silicium permettent la transmission OFDM de manière efficace. Le tableau D.5 donne l'efficacité spectrale

atteint avec les émetteurs photoniques sur silicium en comparaison avec des émetteurs commerciaux à large-bande. L'efficacité des dispositifs photoniques sur silicium est un peu plus faible, principalement due à la limitation en bande passante de ces composants. Pour finaliser, la plateforme de simulation développée est laissée comme un héritage pour les travaux futurs dans ce domaine.

	Photonique Silicium	Commercial
Laser modulé en directe	3.4bps/Hz (DBR)	4bps/Hz (DFB)
Modulateur externe	4.2bps/Hz (Anneau)	4.5bps/Hz (MZM)

Tableau D.5: Comparaison des efficacités spectrales des émetteurs photoniques sur silicium et commerciaux.

Bibliographie

[1] Intel. (2013) What happens in an internet minute ? [Online]. Available : http://www.intel.com/content/www/us/en/communications/internet-minute-infographic.html

[2] ITU-T. (2012) Global FTTH/B subscribers reach 67 million at mid-2011. [Online]. Available : http://www.itu.int/ITU-D/ict/newslog/Global+FTTHB+Subscribers+Reach+67+Mln+At+Mid2011.aspx

[3] Roland Montagne, "FTTx Markets : Global perspective," in *FTTH Forum*, 2011.

[4] "The Zettabyte Era - Trends and Analysis," Cisco, White Paper, 2013.

[5] Martin Schell, "Optical Integration : Technology and Economics," in *ECOC 2012 - Market Focus*. Fraunhofer Heinrich Hertz Institute, 2012.

[6] M. Kawahata, "Hi-ovis (higashi ikoma optical visual information system) development project," in *Two-Way Cable Television*. Springer, 1977, pp. 135–142.

[7] C.-H. Yeh and S. Chi, "Self-healing ring-based time-sharing passive optical networks," *IEEE Photon. Technol. Lett.*, vol. 19, no. 15, pp. 1139–1141, 2007.

[8] C. H. Yeh, C. W. Chow, S. P. Huang, J. Y. Sung *et al.*, "Ring-Based WDM Access Network Providing Both Rayleigh Backscattering Noise Mitigation and Fiber-Fault Protection," *J. Lightw. Technol.*, vol. 30, no. 20, pp. 3211–3218, October 2012.

[9] *Recommandation ITU-T G.993.2 : Very high speed digital subscriber line transceivers 2 (VDSL2)*, ITU-T Std., 2011. [Online]. Available : https://www.itu.int/rec/T-REC-G.993.2/en

[10] P. W. Shumate, "Fiber-to-the-Home : 1977–2007," *J. Lightw. Technol.*, vol. 26, no. 9, pp. 1093–1103, 2008.

[11] L. Hutcheson, "FTTx : Current status and the future," *Communications Magazine, IEEE*, vol. 46, no. 7, pp. 90–95, 2008.

[12] Elaine Wong, "Next-Generation Broadband Access Networks and Technologies," *J. Lightw. Technol.*, vol. 30, no. 4, pp. 597–608, February 2012.

[13] *Recommandation ITU–T 983.1 : Broadband optical access systems based on Passive Optical Networks (PON)*, ITU-T Std., 2005. [Online]. Available : https://www.itu.int/rec/T-REC-G.983.1/en

[14] *Recommandations ITU-T G.984.1 : Gigabit-capable passive optical networks (GPON) : General characteristics*, ITU-T Std., 2008. [Online]. Available : https://www.itu.int/rec/T-REC-G.984.1/en

[15] "Next-generation PON and the future of fiber," Alcatel-Lucent Bell-Labs, White Paper, 2010.

[16] Frank Effenberger, "The XG-PON System : Cost Effective 10 Gb/s Access," *J. Lightw. Technol.*, vol. 29, no. 4, pp. 403–409, February 2011.

[17] *Recommandation ITU-T G.987.1 10-Gigabit-capable passive optical networks (XG-PON) : General Requirements*, ITU-T Std., 2010.

[18] Shweta Jain, Frank Effenberger, Andrea Szabo, Zhishan Feng *et al.*, "World's First XG-PON Field Trial," *Optical Fiber Communication Conference (OFC)*, 2010.

[19] D. van Veen, D. Suvakovic, M. F. Lau, H. Krimmel *et al.*, "Demonstration of a symmetrical 10/10 Gbit/s XG-PON2 system," in *Optical Fiber Communication Conference (OFC)*, 2011.

[20] Philippe Chanclou, Anna Cui, Frank Geilhardt, Hirotaka Nakamura *et al.*, "Network operator requirements for the next generation of optical access networks," *IEEE Netw.*, vol. 26, no. 2, pp. 8–14, 2012.

[21] *802.3ah-2004 - IEEE Standard for Information technology - Local and metropolitan area networks*, IEEE Std., 2004. [Online]. Available : http://standards.ieee.org/findstds/standard/802.3ah-2004.html

[22] *802.3av-2009 - IEEE Standard for Information technology– Local and metropolitan area networks– Specific requirements*, IEEE Std., 2009. [Online]. Available : http://standards.ieee.org/findstds/standard/802.3av-2009.html

[23] K. Tanaka, A. Agata, and Y. Horiuchi, "IEEE 802.3av 10G-EPON Standardization and Its Research and Development Status," *J. Lightw. Technol.*, vol. 28, no. 4, pp. 651–661, 2010.

[24] *Recommandation ITU-T G.987.4 10 Gigabit-capable passive optical networks (XG-PON) : Reach extension*, ITU-T Std., 2012.

[25] Duarte Begonha, Michael Gryseels, Sergio Sandoval, and Wim Torfs, "Creating a Fiber Future," McKinsey&Company, White Paper, 2010.

[26] R. P. Davey, D. B. Grossman, M. Rasztovits Wiech, D. B. Payne *et al.*, "Long-Reach Passive Optical Networks," *J. Lightw. Technol.*, vol. 27, no. 3, pp. 273–291, February 2009.

[27] P. Vetter, "Next generation optical access technologies," *European Conference on Optical Comunications (ECOC) 2012*, pp. 1–5, 2012.

[28] F. Effenberger, "XG-PON1 versus NG-PON2 : which one will win ?" in *European Conference on Optical Communication (ECOC)*, 2012.

[29] Yuanqiu Luo, Xiaoping Zhou, Frank Effenberger, Xuejin Yan *et al.*, "Time- and Wavelength-Division Multiplexed Passive Optical Network (TWDM-PON) for Next-Generation PON Stage 2 (NG-PON2)," *J. Lightw. Technol.*, vol. 31, no. 4, pp. 587–593, 2013.

[30] R. Urata, C. Lam, H. Liu, and C. Johnson, "High performance, low cost, colorless ONU for WDM-PON," in *Optical Fiber Communication Conference and Exposition (OFC/NFOEC), 2012 and the National Fiber Optic Engineers Conference.* IEEE, 2012, pp. 1–3.

[31] K. Prince, T. B. Gibbon, R. Rodes, E. Hviid *et al.*, "GigaWaM - Next-generation WDM-PON enabling gigabit per-user data bandwidth," *J. Lightw. Technol.*, vol. 30, no. 10, pp. 1444–1454, 2012.

[32] C.-H. Lee, S.-M. Lee, K.-M. Choi, J.-H. Moon *et al.*, "WDM-PON experiences in Korea [Invited]," *Journal of Optical Networking*, vol. 6, no. 5, pp. 451–464, 2007.

[33] C.-H. Lee, S.-G. Mun, and J.-H. Moon, "WDM-PON Overview," *European Conference on Optical Comunications (ECOC)*, 2009.

[34] J. Zhang and N. Ansari, "Design of WDM PON with tunable lasers : The upstream scenario," *J. Lightw. Technol.*, vol. 28, no. 2, pp. 228–236, 2010.

[35] Peter Ossieur, Cleitus Antony, Alan Naughton, Aisling M. Clarke *et al.*, "Demonstration of a 32 x 512 Split, 100 km Reach, 2 x 32 x 10 Gb/s Hybrid DWDM-TDMA PON Using Tunable External Cavity Lasers in the ONUs," *J. Lightw. Technol.*, vol. 29, no. 24, pp. 3705–3718, December 2011.

[36] N. Fujioka, Tao Chu, and M. Ishizaka, "Compact and Low Power Consumption Hybrid Integrated Wavelength Tunable Laser Module Using Silicon Waveguide Resonators," *J. Lightw. Technol.*, vol. 28, no. 21, pp. 3115–3120, November 2010.

[37] T. Chu, N. Fujioka, and M. Ishizaka, "Compact, lower-power-consumption wavelength tunable laser fabricated with silicon photonic-wire waveguide micro-ring resonators," *Opt. Express*, vol. 17, no. 16, pp. 14 063–14 068, 2009.

[38] Shahram Keyvaninia, Gunther Roelkens, Dries Van Thourhout, Christophe Jany *et al.*, "Demonstration of a heterogeneously integrated III-V/SOI single wavelength tunable laser," *Opt. Express*, vol. 21, no. 3, pp. 3784–3792, February 2013.

[39] A. Le Liepvre, C. Jany, A.Accard, M. Lamponi *et al.*, "Widely wavelength tunable hybrid III-V/silicon laser with 45 nm tuning range fabricated using a wafer bonding technique," *Group Four Photonics Conference (GFP)*, pp. 54–56, 2012.

[40] J. Hulme, J. Doylend, and J. Bowers, "Widely tunable Vernier ring laser on hybrid silicon," *Opt. Express*, vol. 21, no. 17, pp. 19 718–19 722, 2013.

[41] E. Marchena, T. Creazzo, S. B. Krasulick, P. Yu *et al.*, "Integrated Tunable CMOS Laser for Si Photonics," in *Optical Fiber Communication Conference (OFC)*, 2013.

[42] B. R. Koch, E. J. Norberg, B. Kim, J. Hutchinson *et al.*, "Integrated Silicon Photonic Laser Sources for Telecom and Datacom," in *Optical Fiber Communication Conference (OFC)*, 2013.

[43] T. Segawa, S. Matsuo, T. Kakitsuka, T. Sato *et al.*, "Semiconductor double-ring-resonator-coupled tunable laser for wavelength routing," *Quantum Electronics, IEEE Journal of*, vol. 45, no. 7, pp. 892–899, 2009.

[44] G. de Valicourt, A. Le liepvre, F. Vacondio, C. Simonneau *et al.*, "Directly modulated and fully tunable hybrid silicon lasers for future generation of coherent colorless ONU," *Opt. Express*, vol. 20, no. 26, pp. B552–B557, 2012.

[45] A. Borghesani, "Reflective based active semiconductor components for next generation optical access networks," in *European Conference on Optical Communication (ECOC)*, vol. 1, 2010, pp. 9–11.

[46] P. Healey, P. Townsend, C. Ford, L. Johnston *et al.*, "Reflective SOAs for spectrally sliced WDM-PONs," in *Optical Fiber Communication Conference and Exhibit (OFC)*. IEEE, 2002, pp. 352–353.

[47] H. D. Kim, S.-G. Kang, and C.-H. Le, "A low-cost WDM source with an ASE injected Fabry-Perot semiconductor laser," *IEEE Photon. Technol. Lett.*, vol. 12, no. 8, pp. 1067–1069, 2000.

[48] P. Chanclou, F. Payoux, T. Soret, N. Genay *et al.*, "Demonstration of RSOA-based remote modulation at 2.5 and 5 Gbit/s for WDM PON," in *Optical Fiber Communication Conference (OFC)*, 2007.

[49] M. Omella, I. Papagiannakis, B. Schrenk, D. Klonidis *et al.*, "10 Gb/s full-duplex bidirectional transmission with RSOA-based ONU using detuned optical filtering and decision feedback equalization," *Opt. express*, vol. 17, no. 7, pp. 5008–5013, 2009.

[50] K. Y. Cho, U. H. Hong, Y. Takushima, A. Agata *et al.*, "103-Gb/s long-reach WDM PON implemented by using directly modulated RSOAs," *IEEE Photon. Technol. Lett.*, vol. 24, no. 3, pp. 209–211, 2012.

[51] M. Presi, A. Chiuchiarelli, R. Corsini, P. Choudhury *et al.*, "Enhanced 10-gb/s operation of bandwidth-limited R-SOAs without electronic equalization," in *European Conference and Exhibition on Optical Communication (ECOC)*, 2012.

[52] D. Smith, I. Lealman, X. Chen, D. Moodie *et al.*, "Colourless 10Gb/s reflective SOA-EAM with low polarization sensitivity for long-reach DWDM-PON networks," in *European Conference on Optical Communications (ECOC)*, 2009, pp. 1–2.

[53] Q. Guo and A. V. Tran, "Demonstration of 40-Gb/s WDM-PON system using SOA-REAM and equalization," *IEEE Photon. Technol. Lett.*, vol. 24, no. 11, pp. 951–953, 2012.

[54] J. Wei, A. Hamié, R. Gidding, E. Hugues Salas *et al.*, "Adaptively modulated optical OFDM modems utilizing RSOAs as intensity modulators in IMDD SMF transmission systems," *Opt. Express*, vol. 18, no. 8, pp. 8556–8573, 2010.

[55] T. Duong, N. Genay, P. Chanclou, B. Charbonnier *et al.*, "Experimental demonstration of 10 Gbit/s upstream transmission by remote modulation of 1 GHz RSOA using adaptively modulated optical OFDM for WDM-PON single fiber architecture," in *European Conference on Optical Communication (ECOC)*, 2008, pp. 1–2.

[56] R. P. Giddings, E. Hugues Salas, X. Q. Jin, J. L. Wei *et al.*, "Experimental Demonstration of Real-Time Optical OFDM Transmission at 7.5 Gb/s Over 25-km SSMF Using a 1-GHz RSOA," *IEEE Photon. Technol. Lett.*, vol. 22, no. 11, pp. 745–747, June 2010.

[57] C. H. Yeh, C. W. Whow, Y. F. Wu, and H. Y. Chen, "Demonstrations of 10 and 40 Gbps upstream transmission using 1.2GHz RSOA-based ONU in long-reach access networks," *Optical Fiber Technology*, vol. 18, no. 2, pp. 63–67, March 2012.

[58] Tian Dong, Yuan Bao, Yu Ji, Alan Pak Tao Lau *et al.*, "Bidirectional Hybrid OFDM-WDM-PON System for 40-Gb/s Downlink and 10-Gb/s Uplink Transmission Using RSOA Remodulation," *IEEE Photon. Technol. Lett.*, vol. 24, no. 22, pp. 2024–2026, November 2012.

[59] Z. Xu, Y.-K. Yeo, X. Cheng, and E. Kurniawan, "20-Gb/s injection locked FP-LD in a wavelength-division-multiplexing OFDM-PON," in *Optical Fiber Communication Conference (OFC)*, 2012, pp. 1–3.

[60] M.-C. Cheng, Y.-C. Li, S.-Y. Lin, Y.-C. Chi *et al.*, "Directly modulating a long weak-resonant-cavity laser diode at limited bandwidth of 5 GHz with pre-leveled 16-QAM OFDM transmission at 20 Gbit/s," in *Optical Fiber Communication Conference (OFC)*, 2013.

[61] C.-H. Yeh, C.-W. Chow, Y.-F. Wu, S.-P. Huang *et al.*, "Performance of Long-Reach Passive Access Networks Using Injection-Locked Fabry–Perot Laser Diodes With Finite Front-Facet Reflectivities," *J. Lightw. Technol.*, vol. 31, no. 12, pp. 1929–1934, 2013.

[62] Q. W. Zhang, E. Hugues Salas, R. P. Giddings, M. Wang *et al.*, "Experimental demonstrations of record high REAM intensity modulator-enabled 19.25Gb/s real-time end-to-end dual-band optical OFDM colorless transmissions over 25km SSMF IMDD systems," *Opt. Express*, vol. 21, no. 7, pp. 9167–9179, April 2013.

[63] J. Xu, L.-K. Chen, and C.-K. Chan, "Phase-modulation-based loopback scheme for Rayleigh noise suppression in 10-Gb/s carrier-distributed WDM-PONs," *IEEE Photon. Technol. Lett.*, vol. 22, no. 18, pp. 1343–1345, 2010.

[64] J. Xu, M. Li, and L.-K. Chen, "Rayleigh noise reduction in 10-Gb/s carrier-distributed WDM-PONs using in-band optical filtering," *J. Lightw. Technol.*, vol. 29, no. 24, pp. 3632–3639, 2011.

[65] L. Banchi, R. Corsini, M. Presi, F. Cavaliere *et al.*, "Enhanced reflection tolerance in WDM-PON by chirped RZ modulation," *Electronics letters*, vol. 46, no. 14, pp. 1009–1011, 2010.

[66] S. Straullu, F. Forghieri, V. Ferrero, and R. Gaudino, "Optimization of self-coherent reflective PON to achieve a new record 42 dB ODN power budget after 100 km at 1.25 Gbps," *Opt. Express*, vol. 20, no. 28, pp. 29 590–29 598, 2012.

[67] S. Bidnyk, M. Pearson, A. Balakrishnan, M. Gao *et al.*, "Silicon-on-insulator platform for building fiber-to-the-home transceivers," in *Optical Fiber Communication Conference (OFC)*, 2007.

[68] K. Wada, S. Park, and Y. Ishikawa, "Si photonics and fiber to the home," *Proceedings of the IEEE*, vol. 97, no. 7, pp. 1329–1336, 2009.

[69] J. Zhang, T.-Y. Liow, G.-Q. Lo, and D.-L. Kwong, "10Gbps monolithic silicon FTTH transceiver without laser diode for a new PON configuration," *Opt. Express*, vol. 18, no. 5, pp. 5135–5141, 2010.

[70] Lin Xu, K. Padmaraju, Long Chen, M. Lipson *et al.*, "10-Gb/s Access Network Architecture Based on Micro-Ring Modulators With Colorless ONU and Mitigated Rayleigh Backscattering," *IEEE Photon. Technol. Lett.*, vol. 23, no. 13, pp. 914–916, July 2011.

[71] Lin Xu, Qi Li, N. Ophir, K. Padmaraju *et al.*, "Colorless Optical Network Unit Based on Silicon Photonic Components for WDM PON," *IEEE Photon. Technol. Lett.*, vol. 24, no. 16, pp. 1372–1374, August 2012.

[72] W. A. Zortman, A. L. Lentine, D. C. Trotter, and M. R. Watts, "Long-Distance Demonstration and Modeling of Low-Power Silicon Microdisk Modulators," *IEEE Photon. Technol. Lett.*, vol. 23, no. 12, pp. 819–821, June 2011.

[73] Kazuhiro Goi, Kenji Oda, Hiroyuki Kusaka, Yoshihiro Terada *et al.*, "11-Gbps 80-km Transmission Performance of Zero-Chirp Silicon Mach-Zehnder Modulator," *European Conference on Optical Comunications (ECOC)*, 2012.

[74] Aleksandr Biberman, Sasikanth Manipatruni, Noam Ophir, Long Chen *et al.*, "First demonstration of long-haul transmission using silicon microring modulators," *Opt. Express*, vol. 18, no. 15, pp. 15 544–15 552, July 2010.

[75] Huaxiang Yi, Qifeng Long, Wei Tan, Li Li *et al.*, "Demonstration of low power penalty of silicon MachŰZehnder modulator in long-haul transmission," *Opt. Express*, vol. 20, no. 25, pp. 27 562–27 568, December 2012.

[76] S. Cheung, L. Chan, C. Chan, D. Tong *et al.*, "Demonstration of an ONU for WDM access network with downstream BPSK and upstream remodulated OOK data using injection-locked FP laser," in *European Conference on Optical Communication (ECOC)*, vol. 3, 2001, pp. 358–359.

[77] M. Presi, R. Proietti, K. Prince, G. Contestabile *et al.*, "A 80 km reach fully passive WDM-PON based on reflective ONUs," *Opt. Express*, vol. 16, no. 23, pp. 19 043–19 048, 2008.

[78] S. Jang, B. W. Kim, C.-S. Lee, E.-S. Jung *et al.*, "A bidirectional RSOA based WDM-PON utilizing a SCM signal for down-link and a baseband signal for up-link," in *Optical Fiber Communication Conference (OFC)*, 2007.

[79] Ming-Fang Huang, Jianjun Yu, Dayou Qian, N. Cvijetic *et al.*, "Lightwave centralized WDM-OFDM-PON network employing cost-effective directly modulated laser," *Optical Fiber Communication Conference (OFC)*, pp. 1–3, 2009.

[80] S.-J. Park, Y.-B. Choi, S. P. Jung, K. Y. Cho *et al.*, "Hybrid WDM/TDMA-PON using self-homodyne and differential coding," *IEEE Photon. Technol. Lett.*, vol. 21, no. 7, pp. 465–467, 2009.

[81] K. Cho, K. Tanaka, T. Sano, S. Jung *et al.*, "Long-reach coherent WDM PON employing self-polarization-stabilization technique," *J. Lightw. Technol.*, vol. 29, no. 4, pp. 456–462, 2011.

[82] B. Charbonnier, A. Lebreton, S. Straullu, V. Ferrero *et al.*, "Self-coherent single wavelength SC-FDMA PON uplink for NG-PON2," *Optical Fiber Communication Conference (OFC)*, pp. 1–3, 2012.

[83] S. P. Jung, Y. Takushima, K. Y. Cho, S. J. Park *et al.*, "Demonstration of RSOA-based WDM PON employing self-homodyne receiver with high reflection tolerance," in *Optical Fiber Communication Conference (OFC)*, 2009.

[84] K. Cho, U. Hong, S. Jung, Y. Takushima *et al.*, "Long-reach 10-Gb/s RSOA-based WDM PON employing QPSK signal and coherent receiver," *Opt. Exp*, vol. 20, no. 14, p. 15, 2012.

[85] H. Shim, K. Cho, U. Hong, Y. Chung *et al.*, "Transmission of 40-Gb/s QPSK upstream signal in RSOA-based coherent WDM PON using offset PDM technique," *Optics express*, vol. 21, no. 3, pp. 3721–3725, 2013.

[86] R. Gaudino, "Advantages of Coherent Detection in Reflective PONs," *Optical Fiber Communication Conference (OFC)*, 2013.

[87] Ed Harstead, Dora van Veen, and Peter Vetter, "Technologies for NGPON2 : Why I think 40G TDM PON (XLG-PON) is the clear winner," Alcatel-Lucent, White Paper, 2012.

[88] E. Harstead and R. Sharpe, "Future fiber-to-the-home bandwidth demands favor time division multiplexing passive optical networks," *Communications Magazine, IEEE*, vol. 50, no. 11, pp. 218–223, 2012.

[89] D. van Veen, V. E. Houtsma, P. Winzer, and P. Vetter, "26-Gbps PON Transmission over 40-km using Duobinary Detection with a Low Cost 7-GHz APD-Based Receiver," in *European Conference and Exhibition on Optical Communication (ECOC)*, 2012.

[90] K. Kechaou, T. Anfray, K. Merghem, C. Aupetit Berthelemot *et al.*, "NRZ Transmission Range Record at 40-Gb/s in Standard Fiber Using a Dual Electro-absorption Modulated Laser," in *European Conference and Exhibition on Optical Communication (ECOC)*, 2012.

[91] R. Gaudino, V. Curri, R. Cigliutti, and G. Bosco, "Coherent PON for NG-PON2 : 40Gbps Downstream Transmission with 40dB Power Margin using Commercial DFB Lasers and no Optical Amplification," *International Conference on Microelectronics, Optoelectronics, and Nanoelectronics*, 2011.

[92] X. Meng, Y. Liu, Y. Shi, X. Chen *et al.*, "112 Gbit/s long-reach real-time coherent passive optical network downlink transmission experiment based on polarization multiplexing quadrature phase shift keying format," *Optical Engineering*, vol. 51, no. 4, pp. 040 505–1, 2012.

[93] N. Sotiropoulos, T. Koonen, and H. de Waardt, "Advanced Differential Modulation Formats for Optical Access Networks," *J. Lightw. Technol.*, vol. 31, no. 17, pp. 2829–2843, 2013.

[94] L. A. Neto, A. Gharba, P. Chanclou, N. Genay *et al.*, "High bit rate burst mode optical OFDM for next generation passive optical networks," *European Conference on Optical Comunications (ECOC)*, pp. 1–3, 2010.

[95] H. Yang, J. Li, B. Lin, Y. Wan *et al.*, "DSP-Based Evolution From Conventional TDM-PON to TDM-OFDM-PON," *J. Lightw. Technol.*, vol. 31, no. 16, pp. 2735–2741, 2013.

[96] C. Wanga, , F. Shiha, C. Yehb *et al.*, "10 Gb/s TDM passive optical networks using four wavelengths multiplexed channels," *Optics Communications*, vol. 282, pp. 2476–2479, 2009.

[97] C.-H. Yeh, C.-W. Chow, C.-H. Wang, Y.-F. Wu *et al.*, "Using OOK Modulation for Symmetric 40-Gb/s Long-Reach Time-Sharing Passive Optical Networks," *IEEE Photon. Technol. Lett.*, vol. 22, no. 9, pp. 619–621, 2010.

[98] B. Charbonnier, N. Brochier, and P. Chanclou, "Reflective polarisation independent Mach-Zenhder modulator for FDMA/OFDMA PON," *Electronics Letters*, vol. 46, no. 25, pp. 1682–1683, 2010.

[99] FAON project website. [Online]. Available : http://www.anr-faon.fr/introduction.php

[100] FABULOUS project website. [Online]. Available : http://www.fabulous-project.eu/

[101] B. Charbonnier, S. Menezo, P. O'Brien, A. Lebreton *et al.*, "Silicon photonics for next generation FDM/FDMA PON," *IEEE/OSA Journal of Optical Communications and Networking*, vol. 4, no. 9, September 2012.

[102] A. Lebreton and B. Charbonnier, "Towards 40Gbps downstream FDM PON." in *International Conference on Optical Networking Design and Modeling (ONDM)*, 2013, pp. 304–308.

[103] Aurélien Lebreton, Benoît Charbonnier, Giovanni Beninca de Farias, Philippe Chanclou *et al.*, "Low Complexity FDM/FDMA Approach for Future PON," *Optical Fiber Communication Conference (OFC)*, 2013.

[104] S. Menezo, B. Charbonnier, G. Benica De Farias, D. Thomson *et al.*, "Reflective Silicon Mach Zehnder Modulator With Faraday Rotator Mirror effect for self-coherent transmission," in *Optical Fiber Communication Conference (OFC)*, 2013.

[105] D. Taillaert, H. Chong, P. I. Borel, L. H. Frandsen *et al.*, "A compact two-dimensional grating coupler used as a polarization splitter," *IEEE Photon. Technol. Lett.*, vol. 15, no. 9, pp. 1249–1251, 2003.

[106] S. Keyvaninia, G. Roelkens, D. Van Thourhout, G. Duan *et al.*, "A highly efficient electrically pumped optical amplifier integrated on a SOI waveguide circuit," in *Group IV Photonics Conference (GFP)*, 2012, pp. 222–224.

[107] Laurent Vivien, Andreas Polzer, Delphine Marris Morini, Johann Osmond *et al.*, "Zero-bias 40Gbit/s germanium waveguide photodetector on silicon," *Opt. Express*, vol. 20, no. 2, pp. 1096–1101, January 2012.

[108] D. F. Logan, P. Velha, M. Sorel, R. M. De La Rue *et al.*, "Monitoring and tuning microring properties using defect-enhanced silicon photodiodes at 1550 nm," *IEEE Photon. Technol. Lett.*, vol. 24, no. 4, pp. 261–263, 2012.

[109] Neda Cvijetic, Ming-Fang Huang, Ezra Ip, Yin Shao *et al.*, "1.92Tb/s coherent DWDM-OFDMA-PON with no high-speed ONU-side electronics over 100km SSMF and 1 :64 passive split," *Opt. Express*, vol. 19, no. 24, pp. 24 540–24 545, November 2011.

[110] L. A. Neto, P. Chanclou, B. Charbonnier, N. Genay *et al.*, "Up to 40Gb/s optically amplified AMOOFDM for next generation PON networks," in *Optical Fiber Communication Conference (OFC)*, 2011, pp. 1–3.

[111] Dar-Zu Hsu, Chia-Chien Wei, Hsing-Yu Chen, Yi-Cheng Lu *et al.*, "A 40-Gbps OFDM LR-PON system over 100-km fiber employing an economical 10-GHz-based transceiver," in *Optical Fiber Communication Conference (OFC)*, 2012, pp. 1–3.

[112] C. H. Yeh, C. W. Chow, H. Y. Chen, and B. W. Chen, "Using adaptative four-band OFDM modulation with 40 Gb/s DS and 10 Gb/s US signals for next generation LR-PON," *Opt. Express*, vol. 19, no. 27, pp. 26 150–26 160, December 2011.

[113] J. von Hoyningen Huene, C. Ruprecht, A. Ali, and W. Rosenkranz, "Experimental IM/DD OFDMA transmission with scalable receiver frontend for PON scenarios," in *Optical Fiber Communication Conference (OFC)*, 2012.

[114] G. Stepniak, "Low-cost OFDM Direct Detection Passive Optical Network," *Microwave and Optical Technology Letters*, vol. 55, no. 10, pp. 2504–2507, 2013.

[115] T. N. Duong, C. Milion, N. Genay, E. Grard *et al.*, "Very high bit rate transmission for NGPON using AMOOFDM direct modulation of linear laser," in *Optical Fiber Communication Conference*, no. OTuO3, 2010, pp. 1–3.

[116] W. Yan, T. Tanaka, B. Liu, M. Nishihara *et al.*, "100 Gb/s Optical IM-DD Transmission with 10G-Class Devices Enabled by 65 GSamples/s CMOS DAC Core," in *Optical Fiber Communication Conference*. Optical Society of America, 2013. [Online]. Available : http://www.opticsinfobase.org/abstract.cfm?URI=OFC-2013-OM3H.1

[117] Jianjun Yu, Ming-Fang Huang, Dayou Qian, Lin Chen *et al.*, "Centralized Lightwave WDM-PON Employing 16-QAM Intensity Modulated OFDM Downstream and OOK Modulated Upstream Signals," *IEEE Photon. Technol. Lett.*, vol. 20, no. 18, pp. 1545–1547, September 2008.

[118] Dayou Qian, N. Cvijetic, Yue-Kai Huang, Jianjun Yu *et al.*, "100km long reach upstream 36Gb/s-OFDMA-PON over a single wavelength with source-free ONUs," in *Proc. 35th European Conf. Optical Communication ECOC '09*, 2009, pp. 1–2.

[119] A. Agmon, M. Nazarathy, D. Marom, S. Ben Ezra *et al.*, "Bi-directional Ultra-dense Polarization-diverse OFDM/WDM PON with Laserless Colorless 1Gb/s ONUs Based on Si PICs and $<$ 417 MHz mixed-signal ICs," *Optical Fiber Communication Conference (OFC)*, 2013.

[120] D. F. Hewitt, "Orthogonal Frequency Division Multiplexing using Baseband Optical Single Sideband for Simpler Adaptive Dispersion Compensation," in *Proc. Conf. Optical Fiber Communication and the National Fiber Optic Engineers Conf. OFC/NFOEC 2007*, 2007, pp. 1–3.

[121] X. Zheng, X. liu, C. Hou, Y. Shao *et al.*, "A Novel OFDM-PON Architecture Using Single-Side-Band OFDM for Down Stream and Sub-carrier Multiplexed ASK for Up Stream," in *Proc. Asia Communications and Photonics Conf. and Exhibition (ACP)*, 2009, pp. 1–2.

[122] Dayou Qian, Shu-Hao Fan, N. Cvijetic, Junqiang Hu *et al.*, "64/32/16QAM-OFDM using direct-detection for 40G-OFDMA-PON downstream," in *Proc. and the National Fiber Optic Engineers Conf. Optical Fiber Communication Conf. and Exposition (OFC/NFOEC)*, 2011, pp. 1–3.

[123] Bo Zhao and Xue Chen, "A 40Gbps SSB-OFDMA-PON Architecture Using Direct-Detection and Source-Free ONUs Supporting Dynamic Bandwidth Allocation," in *Proc. Third Int Communications and Mobile Computing (CMC) Conf*, 2011, pp. 223–225.

[124] N. Cvijetic, M. Cvijetic, M. F. Huang, E. Ip *et al.*, "Terabit Optical Access Networks Based on WDM-OFDMA-PON," *J. Lightw. Technol.*, vol. 30, no. 4, pp. 493–403, February 2012.

[125] Bangjiang Lin, Juhao Li, Hui Yang, Yangsha Wan *et al.*, "Comparison of DSB and SSB transmission for OFDM-PON [Invited]," *IEEE/OSA Journal of Optical Communications and Networking*, vol. 4, no. 11, pp. B94–B100, 2012.

[126] B. Schmidt, A. J. Lowery, and L. B. Du, "Low sample rate transmitter for direct-detection optical OFDM," in *Proc. Conf. Optical Fiber Communication - incudes post deadline papers OFC 2009*, 2009, pp. 1–3.

[127] D. Qian, J. Hu, J. Yu, P. N. Ji *et al.*, "Experimental Demonstration of a Novel OFDM-A Based 10Gb/s PON Architecture," *European Conference on Optical Comunications (ECOC)*, pp. 1–2, 2007.

[128] D. Qian, J. Hu, P. N. Ji, T. Wang *et al.*, "10-Gb/s OFDMA-PON for Delivery of Heterogeneous Services," *Proc. Conf. Optical Fiber communication/National Fiber Optic Engineers Conf. OFC/NFOEC 2008*, pp. 1–3, 2008.

[129] Dayou Qian, Junqiang Hu, P. Nan Ji, and Ting Wang, "10.8-Gb/s OFDMA-PON transmission performance study," *Proc. Conf. Optical Fiber Communication - incudes post deadline papers OFC 2009*, pp. 1–3, 2009.

[130] Dayou Qian, Junqiang Hu, and Ting Wang, "Hybrid 2.5G/10G co-existing OFDMA-PON employing single receiver at the OLT," *Proc. and the National Fiber Optic Engineers Conf. Optical Fiber Communication Conf. and Exposition (OFC/NFOEC)*, pp. 1–3, 2011.

[131] X. Jin, E. Hugues Salas, R. Giddings, J. Wei *et al.*, "First real-time experimental demonstrations of 11.25 Gb/s optical OFDMA PONs with adaptive dynamic bandwidth allocation," *Opt. Express*, vol. 19, no. 21, pp. 20 557–20 570, 2011.

[132] L. A. Neto, G. B. de Farias, N. Genay, S. Menezo *et al.*, "On the limitations of IM/DD WDM-FDMA-OFDM PON with single photodiode for upstream transmission," *OFC/NFOEC*, 2012.

[133] X. Q. Jin and J. M. Tang, "Experimental Investigations of Wavelength Spacing and Colorlessness of RSOA-Based ONUs in Real-Time Optical OFDMA PONs," *J. Lightw. Technol.*, vol. 30, no. 16, pp. 2603–2609, August 2012.

[134] L. Anet Neto, D. Erasme, N. Genay, P. Chanclou *et al.*, "Simple Estimation of Fiber Dispersion and Laser Chirp Parameters Using the Downhill Simplex Fitting Algorithm," *J. Lightw. Technol.*, vol. 31, no. 2, pp. 334–342, January 2013.

[135] X. Jin, J. Groenewald, E. Hugues Salas, R. Giddings *et al.*, "Upstream Power Budgets of IMDD Optical OFDMA PONs Incorporating RSOA Intensity Modulator-Based Colorless ONUs," *J. Lightw. Technol.*, vol. 31, no. 12, pp. 1914–1920, 2013.

[136] N. Cvijetic, Dayou Qian, Junqiang Hu, and Ting Wang, "44-Gb/s/lambda upstream OFDMA-PON transmission with polarization-insensitive source-free ONUs," *Proc. Conf Optical Fiber Communication (OFC), collocated National Fiber Optic Engineers Conf. (OFC/NFOEC)*, pp. 1–3, 2010.

[137] N. Cvijetic, Ming-Fang Huang, E. Ip, Yue-Kai Huang *et al.*, "1.2 Tb/s symmetric WDM-OFDMA-PON over 90km straight SSMF and 1x32 passive split with digitally-selective ONUs and coherent receiver OLT," *Proc. and the National Fiber Optic Engineers Conf. Optical Fiber Communication Conf. and Exposition (OFC/NFOEC)*, 2011.

[138] N. Cvijetic, "OFDM for next generation optical access networks," *Proc. and the National Fiber Optic Engineers Conf. Optical Fiber Communication Conf. and Exposition (OFC/NFOEC)*, pp. 1–30, 2011.

[139] Govind P. Agrawal, *Fiber-Optic Communication Systems Fourth Edition*, 3rd ed. John Wiley & Sons, 2002.

[140] G. P. Agrawal, "Fiber-Optic Communication Systems," Institute of Optics - University of Rochester, White Paper, 2007.

[141] G. P. Agrawal and M. Potasek, "Effect of frequency chirping on the performance of optical communication systems," *Optics letters*, vol. 11, no. 5, pp. 318–320, 1986.

[142] A. Gnauck, S. Korotky, J. Veselka, J. Nagel *et al.*, "Dispersion penalty reduction using an optical modulator with adjustable chirp," *IEEE Photon. Technol. Lett.*, vol. 3, no. 10, pp. 916–918, 1991.

[143] G. P. Agrawal and N. K. Dutra, *Semiconductor Lasers*, 2nd ed. New York : Van Nostrand Reinhold, 1993.

[144] S. L. Chuang, *Physics of Optoelectronic Devices*, Wiley, Ed., Hoboken, NJ, 2008.

[145] Dung Tien Pham, Moon-Ki Hong, Jeong-Min Joo, Eun-Soo Namb *et al.*, "Laser phase noise and OFDM symbol duration effects on the performance of direct-detection based optical OFDM access network," *Optical Fiber Technology*, vol. 17, pp. 252–257, March 2011.

[146] J. Michel, R. E. Camacho Aguilera, Y. Cai, N. Patel *et al.*, "An electrically pumped Ge-on-Si laser," in *Optical Fiber Communication Conference (OFC)*, 2012.

[147] E. E. Friedrich, M. G. Oberg, B. Broberg, S. Nilsson *et al.*, "Hybrid integration of semiconductor lasers with Si-based single-mode ridge waveguides," *J. Lightw. Technol.*, vol. 10, no. 3, pp. 336–340, 1992.

[148] H. Park, A. W. Fang, S. Kodama, and J. E. Bowers, "Hybrid silicon evanescent laser fabricated with a silicon waveguide and III-V offset quantum well," *Opt. Express*, vol. 13, pp. 9460–9464, 2005.

[149] Alexander W. Fang, Hyundai Park, Oded Cohen, Richard Jones *et al.*, "Electrically pumped hybrid AlGaInAs-silicon evanescent laser," *Opt. Express*, vol. 14, no. 20, pp. 9203–9210, October 2006.

[150] A. W. Fang, R. Jones, H. Park, O. Cohen *et al.*, "Integrated AlGaInAs-silicon evanescent racetrack laser and photodetector," *Opt. Express*, vol. 15, no. 5, pp. 2315–2322, 2007.

[151] A. W. Fang, M. N. Sysak, B. R. Koch, R. Jones *et al.*, "Single-Wavelength Silicon Evanescent Lasers," *IEEE J. Sel. Topics Quantum Electron.*, vol. 15, no. 3, pp. 535–544, 2009.

[152] A. Yariv and X. Sun, "Supermode si/iii-v hybrid lasers, optical amplifiers and modulators : A proposal and analysis," *Opt. express*, vol. 15, no. 15, pp. 9147–9151, 2007.

[153] B. Ben Bakir, A. Descos, N. Olivier, D. Bordel *et al.*, "Electrically driven hybrid Si/III-V Fabry-Pérot lasers based on adiabatic mode transformers," *Opt. Express*, vol. 19, no. 11, pp. 10 317–10 415, May 2011.

[154] B. B. Bakir, A. Descos, N. Olivier, D. Bordel *et al.*, "Hybrid Si/III–V lasers with adiabatic coupling," in *Proc. 8th IEEE Int Group IV Photonics (GFP) Conf*, 2011, pp. 169–171.

[155] A. Descos, C. Jany, D. Bordel, H. Duprez *et al.*, "Heterogeneously Integrated III-V/Si Distributed Bragg Reflector Laser with Adiabatic Coupling," in *European Conference on Optical Communication (ECOC)*, 2013.

[156] S. Stankovic, G. Roelkens, D. Van Thourhout, R. Baets *et al.*, "Hybrid iii-v/silicon laser based on dvs-bcb bonding," in *Proceedings Symposium IEEE/LEOS Benelux Chapter, 2008, Twente*. IEEE-LEOS, 2008.

[157] M. Lamponi, S. Keyvaninia, C. Jany, F. Poingt *et al.*, "Low-Threshold Heterogeneously Integrated InP/SOI Lasers With a Double Adiabatic Taper Coupler," *IEEE Photon. Technol. Lett.*, vol. 24, no. 1, pp. 76–78, 2012.

[158] C. L. M. Daunt and F. H. Peters, "Correction methods for electroabsorption modulator-based phase-shift keying photonic integrated circuits," *IEEE J. Sel. Topics Quantum Electron.*, vol. 19, no. 6, p. 3300307, 2013.

[159] Fumio Koyama and Kenichi Iga, "Frequency Chirping in External Modulators," *J. Lightw. Technol.*, vol. 6, no. 1, pp. 87–93, January 1988.

[160] Matthias Seimetz, *High-Order Modulation for Optical Fiber Transmission.* Springer, 2009.

[161] J. C. Cartledge, "Comparison of effective α-parameters for semiconductor Mach-Zehnder optical modulators," *J. Lightw. Technol.*, vol. 16, no. 3, pp. 372–379, 1998.

[162] P. Dainesi, A. Kung, M. Chabloz, A. Lagos *et al.*, "CMOS compatible fully integrated Mach-Zehnder interferometer in SOI technology," *IEEE Photon. Technol. Lett.*, vol. 12, no. 6, pp. 660–662, 2000.

[163] Ansheng Liu, Richard Jones, Ling Liao, Dean Samara Rubio *et al.*, "A high-speed silicon optical modulator based on a metalŰoxideŰsemiconductor capacitor," *Nature*, vol. 427, pp. 615–618, February 2004.

[164] R. Soref and B. Bennett, "Electrooptical effects in silicon," *IEEE J. Quantum Electron.*, vol. 23, no. 1, pp. 123–129, January 1987.

[165] Ling Liao, Dean Samara Rubio, Michael Morse, Ansheng Liu *et al.*, "High speed silicon Mach-Zehnder modulator," *Optics Express*, vol. 13, no. 8, pp. 3129–3135, April 2005.

[166] B. Milivojevic, C. Raabe, A. Shastri, M. Webster *et al.*, "112Gb/s DP-QPSK Transmission Over 2427km SSMF Using Small-Size Silicon Photonic IQ Modulator and Low-Power CMOS Driver," in *Optical Fiber Communication Conference (OFC)*, 2013.

[167] X. Luo, X. Tu, J. Song, L. Ding *et al.*, "Slope efficiency and spurious-free dynamic range of silicon Mach-Zehnder modulator upon carrier depletion and injection effects," *Opt. express*, vol. 21, no. 14, pp. 16 570–16 577, 2013.

[168] Qianfan Xu, Sasikanth Manipatruni, Brad Schmidt, Jagat Shakya *et al.*, "12.5 Gbit/s carrier-injection-based silicon micro-ring silicon modulators," *Opt. Express*, vol. 15, no. 2, pp. 430–436, January 2007.

[169] S. Akiyama, T. Baba, M. Imai, T. Akagawa *et al.*, "50-Gb/s silicon modulator using 250um-Long phase shifter based-on forward-biased pin diodes," in *Proc. IEEE 9th Int Group IV Photonics (GFP) Conf*, 2012, pp. 192–194.

[170] T. Baba, S. Akiyama, M. Imai, N. Hirayama *et al.*, "50-Gb/s ring-resonator-based silicon modulator," *Opt. express*, vol. 21, no. 10, pp. 11 869–11 876, 2013.

[171] F. Gardes, G. Reed, N. Emerson, and C. Png, "A sub-micron depletion-type photonic modulator in silicon on insulator," *Opt. Express*, vol. 13, no. 22, pp. 8845–8854, 2005.

[172] Gilles Rasigade, "Modulateur optique haute-fréquence sur substrat silicium-sur-isolant," Ph.D. dissertation, Université Paris-Sud, 2010.

[173] D. Marris Morini, L. Vivien, J. M. Fédéli, E. Cassan *et al.*, "Low loss and high speed silicon optical modulator based on a lateral carrier depletion structure," *Opt. express*, vol. 16, no. 1, pp. 334–339, 2008.

[174] Ansheng Liu, Ling Liao, Doron Rubin, Hat Nguyen *et al.*, "High-speed optical modulation based on carrier depletion in a silicon waveguide," *Opt. Express*, vol. 15, no. 2, pp. 660–668, January 2007.

[175] M. R. Watts, D. C. Trotter, R. W. Young, and A. L. Lentine, "Ultralow power silicon microdisk modulators and switches," in *Group IV Photonics, 2008 5th IEEE International Conference on*, 2008, pp. 4–6.

[176] Xi Xiao, Xianyao Li, Hao Xu, Yingtao Hu *et al.*, "44-Gb/s Silicon Microring Modulators Based on Zigzag PN Junctions," *IEEE Photon. Technol. Lett.*, vol. 24, no. 19, pp. 1712–1714, October 2012.

[177] X. Xiao, H. Xu, X. Li, Z. Li *et al.*, "60 Gbit/s Silicon Modulators with Enhanced Electro-optical Efficiency," in *Optical Fiber Communication Conference (OFC)*, 2013.

[178] Zhi-Yong Li, Dan-Xia Xu, W. Ross McKinnon, Siegfried Janz *et al.*, "Silicon waveguide modulator based on carrier depletion in periodically interleaved PN junctions," *Opt. Express*, vol. 17, no. 18, pp. 15 947–15 958, August 2009.

[179] P. Dong, X. Liu, C. Sethumadhavan, L. L. Buhl *et al.*, "224-Gb/s PDM-16-QAM Modulator and Receiver based on Silicon Photonic Integrated Circuits," in *Optical Fiber Communication Conference (OFC)*, 2013.

[180] P. Dong, C. Xie, L. L. Buhl, and Y.-K. Chen, "Silicon Microring Modulators for Advanced Modulation Formats," in *Optical Fiber Communication Conference (OFC)*, 2013.

[181] Po Dong, Chongjin Xie, Long Chen, Nicolas K. Fontaine *et al.*, "Experimental demonstration of microring quadrature phase-shift keying modulators," *Optics Letters*, vol. 37, no. 7, pp. 1178–1180, April 2012.

[182] K. Xu, L.-G. Yang, J.-Y. Sung, Y. M. Chen *et al.*, "Compatibility of Silicon Mach-Zehnder Modulators for Advanced Modulation Formats," *J. Lightw. Technol.*, vol. 31, no. 15, pp. 2550–2554, 2013.

[183] Ning-Ning Feng, Shirong Liao, Dazeng Feng, Po Dong *et al.*, "High speed carrier-depletion modulators with 1.4V-cm $V_\pi L$ integrated on 0.25μm silicon-oninsulator waveguides," *Optics Express*, vol. 18, no. 8, pp. 7994–7999, April 2010.

[184] D. J. Thomson, F. Y. Gardes, J.-M. Fedeli, S. Zlatanovic *et al.*, "50-Gb/s Silicon Optical Modulator," *IEEE Photon. Technol. Lett.*, vol. 24, no. 4, pp. 234–236, 2012.

[185] G. Li, X. Zheng, H. Thacker, J. Yao *et al.*, "40 Gb/s thermally tunable CMOS ring modulator," in *Proc. IEEE 9th Int Group IV Photonics (GFP) Conf*, 2012, pp. 1–3.

[186] G. Rasigade, M. Ziebell, D. Marris Morini, J.-M. Fédéli *et al.*, "High extinction ratio 10 Gbit/s silicon optical modulator," *Optics express*, vol. 19, no. 7, pp. 5827–5832, 2011.

[187] Melissa Ziebell, Delphine Marris Morini, Gilles Rasigade, Jean-Marc Fédéli *et al.*, "40 Gbit/s low-loss silicon optical modulator based on a pipin diode," *Opt. Express*, vol. 20, no. 20, pp. 10 591–10 596, May 2012.

[188] E. Timurdogan, C. M. Sorace Agaskar, A. Biberman, and M. R. Watts, "Vertical Junction Silicon Microdisk Modulators at 25Gb/s," in *Optical Fiber Communication Conference (OFC)*, 2013.

[189] J. C. Rosenberg, W. M. J. Green, S. Assefa, D. M. Gill *et al.*, "A 25 Gbps silicon microring modulator based on an interleaved junction," *Opt. Express*, vol. 20, no. 24, pp. 26 411–26 423, November 2012.

[190] G.Rasigade, D.Marris Morini, M.Ziebell, E.Cassan *et al.*, "Analytical model for depletion-based silicon modulator simulation," *Opt. Express*, vol. 19, no. 5, pp. 3919–3924, February 2011.

[191] *BeamPROP RSoft - User Guide*, RSoft, 2011.

[192] D. J. Thomson, F. Y. Gardes, G. T. Reed, F. Milesi *et al.*, "High speed silicon optical modulator with self aligned fabrication process," *Opt. Express*, vol. 18, no. 18, pp. 19 064–19 069, 2010.

[193] Po Dong, Long Chen, and Young-kai Chen, "High-speed low-voltage single-drive push-pull silicon Mach-Zehnder modulators," *Opt. Express*, vol. 20, no. 6, pp. 6163–6169, March 2012.

[194] F. Vacondio, M. Mirshafiei, J. Basak, Ansheng Liu *et al.*, "A Silicon Modulator Enabling RF Over Fiber for 802.11 OFDM Signals," *IEEE J. Sel. Topics Quantum Electron.*, vol. 16, no. 1, pp. 141–148, 2010.

[195] A. Khilo, C. M. Sorace, and F. X. Kärtner, "Broadband linearized silicon modulator," *Optics Express*, vol. 19, no. 5, pp. 4485–4500, 2011.

[196] Matthew Streshinsky, Ali Ayazi, Zhe Xuan, Andy Eu-Jin Lim *et al.*, "Highly linear silicon traveling wave Mach-Zehnder carrier depletion modulator based on differential drive," *Opt. Express*, vol. 21, no. 3, pp. 3818–3825, February 2013.

[197] M. Sauer, A. Kobyakov, and J. George, "Radio over fiber for picocellular network architectures," *J. Lightw. Technol.*, vol. 25, no. 11, pp. 3301–3320, 2007.

[198] "Application note - spurious free dynamic range," Fiber-Span, White Paper, 2008. [Online]. Available : http://www.fiber-span.com/Application_Note_Spurious%20Free%20Dynamic%20Range.pdf

[199] K. J. Williams, L. T. Nichols, and R. D. Esman, "Photodetector nonlinearity limitations on a high-dynamic range 3 GHz fiber optic link," *J. Lightw. Technol.*, vol. 16, no. 2, p. 192, 1998.

[200] C. Chauveau, P. Labeye, J. Fedeli, J. Hazart *et al.*, "Validation of an analytical model of si-ring resonators for designing a 1x8 multiplexer in SCISSOR configuration," in *Proc. ICO Int Information Photonics (IP) Conf*, 2011, pp. 1–2.

[201] A. M. Gutierrez, A. Brimont, G. Rasigade, M. Ziebell *et al.*, "Ring-Assisted MachŰZehnder Interferometer Silicon Modulator for Enhanced Performance," *J. Lightw. Technol.*, vol. 30, no. 30, pp. 9–14, January 2012.

[202] A. Yariv, "Universal relations for coupling of optical power between microresonators and dielectric waveguides," *Electronics Letters*, vol. 36, no. 4, pp. 321–322, 2000.

[203] J. F. Buckwalter, Xuezhe Zheng, Guoliang Li, K. Raj *et al.*, "A Monolithic 25-Gb/s Transceiver With Photonic Ring Modulators and Ge Detectors in a 130-nm CMOS SOI Process," *IEEE J. Solid-State Circuits*, vol. 47, no. 6, pp. 1309–1322, June 2012.

[204] Lin Zhang, Yunchu Li, Jeng-Yuan Yang, Muping Song *et al.*, "Silicon-Based Microring Resonator Modulators for Intensity Modulation," *IEEE J. Sel. Topics Quantum Electron.*, vol. 16, no. 1, pp. 149–158, January/February 2010.

[205] B. E. Little, S. T. Chu, H. A. Haus, J. Foresi *et al.*, "Microring resonator channel dropping filters," *J. Lightw. Technol.*, vol. 15, no. 6, pp. 998–1005, June 1997.

[206] Muping Song, Lin Zhang, Raymond G. Beausoleil, and Alan E. Willner, "Nonlinear Distortion in a Silicon Microring-Based Electro-Optic Modulator for Analog Optical Links," *IEEE J. Sel. Topics Quantum Electron.*, vol. 16, no. 1, pp. 185–191, January/February 2010.

[207] A. M. Gutiérrez, J. V. Galan, J. Herrera, A. Brimont *et al.*, "Silicon-Based Electro-Optic Modulators for Linear and Nonlinear Radio-over-Fiber Applications," in *IEEE International Topical Meeting on Microwave Photonics*, 2012.

[208] A. Gutierrez, J. Galan, J. Herrera, A. Brimont *et al.*, "High linear ring-assisted MZI electro-optic silicon modulators suitable for radio-over-fiber applications," in *Group IV Photonics (GFP), 2012 IEEE 9th International Conference on.* IEEE, 2012, pp. 57–59.

[209] Ali Ayazi, Tom Baehr Jones, Yang Liu, Andy Eu-Jin Lim *et al.*, "Linearity of silicon ring modulators for analog optical links," *Optics Express*, vol. 20, no. 12, pp. 13 115–13 122, June 2012.

[210] P. Binetti, X. Leijtens, T. de Vries, Y. Oei *et al.*, "InP/InGaAs Photodetector on SOI Photonic Circuitry," *Photonics Journal, IEEE*, vol. 2, no. 3, pp. 299–305, 2010.

[211] Laurent Vivien, Johann Osmond, Jean-Marc Fédéli, Delphine Marris Morini *et al.*, "42 GHz P.I.N Germanium photodetector integrated in a silicon-on-insulator waveguide," *Opt. Express*, vol. 17, no. 8, pp. 6252–6257, April 2009.

[212] Y. Kang, Z. Huang, Y. Saado, J. Campbell *et al.*, "High performance Ge/Si avalanche photodiodes development in intel," in *Proc. and the National Fiber Optic Engineers Conf. Optical Fiber Communication Conf. and Exposition (OFC/NFOEC)*, 2011, pp. 1–3.

[213] Yimin Kang, Han-Din Liu, Mike Morse, Mario J. Paniccia *et al.*, "Monolithic Germanium/Silicon Avalanche Photodiodes with 340GHz gain-bandwidth product," *Nature Photonics*, vol. 3, pp. 59–63, January 2009.

[214] K. Yonenaga and N. Takachio, "A fiber chromatic dispersion compensation technique with an optical SSB transmission in optical homodyne detection systems," *IEEE Photon. Technol. Lett.*, vol. 5, no. 8, pp. 949–951, August 1993.

[215] M. Sieben, J. Conradi, and D. E. Dodds, "Optical single sideband transmission at 10 Gb/s using only electrical dispersion compensation," *J. Lightw. Technol.*, vol. 17, no. 10, pp. 1742–1749, October 1999.

[216] B. Escrig, "Communications Numeriques - Notes de cours," ENSEIRB, White Paper, 2009.

[217] Jigesh Patel, "User day : Optsim and Modesys," Synopsis, White Paper, 2013.

[218] J. Smith, "Odd-Bit Quadrature Amplitude-Shift Keying," *IEEE Trans. Commun.*, vol. 23, no. 3, pp. 385–389, 1975.

[219] G. Foschini, R. Gitlin, and S. Weinstein, "Optimization of two-dimensional signal constellations in the presence of Gaussian noise," *Communications, IEEE Transactions on*, vol. 22, no. 1, pp. 28–38, 1974.

[220] R. A. Shafik, S. Rahman, and A. Razibul Islam, "On the Extended Relationships Among EVM, BER and SNR as Performance Metrics," in *Proc. Int. Conf. Electrical and Computer Engineering ICECE '06*, 2006, pp. 408–411.

[221] Robert W. Chang, "Synthesis of band-limited orthogonal signals for multichannel data transmission," *The Bell System Techical Journal*, pp. 1775–1796, 1966.

[222] William Shieh and Ivan Djordjevic, *OFDM for Optical Communication.* Elsevier, 2010.

[223] P. S. Chow, J. M. Cioffi, and J. A. C. Bingham, "A practical discrete multitone transceiver loading algorithm for data transmission over spectrally shaped channels," *IEEE Trans. Commun.*, vol. 43, no. 234, pp. 773–775, 1995.

[224] J. Campello, "Optimal discrete bit loading for multicarrier modulation systems," *Proc. IEEE Int Information Theory Symp*, 1998.

[225] G. D. Bergland, "Numerical analysis : A fast fourier transform algorithm for real-valued series," *Communications of the ACM*, vol. 11, no. 10, pp. 703–710, 1968.

[226] H. V. Sorensen, D. Jones, M. Heideman, and C. Burrus, "Real-valued fast fourier transform algorithms," *Acoustics, Speech and Signal Processing, IEEE Transactions on*, vol. 35, no. 6, pp. 849–863, 1987.

[227] R. O'Neill and L. Lopes, "Envelope variations and spectral splatter in clipped multicarrier signals," *Personal, Indoor and Mobile Radio Communications, 1995. Sixth IEEE International Symposium on*, vol. 1, pp. 71–75, 1995.

[228] A. Jones, "Block coding scheme for reduction of peak to mean envelope power ratio of multicarrier transmission schemes," *Electronics Letters*, vol. 30, no. 25, pp. 2098–2099, 1994.

[229] S. Muller and J. Huber, "OFDM with reduced peak-to-average power ratio by optimum combination of partial transmit sequences," *Electronics Letters*, vol. 33, no. 5, pp. 368–369, 1997.

[230] Tao Jiang and Yiyan Wu, "An Overview : Peak-to-Average Power Ratio Reduction Techniques for OFDM Signals," *IEEE Trans. Broadcast.*, vol. 54, no. 2, pp. 257–268, 2008.

[231] D. J. G. Mestdagh, "Calculation of ADC resolution for DMT modulation," *Electronics Letters*, vol. 31, no. 16, pp. 1315–1316, 1995.

[232] Sian Chong Jeffrey Lee, "Discrete Multitone Modulation for Short-Range Optical Communications," Ph.D. dissertation, Technische Universiteit Eindhoven, 2009.

[233] Wei-Ren Peng, Bo Zhang, Xiaoxia Wu, Kai-Ming Feng *et al.*, "Compensation for I/Q Imbalances and Bias Deviation of the Mach–Zehnder Modulators in Direct-Detected Optical OFDM Systems," *IEEE Photon. Technol. Lett.*, vol. 21, no. 2, pp. 103–105, January 2009.

[234] Abdullah Al Amin, Sander L. Jansen, Hidenori Takahashi, Itsuro Morita *et al.*, "A hybrid IQ imbalance compensation method for optical OFDM transmission," *Opt. Express*, vol. 18, no. 5, pp. 4859–4866, March 2010.

[235] M. Speth, S. A. Fechtel, G. Fock, and H. Meyr, "Optimum receiver design for wireless broad-band systems using OFDM. I," *IEEE Trans. Commun.*, vol. 47, no. 11, pp. 1668–1677, 1999.

[236] T. M. Schmidl and D. C. Cox, "Robust frequency and timing synchronization for OFDM," *IEEE Trans. Commun.*, vol. 45, no. 12, pp. 1613–1621, 1997.

[237] W. Shieh, H. Bao, and Y. Tang, "Coherent Optical OFDM : theory and design," *Opt. Express*, vol. 16, no. 2, pp. 841–859, January 2008.

[238] G. H. Smith, D. Novak, and Z. Ahmed, "Overcoming chromatic-dispersion effects in fiber-wireless systems incorporating external modulators," *IEEE Trans. Microw. Theory Tech.*, vol. 45, no. 8, pp. 1410–1415, August 1997.

[239] F. Devaux, Y. Sorel, and J. F. Kerdiles, "Simple measurement of fiber dispersion and of chirp parameter of intensity modulated light emitter," *J. Lightw. Technol.*, vol. 11, no. 12, pp. 1937–1940, December 1993.

[240] L. Bjerkan, A. Royset, L. Hafskjaer, and D. Myhre, "Measurement of laser parameters for simulation of high-speed fiberoptic systems," *J. Lightw. Technol.*, vol. 14, no. 5, pp. 839–850, May 1996.

[241] L. A. Neto, P. Chanclou, B. Charbonnier, A. Gharba *et al.*, "On the interest of chirped lasers for AMOOFDM transmissions in long distance PON networks," *OFC/NFOEC*, pp. 1–3, 2011.

[242] J. M. B. Oliveira, H. M. Salgado, and M. R. D. Rodrigues, "Large signal analysis of Mach-Zehnder modulator intensity response in a linear dispersive fiber," *Proceedings of the London Communications Symposium*, September 2006.

[243] L. Anet Neto, D. Erasme, N. Genay, J. Guillory *et al.*, "Experimental Investigation of Dispersion-induced Distortions in IMDD OFDM PON Transmissions," in *Proc. 38th European Conf Optical Communication (ECOC) and Exhibition*, 2012.

[244] C. Sanchez, B. Ortega, J. L. Wei, J. Tang *et al.*, "Analytical formulation of directly modulated OOFDM signals transmitted over an IM/DD dispersive link," *Opt. Express*, vol. 6, no. 21, pp. 7651–7666, 2013.

[245] Dar-Zu Hsu, Chia ChienWei, Hsing-Yu Chen, Yi-Cheng Lu *et al.*, "SSII cancellation in an EAM-based OFDM-IMDD transmission system employing a novel dynamic chirp model," *Opt. Express*, vol. 21, no. 1, pp. 533–543, January 2013.

[246] B. J. C. Schmidt, A. J. Lowery, and J. Armstrong, "Experimental Demonstrations of Electronic Dispersion Compensation for Long-Haul Transmission Using Direct-Detection Optical OFDM," *J. Lightw. Technol.*, vol. 26, no. 1, pp. 196–203, January 2008.

[247] Wei-Ren Peng, Xiaoxia Wu, V. R. Arbab, Kai-Ming Feng *et al.*, "Theoretical and Experimental Investigations of Direct-Detected RF-Tone-Assisted Optical OFDM Systems," *J. Lightw. Technol.*, vol. 27, no. 10, pp. 1332–1339, May 2009.

[248] Wei-Ren Peng, Xiaoxia Wu, Vahid R. Arbab, Bishara Shamee *et al.*, "Experimental Demonstration of 340 km SSMF Transmission Using a Virtual Single Sideband OFDM Signal that Employs Carrier Suppressed and Iterative Detection Techniques," *Optical Fiber Communication Conference (OFC)*, 2008.

[249] Arthur James Lowery, Liang Bangyuan Du, and Jean Armstrong, "Performance of OOFDM in Ultralong-Haul WDM Ligthwave Systems," *J. Lightw. Technol.*, vol. 25, no. 1, pp. 131–138, January 2007.

[250] R. P. Giddings, X. Jin, H. Kee, X. Yang *et al.*, "First Experimental Demonstration of Real-Time Optical OFDM Transceivers," *European Conference on Optical Comunications (ECOC)*, September 2009.

[251] James W. Cooley and John W. Tukey, "An algorithm for the machine calculation of complex Fourier series," *Math. Comput.*, vol. 19, pp. 297–301, 1965.

[252] Charles Van Loan, *Computational Frameworks for the Fast Fourier Transform*, S. for Industrial and A. Mathematics, Eds. SIAM, 1992.

[253] Markus Püschel, José M. F. Moura, Jeremy Johnson, David Padua *et al.*, "SPIRAL : Code Generation for DSP Transforms," *Proceedings of the IEEE, special issue on "Program Generation, Optimization, and Adaptation"*, vol. 93, no. 2, pp. 232– 275, 2005.

[254] Y. Benlachtar, P. M. Watts, R. Bouziane, P. A. Milder *et al.*, "Real-Time Digital Signal Processing for the Generation of Optical Orthogonal Frequency-Division-Multiplexed Signals," *IEEE J. Sel. Topics Quantum Electron.*, vol. 16, no. 5, pp. 1235–1244, 2010.

[255] X. Q. J. R. P. Giddings and J. M. Tang, "Experimental demonstration of real-time 3Gb/s optical OFDM transceivers," *Opt. Express*, vol. 17, no. 19, pp. 16 654–16 665, September 2009.

[256] R. P. Giddings, X. Q. Jin, and J. M. Tang, "First experimental demonstration of 6Gb/s realtime optical OFDM transceivers incorporating channel estimation and variable power loading," *Opt. Express*, vol. 17, no. 22, pp. 19 727–19 738, October 2009.

[257] R. P. Giddings, X. Q. Jin, E. Hugues Salas, E. Giacoumidis *et al.*, "Experimental demonstration of a record high 11.25Gb/s real-time optical OFDM transceiver supporting 25km SMF end-to-end transmission in simple IMDD systems," *Opt. Express*, vol. 18, no. 6, pp. 5541–5555, March 2010.

[258] E. Hugues Salas, R. Giddings, X. Jin, J. L. Wei *et al.*, "Real-time experimental demonstration of low-cost VCSEL intensity-modulated 11.25Gb/s optical OFDM signal transmission over 25km PON systems," *Opt. Express*, vol. 19, no. 4, pp. 2979–2988, February 2011.

[259] R. P. Giddings, E. Hugues Salas, Benoit Charbonnier, *et al.*, "Experimental Demonstration of Real-Time Optical OFDM Transmission at 11.25 Gb/s Over 500-m MMFs Employing Directly Modulated DFB Lasers," *IEEE Photon. Technol. Lett.*, vol. 23, no. 1, pp. 51–53, January 2011.

[260] E. Hugues Salas, X. Q. Jin, R. P. Giddings, Y. Hong *et al.*, "Directly Modulated VCSEL-Based Real-Time 11.25-Gb/s Optical OFDM Transmission Over 2000-m Legacy MMFs," *IEEE Photonics Journal*, vol. 4, no. 1, pp. 143–155, February 2012.

[261] R. P. Giddings, E. Hugues Salas, and J. M. Tang, "Experimental demonstration of record high 19.125Gb/s real-time end-to-end dual-band optical OFDM transmission over 25km SMF in a simple EML-based IMDD system," *Opt. Express*, vol. 20, no. 18, pp. 20 666–20 679, August 2012.

[262] E. Hugues Salas, R. Giddings, and J. Tang, "First Experimental Demonstration of Real-Time Adaptive Transmission of 20Gb/s Dual-band Optical OFDM Signals over 500m OM2 MMFs," *OFC/NFOEC*, 2013.

[263] R. Bouziane, P. A. Milder, R. Koutsoyannis, Y. Benlachtar *et al.*, "Design studies for ASIC implementations of 28GS/s optical QPSK- and 16-QAM-OFDM transceivers," *Opt. Express*, vol. 19, no. 21, pp. 20 857–20 864, October 2011.

[264] P. A. Milder, R. Bouziane, R. Koutsoyannis, C. R. Berger *et al.*, "Design and simulation of 25 Gb/s optical OFDM transceiver ASICs," *Opt. Express*, vol. 19, no. 26, pp. B337–B341, December 2011.

[265] Y. M. Greshishchev, D. Pollex, Shing-Chi Wang, M. Besson *et al.*, "A 56GS/S 6b DAC in 65nm CMOS with 256x6b memory," in *Proc. IEEE Int. Solid-State Circuits Conf. Digest of Technical Papers (ISSCC)*, 2011, pp. 194–196.

[266] J. Savoj, A. Abbasfar, A. Amirkhany, M. Jeeradit *et al.*, "A 12-GS/s Phase-Calibrated CMOS Digital-to-Analog Converter for Backplane Communications," *IEEE J. Solid-State Circuits*, vol. 43, no. 5, pp. 1207–1216, 2008.

[267] P. Schvan, D. Pollex, and T. Bellingrath, "A 22GS/s 6b DAC with integrated digital ramp generator," in *Proc. Digest of Technical Papers Solid-State Circuits Conf. ISSCC. 2005 IEEE Int*, 2005, pp. 122–588.

[268] *Factsheet - LEIA 55-65 GSa/s 8-bit DAC*, Fujitsu Semiconductor Europe, 2012.

[269] Y. M. Greshishchev, J. Aguirre, M. Besson, R. Gibbins *et al.*, "A 40GS/s 6b ADC in 65nm CMOS," in *Proc. IEEE Int. Solid-State Circuits Conf. Digest of Technical Papers (ISSCC)*, 2010, pp. 390–391.

[270] M. El Chammas and B. Murmann, "A 12-GS/s 81-mW 5-bit Time-Interleaved Flash ADC With Background Timing Skew Calibration," *IEEE J. Solid-State Circuits*, vol. 46, no. 4, pp. 838–847, 2011.

[271] Chun-Cheng Huang, Chiao Tung, Chung-Yi Wang, and Jieh-Tsorng Wu, "A CMOS 6-Bit 16-GS/s time-interleaved ADC with digital background calibration," *VLSI Circuits (VLSIC), IEEE Symposium on*, 2010.

[272] P. Schvan, J. Bach, C. Fait, P. Flemke *et al.*, "A 24GS/s 6b ADC in 90nm CMOS," in *Proc. Digest of Technical Papers. IEEE Int. Solid-State Circuits Conf. (ISSCC)*, 2008, pp. 544–634.

[273] *Factsheet - LUKE-ES 55-65 GSa/s 8 bit ADC*, Fujitsu Semiconductor Europe, 2012.

[274] J. L. Wei, J. D. Ingham, D. G. Cunningham, R. V. Penty *et al.*, "Performance and Power Dissipation Comparisons Between 28 Gb/s NRZ, PAM, CAP and Optical OFDM Systems for Data Communication Applications," *J. Lightw. Technol.*, vol. 30, no. 20, pp. 3273–3280, October 2012.

[275] Yang Gao, Jianjun Yu, Jiangnan Xiao, Zizheng Cao *et al.*, "Direct-Detection Optical OFDM Transmission System With Pre-Emphasis Technique," *J. Lightw. Technol.*, vol. 29, no. 14, pp. 2138–2145, July 2011.

[276] J. A. Nelder and R. Mead, "A simplex method for function minimization," *The computer journal*, vol. 7, no. 4, pp. 308–313, 1965.

[277] H. Yang, S. C. Jeffrey Lee, E. Tangdiongga, C. Okonkwo *et al.*, "47.4 Gb/s Transmission Over 100 m Graded-Index Plastic Optical Fiber Based on Rate-Adaptive Discrete Multitone Modulation," *J. Lightw. Technol.*, vol. 28, no. 4, pp. 352–359, February 2010.

[278] R. Bouziane, P. Milder, R. Koutsoyannis, Y. Benlachtar *et al.*, "Dependence of optical OFDM transceiver ASIC complexity on FFT size," in *Optical Fiber Communication Conference and Exposition (OFC/NFOEC), and the National Fiber Optic Engineers Conference*, 2012, pp. 1–3.

[279] Cheng Zhang, Peng Guo, Qing Yin, Devang Parekh *et al.*, "30-Gbit/s OFDM Intensity Modulation of 1550-nm VCSEL," *Proc. Asia Communications and Photonics Conf. and Exhibition (ACP)*, 2012.

[280] K. Goi, H. Kusaka, A. Oka, Y. Terada *et al.*, "DQPSK/QPSK Modulation at 40-60 Gb/s using Low-Loss Nested Silicon Mach-Zehnder Modulator," in *Optical Fiber Communication Conference (OFC)*, 2013.

[281] Long Chen, Po Dong, and Young-Kai Chen, "Chirp and Dispersion Tolerance of a Single-Drive Push–Pull Silicon Modulator at 28 Gb/s," *IEEE Photon. Technol. Lett.*, vol. 24, no. 11, pp. 936–938, June 2012.

[282] L. Chen, C. R. Doerr, P. Dong, and Y. Chen, "Monolithic silicon chip with 10 modulator channels at 25 Gbps and 100-GHz spacing," *Opt. Express*, vol. 19, no. 26, pp. B946–951, 2011.

[283] Sheng Liu, David J. Thomson, Frederic Y. Gardes, Jean-Marc Fedeli *et al.*, "Characterization of the Chirp of Silicon Optical Modulators," *European Conference on Optical Comunications (ECOC)*, 2012.

[284] Po Dong, Chongjin Xie, Long Chen, Lawrence L. Buhl *et al.*, "112-Gb/s monolithic PDM-QPSK modulator in silicon," *Opt. Express*, vol. 20, no. 26, pp. B624–B629, December 2012.

[285] Chih-Fan Liao and Shen-Iuan Liu, "40 Gb/s Transimpedance-AGC Amplifier and CDR Circuit for Broadband Data Receivers in 90 nm CMOS," *IEEE J. Solid-State Circuits*, vol. 43, no. 3, pp. 642–655, March 2008.

[286] James E. A. Whiteaway, G. H. B. Thompson, Andrew J. Collar, and Christopher J. Armistead, "The design assessment of $\lambda/4$ phase-shifted DFB laser structures," *IEEE J. Quantum Electron.*, vol. 25, no. 6, pp. 1261–1279, 1989.

[287] Chia-Chien Wei, "Analysis and iterative equalization of transient and adiabatic chirp effects in DML-based OFDM transmission systems," *Opt. Express*, vol. 20, no. 23, pp. 25 774–25 789, November 2012.

[288] J. M. Tang, P. M. Lane, and K. Alan Shore, "High-Speed Transmission of Adaptively Modulated Optical OFDM Signals Over Multimode Fibers Using Directly Modulated DFBs," *J. Lightw. Technol.*, vol. 24, no. 1, pp. 429–441, January 2006.

[289] X. Jin, R. Giddings, E. Hugues Salas, and J. Tang, "Real-time experimental demonstration of optical OFDM symbol synchronization in directly modulated DFB laser-based 25km SMF IMDD systems," *Opt. express*, vol. 18, no. 20, pp. 21 100–21 110, 2010.

[290] R. P. Giddings, "Real-time Digital Signal Processing for Future Optical Access Networks," in *Optical Fiber Communication Conference (OFC)*. Optical Society of America, 2013. [Online]. Available : http://www.opticsinfobase.org/abstract.cfm?URI=OFC-2013-OM3H.5

[291] J. M. Cioffi, "A Multicarrier Primer," Amati Communication Corporation and Stanford University, White Paper, 1991.

[292] J. M. Cioffi, "Advanced Digital Communication (Course Reader)," Stanford University, White Paper, June 2009. [Online]. Available : http://www.stanford.edu/class/ee379c

[293] I. Kalet, "The multitone channel," *IEEE Trans. Commun.*, vol. 37, no. 2, pp. 119–124, 1989.

[294] P. K. Vitthaladevuni, M.-S. Alouini, and J. C. Kieffer, "Exact BER computation for cross QAM constellations," *IEEE Trans. Wireless Commun.*, vol. 4, no. 6, pp. 3039–3050, 2005.

[295] Kyongkuk Cho and Dongweon Yoon, "On the general BER expression of one- and two-dimensional amplitude modulations," *IEEE Trans. Commun.*, vol. 50, no. 7, pp. 1074–1080, 2002.

List of Abbreviations

10G-EPON 10-Gigabit Ethernet Passive Optical Network
ADC Analog-to-Digital Converter
AON Active Optical Networks
APD Avalanche Photodiode
ASE Amplified Spontaneous Noise
ASIC Application-Specific Integrated Circuits
AWG Arbitrary Waveform Generator
AWGN Additive White Gaussian Noise
B2B Back-to-back
BER Bit Error Rate
BiCMOS Bipolar CMOS
BPM Beam Propagation Method
BPSK Binary Phase-Shift Keying
CCDF Complementary Cumulative Density Function
CDMA Code-Division Multiple Access
CFO Carrier Frequecy Offset
CMOS Complementary Metal-Oxide-Semiconductor
CO Central Office
CP1dB 1dB Compression Point
CSPR Carrier-to-Signal Power Ratio
CW Continuous Wave
D8PSK Differential 8-Phase Shift Keying
DAC Digital-to-Analog Converter
DBR Distributed Bragg Reflector
DCF Dispersion-compensation Fiber
DFB Distributed Feedback Laser
DFE Decision Feedback Equalizer
DI Delay Interferometer
DL Downlink
DML Directly Modulated Laser
DQPSK Differential Quadrature Phase-Shift Keying
DSB Dual-side Band
DSO Digital Sampling Oscilloscope
DSP Digital Signal Processor
DUT Device Under Test
DVS-BCB Benzocyclobutene
DWDM Dense Wavelength Division Multiplexing

EA Electrical Amplifier
EAM Electro-absorption Modulator
ECL External Cavity Laser
EDFA Erbium-dopped Fiber Amplifier
ENOB Effective Number of Bits
ER Extinction Ratio
EVM Error Vector Magnitude
FDM Frequency Division Multiplexing
FDMA Frequency Division Multiple Access
FDTD Finite Difference Time Domain
FEC Forward Error Correction
FFT Fast-Fourier Transform
FP Fabry-Perot
FPGA Field-Programmable Gate Array
FSAN Full Service Access Network
FSR Free Spectral Range
FTTH/B Fiber-to-the-Home/Building
FWHM Full Width at Half Maximum
G-EPON Gigabit Ethernet Passive Optical Network
G-PON Gigabit Passive Optical Network
GVD Group Velocity Dispersion
HD3 Third-order Harmonic Distortion
ICI Inter-carrier Interference
IF Intermediate Frequency
IFFT Inverse Fast-Fourier Transform
IM/DD Intensity-Modulated/Directly-Detected
IP3 Third-Order Interception Point
ISI Inter-symbol Inteference
ITU International Telecommunication Union
ITU-T International Telecommunication Union-Telecommunication Standardization Sector
LO Local Oscillator
LPF Lowpass Filter
LR-PON Long-reach Passive Optical Networks
LTE Long-Term Evolution
MMF Multi-Mode Fiber
MMI Multimode Interferometer
MOS Metal-oxide-semiconductor
MZI Mach-Zehnder Interferometer
MZM Mach-Zehnder Modulator
NEP Noise Equivalent Power
NG-PON1 Next Generation Passive Optical Networks : Stage 1
NG-PON2 Next Generation Passive Optical Networks : Stage 2
NRZ Non-Return to Zero
ODN Optical Distribution Network
OFDM Orthogonal Frequency Division Multiplexing
OFDMA Orthogonal Frequency Division Multiple Access

OFC Optical Fiber Communication Conference
OLT Optical Line Terminal
OM Optical Modulator
OMI Optical Modulation Index
ONT Optical Network Terminal
ONU Optical Network Unit
OOK On-Off Keying
OSNR Optical Signal-to-Noise ratio
PAPR Peak-to-Average Power Ratio
PBS Polarization Beam Splitter
PM Polarization-Multiplexing
PMD Polarization Mode Dispersion
PON Passive Optical Networks
PRBS Pseudo-Random Binary Sequence
PSD Power Spectral Density
PSK Phase-Shift Keying
PtP Point-to-Point
QAM Quadrature Amplitude Modulation
QPSK Quadrature Phase-Shift Keying
RBS Rayleigh Backscattering
REAM Reflective Electro-absorption Modulator
RF Radio-Frequency
RIN Relative Intensity Noise
RMS Root Mean Square
RSOA Reflective Semiconductor Optical Amplifier
RZ Return to Zero
SER Symbol Error Rate
SFDR Spurious-free Dynamic Range
SFO Sampling Frequecy Offset
SMF Single-mode Fiber
SMSR Side-mode Suppression Ratio
SNR Signal-to-Noise ratio
SOA Semiconductor Optical Amplifier
SOI Silicon-on-Insulator
SOP State of Polarization
SSB Single-Side Band
SSBI Signal-to-Signal Beat Interference
TDM Time-division Multiplexing
TDMA Time Division Multiple Access
TE Transverse Electric
TIA Transimpedance Amplifier
TWDM Time and Wavelength Division Multiplexing
TWE Travelling-wave Electrode
UL Uplink
VCSEL Vertical Cavity Surface Emiting Laser
VDSL Very-high-bit-rate DSL

VDSL2 Very-high-bit-rate DSL 2
VEA Variable Electrical Attenuator
VNA Vector Network Analyser
VOA Variable Optical Attenuator
WDM Wavelength-Division Multiplexing
WDMA Wavelength-Division Multiple Access
WLAN Wireless Local Area Network
xDSL Digital Subscriber Line
XG-PON 10-Gigabit Passive Optical Network
XG-PON1 10-Gigabit Passive Optical Network 1
XG-PON2 10-Gigabit Passive Optical Network 2

List of Publications

Journal

1. **G. Beninca de Farias**, S. Menezo, B. Ben Bakir, A. Descos, E. Grellier, "12.4Gbps Adaptive OFDM Modulation of a 1550nm Hybrid III/V-on-Silicon Laser over 50km SMF-link", *IEEE Photonics Technology Letters*, Vol. 25, No. 19, October 2013, pp. 1871-1874.

International Conferences

2. **G. Beninca De Farias**, S. Menezo, O. Dubray, D. Marris-Morini, L. Vivien, A. Myko, B. Blampey, "Up to 64-QAM Modulation of a Silicon-Ring-Resonator-Modulator," *Optical Fiber Communication Conference (OFC)*, 2014.
3. A. Descos, C. Jany, D. Bordel, H. Duprez, **G. Beninca de Farias**, P. Brianceau, S. Menezo and B. Ben Bakir, "Heterogeneously Integrated III-V/Si Distributed Bragg Reflector Laser with Adiabatic Coupling," *European Conference on Optical Communications (ECOC)*, 2013.
4. **G. Beninca de Farias**, S. Menezo, A. Descos, B. Ben Bakir, E. Grellier, "Up to 21.5Gbps Direct Adaptive OFDM Modulation of a Hybrid III/V-on-Silicon Laser," *Conference on Lasers and Electro-Optics (CLEO)*, 2013.
5. S. Menezo, E. Grellier, **G. Beninca de Farias**, A. Descos, B. Ben Bakir, D. Thomson, J. M. Fedeli, C. Chauveau, C. Kopp, P. Grosse, D. Fowler, "Evaluation of optical interconnects built up from a complete CMOS-Photonics-devices-library," *Optical Interconnects Conference (OIC)*, 2013.
6. A. Lebreton, B. Charbonnier, **G. Beninca de Farias**, P. Chanclou, R. Dong, J. Le Masson and S. Menezo, "Low Complexity FDM/FDMA Approach for Future PON," *Optical Fiber Communication Conference (OFC)*, 2013.
7. S. Menezo, B. Charbonnier, **G. Beninca de Farias**, D. Thomson, P. Grosse, A. Myko, J. M. Fedeli, B. Ben Bakir, G. T. Reed, A. Lebreton, "Reflective Silicon Mach Zehnder Modulator with Faraday Rotator Mirror effect for self-coherent transmission," *Optical Fiber Communication Conference (OFC)*, 2013.
8. S. Menezo, **G. Beninca de Farias**, B. Ben Bakir, A. Descos, N. Genay, "12.6Gbps Direct OFDM Modulation of a Hybrid III-V-on-Silicon laser," *Group Four Photonics Conference (GFP)*, 2012.
9. L. Anet Neto, **G. Beninca de Farias**, N. Genay, S. Menezo, B. Charbonnier, P. Chanclou, C. Auptit-Berthelemot, "On the Limitations of IM/DD WDM-FDMA-OFDM PON with Single Photodiode for Upstream Transmission," *Optical Fiber Communication Conference (OFC)*, 2012.

National Conferences

10. **G. Beninca de Farias** and S. Menezo, "Démonstration Expérimentale d'une Transmission OFDM Optique Adaptative sur 50km de fibre monomode atteignant 11Gbps avec 3GHz de Bande Passante," *Journées Nationales d'Optique Guidée (JNOG)*, 2012.
11. **G. Beninca de Farias**, S. Menezo, M. Huchard and D. Mestdagh, "Validation de la Plateforme de Simulation OFDM optique pour transmission long-haul avec détection directe," *Journées Nationales du Réseau Doctoral en Micro-nanoélectronique (JNRDM)*, 2011.

Patents

12. **G. Beninca de Farias** and Sylvie Menezo, "Dispositif de génération dúne modulation d'un signal optique," French Patent, Number 1358376, 2 September 2013.

Abstract : In the context of Passive Optical Networks (PON), future generations should provide improved aggregated data-rate, increased number of users and reach, as well as low-cost transceivers. Optical Orthogonal Frequency Division Multiplexing (OFDM) combined with silicon photonics technology can fulfill both these requirements. In this thesis, transmitter solutions for PONs and based on Silicon Photonics technology are proposed and assessed. For that purpose, a dedicated simulation platform is developed, together with an experimental test-bed, enabling several transmitter solutions to be evaluated in different link architectures. They are used to benchmark state-off-the-art/off-the-shelf optical components with silicon photonics components. Results show that the Silicon photonics components allow very efficient modulation formats with relatively low penalty as compared to commercial solutions. Besides, recent developments on high-speed digital signal processing and D/A-A/D converters, using CMOS technologies, make optical-OFDM an attractive solution for future PONs as full-Silicon-transmitters could be used.

Keywords : Optical Communications, Silicon Photonics, OFDM, Optical Modulation, Signal Processing.

Résumé : Dans le contexte des réseaux optiques passifs (PON), les générations futures doivent fournir une augmentation du débit agrégé, du nombre d'utilisateurs, et de la portée des transmissions, tout en implémentant des solutions d'émetteurs-récepteurs bas coût. La combinaison entre Orthogonal Frequency Division Multiplexing (OFDM) Optique et la technologie Photonique sur Silicium peut répondre á ces besoins. Dans les travaux de thÃĺse rapportés ici, sont proposées et étudiées différentes solutions de transmetteurs pour les PONs, basées sur la technologie Photonique Silicium. Une plateforme de simulation ainsi qu'un banc expérimental ont été mis en place afin d'évaluer plusieurs solutions de transmetteurs, implémentées suivant différentes architectures de liens. La simulation et l'expérimentation permettent ainsi de comparer des composants de technologie différentes, et á l'état de l'art, avec les composants de la technologie Photonique Silicium. Les résultats montrent que les solutions "Photonique Silicium" permettent d'atteindre des formats de modulations efficaces avec des pénalités relativement faibles comparées aux solutions sur étagÃĺre á l'état de l'art. Par ailleurs, le développement récent en technologies CMOS, d'algorithmes de traitement numérique du signal et de convertisseurs numériques-analogiques á haut débit font de l'OFDM une solution trÃĺs attractive pour les futures générations de PONs, puisque des transmetteurs tout-Silicium peuvent désormais Ãłtre envisagés.

Mots clés : Communications Optiques, Photonique sur Silicium, OFDM, Modulation Optique, Traitement du Signal.